



THE UNIVERSITY
of ADELAIDE

POWDER METALLURGY SYNTHESIS OF
FERROMAGNETIC HEUSLER ALLOYS: FEASIBILITY
AND MICROSTRUCTURAL CHARACTERIZATION
STUDIES

School of Mechanical Engineering
The University of Adelaide

Riaz Ahamed Ahamed Khan

PhD Thesis

December 2019

Powder metallurgy synthesis of ferromagnetic Heusler alloys: Feasibility and microstructural characterization studies

Abstract

Ni-Mn-X (X – Ga, Sn, In, Sb) based ferromagnetic Heusler alloys are deemed to be multiferroic materials with the multiferroicity realized by engineering reversibility through composition tuning, of an inherent first-order diffusionless martensitic phase transformation and a second-order magnetic transition accompanying the first with the application of an electromagnetic field. Martensitic phase transformation transforms high-temperature austenite phase to low-temperature martensite phase while magnetic transition changes the electromagnetic ordering in the phases. The engineered reversibility of the magnetostructural transformations is brought with remarkable functional changes such as change in entropy, saturation magnetization, strain recovery, etc. that offer great scope for applications. There are examples in literature of such alloys with great potential for magnetic refrigeration by virtue of a giant entropy change, or with potential for magnetic shape memory effect because of giant magnetic field-induced strains. However, the most interesting characteristics of these alloys is their ability in the conversion of waste heat into electricity on account of the sudden thermally induced surge in saturation magnetization around the phase transformation, suitably utilized to generate electricity.

A majority of these ferromagnetic Heusler alloys have been synthesised by liquid processing method of arc/induction-melting of high purity elements in a controlled environment usually followed by annealing. Synthesis procedures which are a sequel to arc/induction melting such as rapid solidification by melt-spinning, directional

solidification etc. are also prevalent. Solid processing through powder metallurgy is sparsely employed on pre-alloyed powders of these alloys and not elemental powders even though use of elemental powders is advantageous for reasons such as good compaction characteristics and ease of obtaining new alloy compositions through precise control of stoichiometry.

Ferromagnetic Heusler alloys of compositions discussed herein are meant to transform martensitically and vice versa, irrespective of the way they are synthesized. Do these alloys necessarily have to be synthesized through liquid processing? The question is broader in concept and the lack of literature on solid processed ferromagnetic shape memory Heusler alloys provided scope for investigation of the feasibility of adopting conventional pressure-less sintering process as a cost-effective alternative to casting. This research therefore endeavoured to explore the feasibility of solid processing of ferromagnetic Heusler alloys through conventional sintering using elemental powders.

The starting composition was $\text{Ni}_{45}\text{Co}_5\text{Mn}_{40}\text{Sn}_{10}$. The choice of composition was the singular magnetostructural behaviour at phase transformation of the cast composition that drove its potential as an energy material similar to or even better than thermoelectric materials. Two sets of alloys were prepared – a quinary $\text{Ni}_{45}\text{Co}_5\text{Mn}_{40}(\text{Sn},\text{Cu})_{10}$ and quaternary $\text{Ni}_{45}\text{Co}_5\text{Mn}_{40}\text{Sn}_{10}$ using the conventional press and sinter procedure. The quinary compacts were prepared at a compaction load of 70 KN (184 MPa) and sintered at two different temperatures of 950°C and 1050°C for 24 h in order to first study the feasibility of powder processing in fabricating these alloys. The addition of Cu in the quinary composition was to understand the effect of compositional change on the transformation temperatures. With the results of the quinary alloy turning out to be favourable, quaternary alloys were then synthesized in order to understand the effect of process parameters such as

compaction pressure, temperature and time of sintering on the magnetostructural characteristics of these alloys. The quaternary compacts were prepared at two different compaction loads of 70 KN (184 MPa) and 80 KN (210 MPa). Sintering on them was carried out at two different temperatures of 950 °C and 1050 °C at sintering times of 12, 24, 72 and 144 h. With the use of standard characterization techniques of differential scanning calorimetry, optical/electron microscopy including transmission electron microscopy, X-ray diffraction and magnetization testing various issues concerning synthesis and characterization of ferromagnetic Heusler alloys using powder metallurgy are reported and discussed.

Declaration

I certify that this work contains no material which has been accepted for the award of any other degree or diploma in my name, in any university or other tertiary institution and, to the best of my knowledge and belief, contains no material previously published or written by another person, except where due reference has been made in the text. In addition, I certify that no part of this work will, in the future, be used in a submission in my name, for any other degree or diploma in any university or other tertiary institution without the prior approval of the University of Adelaide and where applicable, any partner institution responsible for the joint award of this degree.

I give consent to this copy of my thesis, when deposited in the University Library, being made available for loan and photocopying, subject to the provisions of the Copyright Act 1968. The author acknowledges that copyright of published works contained within this thesis resides with the copyright holder(s) of those works.

I also give permission for the digital version of my thesis to be made available on the web, via the University's digital research repository, the Library Search and also through web search engines, unless permission has been granted by the University to restrict access for a period of time.

I acknowledge the support I have received for my research through the provision of an Australian Government Research Training Program Scholarship.

Riaz Ahamed Ahamed Khan

23/12/19

Date

List of Publications

1. Ahamed, R, Ghomashchi, R, Xie, Z, Chen, L, Munroe, P & Xu, S 2018, 'Powder processing and characterisation of a quinary Ni-Mn-Co-Sn-Cu Heusler alloy', Powder Technology, vol. 324, pp. 69-75.
2. Ahamed, R, Ghomashchi, R, Xie, Z, Chen, L 2019, 'Powder Metallurgy Synthesis of Heusler Alloys: Effects of Process Parameters', Materials, vol. 12, 1596.

List of publications (not used in this thesis)

3. Ahamed Khan, R.A, Ghomashchi, R, Xie, Z, Chen, L 2018, 'Ferromagnetic Shape Memory Heusler Materials: Synthesis, Microstructure Characterization and Magnetostructural Properties', Materials, vol. 11, 988.
4. Ahamed Khan, R.A.; Ghomashchi, R.; Xie, Z.; Chen, L, 'Techniques to characterize ternary and quaternary magnetic shape memory alloys'. (In manuscript form).

Summary of each paper

Paper 1 (Published)

Ni-Co-Mn-Sn alloys were sintered from elemental powders at a temperature of 1050 °C for 24 h. The resulting microstructures and physical properties were characterized by differential scanning calorimetry, X-ray diffraction, optical/electron microscopy and SQUID magnetometry. The use of the alloys in energy conversion was satisfactorily tested. The new alloys exhibited a distinct martensitic transformation when cooled to room temperature. The presence of Cu in the powders moved the transformation temperature toward a higher value. The findings of this study demonstrate that powder processing could be applied to replace time-consuming arc/induction melting process in the development of high performance Heusler alloys at a lower cost.

Paper 2 (Published)

Ni₄₅Co₅Mn₄₀Sn₁₀ Heusler alloy was fabricated with elemental powders, using a powder processing route of press and sinter, in place of vacuum induction melting or arc melting route. The effects of process parameters, such as compaction load, sintering time, and temperature, on the transformation characteristics and microstructures of the alloy were investigated. While the effect of compaction pressure was not significant, those of sintering time and temperature are important in causing or annulling martensitic transformation, which is characteristic of Heusler alloys. The processing condition of 1050 °C/24 h was identified to be favourable in producing ferromagnetic Heusler alloy. Longer durations of sintering resulted in an increased γ -phase fraction, which acts as an impediment to the structural transformation.

Paper 3 (Published; included in Appendix 1)

An overview of the processing, characterization and magnetostructural properties of ferromagnetic NiMnX (X = group IIIA–VA elements) Heusler alloys is presented. This type of alloy is multiferroic – exhibits more than one ferroic property, and is hence multifunctional. Examples of how different synthesis procedures influence the magnetostructural characteristics of these alloys are shown. Significant microstructural factors, such as the crystal structure, atomic ordering, volume of unit cell, grain size and others, which have a bearing on the properties, have been reviewed. An overriding factor is the composition which, through its tuning, affects the martensitic and magnetic transitions, the transformation temperatures, microstructures and, consequently, the magnetostructural effects.

Paper 4 (In manuscript form; included in Appendix 2)

Ni-Mn-X (X = group IIIA-VA elements) Heusler alloys have been seen to exhibit multiferroic effects such as magnetic/metamagnetic shape memory (MSM/MMSM), magnetocaloric (MC), direct energy conversion etc. and have a large potential for diverse applications in actuation, magnetic refrigeration and conversion of low grade waste heat into electricity. Beneath the multifunctional potential of these alloys is a magnetostructural coupling encompassing structural and magnetic transformations which in turn depends on alloy compositions. As compositions are varied different crystal structures are evolved and it becomes essential that the structures are accurately characterized for their microstructures. This paper provides a short review of characterization techniques such as X-ray diffraction, transmission electron microscopy and differential scanning microscopy with examples from literature. Emphasis is laid on XRD and TEM which are very important for microstructural characterization.

Acknowledgements

First and foremost I thank the Lord Almighty for His blessings.

I would like to express my sincere thanks to my supervisors Dr Lei Chen, Associate Professor Dr Reza Ghomashchi and Professor Dr Zonghan Xie for their tremendous support, assistance, guidance, advice, feedback and counsel, throughout my candidature. A very special thanks to Dr Reza Ghomashchi who walked the extra mile in supervision.

I thank all at the University of Adelaide who partly or substantially helped me in my work. They include all the good people at the Engineering Workshop and Administration – Mechanical Engineering, Chapman Lab – Civil Engineering, Materials Analysis Lab – Chemical Engineering, Adelaide Microscopy, Institute of Photonics and Advanced Sensing, Johnson and Badgers Laboratories, Mawson Lab and CSIRO, Waite Campus. My thanks are also due to Future Industries Institute – University of South Australia, School of Physics – University of Western Australia, Professor Dr Paul Munroe and Dr Song Xu of University of New South Wales, Advanced Centre for Materials Science, Indian Institute of Technology Kanpur and all colleagues particularly Dr Md. Raihanuzzaman Rumman for his critical inputs to my review article.

Finally I thank my wife and children for their pristine love, patience and support.

Table of Contents

Abstract	i
Declaration	iv
List of Publications	v
Summary of each paper	vi
Acknowledgements	viii
Table of Contents	ix
List of Figures	xii
List of Tables	xvii
Abbreviations	xviii
Definitions of terms	xx
1 Introduction	1
1.1 Multiferroic: Heusler materials and multiferroic effects	1
1.1.1 Martensitic transformation	2
1.1.2 Heusler materials	3
1.1.3 Multiferroic effects	5
1.2 Synthesis	6
1.3 Contributions arising from this thesis	7
2 Background – Fundamental Concepts	10
2.1 Magnetostructural effects seen in Heusler alloys	10
2.1.1 Magnetocaloric effect	11
2.1.2 Magnetic/metamagnetic shape memory effect	12
2.1.3 Direct energy conversion	15
3 Processing and Characterization of Heusler alloys	19
3.1 Introduction	19
3.2 Liquid processing	19

3.2.1	A review of liquid processed Heusler alloys-----	21
3.2.2	Magnetostructural effects seen in liquid processed alloys -----	24
3.2.3	Characterization of liquid processed alloys -----	27
3.2.3.1	Differential scanning calorimetry-----	27
3.2.3.2	Optical microscopy -----	32
3.2.3.3	Electron Microscopy – scanning electron microscope (SEM), transmission electron microscope (TEM), electron probe microanalysis (EPMA)-----	37
3.2.3.4	X-ray diffraction (XRD) -----	45
3.2.3.5	Magnetometry -----	53
3.2.4	Effects of microstructure on properties -----	58
3.2.5	Heat treatment of ferromagnetic Heusler alloys-----	61
3.2.6	Phase equilibria -----	62
3.3	Solid Processing -----	68
3.3.1	Powder metallurgy – powder production, mixing and consolidation -----	68
3.3.1.1	Sintering – pressure-assisted and pressureless -----	70
3.3.1.2	Mechanism of sintering, densification and transport mechanisms-----	72
3.3.2	A review of solid processed Heusler alloys -----	75
3.3.3	Magnetostructural effects seen in solid processed alloys -----	79
3.3.4	Characterization of solid processed alloys -----	82
3.4	Summary -----	84
4	Materials and Experimental Procedure -----	87
4.1	Powder characterization – particle size and distribution -----	87
4.2	Fabrication processing -----	90
4.2.1	Powder mixing and compaction -----	90
4.2.2	Pressureless sintering in Ar atmosphere-----	91
4.3	Density measurements-----	92
4.4	Metallography -----	93
4.5	Hardness measurements -----	94

4.6	Differential scanning calorimetry -----	95
4.7	Microstructural analysis -----	96
4.7.1	X-ray diffraction -----	96
4.7.2	Optical microscopy -----	96
4.7.3	Scanning electron microscopy -----	97
4.7.4	Transmission electron microscopy -----	99
4.7.5	Electron probe microanalysis (EPMA) -----	99
4.7.6	Magnetization measurements -----	100
5	Powder processing and characterisation of a quinary Ni-Mn-Co-Sn-Cu Heusler alloy -----	102
6	Powder metallurgy synthesis of Heusler alloys: Effects of Process Parameters -----	112
7	Conclusions -----	132
7.1	Significance of this study and future work -----	135
8	References -----	137
9	Appendix 1 -----	153
	Ferromagnetic Shape Memory Heusler Materials: Synthesis, Microstructure Characterization and Magnetostructural Properties.-----	153
10	Appendix 2-----	190
	Techniques to characterize ternary and quaternary magnetic shape memory alloys.-----	190

List of Figures

- Figure 1. Schematic representation of the Bain lattice correspondence between principal axes of b.c.t. martensite and f.c.c. austenite (γ) unit cells. The Bain strain involves a contraction along $[001]\alpha'$ and expansions parallel to $[100]\alpha'$ and $[010]\alpha'$ to generate an α' cell of appropriate dimensions (Muddle & Nie 2001).-----3
- Figure 2. The list of elements in the periodic table for the formation of Heusler (X_2YZ) and half-Heusler (XYZ) alloys (Hooshmand Zaferani, Ghomashchi & Vashae 2019).-----5
- Figure 3. Mechanism of shape memory effect and superelasticity illustrated (Otsuka & Kakeshita 2002). ----- 13
- Figure 4. Schematic representation of magnetic shape-memory effect (adapted from (Planes, Mañosa & Acet 2009)). ----- 14
- Figure 5. (a) Schematic of the experimental setup for the measurement of induced emf: C, coil; R, heat source; M, permanent magnet; S, $Ni_{45}Co_5Mn_{40}Sn_{10}$; T, thermocouple; V, voltmeter; (b) actual view of the experimental setup (Srivastava et al. 2011) ----- 16
- Figure 6. (a) Magnetization vs. temperature under 1 T field; (b) Voltage vs. temperature (Srivastava et al. 2011).----- 17
- Figure 7. DSC curves showing forward and reverse martensitic transformation and Curie temperature of $Ni_{42}Co_8Mn_{39}Sn_{11}$ alloy (Lázpita et al. 2016). ----- 28
- Figure 8. DSC plots of $Ni_{50}Mn_{50-x}Sn_x$ alloys undergoing martensitic transformations (a) $x=15$; (b) $x=13$; (c) $x=0.10$; (d) $x=0.05$ (Krenke, Acet, et al. 2005).----- 29
- Figure 9. (a) DSC curve of $Ni_{46}Co_4Mn_{39}Sn_{11}$ alloy in $Ni_{50-x}Co_xMn_{39}Sn_{11}$ system; (b) Composition dependence of transformation temperatures in $Ni_{50-x}Co_xMn_{39}Sn_{11}$ alloys (Cong, D.Y., Roth & Schultz 2012).----- 30
- Figure 10. DSC curves of: (a) $Ni_{50}Mn_{34.5}In_{15.5}$ alloy (Ito, W et al. 2007); (b) $Mn_{50}Ni_{40-x}In_{10}Co_x$ alloys (Wu et al. 2011). ----- 30
- Figure 11. DSC curves of: (a) $Ni_{50}Mn_{32.7}Cu_{1.3}In_{16}$ alloy; (b) $Ni_{50}Mn_{32.4}Cu_{1.6}In_{16}$ alloy (Kaya, M. et al. 2014).----- 31
- Figure 12. DSC data $Ni_{50}Mn_{37}Sn_{13}$ showing the effect of heat treatment duration at 950 °C on the occurrence, temperature, and sharpness of the martensitic shape memory transformation (Schlagel, McCallum & Lograsso 2008). ----- 31

Figure 13. Optical micrographs of $\text{Ni}_{0.50}\text{Mn}_{0.50-x}\text{Sn}_x$ revealing L2_1 structure for $x = 0.25$, 10M for $x = 0.13$, 14M for $x = 0.10$ and L1_0 for $x = 0.05$ (Krenke, Acet, et al. 2005).

----- 33

Figure 14. Optical micrographs of $\text{Ni}_{50}\text{Mn}_{37}\text{Sn}_{13}$ showing the effect of heat treatment: (a) as-cast; (b) 1 h; (c) 2 h; (d) 72 h at 950°C . (Schlagel, McCallum & Lograsso 2008).

----- 34

Figure 15. Optical micrographs of (a) $\text{Ni}_{43}\text{Co}_7\text{Mn}_{39}\text{Sn}_{11}$ alloy after 14 days at 900°C (b) after 5 days at 950°C (c) after 15 days at 950°C (d) $\text{Ni}_{44.5}\text{Co}_{5.5}\text{Mn}_{39.5}\text{Sn}_{10.5}$ at uncontrolled cooling rate; (e) $\text{Ni}_{45}\text{Co}_5\text{Mn}_{40}\text{Sn}_{10}$ at $10^\circ\text{C}/\text{min}$ and (f) $\text{Ni}_{43}\text{Co}_7\text{Mn}_{39}\text{Sn}_{11}$ at $10^\circ\text{C}/\text{min}$ [(a)-(f) (Pérez-Sierra, A.M. et al. 2015)] (g) $\text{Ni}_{40}\text{Co}_{10}\text{Mn}_{39}\text{Sn}_{11}$ (Cong, D.Y., Roth & Schultz 2012) (h) $\text{Ni}_{47}\text{Al}_{25}\text{Fe}_{11}\text{Co}_{17}$ (Oikawa et al. 2006).

----- 36

Figure 16. BSE images of $\text{Ni}_{38}\text{Co}_{12}\text{Mn}_{41}\text{Sn}_9$ (Chen, F et al. 2013): (a) as-cast ; (b) annealed at 1173 K for 1 h; (c) as-spun ribbon: (d) & (e) $\text{Ni}_{44.1}\text{Mn}_{35.1}\text{Sn}_{10.8}\text{Co}_{10}$ alloy at different magnifications (Yu et al. 2014); (f) $\text{Ni}_{45}\text{Co}_5\text{Mn}_{40}\text{Sn}_{10}$; (g) $\text{Ni}_{44.5}\text{Co}_{5.5}\text{Mn}_{39.5}\text{Sn}_{10.5}$; (h) $\text{Ni}_{43}\text{Co}_7\text{Mn}_{39}\text{Sn}_{11}$ [(f)-(h) (Pérez-Sierra, A.M. et al. 2015)]

----- 39

Figure 17. BSE images of $\text{Ni}_{43}\text{Mn}_{42}\text{Co}_4\text{Sn}_{11}$ alloy: (a) solutionized bulk; (b) solutionized ribbon (Bruno, Nickolaus M. et al. 2014).

----- 40

Figure 18. SEM micrographs of $\text{Ni}_{50}\text{Mn}_{37}\text{Sn}_{13}$ showing the effects of heat treatment at 950°C followed by water quench: (a) as-cast; (b) 1 h; (c) 2 h; (d) 72 h; (e) EDS line scans spanning $500\ \mu\text{m}$ on $\text{Ni}_{50}\text{Mn}_{37}\text{Sn}_{13}$ samples after different lengths of heat treatment at 950°C . The frequency and range of the compositional changes decrease with heat treatment (Schlagel, McCallum & Lograsso 2008).

----- 40

Figure 19. Bright field TEM images of: (a) $\text{D0}_3/\text{martensite}$; (b) martensite plates; (c) $\gamma/\text{L2}_1$ phases; (d) SAED patterns of the 6-layered martensite of 1 variant; (e) SAED patterns of the 6-layered martensite of 2 variants nearly orthogonal; (f) high resolution TEM image of the microtwinned 6-layered martensite (Pérez-Sierra, A.M. et al. 2015).

----- 42

Figure 20. SAED patterns of the face centered cubic γ -phase in metamagnetic shape memory alloys: (a) $\text{Ni}_{45}\text{Co}_5\text{Mn}_{40}\text{Sn}_{10}$, $\text{Ni}_{44.5}\text{Co}_{5.5}\text{Mn}_{39.5}\text{Sn}_{10.5}$ and $\text{Ni}_{43}\text{Co}_7\text{Mn}_{39}\text{Sn}_{11}$ (Pérez-Sierra, A.M. et al. 2015); (b) $\text{Ni}_{44.1}\text{Mn}_{35.1}\text{Sn}_{10.8}\text{Co}_{10}$ (Yu et al. 2014)

----- 43

Figure 21. (a) TEM bright-field image of the 14M martensite in as-cast $\text{Ni}_{50}\text{Mn}_{41}\text{Sn}_9$: (b) corresponding SAED patterns taken from the highlighted area (Zheng et al. 2013).

----- 43

Figure 22. (a) and (b) TEM bright-field images of as-cast $\text{Ni}_{50}\text{Mn}_{39}\text{Sn}_{11}$. (c) - (e) corresponding SAED patterns of 4O, 10M and L1_0 martensites (Zheng et al. 2013).

----- 44

Figure 23. (a) TEM bright-field image of as-cast Ni ₅₀ Mn ₃₇ Sn ₁₃ ; (b) HR TEM image of L ₂₁ austenite and 4O martensite (Zheng et al. 2013).	44
Figure 24. XRD patterns of: (a) as-cast; (b) annealed alloys. The alloys bottom-up are Ni ₄₆ Mn ₄₁ Sn ₁₃ , Ni ₄₈ Mn ₃₉ Sn ₁₃ , Ni ₅₀ Mn ₃₇ Sn ₁₃ , Ni ₅₀ Mn ₃₉ Sn ₁₁ and Ni ₅₀ Mn ₄₁ Sn ₉ (Zheng et al. 2013).	46
Figure 25. XRD patterns of: (a) the 6-layered martensite, D0 ₃ and a mixture of L ₂₁ and γ -phase (Pérez-Sierra, A.M. et al. 2015) (b) bulk and as-spun alloy samples at room temperature (Chen, F et al. 2013)	47
Figure 26. Room temperature XRD patterns of (a) as-spun ribbons and (b) R ₃ ribbons annealed at different temperatures (Das et al. 2013).	48
Figure 27. (a) Rietveld refinement patterns of Ni ₅₀ Mn _{32.7} Cu _{1.3} In ₁₆ alloy (top) and Ni ₅₀ Mn _{32.4} Cu _{1.6} In ₁₆ (bottom) alloy (Kaya, M. et al. 2014); (b) Room temperature XRD patterns of Ni _{50-x} Cu _x Mn ₃₈ Sn ₁₂ (x=0, 2, 4, 6) alloys. For x = 0 and x = 2, the crystal structures are 10M modulated martensitic structures. For x = 6 the structure is L ₂₁ and for x = 4 the structure is a coexistent L ₂₁ and 10M (Jing et al. 2013).	50
Figure 28. Room temperature XRD diffraction patterns of: (a) Ni ₄₄ Cu ₆ Mn ₃₉ Sn ₁₁ alloy (top panel) and Ni ₄₃ Cu ₇ Mn ₃₉ Sn ₁₁ alloy (bottom panel) (Kaya, Melike & Dincer 2017); (b) Ni ₄₂ Co ₈ Mn ₃₉ Sn ₁₁ alloy (Lázpita et al. 2016).	50
Figure 29. X-ray diffraction patterns shown in the range $30^\circ \leq 2\theta \leq 60^\circ$. (a)-(k) show patterns with varying temperature for x = 20.3, 16.2, 15.1, 13.0, 11.4, 11.0, 10.1, 8.8, 7.1 and 5.1 respectively (Çakır et al. 2015).	52
Figure 30. Principle of working of a SQUID magnetometer (National SQUID Facility).	53
Figure 31. (a) – (d) M(T) and M(H) curves of Ni _{0.50} Mn _{0.35} Sn _{0.15} alloy (Krenke, Acet, et al. 2005)	55
Figure 32. (a) Magnetization as a function of temperature for Ni ₅₀ Mn ₃₇ Sn ₁₃ alloy in the as-cast condition and annealed at 950 °C for 2h and 4w (Schlagel, McCallum & Lograsso 2008); (b) Magnetization vs Temperature curves of Ni ₅₀ Mn _{50-x} Sn _x (x = 13, 14,15 & 16). For x = 13 the magnetization data was measured at 5 T and 0.1 T while for others the applied field was 5 T (Khan et al. 2008).	56
Figure 33. M-T curve under a magnetic field of 0.05 T in the temperature range of 500 - 300 K of Ni ₄₅ Co ₅ Mn ₃₉ Sn ₁₁ alloy; (b) M-H curves of the austenite at 355 K and 365 K (below T _c) of Ni ₄₅ Co ₅ Mn ₃₉ Sn ₁₁ alloy; (Inset) M-H curve of martensite at 180 K of sigmoid shape(Cong, D.Y., Roth & Schultz 2012).	57

Figure 34. (a) Vertical section of the $\text{Ni}_{50}\text{Mn}_{50-x}\text{Sn}_x$ ($0 \leq x \leq 50$ at%) (Wachtel, Henninger & Predel 1983); (b) Phase diagram of $\text{Ni}_{50-x}\text{Co}_x\text{Mn}_{39}\text{Sn}_{11}$ ($0 \leq x \leq 10$) alloy system (Cong, D.Y., Roth & Schultz 2012). ----- 64

Figure 35. Phase diagram of $\text{Ni}_{50}\text{Mn}_{50-x}\text{Sn}_x$ alloys. Filled circles represent austenite-martensite transition temperatures, open circles correspond to the martensitic and austenitic Curie temperatures. Intermartensitic transition temperatures are shown by red triangles (Çakır et al. 2015).----- 65

Figure 36. Phase diagram of $\text{Ni}_{45}\text{Co}_5\text{Mn}_{40}\text{Sn}_{10}$ alloy developed using ThermoCalc (Yeldhose 2015). ----- 67

Figure 37. The circle approximation for the neck saddle surface (convex curvature is described by the diameter X while concave curvature is described by the diameter p) enables linkage between neck size and neck volume. A modified geometry with center-center attraction links neck size to sintering shrinkage (German 2014b). ----- 71

Figure 38. Graphical representation of the sintering stages, assuming the spherical particles start as a loose structure. Neck growth produces densification, round pores, and a strong body. Grain boundaries form at the particle contacts and grow as the necks merge (German 2014b). ----- 72

Figure 39. Mass transport paths illustrated in the two sphere sintering model. E-C, evaporation-condensation; SD, surface diffusion; VD, volume diffusion; GD, grain boundary diffusion; PF, plastic flow (Xu 2000). ----- 73

Figure 40. Sintering time dependence of porosity fraction (Ito, K et al. 2010) ----- 76

Figure 41. Porous sample sintered for: (a) 12 h; (b) 96 h; (c) 144 h (Ito, K et al. 2010); (d) sample synthesized by spark plasma sintering (Ito, K et al. 2009). ----- 80

Figure 42. X-Ray diffraction patterns of sintered alloys in 2θ range a) $30 - 115^\circ$; (b) $45 - 55^\circ$. (Maziarz, W. et al. 2017). ----- 83

Figure 43. Set of TEM microstructures consist of (a) STEM-HAADF image; (b) and (c) bright field images and corresponding selected area diffraction patterns of In0 sintered sample (Maziarz, W. et al. 2017). ----- 83

Figure 44. Thermo-magnetization curves measured at low magnetic field (100 Oe) during field cooling (FC) and field heating (FH) with superimposed DSC curves in the same temperature range for a) In0 and b) In5 sintered samples (Maziarz, W. et al. 2017).----- 84

Figure 45. Mastersizer 2000 used in particle size analysis ----- 88

Figure 46. Particle size distribution of constituent powders (reproduced from (Ahamed et al. 2018)) and (inset) SEM micrograph of Sn powder.----- 89

Figure 47. (a) Die and punch; (b) a pair of green and sintered compacts ----- 91

Figure 48. (a) BSE image of sample 1 (refer Table 2); (b) Compositional map of phase MnK/NiK/SnL/CoK; (c) Element overlay; (d) to (h) Elemental distribution of Sn, Mn, Co, Ni and Cu respectively; (i) and (inset) Composition of phase shown in red in (b).----- 98

Figure 49. Ni₄₅Co₅Mn₄₀Sn₁₀ alloy (a) M-T under 1 T field; (b) DSC plot; (c) M-H curve of martensite; (d) M-H curve of austenite (Srivastava et al. 2011). ----- 101

List of Tables

Table 1. Examples of liquid processed alloys -----	21
Table 2 Geometric changes in the Three Stages of Sintering for Monosize Spheres (German 2014b)-----	72
Table 3 Particle sizes of different powders -----	89
Table 4. Processing conditions used for the preparation of the alloy samples -----	92
Table 5. Table shows the metallographic preparation for microstructural analysis-----	94

Abbreviations

AF	Antiferromagnetic
BSE	Backscatter electrons
C-DIC	Circular differential interference contrast
COD	Crystallography open database
DB-FIB	Dual beam focused ion beam system
DIC	Differential interference contrast
DSC	Differential scanning calorimetry
EDS	Energy-dispersive spectroscopy
EPMA	Electron probe microanalysis
FC	Field cooled
FESEM	Field emission scanning electron microscope
FH	Field heated
FM	Ferromagnetic
FP	Fundamental parameter
GNLTM	Geometric nonlinear theory of martensite
HTSMA	High temperature shape alloys
ICDD	International Centre for Diffraction Data
IUPAC	International Union of Pure and Applied Chemistry
JCPDS	Joint Committee on Powder Diffraction Standards
MC	Magnetocaloric
MCE	Magnetocaloric effect
MFIS	Magnetic field induced strain
M-H	Magnetization vs applied field
MMSME	Metamagnetic shape memory effect

MSM	Magnetic shape memory
MSME	Magnetic shape memory effect
M-T	Magnetization vs temperature
OM	Optical microscopy
PM	Powder metallurgy
RKKY	Ruder-Kittel-Kasuya-Yosida
SEM	Scanning electron microscope
SME	Shape memory effect
SQUID	Superconducting quantum interference device
STEM-HAADF	Scanning transmission electron micrograph high angle angular dark field
TEM	Transmission electron microscope
WDS	Wavelength-dispersive spectroscopy
XRD	X-ray diffraction
ZFC	Zero field cooled

Definitions of terms

Antiferromagnetic

The alignment of the spin moments of neighbouring atoms or ions in opposite, or antiparallel, arrangement throughout the material is called antiferromagnetism. There is no net magnetic moment. Materials with such behaviour (e.g. MnO) are antiferromagnetic.

Austenite

A phase in Heusler alloys with a $L2_1$ cubic structure.

Austenite start temperature

The temperature at which the transformation from martensite to austenite begins on heating. It is denoted by A_S .

Austenite finish temperature

The temperature at which the transformation from martensite to austenite finishes on heating. It is denoted by A_F .

Brillouin zone

A Brillouin zone is a particular choice of the unit cell of the reciprocal lattice. It is constructed as the set of points enclosed by the Bragg planes, the planes perpendicular to a connection line from the origin to each lattice point and passing through the midpoint.

Curie temperature

The temperature at which the ferromagnetic property of ferromagnets disappears as a result of thermal agitation. It is denoted by T_C .

Fermi surface

Fermi surface is an abstract interface that defines allowable energies of electrons in a solid.

Electrons in a solid lie within valence bands or conduction bands. Each electron has a specific energy which at absolute zero may not exceed a value called the Fermi energy. In a three dimensional momentum space the Fermi energy defines a volume whose surface known as the Fermi surface separates the occupied electronic states within the volume from the empty ones without it.

Ferroelectricity

Ferroelectricity refers to the reversible spontaneous polarization (P) of a material upon application of an electric field (E).

Ferroelasticity

Ferroelasticity refers to the spontaneous occurrence of a strain (ϵ) in a material upon application of an external stress (σ).

Ferromagnetic

Ferromagnetic materials possess permanent magnetic moments in the absence of external fields and manifest very large and permanent magnetizations.

Ferromagnetism

Ferromagnetism refers to a spontaneous and reversible magnetization (M) occurring in a material upon application of an external magnetic field (H).

Heusler materials

Heusler materials, discovered by Fritz Heusler, are materials which can be magnetic even though the constituent elements are non-magnetic or semiconducting even though the constituent elements are metals.

Intermartensitic transformations

Intermartensitic transformations happen when the martensitic phase transforms to other modulated phases at lower temperatures. These are important because reversal back to the original martensitic phase may be difficult and may lead to loss of magnetic shape memory effect.

Magnetic anisotropy

Magnetic anisotropy is the directional dependence of a material's magnetic properties. The magnetic moment of magnetically anisotropic materials will tend to align with an 'easy axis', which is an energetically favourable direction of spontaneous magnetization. The two opposite directions along an easy axis are usually equivalent, and the actual direction of magnetization can be along either of them. Magnetic anisotropy is a prerequisite for hysteresis in ferromagnets.

Magnetic/metamagnetic shape memory effect

Magnetic shape memory effect refers to the reverting back to the original orientation in the austenite phase, the stressed martensite variants of the martensite phase, when heated to above austenite finish temperature.

Metamagnetic shape memory effect refers to the recoverability upon heating, of large strains when a reverse transformation from the martensite to austenite is induced by the application of a magnetic field.

Magnetocaloric effect

Magnetocaloric effect is the reversible change of temperature accompanying the change of magnetization of a ferromagnetic or paramagnetic material. A positive value of entropy change is termed as inverse magnetocaloric effect. A negative entropy change is termed as conventional magnetocaloric effect.

Martensite

The phase to which austenite transforms upon cooling and has several modulated structures, denoted by $L1_0$, $4O$, $10M$ and $14M$.

Martensite start temperature

The temperature at which the transformation from austenite to martensite begins on cooling. It is denoted by M_S .

Martensite finish temperature

The temperature at which transformation from austenite to martensite finishes on cooling. It is denoted by M_F .

Martensitic transformation

Martensitic transformation is a diffusionless transformation in which the change in crystal structure results from the homogeneous deformation of the high-temperature face-centred cubic (f.c.c) solid solution termed austenite (γ), to a distorted tetragonal structure termed martensite (α').

Multiferroic

A material is said to be multiferroic when the simultaneous exhibit of multiple ferroic behaviours of ferroelectricity, ferroelasticity and ferromagnetism is observed in it.

Paramagnetic

A paramagnetic material has an unpaired electron because of which there is a net spin. This however does not result in macroscopic magnetization in the absence of an external magnetic field because thermal energy randomizes the spin orientations. It is therefore non-magnetic as it does not retain magnetization in the absence of a magnetic field.

Twin boundary motion

Twinning is a primary deformation mode in crystalline solids in which a fraction of the original lattice is reoriented into its mirror image through a displacement of lattice points by some integral fraction of spacing between equivalent lattice sites. Twin boundary is the grain boundary across which the mirror lattice symmetry is seen. Martensite phase is a heavily twinned phase. For shape memory effect, when the martensite is deformed by the application of stress, the deformation happens through the motion of twin boundaries.

Second neighbour ordering

This refers to the ordering within one sublattice of the basic bcc unit cell, such that this sublattice alternates atoms from different elements which introduces a face centred symmetry in the unit cell.

Superspin glass

Superspin glass has a spin-configuration which is random in nature, similar to a paramagnet frozen in time.

Super paramagnetic

Super paramagnetism is defined as the property due to which in some materials the magnetic moments change their direction at nano scale and behave like a paramagnet even below Curie temperature when no magnetic field is applied and at the same time they shown high magnetic susceptibility like ferromagnets.

Zeeman energy

The potential energy of a magnetized body in an external magnetic field.

1 Introduction

The advancement in materials technology is an enabling element of the exponential rate of technology development. It is now an era of synthesis or integration of new and improved materials with electronics, our environment, and even our human bodies via medical implants. The early classification of eras such as Bronze Age and Iron Age based on material class is now deemed inapposite (McDowell et al. 2010). The materials tree prescribed by (Ashby, Shercliff & Cebon 2007) comprising metals, polymers, elastomers, glasses, ceramics and hybrids (composite materials made by combining two or more of the others) will however hold water for a long time to come. Multifunctional materials, engineered or natural, are known to perform multiple functions by virtue of specific properties and form part of the materials tree. Multifunctionality is achieved among other means, by using multiferroic materials which respond to stimuli such as stress, electric and magnetic fields. A material is said to be multiferroic when the simultaneous exhibit of multiple ferroic behaviours of ferroelasticity, ferroelectricity and ferromagnetism is observed in it.

1.1 Multiferroic: Heusler materials and multiferroic effects

The subject of synthesis of multiferroic materials has seen an upsurge in research driven by potential technological significance that will come with it. To this extent an understanding of multiferroic behaviour becomes essential to the study of multiferroic materials synthesis. A ferroic material adopts a spontaneous, switchable internal alignment: Just as a magnetic field switches alignment of electron spins in ferromagnetics or an electric field switches electric dipole-moment alignment in ferroelectrics or a stress field switches strain alignment

in ferroelastics (Spaldin, Cheong & Ramesh 2010). Multiferroic however is largely understood as a combination of ferroelectricity and ferromagnetism in the same phase in what is known as magnetoelectric coupling (Eerenstein, Mathur & Scott 2006). The largely studied multiferroic was bismuth ferrite (BiFeO_3) in which the electric-field control of ferromagnetism was achieved through theory and experiments (Spaldin, Cheong & Ramesh 2010).

Various factors such as chemistry, symmetry, conductivity (conductor/insulator), mechanical distortion, etc. do not place any constraint on a material being multiferroic. (James & Zhang 2005) proposed an alternative to the realization of multiferroic behaviour in materials: Whereas conflicting properties like ferroelectricity and ferromagnetism are difficult to unite in a single phase, can possibly be combined in multiphase materials. The underlying phenomenon is a first-order phase transformation in which the lattice parameters and consequently the shape, change, leading to coexistent phases with different properties. If the transformation is reversible it then boils down to controlling the volume fraction of the phases. Certain characteristics such as (a) interphase boundary (b) phase transformation by application of thermal/magnetic/stress fields (c) sufficiently fast kinetics of transformation and (d) reversibility are to be simultaneously satisfied for this to happen. A diffusionless transformation such as martensitic transformation which also involves distortion was thought to be the significant requirement because changes in lattice parameters lead to changes in electromagnetic properties, implying a lattice parameter sensitivity of these properties (James & Zhang 2005).

1.1.1 Martensitic transformation

Martensitic transformation is a diffusionless transformation in which the change in crystal

structure results from the homogeneous deformation of the high-temperature face-centred cubic (f.c.c) solid solution termed austenite (γ), to a distorted tetragonal structure termed martensite (α') (Muddle & Nie 2001). A Bain correspondence between the f.c.c austenite and the body-centred tetragonal (b.c.t) martensite in iron which identifies a b.c.t cell within the f.c.c structure, shown in Figure 1 is sufficiently general to represent all martensitic transformations (Bhadeshia 2001). Martensitic transformation has been seen to be essential for multiferroic and multifunctional behaviour (Srivastava et al. 2011).

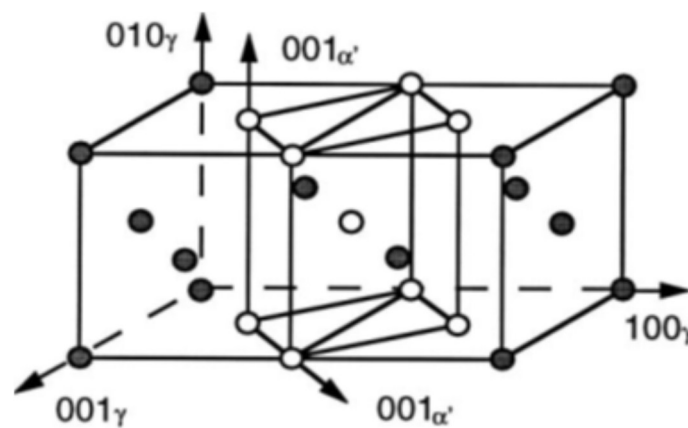


Figure 1. Schematic representation of the Bain lattice correspondence between principal axes of b.c.t. martensite and f.c.c. austenite (γ) unit cells. The Bain strain involves a contraction along $[001]_{\alpha'}$ and expansions parallel to $[100]_{\alpha'}$ and $[010]_{\alpha'}$ to generate an α' cell of appropriate dimensions (Muddle & Nie 2001).

1.1.2 Heusler materials

Heusler materials (e.g., Cu_2MnAl : magnetic even though constituent elements are nonmagnetic, TiNiSn : semiconducting even though constituent elements are metals), discovered by Fritz Heusler in 1903, are multiferroic by phase transformation involving sensitivity of electromagnetic properties to lattice changes. For instance, Ni_2MnGa transformed from austenite to martensite with an increase of saturation magnetization of

about 25% accompanied by a dramatic change in the magnetic anisotropy (Tickle & James 1999). This was explained by the fact that during the martensitic transformation the lattice structure of the Heusler Ni_2MnGa material expanded placing the Mn atoms far apart. The multiferroic nature of Heusler materials came to be known and prominent multiferroic effects such as magnetic shape memory (MSM) and magnetocaloric (MC) were already being explored.

A remarkable breakthrough in the exploration of multiferroic effects was the discovery of the potential of these alloys for use in direct energy conversion of low waste heat. This was demonstrated in the singular composition of $\text{Ni}_{45}\text{Co}_5\text{Mn}_{40}\text{Sn}_{10}$ Heusler alloy (Srivastava et al. 2011), which with an optimum geometry could give a power density comparable with that of a commercial thermoelectric generator. Low thermal hysteresis and reversibility of transformations governed by the lattice parameter sensitivity of electromagnetic properties were fundamental to the novel idea of energy conversion at small temperature difference of $\sim 10 - 100$ °C. With huge natural and man-made energy resources at small temperature difference abundantly existing to be reclaimed, this energy conversion if made available, could change the global energy landscape.

Heusler compounds are usually ternary compounds and fall into two categories, the half-Heusler with 1:1:1 stoichiometry and the Heusler with 2:1:1 stoichiometry (Graf, Felser & Parkin 2011). Half-Heusler materials have a general formula XYZ, with X and Y having distinct cationic character and Z being anionic. For purpose of nomenclature the most electropositive element is placed at the beginning and the most electronegative element is placed at the end. Heusler compounds have a general formula X_2YZ where X and Y are transition metals and Z is a main group element, Figure 2. Again for purpose of nomenclature prescribed by International Union of Pure and Applied Chemistry (IUPAC),

the metal which exists twice is placed at the beginning and the main group element is placed at the end as in Co_2MnSi , Fe_2VAl . There are exceptions as in LiCu_2Sb and YPd_2Sb wherein the metal which exists twice is placed in the middle and the most electropositive element is placed at the beginning. They crystallize in the cubic space group $\text{Fm}\bar{3}\text{m}$ (space group no. 225) with $L2_1$ atomic order. X_2YZ compounds display all kinds of magnetic behaviour and multifunctional magnetic properties (Graf, Felser & Parkin 2011). Heusler materials of the Ni-Mn-X (X = Sn, In, Sb, Ga) system have turned out to be enormously multifunctional. Research on this material system is now being directed from science towards their technological significance.

		X	Y	Z	X	Y																																						
		or or																																										
		Y Z																																										
H																He																												
Li	Be										B	C	N	O	F	Ne																												
Na	Mg										Al	Si	P	S	Cl	Ar																												
K	Ca	Sc	Ti	V	Cr	Mn	Fe	Co	Ni	Cu	Zn	Ga	Ge	As	Se	Br	Kr																											
Rb	Sr	Y	Zr	Nb	Mo	Tc	Ru	Rh	Pd	Ag	Cd	In	Sn	Sb	Te	I	Xe																											
Cs	Ba	Lu	Hf	Ta	W	Re	Os	Ir	Pt	Au	Hg	Tl	Pb	Bi	Po	At	Rn																											
Fr	Ra	↓	Lr	Rf	Db	Sg	Bh	Hs	Mt	Ds	Rg	Uub																																
		<table border="1" style="width: 100%; border-collapse: collapse;"> <tr> <td style="background-color: red;">La</td><td style="background-color: red;">Ce</td><td style="background-color: red;">Pr</td><td style="background-color: red;">Nd</td><td style="background-color: red;">Pm</td><td style="background-color: red;">Sm</td><td style="background-color: red;">Eu</td><td style="background-color: red;">Gd</td><td style="background-color: red;">Tb</td><td style="background-color: red;">Dy</td><td style="background-color: red;">Ho</td><td style="background-color: red;">Er</td><td style="background-color: red;">Tm</td><td style="background-color: red;">Yb</td> </tr> <tr> <td style="background-color: red;">Ac</td><td style="background-color: red;">Th</td><td style="background-color: red;">Pa</td><td style="background-color: red;">U</td><td style="background-color: red;">Np</td><td style="background-color: red;">Pu</td><td style="background-color: red;">Am</td><td style="background-color: red;">Cm</td><td style="background-color: red;">Bk</td><td style="background-color: red;">Cf</td><td style="background-color: red;">Es</td><td style="background-color: red;">Fm</td><td style="background-color: red;">Md</td><td style="background-color: red;">No</td> </tr> </table>															La	Ce	Pr	Nd	Pm	Sm	Eu	Gd	Tb	Dy	Ho	Er	Tm	Yb	Ac	Th	Pa	U	Np	Pu	Am	Cm	Bk	Cf	Es	Fm	Md	No
La	Ce	Pr	Nd	Pm	Sm	Eu	Gd	Tb	Dy	Ho	Er	Tm	Yb																															
Ac	Th	Pa	U	Np	Pu	Am	Cm	Bk	Cf	Es	Fm	Md	No																															

Figure 2. The list of elements in the periodic table for the formation of Heusler (X_2YZ) and half-Heusler (XYZ) alloys (Hooshmand Zaferani, Ghomashchi & Vashae 2019).

1.1.3 Multiferroic effects

Multiferroic effects such as magnetic/metamagnetic shape memory (MSM/MMSM), magnetocaloric (MC) and direct energy conversion result from a combined first-order and second-order structural and magnetic transitions respectively. The former transforms high-

temperature austenite phase to low-temperature martensite phase and the latter brings about a change in electromagnetic ordering in the phases in a biased field. The outcome of the two transitions is magnetostructural coupling. This works as an indirect oscillatory Ruder-Kittel-Kasuya-Yosida (RKKY) (Roy 2013) exchange interaction for magnetic ordering. Together with the influence of band Jahn-Teller (J-T) effect (Haritha et al. 2010) which induces martensitic transformation through hybridization of electronic states, the magnetostructural coupling drives the multifunctional behaviour of Heusler alloys. In Ni-Mn-X Heusler materials which are multiferroic by choice, martensitic transformation and magnetostructural coupling are the mainstay of multifunctionality.

1.2 Synthesis

Ferromagnetic Heusler materials are synthesized through both liquid and solid processing routes. The commonly employed processing route is the liquid route through melting and casting. A majority of alloys of the Ni-Mn-X system have been synthesized through arc/induction melting under controlled conditions and through variants of the liquid processing route such as melt-spinning, directional solidification using Bridgman-Stockbarger (Chen, F et al. 2017) and Czochralski (Laudise et al. 1992) techniques, including Taylor-Ulitovsky method (Larin et al. 2002) of fabricating glass-coated microwires of magnetocaloric materials (Shevyrtalov, Zhukov, et al. 2018; Zhukov et al. 2013). Combinatorial thin-film composition spread methods are beginning to be used (Famodu et al. 2004; Takeuchi et al. 2003). Computational design based on density functional theory using CASTEP software yielded a composition $\text{Ni}_{40}\text{Co}_8\text{Mn}_{37}\text{Sn}_9\text{Cu}_6$ which after synthesis by arc-melting exhibited a remarkably high magnetic entropy change of 34.8 J/kgK (Zhang et al. 2019). Solid processing is by powder metallurgy (PM) (Ito, K et al. 2010; Ito, K et al. 2009). Sintering techniques include pressureless sintering, spark

plasma and solid state replication to obtain a porous alloy sample. PM has been widely applied on conventional shape memory alloys for reasons such as obtaining desired martensitic transformation temperatures, transformation width (range) and hysteresis, as in Cu-Al-Ni (Ibarra et al. 2004), drop in transformation temperatures, as in Ti-Ni-Cu (Kim, Y-W et al. 2012) and significant reduction in the number of secondary phases using vapour phase calciothermic reduction (VPCR) (Bertheville 2005) in solid state sintering of $\text{Ni}_{50}\text{Ti}_{50-x}\text{Zr}_x$.

Synthesis of ferromagnetic Heusler alloys by PM is often not the preferred choice of processing because it resulted in incomplete martensitic transformation (Ito, K et al. 2008) or evolved secondary phases (Ito, K et al. 2009) which are detrimental to the magnetostructural transformation and properties. This is ambiguous as literature on PM processed Heusler alloys is very scant. Besides, PM processed alloys resembled cast alloys from whatever little has been reported so far. Furthermore it is alloy powders and not elemental powders that have been used (Ito, K et al. 2010; Ito, K et al. 2011; Ito, K et al. 2009; Monroe et al. 2012). It becomes clear that the PM route using elemental powders for synthesizing ferromagnetic Heusler alloys has not been explored and offers an enormous scope for exploration.

1.3 Contributions arising from this thesis

The scope for employing PM is vast in terms of characterization using different solid processes, their process parameters governing the synthesis, transport properties of the PM alloys, their magnetostructural transformations and microstructural characteristics. The choice of the PM process for fabricating the alloys and the choice of composition is dependent on the advantages of using it over liquid processing and the remarkable

magnetostructural properties associated with the composition. Conventional pressure-less sintering process is certainly a cost-effective alternative to liquid processing in terms of compositional control. A composition such as $\text{Ni}_{45}\text{Co}_5\text{Mn}_{40}\text{Sn}_{10}$ with a phenomenal saturation magnetization at phase transformation that is reversible would be ideal for exploration of feasibility of the PM route. With the objectives narrowed down to study the feasibility of conventional press and sinter method of fabrication using elemental powders of an important alloy used for energy generation, this study also examines the effects of process parameters on the transformations and microstructural characteristics of the sintered alloys. The insights gained from this study, as can be read from its chapters that follow, are vital for the development and application of new generation of ferromagnetic Heusler alloys through PM route.

Chapter 1 of the thesis provides a brief overview of what Heusler alloys are and why they are interesting multiferroic materials.

Literature review for the thesis is presented in Chapters 2 and 3.

Chapter 2 presents a background and brief understanding of fundamental concepts and important phenomena associated with the multifunctional attributes of Ni-Mn-based ferromagnetic Heusler alloys. This understanding is essential for any microstructural characterization study to be carried out.

Chapter 3 provides a review of the alloy synthesis via liquid processes, their application on ferromagnetic Heusler alloys, microstructural characterization and microstructural effects on properties of the alloys. It also includes a review of the alloy synthesis via solid processing techniques, a short review on their application on ferromagnetic Heusler alloys, characterization and magnetostructural properties of solid processed alloys. This chapter enables a comparison between liquid and solid processed alloys. In the absence of sufficient literature on solid processed alloys, data on liquid processed and solid processed conventional shape memory alloys can be used as benchmarks to synthesize and

characterize the powder processed ferromagnetic Heusler alloys.

Chapter 4 details the experiments carried out. While use of various characterization equipment is mentioned in the next two chapters, this chapter provides more detail about the process and equipment.

Chapter 5 presents the results of a quinary alloy, published as a journal paper. It has been demonstrated that powder processing could be applied to replace time-consuming arc/induction melting process in the development of high performance Heusler alloys at a lower cost.

Chapter 6 presents the results of a quaternary alloy published as a journal paper. The effects of process parameters such as compaction load (pressure), sintering temperature and duration on the transformation characteristics and microstructures of the alloy are investigated and reported.

Both Chapter 5 and Chapter 6 may contain excerpts from Chapters 1, 2 and 3 or vice versa, however it has been endeavoured to avoid duplication of text and data as much as possible including in Chapter 4 except where necessary.

Chapter 7 gives the conclusion and future work in this area.

Appendix 1 is published as a review article and contains three sections carrying fundamental concepts, methods of synthesis and characterization and microstructural effects on the properties of ferromagnetic Heusler alloys respectively. This review strengthens the understanding of physical, material and metallurgical aspects of ferromagnetic Heusler alloys. Materials scientists and researchers can approach the task of synthesis and microstructural characterization of such alloys with a sound knowledge rather than do it ambiguously.

Appendix 2 in manuscript form details the characterization techniques for ternary and quaternary alloys with emphasis on X-ray diffraction. From this again researchers will know what to look for during X-ray characterization of ferromagnetic Heusler materials.

2 Background – Fundamental Concepts

2.1 Magnetostructural effects seen in Heusler alloys

Martensitic transformation which is the key to the emergence of various magnetostructural effects is dependent on the alloy composition largely represented as the valence electron concentration (e/a). In NiMn-based alloys this ratio is calculated as concentration-weighted average of the valence (s, p and d) electrons using the expression

$$\frac{e}{a} = f_{Ni}e^{Ni} + f_{Mn}e^{Mn} + f_Xe^X + f_Ze^Z \quad \text{where}$$

f_{Ni} , f_{Mn} , f_X , f_Z represent the atomic fractions of elements,

e^{Ni} , e^{Mn} , e^X , e^Z are the corresponding numbers of valence electrons and

X, Z represent the third and fourth elements of a quaternary NiMn-based alloy

The composition dependence of martensitic transformation is explained as formation of martensite in response to a free energy build-up in the alloy when an increase in e/a ratio destabilizes the parent $L2_1$ -structured austenite. The electrons above the Fermi surface move to the corner states of the (1 1 0) Brillouin zone distorting the lattice structure to minimize the free energy. An additional consideration is that a unit-cell contraction of the parent austenite changes the relative positions between the Fermi surface and Brillouin zone and causes martensitic transformation (Zheng et al. 2013). When elements with smaller atomic radius such as Ge or Ga are substituted for larger elements such as Sn or In, the phase transition temperatures are seen to increase (Zheng et al. 2013). On the other hand, substitution of larger isoelectronic elements (elements having the same electron configuration in the outermost valence shells) with smaller atomic radius elements increases the unit-cell volume and suppresses the martensitic transformation (Zheng et al. 2013).

The Heusler alloy composition not only influences the martensitic transformation but also the magnetic transition (Ito, W et al. 2007). Various multifunctional effects arising from magnetostructural transformations are composition dependent as well and are elucidated later in this text. The different magnetostructural effects seen in Heusler alloys are briefly explained below.

2.1.1 Magnetocaloric effect

In a magnetic material, the thermal and magnetic properties are interdependent leading to magnetocaloric effect (MC), induced whenever a magnetic field is applied to it or removed. In other words, it is the reversible change of temperature accompanying the change of magnetization of a ferromagnetic or paramagnetic material. Such change should not be mistaken with the much smaller hysteresis heating effect, which is irreversible. It is characterized through magnetization measurement, direct and indirect adiabatic temperature change measurement if the field is adiabatic, field dependent specific heat measurement and direct measurement of isothermal entropy change (ΔS) if the field is isothermal. A magnetic entropy change (ΔS) of ~ 4.1 J/kg K under a magnetic field of 0.9 T, associated with martensitic transformation was reported in $\text{Ni}_{51.5}\text{Mn}_{22.7}\text{Ga}_{25.8}$, which was comparable with an entropy change of ~ 4.2 J/kg K under 1.5 T in Gd (Hu, Shen & Sun 2000). The archetypal NiMnGa system came to be the most studied in the Ni-Mn-X material system in terms of both magnetostructural and magnetocaloric characteristics.

Magnetization measurements are carried out on a vibrating sample magnetometer (VSM) to determine $M(H, T)$ - the temperature and magnetic field dependence of magnetization in the alloy sample. The magnetization so measured is applied in the Maxwell relation $\left(\frac{\partial S}{\partial T}\right)_T = \mu_0 \left(\frac{\partial M}{\partial T}\right)_H$ to compute ΔS (Smith et al. 2012). The adiabatic temperature

change ΔT_{ad} is measured by varying the applied field on the sample kept quasi-adiabatic. The magnetic field is varied either by keeping the sample stationary and changing the field or moving the sample relative to a constant magnetic field. Field dependent specific heat measurements are possible on either scanning calorimeters where the temperature is changed continuously as the heat flux between the sample and a thermal bath is measured or heat pulse calorimeters with Peltier elements as heat flow sensors where a small amount of heat is added at a time after which the sample temperature is measured. High-sensitivity differential scanning calorimeters with Peltier elements are used to measure isothermal entropy change directly.

The product of the changes in isothermal field-induced entropy (ΔS) and the adiabatic field-induced temperature (ΔT), $|\Delta S \Delta T|$ is maximum when the magnetization change at the transition is maximum for an optimal composition in ferromagnetic Heusler alloys (Planes, Manosa & Acet 2013). The observed large isothermal entropy change is broken up into the magnetic and structural entropy changes arising out of the spin-lattice coupling (Planes, Manosa & Acet 2009; Roy 2013), occurring at the point where the martensitic transformation temperature and the magnetic transition temperature are close to one another (Franco et al. 2012). A positive value of entropy change is termed as inverse effect and is related to the magneto-crystalline anisotropy of the martensitic phase. The inverse effect is more pronounced when the difference between the martensitic transition and Curie temperatures is an appreciable value. Conversely a negative entropy change is termed conventional effect and the change from inverse to conventional occurs as the martensitic transformation temperature approached the Curie temperature at higher values of applied field (Franco et al. 2012; Schlagel et al. 2008).

2.1.2 Magnetic/metamagnetic shape memory effect

Magnetic shape memory effect (MSM) is understood in the context of conventional shape-memory effect. Both magnetic and conventional shape-memory are outcomes of martensitic transformation which is diffusionless. A schematic diagram of shape-memory effect is presented in Figure 3. The parent austenite phase (usually cubic, shown green) when cooled to a temperature below M_f (martensite finish temperature) changes into martensite. The difference in symmetry between the austenite and martensite which is low in symmetry will cause multiple variants of martensite to form, seen as zig zag structures (red and blue) in the Figure 3.

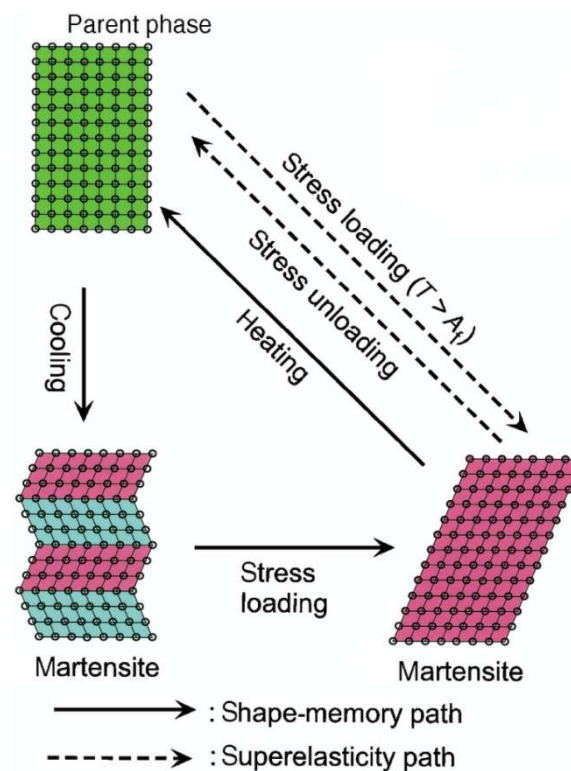


Figure 3. Mechanism of shape memory effect and superelasticity illustrated (Otsuka & Kakeshita 2002).

These variants or domains accommodate the elastic strains around the martensite in a process called self-accommodation. Upon the application of a stress the martensite further deforms (structure in red) by twin boundary motion. If the sample is heated to above the austenite finish temperature A_f , the martensite variants which rearranged under stress revert back to the original orientation in austenite phase. This phenomenon is called shape memory

effect (Otsuka & Kakeshita 2002). Superelasticity is when the sample is directly stressed above A_f , the strains are recovered upon unloading as in shape memory effect provided the applied stress does not cause slip in the structure. The magnitude of the applied stress is critical to prevent slip.

Magnetic shape memory is similar to conventional shape memory except that the applied magnetic field deforms the sample just as the applied stress does in the latter. A schematic diagram of magnetic shape memory effect is shown in Figure 4. Shape memory is realized by heating the alloy to above the austenite finish temperature A_f . Elaborating further there are magnetic domains within each variant below Curie temperature with the magnetization pointing along the easy axis such that the magnetostatic energy is minimum.

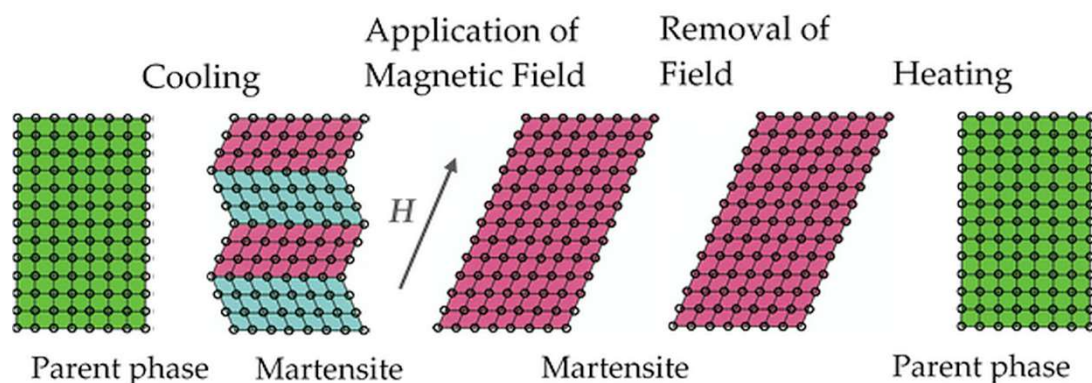


Figure 4. Schematic representation of magnetic shape-memory effect (adapted from (Planes, Mañosa & Acet 2009)).

Upon the application of a magnetic field the magnetic moments tend to align along the applied field. This alignment is limited to within the variants if the magnetic anisotropy is weak. However if the magnetic anisotropy is strong, the magnetic domains and hence the

structural domains rotate utilizing the difference in Zeeman energy¹ between the variants such that their easy axes are aligned with the applied field to cause significant deformation which is recovered upon heating.

MSM effect in Ni₂MnGa was first reported by (Ullakko et al. 1996). The strain change in the martensite phase as the direction of applied field of 10 kOe changed through 90° from [0 0 1] to [1 1 0] was 0.19%, solely due to twin boundary motion in the martensite. Othermultiferroic effects such as metamagnetic shape memory (MMSM) effect were discovered later on. MMSM effect in off-stoichiometric Ga-free alloys refers to the recoverability upon heating of large strains when a reverse martensitic transformation from the product phase to parent phase is induced by the application of a magnetic field. A 3% deformation and almost full recovery of the original shape of the alloy was reported in Ni₄₅Co₅Mn_{36.7}In_{13.3} single crystal during a reverse transformation from the antiferromagnetic (or paramagnetic) martensite to the ferromagnetic parent phase at 298 K under the influence of an external magnetic field (Kainuma, Imano, Ito, Sutou, et al. 2006).

2.1.3 Direct energy conversion

The direct conversion of thermal energy (waste heat) to electricity is a more recent phenomenon, exhibited by a singular quaternary ferromagnetic Heusler alloy. A sudden and large thermally induced change in magnetization in a biased magnetic field initiated by phase transition was utilized to generate a voltage of 0.6 mV. This was by using the fundamental dipolar relationship between magnetization M , magnetic induction (magnetic

¹ The potential energy of a magnetized body in an external magnetic field.

flux density) B and magnetic field H , given by $B = H + 4\pi M$ and Faradays law $curl E = \frac{1}{c} \frac{dB}{dt}$ based on the premise that the magnetostructural transformation essentially induces a non-zero dB/dt (Srivastava et al. 2011).

Figure 5 (a) shows the schematic of the device used to measure induced emf and Figure 5 (b) was the actual device used by (Srivastava et al. 2011). Figure 6 (a) shows the magnetization vs. temperature of the alloy at a field of 1 T. The phase transformation on heating caused the increase in magnetization from less than 10 emu/cm^3 in the martensite phase to more than 1100 emu/cm^3 in the austenite phase. Figure 6 (b) shows the measured emf vs temperature. The rapid rise in voltage was due to the phase transformation and the fall was due to the fall of magnetization with temperature around the Curie temperature of the alloy (Srivastava et al. 2011).

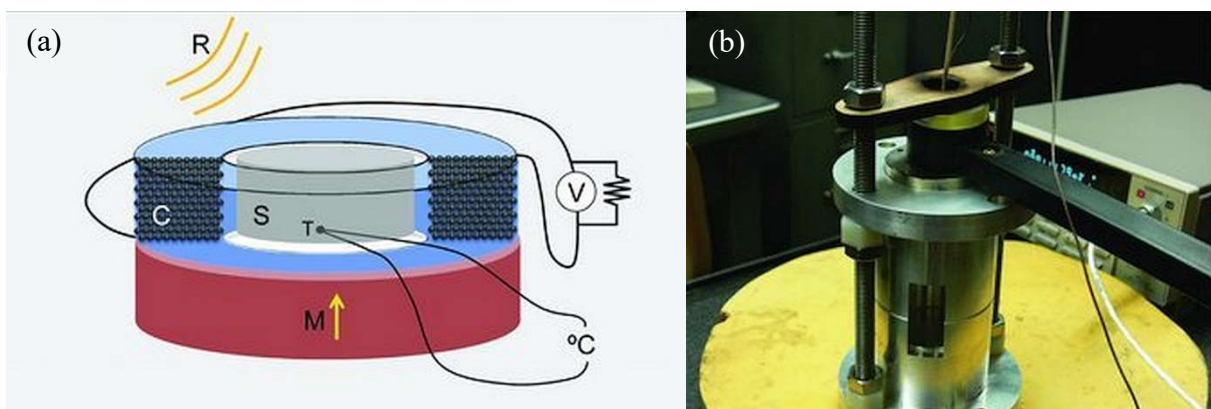


Figure 5. (a) Schematic of the experimental setup for the measurement of induced emf: C, coil; R, heat source; M, permanent magnet; S, $\text{Ni}_{45}\text{Co}_5\text{Mn}_{40}\text{Sn}_{10}$; T, thermocouple; V, voltmeter; (b) actual view of the experimental setup (Srivastava et al. 2011)

The measured voltage compared satisfactorily with the best thermoelectric materials. The Seebeck coefficient which gives a measure of the voltage output of a thermoelectric material is $-230 \mu\text{V/K}$ for Bi_2Te_3 and for the standard Chromel-Constantan is $60 \mu\text{V/K}$. At $\Delta T = 10 \text{ K}$ (temperature interval of phase transformation used for comparison) these values convert

to 2.3 mV and 0.6 mV respectively. With an optimized geometry of the sample material a voltage of 502 mV has been predicted. Similarly with regards to the power density, an

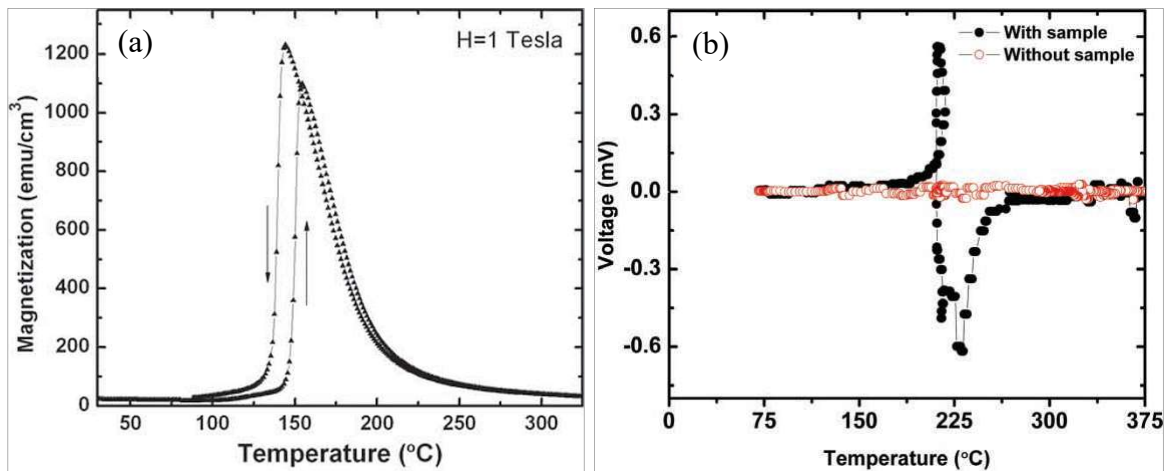


Figure 6. (a) Magnetization vs. temperature under 1 T field; (b) Voltage vs. temperature (Srivastava et al. 2011).

optimized thin plate of the material was predicted to give a power density of 3.1×10^6 erg/cm³.s, which compared favourably with a commercial thermoelectric generator with an equivalent power density of 3.05×10^5 erg/cm³.s (Srivastava et al. 2011).

The idea behind the energy conversion function was the reversibility of martensitic transformation that holds the key to the realization of coexistent phases with different electromagnetic properties. Mathematical conditions called cofactor conditions, adapted from the geometric nonlinear theory of martensite (GNLTM), ensure high reversibility such that switching between phases cyclically does not diminish the electromagnetic properties. The GNLTM solutions correspond to the twinning volume fractions, f and $1 - f$ (Song et al. 2013). When $f = 0$ or $f = 1$, the absence of an elastic transition layer between the austenite and the single variant martensite interface is possible when the middle eigenvalue λ_2 of a transformation stretch matrix 'U' (3 x 3, obtained from X-ray measurements of lattice parameters and knowledge of space groups of the two phases) takes a value 1.

For other volume fractions given by $0 \leq f \leq 1$, two additional conditions corresponding to different twin types are to be satisfied. The volume fraction of the twin variants can then be continuously varied while at the same time keeping the low-elastic-energy interface with austenite (Song et al. 2013). Using these conditions on the basic $\text{Ni}_{50}\text{Mn}_{50-x}\text{Sn}_x$ alloy system a composition $\text{Ni}_{45}\text{Co}_5\text{Mn}_{40}\text{Sn}_{10}$ was perfected with unusual magnetostructural properties (Srivastava, Chen & James 2010). This phenomenon, as envisaged by the researchers, could be taken to the stage of actual application, with the alloy having the potential to be used for harvesting energy from low waste heat sources of the order of less than 200°C (Ahamed Khan et al. 2018).

The efficacy of the compatibility conditions have been proved experimentally in Zn-Au-Cu (Song et al. 2013), Ti-Ni-Pd (Delville et al. 2009) alloys and used in modelling the austenite-martensite interface in shape memory materials (Lei et al. 2010). Optimization of geometric compatibility between the austenite and martensite phases was implemented in the synthesis of Ni-Mn-In alloy (Devi et al. 2019). In the case of $\text{Ni}_{49}\text{Co}_3\text{Mn}_{34}\text{In}_{14}$ alloy, geometric compatibility was realized through a systematic tuning of Mn/In ratio and Co composition (Sun et al. 2019) from a starting composition of $\text{Ni}_{52}\text{Mn}_{35}\text{In}_{13}$. This alloy exhibited remarkable magnetocaloric (16.5 J/kgK), magnetostrain (0.26%) and magnetoresistance (60%) characteristics resulting from a reversible phase transformation at a relatively low inducing field of 3T.

3 Processing and Characterization of Heusler alloys

3.1 Introduction

Ferromagnetic Heusler materials are synthesized through both liquid and solid processing routes. The common processing route is the liquid route through melting and casting, primarily employed for the purpose of attaining compositional homogeneity in the alloy after several rounds of re-melting. Among the other liquid processes, melt-spinning has been largely applied. Solid processing is by powder metallurgy (PM). In this chapter, an elaborate review of the both the liquid and solid processing procedures, ferromagnetic Heusler alloys that have been processed using both routes and their characterization is presented. The importance, motivation and objectives of this work are discussed towards the end.

3.2 Liquid processing

The most commonly employed synthesis procedure on ferromagnetic Heusler alloys is the liquid processing route. The techniques include arc/induction melting under controlled conditions and rapid solidification by melt spinning. (Graf, Felser & Parkin 2011) outline the liquid processing procedure as follows: Melting is carried out in an oxygen-free atmosphere in order to avoid contamination, given that certain elements such as manganese in the Heusler composition may have a high affinity to oxygen. A vacuum level of 10^{-4} mbar (0.01 Pa), an atmosphere of high purity inert (argon) gas together with the addition of oxygen getter materials such as Ta or Ti may be used to improve the sample quality. The stoichiometry of the composition after melting is ensured by compensating for the probable weight loss resulting from the evaporation of certain compositional elements such as Mn,

Sb, Bi etc., during melting. The alloys are melted, turned over and remelted in arc or induction melting furnaces to ensure homogeneous distribution of elements within the sample. Arc melting furnaces use an electric arc struck between an electrode (tungsten) and the metal mix placed in crucibles for melting where temperatures in excess of 2500°C can be reached. Induction melting, on the other hand, combines the advantages of a controlled atmosphere and control of the melting process, where heating is by eddy currents from an induction coil with no direct contact between the metal and coil (Anandh 2009). Its process capability is defined by temperatures of up to 2000°C that can be reached.

Rapid solidification processing with solidification rates ranging from 10^2 K/s (droplet methods) to 10^6 K/s (melt-spinning) to 10^{14} K/s (surface melting) (Suryanarayana 2002) has been a very useful method for preparing ferromagnetic Heusler alloys. The characteristics of rapid solidification processing are extension of solid solubility limits, microstructural refinement and formation of non-equilibrium phases, such as metastable intermediate phases, metallic glasses and quasicrystalline phases. Melt-spinning is gaining wide acceptance for varying reasons such as obtaining textured samples suitable for practical utilization as sensors, actuators and magnetocaloric materials (Caballero-Flores et al. 2015; Wang, W et al. 2015). Synthesis by melt-spinning is by allowing the alloy melt stream jet to solidify rapidly on a fast-rotating and thermally conducting substrate to produce a continuous strip of ribbon of the alloy up to 500 mm in width (Suryanarayana 2002). Wheel speed, nozzle size, ejection pressure and material of the rotating substrate (wheel) are some of the parameters which influence the process. Typical wheel speeds vary from 10 m/s to 60 m/s and the substrate is usually copper.

Melt-spinning lends credence to the fact that the processing methods can tailor the functional attributes of the Heusler alloys by controlling the lattice parameters, interatomic

distance, degree of atomic ordering and microstructure. In Heusler alloys it is employed to control the grain size of the austenite phase, because the martensitic transition can occur only when the austenite grain size is bigger than the martensite plate (Chen, X et al. 2014). Additionally, melt-spinning improves homogeneity in terms of grain size and elemental composition as well as favours avoidance of prolonged annealing.

The physical properties of Heusler alloys are better investigated using single crystals. Bridgman-Stockbarger (Chen, F et al. 2017) and Czochralski (Laudise et al. 1992) techniques are usually employed. In all cases high purity starting elements are essential because the impurities are found at the grain boundaries (Graf, Felser & Parkin 2011).

3.2.1 A review of liquid processed Heusler alloys

NiMn-based Heusler alloys synthesized using liquid processing route include important alloys listed in Table 1.

Table 1. Examples of liquid processed alloys

Alloy system	Process	Attributes	Reference
$\text{Ni}_{50}\text{Mn}_{50-y}\text{X}_y$ (X = In, Sn, Sb; $y=10\sim 16.5$)	Induction melting	Capable of magnetic shape memory	(Sutou et al. 2004)
$\text{Ni}_{0.50}\text{Mn}_{0.50-x}\text{Sn}_x$ ($0.05 \ll x \ll 0.25$)	Arc-melting	Varying strengths of ferromagnetic exchange around martensitic transformation	(Krenke, Acet, et al. 2005)
$\text{Ni}_{0.50}\text{Mn}_{0.50-x}\text{Sn}_x$ ($0.13 \ll x \ll 0.15$)	Arc-melting	With large inverse entropy change leading to a large inverse magnetocaloric effect	(Krenke, Duman, et al. 2005)

Ni-Co-Mn-In	Induction melting	With magnetic field induced shape recovery by reverse phase transformation	(Kainuma, Imano, Ito, Sutou, et al. 2006)
Ni ₄₃ Co ₇ Mn ₃₉ Sn ₁₁	Arc- and induction melting	With magnetic field induced shape recovery by reverse phase transformation	(Kainuma, Imano, Ito, Morito, et al. 2006)
Ni ₄₅ Co ₅ Mn ₄₀ Sn ₁₀	Arc-melting	Potential energy conversion	(Srivastava, Chen & James 2010)
Ni ₄₁ Co ₉ Mn ₄₀ Sn ₁₀	Arc-melting	Large magnetic entropy change and magnetoresistance	(Huang et al. 2015; Huang et al. 2014)
Ni-Co-Mn-Sn	Arc-melting	Solidification processes and effects of heat treatment	(Pérez-Sierra, A.M. et al. 2015)
Mn ₅₀ Ni ₄₀ In ₁₀	Melt spinning	Highly textured polycrystalline ribbons for use in practical devices	(Llamazares et al. 2008)
Ni ₃₈ Co ₁₂ Mn ₄₁ Sn ₉	Melt spinning	Elimination of secondary phases	(Chen, F et al. 2013)
Ni ₄₃ Mn ₄₂ Co ₄ Sn ₁₁	Melt spinning	Enhanced entropy change resulting in increased refrigeration capacity	(Bruno, Nickolaus M. et al. 2014)
Ni _{50-x} Mn _{37+x} Sn _{12.5} (0 << x << 6)	Melt spinning	Tuning of transformation temperature through composition	(Maziarz, W. et al. 2014; Zheng et al. 2014)
Ni-Mn-Sn-Co	Melt spinning	Martensitic crystalline structure	(Zheng et al. 2014)

Preparation of single crystals was suitable to explore magnetostructural effects such as large magnetic field-induced strains as in Ni₂MnGa (Ullakko et al. 1996) or in slightly off-stoichiometric Ni_{47.4}Mn_{32.1}Ga_{20.5} (prepared by Bridgman technique) with 6% field-induced strain (Murray et al. 2000) and Ni_{48.8}Mn_{29.7}Ga_{21.5} with approximately 10% strain (Sozinov, Alexei et al. 2002). Even magnetic field-induced shape recovery by reverse phase transformation (metamagnetic shape memory) was seen on Ni₄₅Co₅Mn_{36.7}In_{13.3} single

crystal (Kainuma, Imano, Ito, Sutou, et al. 2006). Bridgman-Stockbarger method however widened the working temperature range for magnetic entropy change in $\text{Ni}_{40.6}\text{Co}_{8.5}\text{Mn}_{40.9}\text{Sn}_{10}$ alloy even though a large magnetic entropy change and refrigerant capacity above room temperature were observed (Chen, F et al. 2017).

Liquid processing supposedly brings about homogeneity in the material so that desired transition temperatures and magnetostructural effects can be realized. However it is seen that while structural homogenization is quick, compositional homogenization required long periods of annealing in order that the intrinsic magnetostructural behaviour in $\text{Ni}_{50}\text{Mn}_{37}\text{Sn}_{13}$ is not suppressed (Schlagel, McCallum & Lograsso 2008). Melt-spinning with all its advantages is said to retard the martensitic transformation by lowering the transformation temperature compared to the bulk alloy. The reason is that a highly oriented columnar microstructure of a melt-spun ribbon generates internal stresses which hinder lattice distortion to create varied orientations of martensite. This effect observed in melt-spun ribbons is offset by annealing. Examples for this behaviour are seen in $\text{Ni}_{50}\text{Mn}_{37}\text{Sn}_{13}$ ribbons with a transformation temperature around 212 K (Santos et al. 2008) while the bulk alloy transformed at a temperature around 300 K (Krenke, Duman, et al. 2005), in $\text{Ni}_{50}\text{Mn}_{41}\text{Sn}_9$ alloy ribbon the martensitic transformation temperature occurred at around 330 K, which was nearly 150 K less than the bulk alloy (Wang, W et al. 2013) and in $\text{Ni}_{50}\text{Mn}_{36}\text{In}_{14}$ wherein the as-cast ribbons showed lower transformation temperatures than annealed samples (Cai et al. 2008).

From the preceding discussion it is understood that a majority of the ferromagnetic ternary and quaternary NiMn-based Heusler alloys have been synthesized predominantly by liquid processing for the purpose of achieving structural homogenization. Compositional homogenization and other microstructural issues such as elimination of secondary phases

or grain refinement in ribbons have been carried out by subsequent heat treatment.

3.2.2 Magnetostructural effects seen in liquid processed alloys

A good number of liquid processed Heusler alloys are seen to exhibit remarkable magnetostructural effects described earlier, primarily because of the compositional homogenization and also because of composition tuning. $\text{Ni}_{2.19}\text{Mn}_{0.81}\text{Ga}$ exhibited concomitant structural transformation and the magnetic transition with an entropy change of 20 J/kgK when compared to 5 J/kgK in $\text{Ni}_{2.15}\text{Mn}_{0.85}\text{Ga}$ in which only structural transition occurred (Pareti et al. 2003). (Krenke, Duman, et al. 2005) discovered large inverse magnetocaloric effect of 18 J/kgK and 15 J/kgK respectively in arc-melted and annealed (at 1273 K for 2 h) $\text{Ni}_{50}\text{Mn}_{37}\text{Sn}_{13}$ and $\text{Ni}_{50}\text{Mn}_{35}\text{Sn}_{15}$ (composition rewritten) alloys which was comparable with $\text{Gd}_5(\text{Si}_x\text{Ge}_{1-x})_4$ in which the observed giant magnetocaloric effect of -20 J/kgK was due to the simultaneous occurrence of first-order structural and magnetic phase transitions (Pecharsky & Gschneidner 1997). A small tuning of the Ni/Mn ratio reportedly increased the transformation temperature from 248 to 337.5 K and brought about an inverse entropy change of 23.5 J/kgK (with a net refrigeration capacity of 53 J/kg) at 308 K in arc-melted and annealed $\text{Ni}_{50-x}\text{Mn}_{37+x}\text{In}_{13}$ alloy system with $x = 3$ for a field change from 0 to 2 T (Rama Rao et al. 2010). The effect of compositional tuning and homogenization through melting and annealing are also seen in quaternary $\text{Ni}_{50}\text{Mn}_{34}\text{Co}_2\text{Sn}_{14}$ (Yang, LH et al. 2014), $\text{Ni}_{41}\text{Co}_9\text{Mn}_{32}\text{Al}_{18}$ (Kim, Y et al. 2014) and $\text{Ni}_{50}\text{Mn}_{33}\text{Cu}_2\text{Sn}_{15}$ (Gao et al. 2009) alloys.

$\text{Ni}_{55}\text{Mn}_{20.6}\text{Ga}_{24.4}$ and $\text{Ni}_{55}\text{Mn}_{19.6}\text{Ga}_{25.4}$ ribbons with changes in phase transformation temperatures, entropy and refrigeration capacity (Rao et al. 2009), $\text{Ni}_{48}\text{Mn}_{37}\text{In}_{13}$ ribbons with an entropy change of 30.1 J/kgK at martensitic transformation and -6.5 J/kgK at Curie temperatures after both temperatures increased due to annealing (Zhao et al. 2010) and

Ni₄₉Mn₃₉Sn₁₂ ribbons with a large entropy change of 8.2 J/kgK after annealing (Wang, W et al. 2015) show that melt-spinning and annealing influence the degree of atomic order, thermal hysteresis and microstructure in turn affecting the transition temperatures and magnetocaloric effect. Interestingly the wheel speed at which the alloy ribbons are synthesized can influence the magnetocaloric effect and effective refrigerating capacity in NiMn-based ferromagnetic Heusler alloys (Ma, SC et al. 2015). In order to achieve a giant magnetocaloric effect with an isothermal entropy change of 23 J/kgK at a low actuating magnetic field of 2 T, (Cong, D. Y. et al. 2018) added a tiny amount of Al to the Ni-Co-Mn-Sn alloy so as to decrease the stacking fault energy and generate a specific stacking-mediated martensite structure that also improved the geometric compatibility. This alloy with composition Ni₄₀Co₁₀Mn₄₀Sn₉Al₁ also exhibited excellent compressive properties and high fracture toughness similar to structural intermetallics.

Magnetic shape memory in NiMn-based ferromagnetic alloys synthesized preferably as single crystals can be seen in an unstressed Ni₂MnGa (Ullakko et al. 1996) with large magnetic field-induced strain of 0.2% along [001] direction, in slightly off-stoichiometric Ni_{47.4}Mn_{32.1}Ga_{20.5} with 6% field-induced strain (Murray et al. 2000) and Ni_{48.8}Mn_{29.7}Ga_{21.5} with approximately 10% strain (Sozinov, Alexei et al. 2002). Magnetic field-induced shape recovery by reverse phase transformation (metamagnetic shape memory) was seen on Ni₄₅Co₅Mn_{36.7}In_{13.3} single crystal (Kainuma, Imano, Ito, Sutou, et al. 2006). Single crystals exhibited large pseudoelastic recovery besides chemical segregation, or a composition gradient due to which changes in transformation temperatures are obtainable. Single crystals of Ni₄₆Mn₂₄Ga₂₂Co₄Cu₄ were used to establish that a large magnetic field induced strain of 12% is solely dependent on the twinning stress being lower than the maximum equivalent magnetic stress given by $\sigma_{mag}^{max} = K/\varepsilon_0$ i.e. $K/\varepsilon_0 > \sigma_{tw}$ where $\varepsilon_0 = |1 - c/a| \approx 0.1$ is the twinning strain determined by the lattice parameters and K is the magnetic anisotropy

density (Sozinov, A. et al. 2013).

Two off-stoichiometric alloys, $\text{Ni}_{2.19}\text{Mn}_{0.81}\text{Ga}$ (Inoue, Kazuko et al. 2000) and $\text{Ni}_{2.18}\text{Mn}_{0.82}\text{Ga}$ (Inoue, K. et al. 2002) alloys fabricated by arc-melting under argon atmosphere, followed by homogenization at 1073 K for 24h and 100h respectively and then ice water quenched have been used to reiterate the composition dependence of martensitic transformation, the influence of magnetic field on the transformation and shape memory effect. The compositions were adjusted to make the transformation and Curie temperatures coincident so that the application of a magnetic field at above the transformation temperature partially transformed the cubic Heusler phase to a martensite phase which was a combination of orthorhombic and monoclinic phases. This implied possibility of controlling shape memory through an application of a field. The shape memory effect was thermoelastic suggesting that although field-induced strains do not involve phase transformations and are dependent on the twinning stress being lower than the maximum equivalent magnetic stress, recovery is certainly due to thermoelastic martensitic transformation.

While the conversion of magnetic stimuli on the mechanical response of a ferromagnetic shape memory alloy has been studied, the reverse viz. the effect of external mechanical stimuli on the magnetic behaviour of the alloy was also possible to generate a voltage from the variant reorientation mechanism under a biased field. The magnitude of the change depended on the magnetization difference between the hard and easy axes of the martensite. This was demonstrated on single crystals of $\text{Ni}_{51.1}\text{Mn}_{24}\text{Ga}_{24.9}$ alloy in which a voltage output of 60 mV was observed under 5 Hz loading frequency. The peak voltage output vs bias magnetic field plot displayed an increase in voltage output with increasing field followed by a decrease, because the magnetization difference between the easy and

hard axes increased until saturation magnetization (M_s) was reached and dropped upon further increase in the field (Karaman et al. 2007). The example of the singular quaternary arc-melted $\text{Ni}_{45}\text{Co}_5\text{Mn}_{40}\text{Sn}_{10}$ alloy which could generate a voltage of 0.6 mV utilizing a large and sudden thermally induced change in magnetization at phase transition could be a harbinger of direct waste heat to electricity conversion from sources at less than 200 °C.

3.2.3 Characterization of liquid processed alloys

3.2.3.1 Differential scanning calorimetry

Differential scanning calorimetry (DSC) is a technique of thermal analysis, which measures, depending on whether heat is absorbed (endothermic) or liberated (exothermic), the enthalpy of phase transformation in a structurally transforming material as a function of time or temperature. First-order transformations obey the classical Clausius-Clapeyron law and are identified by the evolution of latent heat whereas second-order transitions do not evolve latent heat, however are identified by abrupt variations in compressibility, heat capacity, thermal expansion coefficients, etc.

DSC has several uses. It is often the first step in the characterization sequence, used for the determination of the martensitic and magnetic transition temperatures, heat flow curves, thermal hysteresis and enthalpy/entropy changes in ferromagnetic Heusler alloys (Aksoy et al. 2009; Dubenko et al. 2015; Krenke, Duman, Acet, Wasserman, et al. 2007; Liu et al. 2011). Compositional dependence of martensitic transformation (Krenke, Duman, Acet, Moya, et al. 2007), progressive evolution of the martensitic transformation behaviour in response to increasing Co content in $\text{Mn}_{50}\text{Ni}_{40-x}\text{In}_{10}\text{Co}_x$ (Wu et al. 2011) and the mechanism of suppression and recovery of martensitic transformation in NiCoMnIn alloys fabricated under non-equilibrium conditions

(Wang, ZL et al. 2012) have been established using DSC.

The structural transformation temperatures of interest are the martensitic start (M_S) and finish (M_F) temperatures, exothermic peak of martensitic transformation (M_P), austenitic start (A_S) and finish (A_F) temperatures and the endothermic peak of austenitic transformation (A_P) (Cong, D.Y., Roth & Schultz 2012). Other notations such as T_{AS} , T_{AF} , T_{MS} and T_{MF} respectively for austenitic and martensitic start and finish temperatures are also used (Lázpita et al. 2016). The martensitic transformation temperature T_M is then obtained from $(M_s + M_f + A_s + A_f)/4$. It is also computed as $(M_s + A_f)/2$ (Liu et al. 2011; Srivastava et al. 2011). Thermal hysteresis given by $A_S - M_F$ is desired to be minimum (less than 10 °C) for improved reversibility of phase transformation (Srivastava et al. 2011).

Figure 7 shows the DSC curves of $Ni_{42}Co_8Mn_{39}Sn_{11}$ alloy with martensitic and magnetic transformations clearly seen (Lázpita et al. 2016). The austenitic and martensitic start and finish temperatures are marked on the plot and are determined by drawing tangents to the base and largest slope of the peaks.

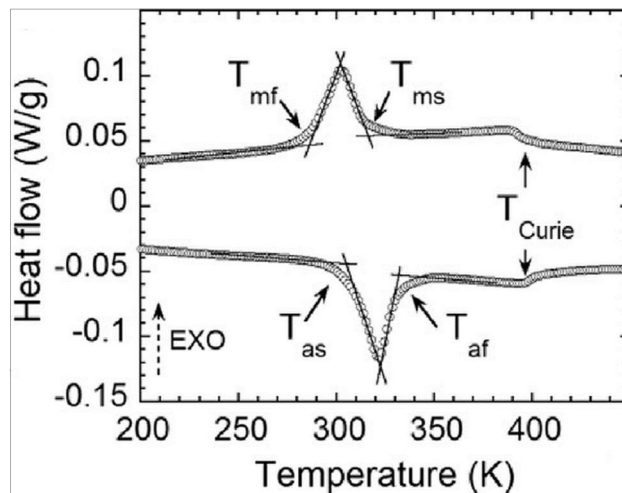


Figure 7. DSC curves showing forward and reverse martensitic transformation and Curie temperature of $Ni_{42}Co_8Mn_{39}Sn_{11}$ alloy (Lázpita et al. 2016).

Figure 8 shows the DSC plots of the ternary $\text{Ni}_{50}\text{Mn}_{50-x}\text{Sn}_x$ alloy system for $5 \leq x \leq 15$. Endothermic and exothermic peaks point up and down to respectively indicate the heating and cooling processes (Krenke, Acet, et al. 2005). The transformation temperatures are determined as shown in Figure 7. The hysteresis width ΔT has been determined by obtaining the difference between the peak temperatures. The martensitic start temperature can be seen to be increasing with decreasing Sn composition.

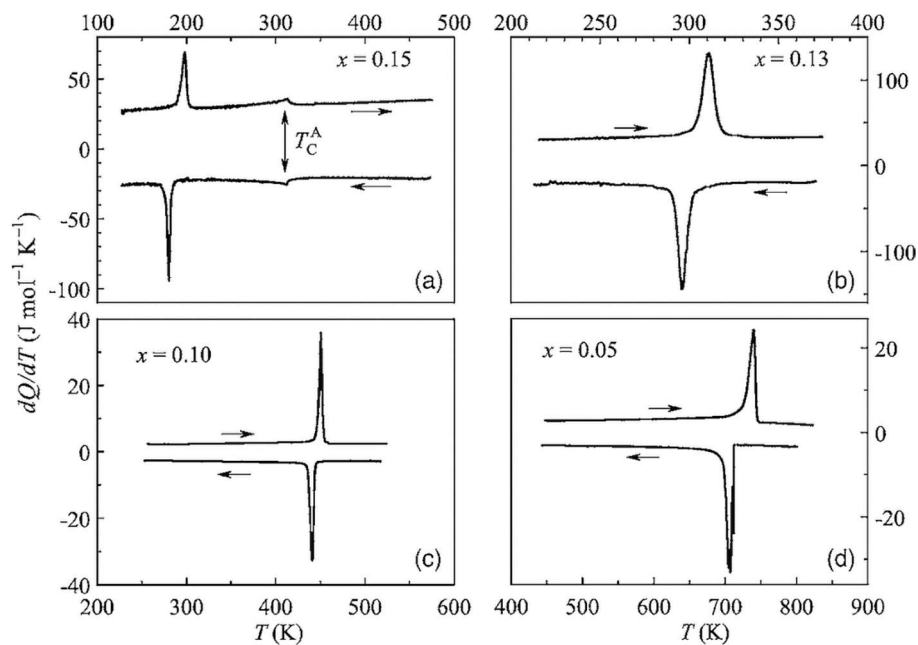


Figure 8. DSC plots of $\text{Ni}_{50}\text{Mn}_{50-x}\text{Sn}_x$ alloys undergoing martensitic transformations (a) $x=15$; (b) $x=13$; (c) $x=0.10$; (d) $x=0.05$ (Krenke, Acet, et al. 2005).

Figure 9 (a) shows the DSC plot of $\text{Ni}_{46}\text{Co}_4\text{Mn}_{39}\text{Sn}_{11}$ in the $\text{Ni}_{50-x}\text{Co}_x\text{Mn}_{39}\text{Sn}_{11}$ ($0 \leq x \leq 10$) alloy system and Figure 9 (b) shows the composition dependence of the transformation temperatures, all decreasing with increasing Co composition (Cong, D.Y., Roth & Schultz 2012). Even in $\text{Ni}_{53-x}\text{Mn}_{25}\text{Ga}_{22}\text{Co}_x$ (at.%, $x = 0, 2, 4, \dots, 14$) alloys the transformation temperatures decreased with increasing Co (Cong, D. Y. et al. 2008). It has to be seen that the decrease in temperatures is slow when $x \leq 4$ and rapid for $x \geq 5$. Figure 10 (a) shows the DSC plot of an example $\text{Ni}_{50}\text{Mn}_{34.5}\text{In}_{15.5}$ alloy in a series of $\text{Ni}_{50}\text{Mn}_{25+x}\text{In}_{25-x}$

x (0Co alloy), $\text{Ni}_{45}\text{Co}_5\text{Mn}_{25+x}\text{In}_{25-x}$ (5Co alloy) and $\text{Ni}_{42.5}\text{Co}_{7.5}\text{Mn}_{25+x}\text{In}_{25-x}$ (7.5Co alloy) systems (Ito, W et al. 2007). The curve is shown to identify Curie temperature T_C as the minimum point of the endothermic peak in the heating curve in this curve. The M_s temperatures of these alloys are seen to increase with increasing In concentration while on the contrary decrease with increase in Co content. The increase or decrease in transformation temperatures is reportedly dependent on whether Mn or Ni is substituted in off-

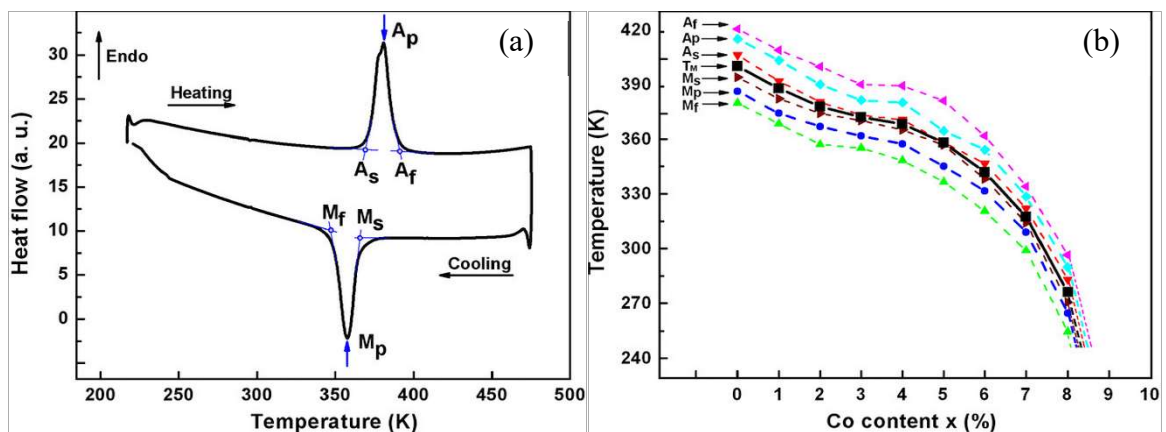


Figure 9. (a) DSC curve of $\text{Ni}_{46}\text{Co}_4\text{Mn}_{39}\text{Sn}_{11}$ alloy in $\text{Ni}_{50-x}\text{Co}_x\text{Mn}_{39}\text{Sn}_{11}$ system; (b) Composition dependence of transformation temperatures in $\text{Ni}_{50-x}\text{Co}_x\text{Mn}_{39}\text{Sn}_{11}$ alloys (Cong, D.Y., Roth & Schultz 2012).

stoichiometric quaternary alloys. Whenever an alloying element substitutes Mn the temperatures increase while they decrease if Ni is substituted (Ahamed et al. 2018).

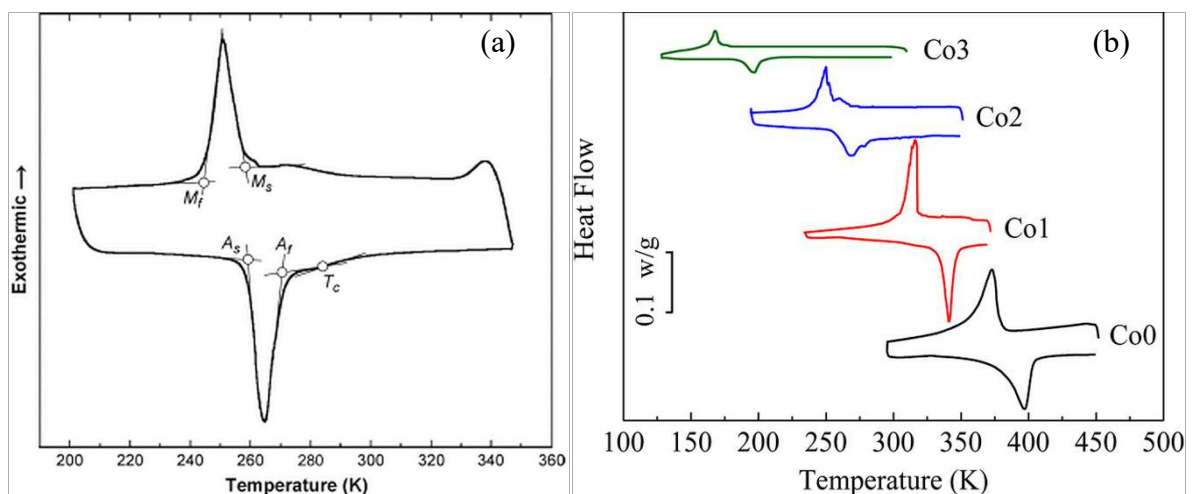


Figure 10. DSC curves of: (a) $\text{Ni}_{50}\text{Mn}_{34.5}\text{In}_{15.5}$ alloy (Ito, W et al. 2007); (b) $\text{Mn}_{50}\text{Ni}_{40-x}\text{In}_{10}\text{Co}_x$ alloys (Wu et al. 2011).

With Co substituting Ni in $\text{Ni}_{50-x}\text{Co}_x\text{Mn}_{39}\text{Sn}_{11}$ alloy system the temperatures are decreasing which is also the case in $\text{Mn}_{50}\text{Ni}_{40-x}\text{In}_{10}\text{Co}_x$ alloys in Figure 10 (b). In yet another example the transformation temperatures are seen to decrease with increasing amounts of Cu, Cu instead of Co substituting for Ni (Jing et al. 2013). On the other hand in $\text{Ni}_{50}\text{Mn}_{34-x}\text{Cu}_x\text{In}_{16}$ ($x = 1.3$ and 1.6), with Cu substituting Mn, the transformation temperatures increase, shown in Figure 11 (Kaya, M. et al. 2014).

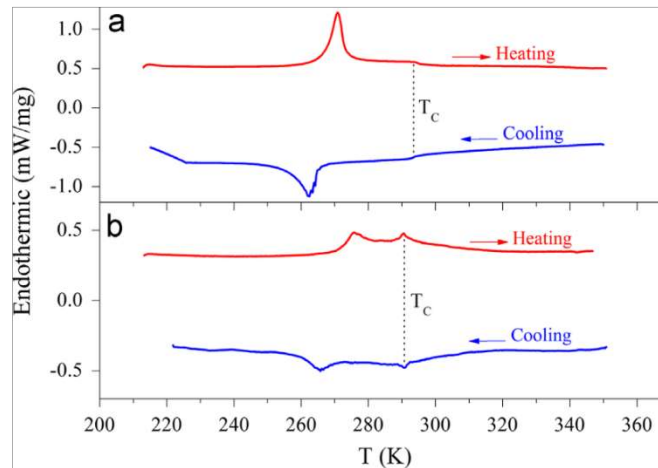


Figure 11. DSC curves of: (a) $\text{Ni}_{50}\text{Mn}_{32.7}\text{Cu}_{1.3}\text{In}_{16}$ alloy; (b) $\text{Ni}_{50}\text{Mn}_{32.4}\text{Cu}_{1.6}\text{In}_{16}$ alloy (Kaya, M. et al. 2014).

DSC scans for $\text{Ni}_{50}\text{Mn}_{37}\text{Sn}_{13}$ are shown in Figure 12 (a) and (b) corresponding to the as-cast and heat-treated samples at various durations of heat-treatment. These curves demonstrate that longer durations of heat treatment lower the compositional variations, which tend to mask the intrinsic martensitic transformation and magnetostructural

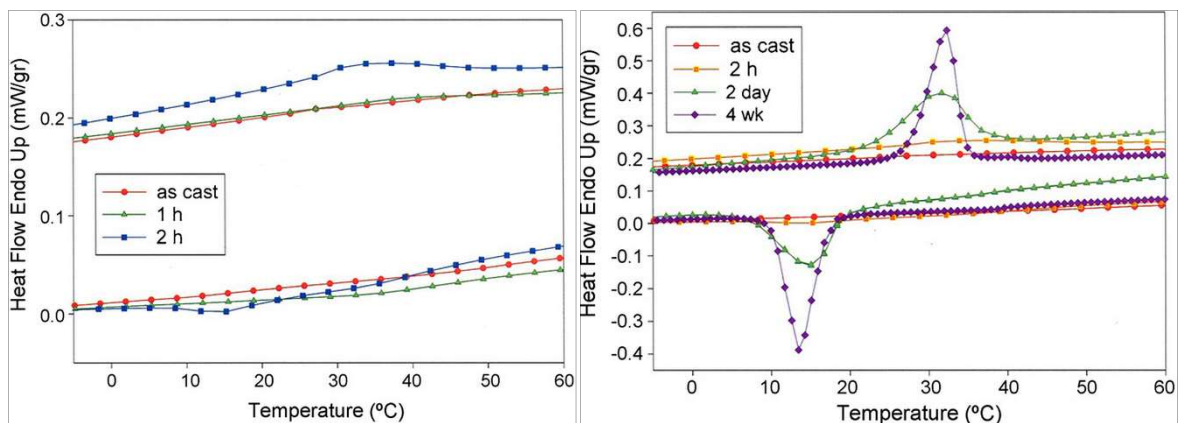


Figure 12. DSC data $\text{Ni}_{50}\text{Mn}_{37}\text{Sn}_{13}$ showing the effect of heat treatment duration at 950°C on the occurrence, temperature, and sharpness of the martensitic shape memory transformation (Schlagel, McCallum & Lograsso 2008).

behaviour. This can be seen from either the absence of or broad variations representing martensitic transformation in DSC curves of as-cast and 1 or 2h annealed samples respectively in Figure 12 (a) and also from the increasing sharpness and intensity of the DSC peaks with increasing duration of annealing in Figure 12 (b).

Among other uses of DSC is determination of metastable phases with properties different from equilibrium phases, obtained through undercooling. Glassy solidification that sometimes occur in ferromagnetic Heusler alloys can be understood by subjecting the material to large undercooling. (Wang, ZL et al. 2012) used DSC to show that the Curie temperature of austenite of an undercooled ($\Delta T = 69$ K, annealed for 10 h) $\text{Ni}_{45}\text{Co}_5\text{Mn}_{36.7}\text{In}_{13.3}$ alloy decreased by 75 K to yield a microstructure with dendrite-like precipitates which is not characteristic of the conventional (low undercooling, $\Delta T=5^\circ\text{C}$) as-cast alloy. After prolonged annealing at 1123 K for 72 h, the austenite Curie temperature increased and the characteristic stripe-like (lath) martensite phase reappeared. The effect of undercooling or non-equilibrium solidification is the lowering of In content in dendrite-like precipitates compared to the matrix with a reduced e/a ratio which caused suppression of martensitic transformation, recovery being facilitated by prolonged annealing (Wang, ZL et al. 2012).

3.2.3.2 Optical microscopy

Optical microscopy (OM) is an important tool for the morphological characterization of microstructures of materials. OM techniques provide insight into the field-induced effects in real space. (Krenke, Acet, et al. 2005) have, through optical microscopy and x-ray diffraction, shown that the $L2_1$ austenite in $\text{Ni}_{50}\text{Mn}_{50-x}\text{Sn}_x$ alloy system transformed as $10M$, $14M$ and $L1_0$ modulated martensitic structures corresponding to its composition with $x =$

25, 13, 10 and 5 respectively. From the micrographs shown in Figure 13 the grain size of both austenite and modulated martensites of this alloy system is within the range 50 – 300 μm . The composition effect was reflected in the morphologies of the modulated martensites. The 10M martensite had broader, parallel plates, 14M had finer, parallel forms and $L1_0$ had disordered plates of intermediate size. The martensites were single phase as no phase separation was observed.

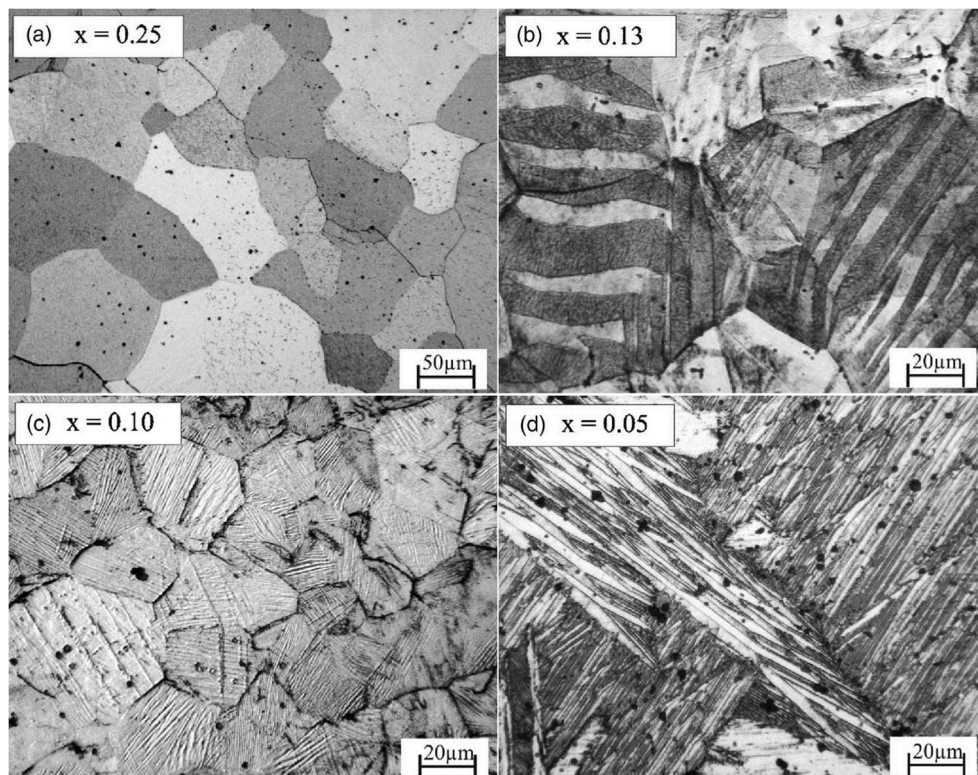


Figure 13. Optical micrographs of $\text{Ni}_{0.50}\text{Mn}_{0.50-x}\text{Sn}_x$ revealing $L2_1$ structure for $x = 0.25$, 10M for $x = 0.13$, 14M for $x = 0.10$ and $L1_0$ for $x = 0.05$ (Krenke, Acet, et al. 2005).

(Schlagel, McCallum & Lograsso 2008) present optical micrographs of $\text{Ni}_{50}\text{Mn}_{37}\text{Sn}_{13}$ in Figure 14 to show the effect of heat-treatment. The as-cast microstructure in Figure 14 (a) is multiphase dendritic structure, which transforms quickly to almost single phase structure in 1 – 2h at 950 $^{\circ}\text{C}$. The quick transformation is attributed to the initial refined structure (small length scale) from chill casting and large range of solubility below the solidus temperature, seen in Figure 14 (b) and (c). After 72 hours the structure is purely single phase, seen in Figure 14 (d).

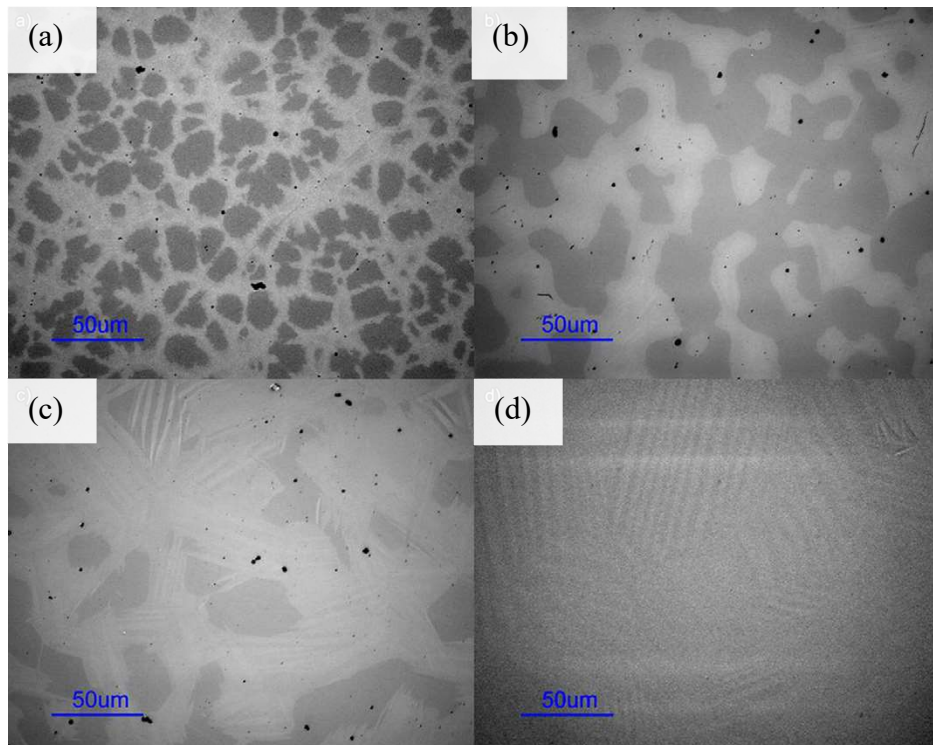


Figure 14. Optical micrographs of Ni₅₀Mn₃₇Sn₁₃ showing the effect of heat treatment: (a) as-cast; (b) 1 h; (c) 2 h; (d) 72 h at 950°C. (Schlagel, McCallum & Lograsso 2008).

Investigations on the solidification process and phases after solidification in metamagnetic Ni_{44.5}Co_{5.5}Mn_{39.5}Sn_{10.5}, Ni₄₃Co₇Mn₃₉Sn₁₁ and Ni₄₅Co₅Mn₄₀Sn₁₀ alloys revealed three phases of: *L*₂₁/martensite, *D*₀₃, and γ -phase (disordered fcc) (Pérez-Sierra, A.M. et al. 2015). The as-cast microstructures are indicative of three phases not in equilibrium because of the fast cooling rate happening when the alloy melt is cast into cold crucibles. Annealed alloys (for different times up to 14 days at 900 °C) confirm the martensitic phases, however in Ni₄₃Co₇Mn₃₉Sn₁₁ alloys, the γ -phase was present at the grain boundaries, seen in Figure 15 (a). Further annealing of Ni₄₃Co₇Mn₃₉Sn₁₁ at 950 °C for different times up to 15 days, in Figure 15 (b) and (c), again revealed γ -phase whose composition depended on the Sn and Mn content. Even at different cooling rates the solidification microstructures revealed the three phases although of different morphologies and relative amounts, shown in Figure 15 (d) – (f).

Three things stand out from these experiments: the multiphase solidification of quaternary metamagnetic Ni-Co-Mn-Sn alloys, dual solidification of $L \rightarrow D0_3 + L2_1$ and the peritectic reaction $D0_3 + L \rightarrow L2_1$ and the γ -phase precipitation from $L2_1$ upon cooling. The peritectic process overrides the $B2$ - $L2_1$ order-disorder transition normally seen in other Ni-based alloys like Ni-Mn-Ga around 650 – 800 °C (Seguí, Pons & Cesari 2007). Both $D0_3$ and $L2_1$ phases exhibit second neighbour ordering² and precipitate directly from the liquid state. $D0_3$ however completely dissolves in $L2_1$ during annealing (Pérez-Sierra, A.M. et al. 2015). The presence of the γ -phase in a metamagnetic shape memory alloy has a detrimental effect on the shape memory effect because it hinders the reorientation of the martensitic variants (Chen, F et al. 2013). They adopted melt-spinning to suppress the formation of the γ -phase in $\text{Ni}_{38}\text{Co}_{12}\text{Mn}_{41}\text{Sn}_9$ cast alloy. The γ -phase formed because the Co-content is higher, at 12at%. The appearance of this phase at higher Co-content in (Cong, D.Y., Roth & Schultz 2012) was however not identified, Figure 15 (g). In Ni-Al based shape memory alloys γ -phase appeared at higher concentration of Co as in $\text{Ni}_{47}\text{Al}_{25}\text{Fe}_{11}\text{Co}_{17}$ alloy, shown in Figure 15 (h) (Oikawa et al. 2006).

² This refers to the ordering within one sublattice of the basic bcc unit cell, such that this sublattice alternates atoms from different elements which introduces a face-centred symmetry in the unit cell (Pérez-Sierra, A.M. et al. 2015).

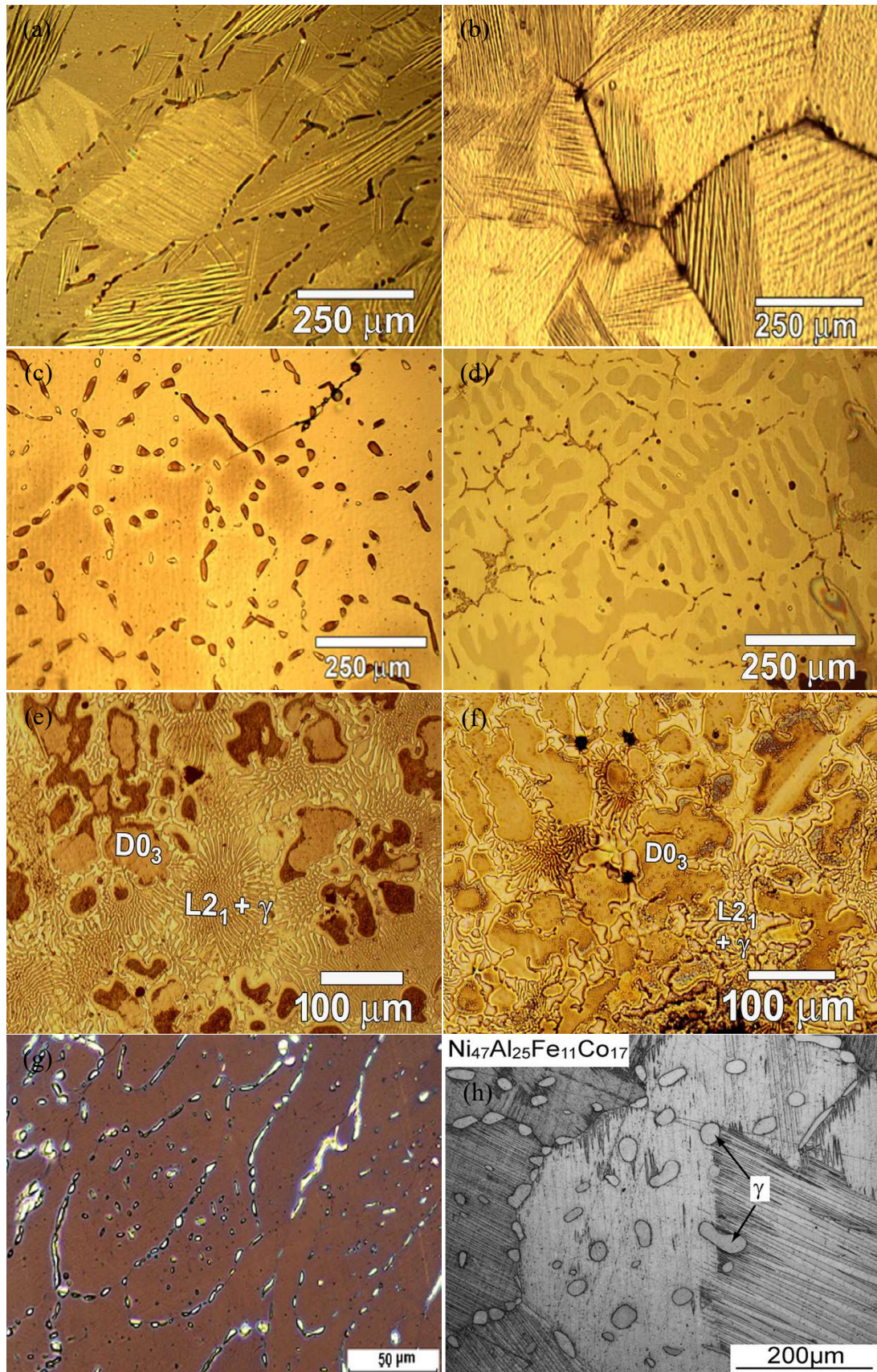


Figure 15. Optical micrographs of (a) $\text{Ni}_{43}\text{Co}_7\text{Mn}_{39}\text{Sn}_{11}$ alloy after 14 days at $900\text{ }^\circ\text{C}$ (b) after 5 days at $950\text{ }^\circ\text{C}$ (c) after 15 days at $950\text{ }^\circ\text{C}$ (d) $\text{Ni}_{44.5}\text{Co}_{5.5}\text{Mn}_{39.5}\text{Sn}_{10.5}$ at uncontrolled cooling rate; (e) $\text{Ni}_{45}\text{Co}_5\text{Mn}_{40}\text{Sn}_{10}$ at $10\text{ }^\circ\text{C}/\text{min}$ and (f) $\text{Ni}_{43}\text{Co}_7\text{Mn}_{39}\text{Sn}_{11}$ at $10\text{ }^\circ\text{C}/\text{min}$ [(a)-(f) (Pérez-Sierra, A.M. et al. 2015)] (g) $\text{Ni}_{40}\text{Co}_{10}\text{Mn}_{39}\text{Sn}_{11}$ (Cong, D.Y., Roth & Schultz 2012) (h) $\text{Ni}_{47}\text{Al}_{25}\text{Fe}_{11}\text{Co}_{17}$ (Oikawa et al. 2006).

3.2.3.3 Electron Microscopy – scanning electron microscope (SEM), transmission electron microscope (TEM), electron probe microanalysis (EPMA)

SEM has a depth of field for resolved detail much greater than the spatial resolution in the field of view. As a result, the flatness of the topological and morphological detail in the optical or transmission electron microscope is replaced by an image that is very similar to the play of light and shade over hills and valleys. An SEM has signal detectors for high energy (backscattered) electrons, low energy (secondary) electrons, and some other signals. Detectors for excited (characteristic) X-rays can provide spectra whose intensity is either a function of energy or the wavelength giving rise to terms such as energy-dispersive spectroscopy (EDS) and wavelength-dispersive spectroscopy (WDS) respectively. Both are used for the determination of the chemical composition of the region of the sample excited under the electron beam. Chemical analysis is carried out as a) an X-ray spectrum for identification of chemical elements at a specified location (point), b) an X-ray line scan for the determination of concentration gradients, segregation at grain boundaries, phase boundaries and interfaces, or c) an X-ray chemical composition map.

SEM techniques are necessary procedures for characterization of materials.

Backscatter electron (BSE) images depict the appearance of the γ -phase in $\text{Ni}_{38}\text{Co}_{12}\text{Mn}_{41}\text{Sn}_9$ metamagnetic shape memory alloy as the dark phase within the inter-dendritic eutectic microstructure in Figure 16 (a), evenly distributed dark phase in Figure 16 (b) and its suppression by the melt-spinning synthesis procedure in Figure 16 (c) wherein only the martensitic twin bands are observed (Chen, F et al. 2013). Chemical analysis of the phases using SEM-EDS (Energy Dispersive Spectrometry) microanalysis revealed the similarity in composition of the matrix phase in the bulk alloy and ribbon. Likewise in $\text{Ni}_{44.1}\text{Mn}_{35.1}\text{Sn}_{10.8}\text{Co}_{10}$ alloy, a coarse dendritic β -phase and lamellar ($\beta+\gamma$) eutectic microstructure formed from which the β -phase transformed to $L2_1$ through an ordering

transition. This is shown in Figure 16 (d) and (e). The γ -phase was indexed to $\text{Ni}_{17}\text{Sn}_3$ with *fcc* structure (Yu et al. 2014). However the absence of the lamellar eutectic structure in the melt-spun ribbons of the same alloy even as the γ -phase formed nano-precipitates along grain boundaries indicated that the secondary phase resulted from a divorced eutectic reaction in limited residual liquid phase after the primary phase formed (Yu et al. 2014). Figures 16 (f) - (h) confirmed the multiphase solidification $\text{Ni}_{45}\text{Co}_5\text{Mn}_{40}\text{Sn}_{10}$, $\text{Ni}_{44.5}\text{Co}_{5.5}\text{Mn}_{39.5}\text{Sn}_{10.5}$ and $\text{Ni}_{43}\text{Co}_7\text{Mn}_{39}\text{Sn}_{11}$ alloys respectively with the γ -phase in contact with the martensite phase in all three alloys. EDS analysis supported the SEM observations (Pérez-Sierra, A.M. et al. 2015).

(Bruno, Nickolaus M. et al. 2014) presented electron micrographs of $\text{Ni}_{43}\text{Mn}_{42}\text{Co}_4\text{Sn}_{11}$ alloy bulk and ribbon samples to emphasize that grain size refinement, shown in Figure 17, through melt-spinning and heat treatment greatly improved the magnetocaloric properties of the alloy. By subjecting the alloy ribbons to secondary heat treatment for 1 h at varying temperatures below the $B2/L2_1$ ordering temperature of around 650-800 °C in addition to the solution heat treatment at 1173 K for 2 h, the authors were able to enhance the refrigeration performance parameters of the ribbons greatly. After secondary heat treatment the ribbons were furnace cooled or rapidly quenched. The sample treated at 673 K and rapidly quenched showed largest magnetization change across martensitic transformation ΔM and smallest ΔT_{comp} . ($\Delta T_{comp} = \Delta T_{hys} + \Delta T_{elas}$, ΔT_{elas} is the average of forward and reverse elastic transformation ranges and ΔT_{hys} is the thermal hysteresis). More importantly the ribbons exhibited ~ 1.7 times larger grain size to specimen thickness (GS/t) ratio than the bulk sample. This meant that less elastic energy is stored in the microstructure requiring less driving force to complete the transformation just as in conventional shape memory alloys wherein the GS/t ratio is inversely proportional to the elastic energy storage, ΔT_{elas} .

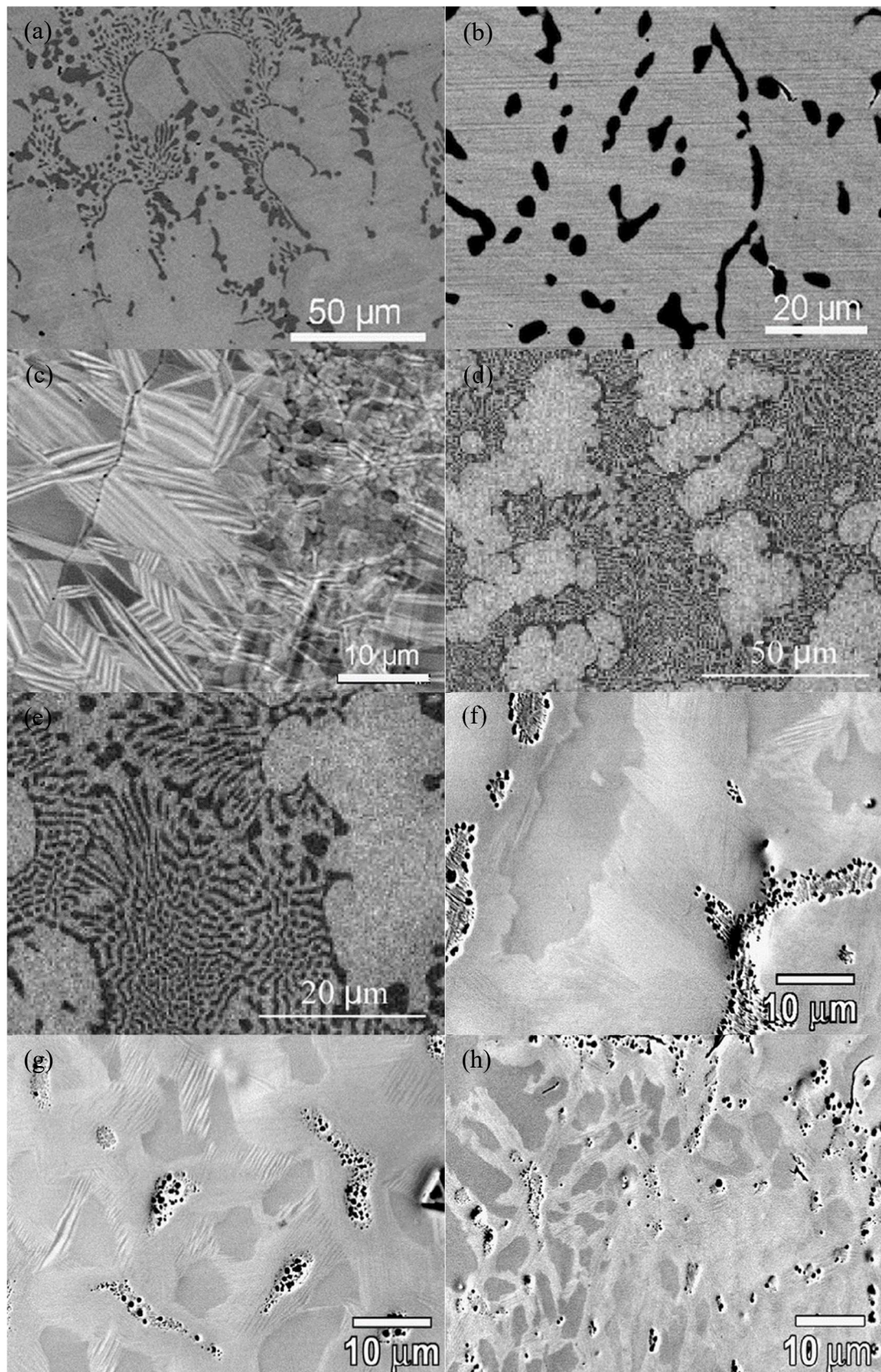


Figure 16. BSE images of $\text{Ni}_{38}\text{Co}_{12}\text{Mn}_{41}\text{Sn}_9$ (Chen, F et al. 2013): (a) as-cast ; (b) annealed at 1173 K for 1 h; (c) as-spun ribbon; (d) & (e) $\text{Ni}_{44.1}\text{Mn}_{35.1}\text{Sn}_{10.8}\text{Co}_{10}$ alloy at different magnifications (Yu et al. 2014); (f) $\text{Ni}_{45}\text{Co}_5\text{Mn}_{40}\text{Sn}_{10}$; (g) $\text{Ni}_{44.5}\text{Co}_{5.5}\text{Mn}_{39.5}\text{Sn}_{10.5}$; (h) $\text{Ni}_{43}\text{Co}_7\text{Mn}_{39}\text{Sn}_{11}$ [(f)-(h) (Pérez-Sierra, A.M. et al. 2015)]

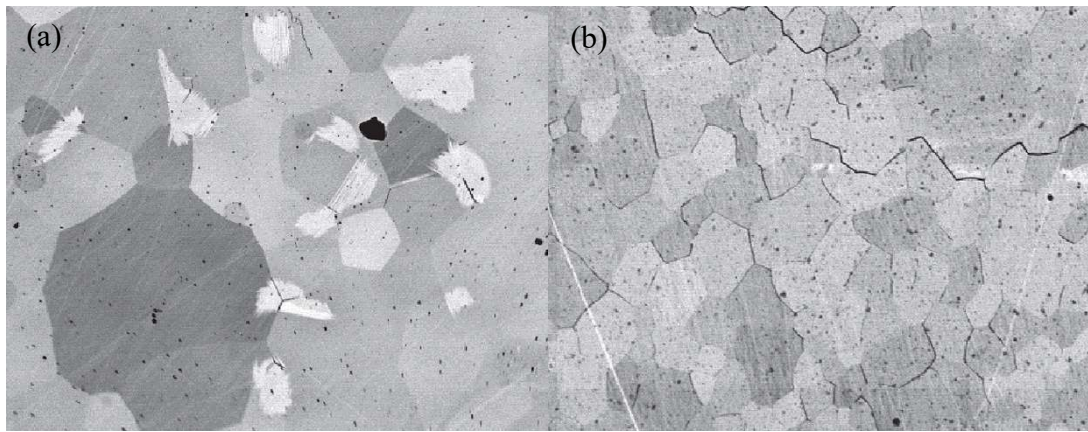


Figure 17. BSE images of $\text{Ni}_{43}\text{Mn}_{42}\text{Co}_4\text{Sn}_{11}$ alloy: (a) solutionized bulk; (b) solutionized ribbon (Bruno, Nickolaus M. et al. 2014).

(Schlagel, McCallum & Lograsso 2008) demonstrate through the use of EDS line scans on $\text{Ni}_{50}\text{Mn}_{37}\text{Sn}_{13}$ alloy that while structural homogenization is rapid the compositional homogenization evolved over extended periods in excess of 72 h. The EDS line scans in Figure 18 (e) across a 500 μm length can be seen to quantify compositional variations in Sn content as a function of homogenization time. For the as-cast structure the variations are marked with their spacing corresponding to the inter-dendritic spacing in it, seen in Figure 18 (a).

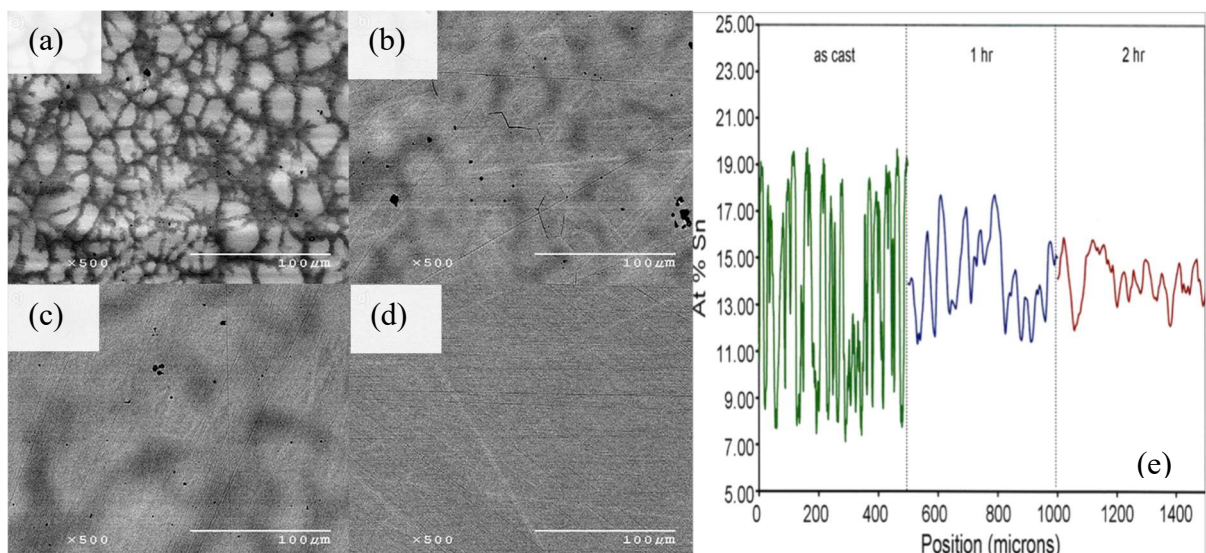


Figure 18. SEM micrographs of $\text{Ni}_{50}\text{Mn}_{37}\text{Sn}_{13}$ showing the effects of heat treatment at 950 C followed by water quench: (a) as-cast; (b) 1 h; (c) 2 h; (d) 72 h; (e) EDS line scans spanning 500 μm on $\text{Ni}_{50}\text{Mn}_{37}\text{Sn}_{13}$ samples after different lengths of heat treatment at 950 C. The frequency and range of the compositional changes decrease with heat treatment (Schlagel, McCallum & Lograsso 2008).

The variations are greatly reduced within the first two hours corresponding to Figure 18 (b) and (c) and are absent after 72 h of annealing in Figure 18 (d). These suggest that chemical homogenization has been reached.

Transmission electron microscopy (TEM) analysis has been effective in identifying the crystal structures of the single phase and in many cases multiphase microstructures resulting from the synthesis. The austenite structure in ferromagnetic Ni-Mn-X (X = Sn, In, Ga, Sb) alloy systems is of $L2_1$ atomic order. The martensite structure varies from a body-centered tetragonal (with $c/a < 1$) to layered $5M$ or $7M$ structures or even unmodulated body-centered tetragonal ($L1_0$, with $c/a > 1$) for compositions different from stoichiometric. $5M$ and $7M$ structures are also referred to as $10M$ and $14M$ respectively. The structural modulations of the martensite are periodic stacking faults of atomic planes along determined crystallographic directions, seen as extra reflections in XRD and TEM characterization. These reflections enable the modulations to be represented as nM , indicating n -fold modulation, where $n = s + 1$ ('s' being the satellite spots lying between the main spots) is the number of unit cells that constitute the superstructure (Righi et al. 2011).

Figure 19 (a) – (f) show bright field, selected area diffraction patterns and high resolution TEM images of the structures of the multiple phases of three metamagnetic shape memory alloys discussed earlier (Pérez-Sierra, A.M. et al. 2015). Figure 19 (a) – (c) depict the bright field images of the $D0_3$ /martensite, martensite plates and the $L2_1/\gamma$ -phase respectively. A martensite structure corresponding to a 6-layered modulated martensite is shown in Figure 17 (d) for a single variant of martensite. This identification is possible by counting the number of satellite spots between principal reflections, in this case 5. Figure 19 (e) shows the 6-layered structures of two variants of martensite almost orthogonal to each other Figure 19 (f) shows the high resolution image of the microtwinned martensite

structure.

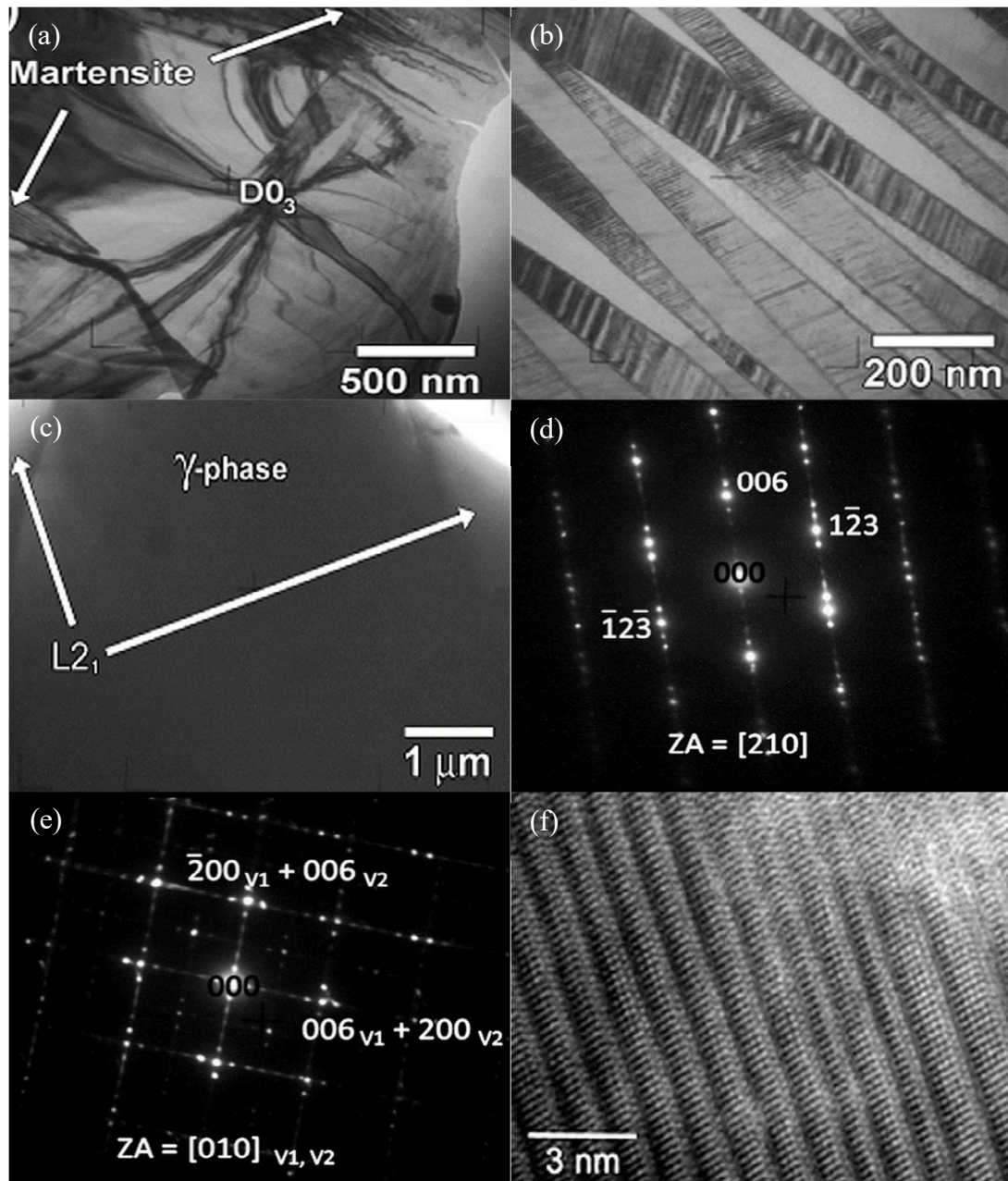


Figure 19. Bright field TEM images of: (a) $D0_3$ /martensite; (b) martensite plates; (c) $\gamma/L2_1$ phases; (d) SAED patterns of the 6-layered martensite of 1 variant; (e) SAED patterns of the 6-layered martensite of 2 variants nearly orthogonal; (f) high resolution TEM image of the microtwinned 6-layered martensite (Pérez-Sierra, A.M. et al. 2015).

Figure 20 (a) and (b) show that the γ -phase is face centred cubic in the alloys $Ni_{45}Co_5Mn_{40}Sn_{10}$, $Ni_{44.5}Co_{5.5}Mn_{39.5}Sn_{10.5}$ and $Ni_{43}Co_7Mn_{39}Sn_{11}$ discussed in (Pérez-Sierra, A.M. et al. 2015) and in $Ni_{44.1}Mn_{35.1}Sn_{10.8}Co_{10}$ (Yu et al. 2014) respectively. (Zheng et al.

2013) used TEM extensively to substantiate the X-ray diffraction analysis identifying $14M$ for $\text{Ni}_{50}\text{Mn}_{41}\text{Sn}_9$, coexistent $4O$, $10M$ and $L1_0$ for $\text{Ni}_{50}\text{Mn}_{39}\text{Sn}_{11}$ and $4O$ for $\text{Ni}_{50}\text{Mn}_{37}\text{Sn}_{13}$ alloys. For $\text{Ni}_{50}\text{Mn}_{41}\text{Sn}_9$ in Figure 21 (a), the martensite is predominantly $14M$. The $14M$ martensite has six satellite spots between the principal spots as shown in Figure 21 (b). $\text{Ni}_{50}\text{Mn}_{39}\text{Sn}_{11}$ with $4O$ modulated martensite showing nanotwinned structures is seen in the bright-field image of Figure 22 (a). $10M$ and $L1_0$ (unmodulated double tetragonal) martensites in the same alloy are seen in Figure 22 (b). SAED patterns in Figure 22 (c) – (e) confirm the structures. The $10M$ structure has four satellite spots while the $L1_0$ martensite has a three-layered periodicity (also referred as $3R$ or $2M$).

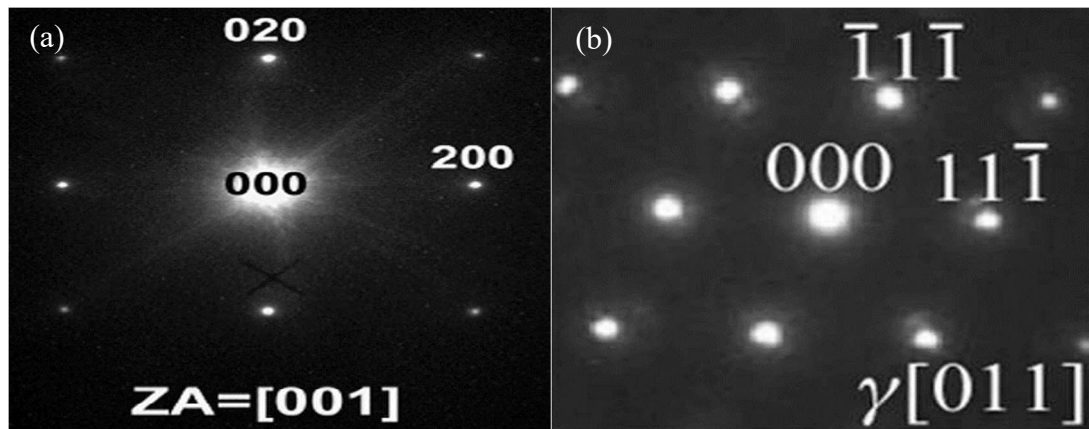


Figure 20. SAED patterns of the face centered cubic γ -phase in metamagnetic shape memory alloys: (a) $\text{Ni}_{45}\text{Co}_5\text{Mn}_{40}\text{Sn}_{10}$, $\text{Ni}_{44.5}\text{Co}_{5.5}\text{Mn}_{39.5}\text{Sn}_{10.5}$ and $\text{Ni}_{43}\text{Co}_7\text{Mn}_{39}\text{Sn}_{11}$ (Pérez-Sierra, A.M. et al. 2015); (b) $\text{Ni}_{44.1}\text{Mn}_{35.1}\text{Sn}_{10.8}\text{Co}_{10}$ (Yu et al. 2014)

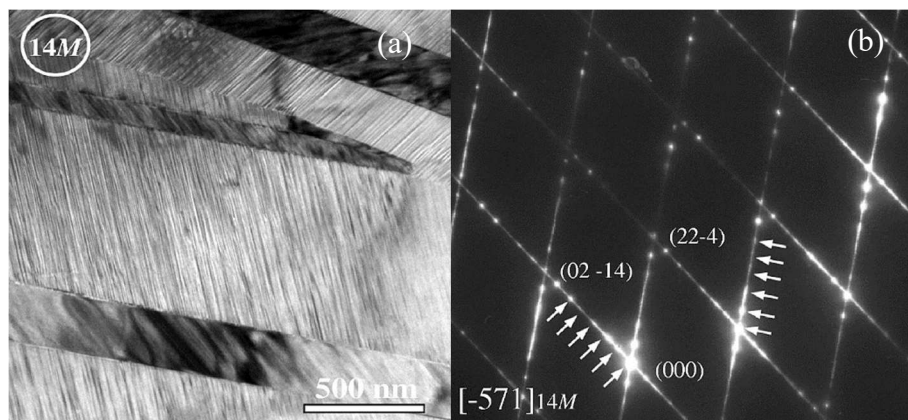


Figure 21. (a) TEM bright-field image of the $14M$ martensite in as-cast $\text{Ni}_{50}\text{Mn}_{41}\text{Sn}_9$; (b) corresponding SAED patterns taken from the highlighted area (Zheng et al. 2013).

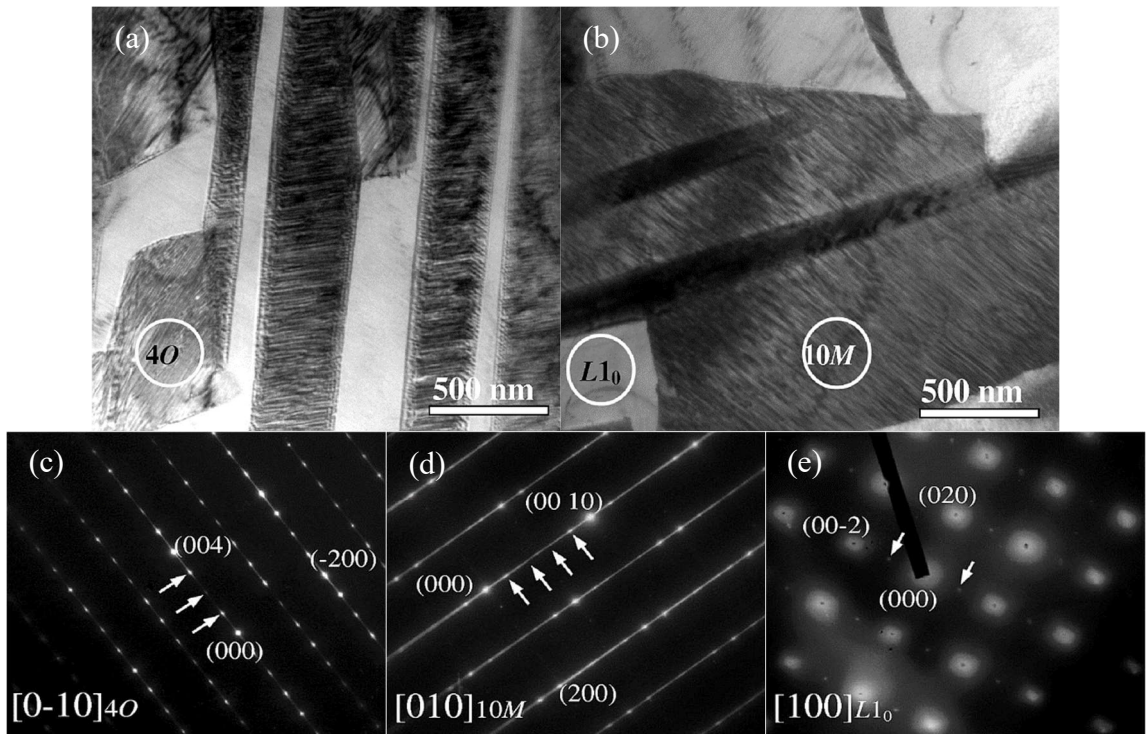


Figure 22. (a) and (b) TEM bright-field images of as-cast $\text{Ni}_{50}\text{Mn}_{39}\text{Sn}_{11}$. (c) - (e) corresponding SAED patterns of 4O, 10M and $L1_0$ martensites (Zheng et al. 2013).

$\text{Ni}_{50}\text{Mn}_{37}\text{Sn}_{13}$ exhibited $L2_1$ austenite and four-layered orthorhombic 4O structure (Zheng et al. 2013). Figure 23 (a) displays high-density twins of martensite plates whereas a high resolution TEM image in Figure 23 (b) displays the coexistence of $L2_1$ and 4O.

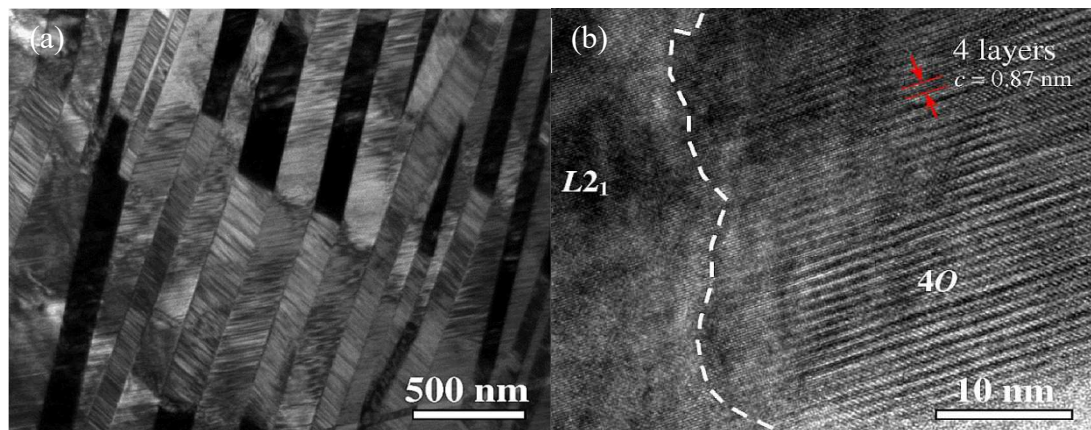


Figure 23. (a) TEM bright-field image of as-cast $\text{Ni}_{50}\text{Mn}_{37}\text{Sn}_{13}$; (b) HR TEM image of $L2_1$ austenite and 4O martensite (Zheng et al. 2013).

EPMA makes a qualitative and quantitative elemental analysis of small regions (lateral and depth dimensions ranging from 50 nm to 5 μm) at the surface of materials of

major, minor and trace elemental concentrations as low as a mass-fraction of $\sim 10^{-5}$ (CAMECA). Quantification to 1% reproducibility is obtained over several days. It is the most precise and accurate microanalysis technique available and all elements from B to U and above can be analysed (CAMECA).

3.2.3.4 X-ray diffraction (XRD)

A diffraction spectrum arising from an elastic scattering of radiations (X-rays, high-energy electrons or neutrons) can be used to understand a crystal lattice structure. A plot between the intensity of the diffracted beam and the scattering angle (twice the diffraction angle) provides microstructural information such as the Bravais point lattice, unit cell dimensions and atomic numbers of the constituent atoms (chemical species). While the intensities of the diffracted spectra are dependent on the atomic numbers, diffraction angles depend on the other two lattice signatures. This spectrum, construed as a ‘fingerprint’ of the crystal structure is usually compared with a diffraction standard such as a JCPDS (Joint Committee on Powder Diffraction Standards) file to determine the phases. The spectrum can also be compared with other calculated spectra and based on the degree of fit the crystal structure is ascertained. X-ray diffraction can be used for determination of particle size, structure refinement by spectrum fitting (Rietveld analysis) and residual stress analysis. This section shows how XRD has been used to identify the austenitic phase, various modulations of the martensitic phase including incommensurate martensite, coexistence of austenite and martensite, γ -phase, other intermetallic phases and the $B2 - L2_1$ transition.

X-ray diffraction patterns shown in Figure 24 of $\text{Ni}_{50}\text{Mn}_{37+x}\text{Sn}_{13-x}$ ($x = 0, 2, 4$) and $\text{Ni}_{50-y}\text{Mn}_{37+y}\text{Sn}_{13}$ ($y = 2, 4$) identify $L2_1$ structure for austenite and $4O$, $10M$ and $14M$ structures for the martensite. The as-cast $\text{Ni}_{50}\text{Mn}_{37}\text{Sn}_{13}$ had $L2_1$ and $4O$ structures which

after homogenization annealing at 1273 K for 4 h, reduced to a fully martensitic structure. X-ray analysis showed the effect of composition on the microstructure. With Mn substituting Sn in $\text{Ni}_{50}\text{Mn}_{37+x}\text{Sn}_{13-x}$ as in $\text{Ni}_{50}\text{Mn}_{39}\text{Sn}_{11}$ and $\text{Ni}_{50}\text{Mn}_{41}\text{Sn}_9$ the structure is

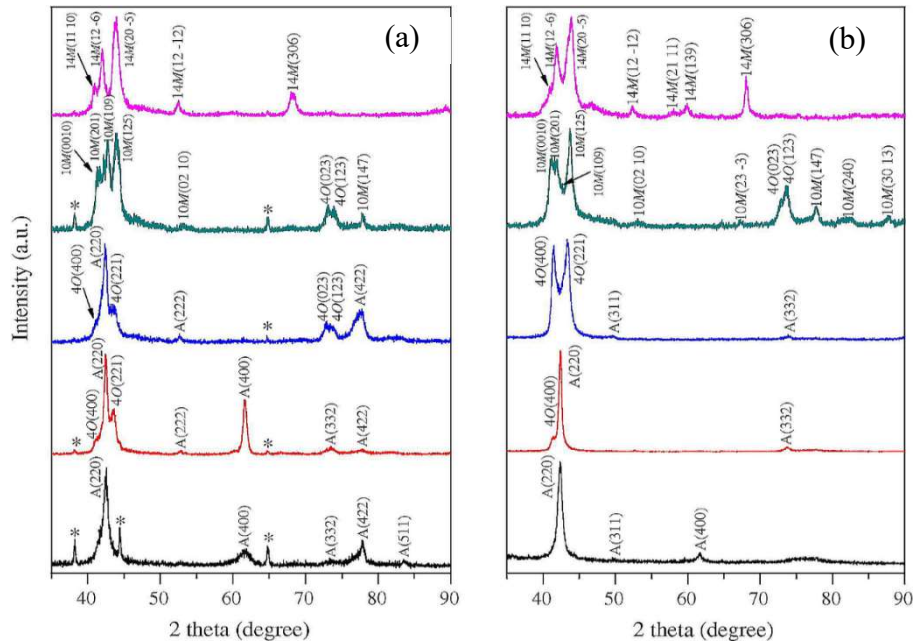


Figure 24. XRD patterns of: (a) as-cast; (b) annealed alloys. The alloys bottom-up are $\text{Ni}_{46}\text{Mn}_{41}\text{Sn}_{13}$, $\text{Ni}_{48}\text{Mn}_{39}\text{Sn}_{13}$, $\text{Ni}_{50}\text{Mn}_{37}\text{Sn}_{13}$, $\text{Ni}_{50}\text{Mn}_{39}\text{Sn}_{11}$ and $\text{Ni}_{50}\text{Mn}_{41}\text{Sn}_9$ (Zheng et al. 2013).

martensitic $10M$ and $14M$ respectively. On the contrary with Mn substituting Ni the structure turns the alloy austenitic, suppressing the martensite (Zheng et al. 2013). The analysis also showed that annealing also eliminates secondary phases such as MnSn_2 (220) and MnNi ((110) and (200)) in $\text{Ni}_{46}\text{Mn}_{41}\text{Sn}_{13}$ as-cast alloy.

X-ray diffraction patterns seen in Figure 25 (a) of the 6-layered martensite, $D0_3$, $L2_1$ and γ phases confirm the observations from electron microscopy in the alloys discussed in (Pérez-Sierra, A.M. et al. 2015). The suppression of the formation of γ -phase as a result of melt-spinning is clear from the diffraction patterns shown in Figure 25 (b). The as-cast structure of the $\text{Ni}_{38}\text{Co}_{12}\text{Mn}_{41}\text{Sn}_9$ alloy consisted of the parent phase, $10M$ martensite and

the γ -phase while the diffraction patterns from the melt-spun sample showed only the parent phase and 10M structure, with no traces of the γ -phase (Chen, F et al. 2013). Identical observations were reported in $\text{Ni}_{44.1}\text{Mn}_{35.1}\text{Sn}_{10.8}\text{Co}_{10}$ as-cast and melt-spun samples wherein the as-cast bulk alloy had a fair amount of $L2_1$ austenite and the γ -phase indexed to $\text{Ni}_{17}\text{Sn}_3$ whereas the melt-spun ribbon the peaks corresponding to γ -phase were very weak (Yu et al. 2014). The appearance of γ -phase is only when the Co content is higher.

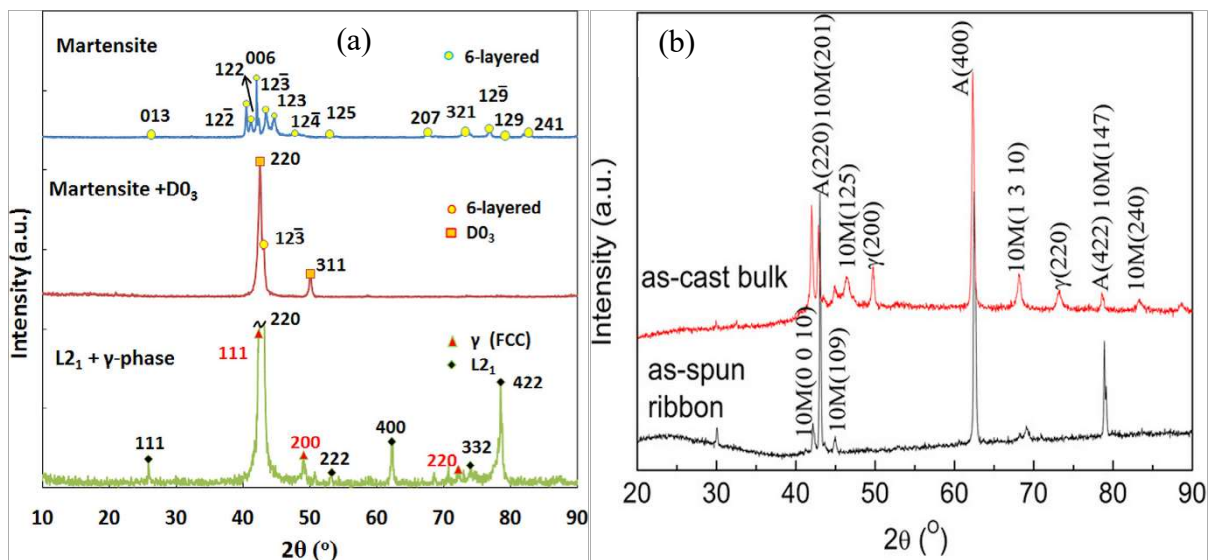


Figure 25. XRD patterns of: (a) the 6-layered martensite, D0₃ and a mixture of L2₁ and γ -phase (Pérez-Sierra, A.M. et al. 2015) (b) bulk and as-spun alloy samples at room temperature (Chen, F et al. 2013)

$(\text{Ni}_{49}\text{Mn}_{39}\text{Sn}_{12})_{100-x}\text{Co}_x$ ($x = 0, 2, 4, 6, 8$) melt-spun ribbons exhibited different structures depending upon the composition of Co. For $x = 0$ and 2 the structure was $L2_1$. The structures were $L2_1$ and 4O, $L2_1$ and 5-layered orthorhombic (10M) and purely 7-layered martensite (14M) for $x = 4, 6$ and 8 respectively (Zheng et al. 2014). The study of solidification rate and heat treatment on the magnetostructural and magnetocaloric properties of $\text{Ni}_{51}\text{Mn}_{34}\text{In}_{14}\text{Si}_1$ melt-spun ribbons revealed that higher wheel speeds and hence higher solidification rates resulted in partially ordered B2 structure instead of the ordered $L2_1$ austenite structure (Das et al. 2013). The authors use X-ray diffraction analysis

to describe the transition from $L2_1$ to $B2$ structure. $L2_1$ structure is identified by reflections from (111) and (311) planes. In Figure 26, the presence of (200) reflection and no $L2_1$

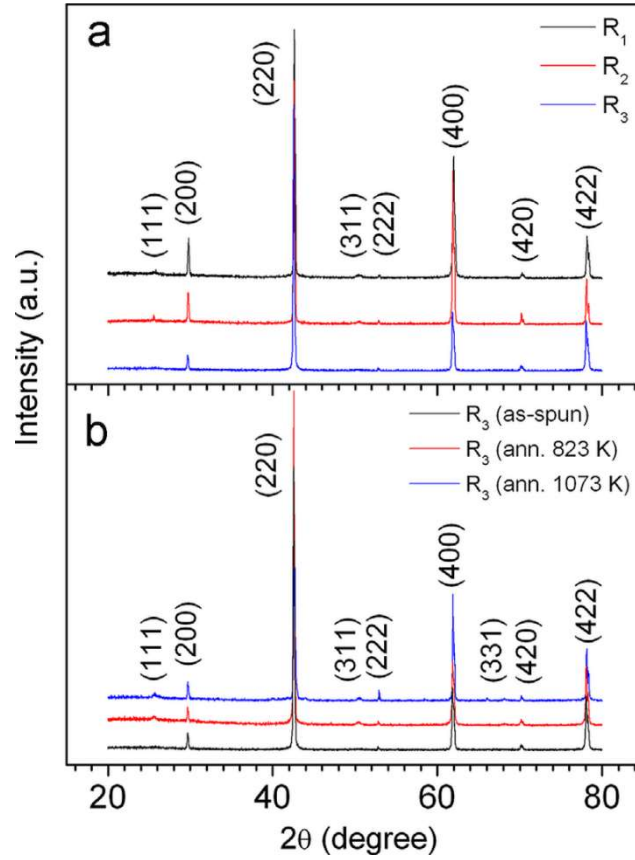


Figure 26. Room temperature XRD patterns of (a) as-spun ribbons and (b) R_3 ribbons annealed at different temperatures (Das et al. 2013).

reflections point to a $B2$ structure. Bragg reflections with non-zero structure factors result from the cubic $L2_1$ structure when the Miller indices are all either even or odd. From the figure for the first three reflections, the structure factors are $F(111) = 4(f_y - f_z)$, $F(200) = 4[2f_x - (f_y + f_z)]$, and $F(220) = 4[2f_x + f_y + f_z]$, where f_x , f_y and f_z are the average scattering amplitudes for respective sublattices X, Y and Z. In the $B2$ structure the atoms from Y and Z sub-lattices are intermixed and hence the structure factor $F(111)$ is zero (no peaks with all odd indices) indicating a transition from $L2_1$ to $B2$. Additionally an estimation of the degree of $L2_1$ order from the patterns using the relation $(I_{111}/I_{220})_{exp}/(I_{111}/I_{220})_{th}$, where I_{hkl} represent the intensity of reflection from the plane with Miller

indices (hkl) and the suffices ‘*exp*’ and ‘*th*’ correspond to experimental and theoretical data, is necessary. A decrease in the degree of order with increasing solidification rate will show that disordered *B2* structures will form as a result of this.

Melt-spun polycrystalline $\text{Ni}_{50-x}\text{Fe}_x\text{Mn}_{40}\text{Sn}_{10}$ ($x = 0, 2, 4, 6, 8$) ribbons showed well-indexed cubic P222 austenite and orthorhombic *6M* martensite above and below the austenite finish and start temperatures in addition to (200) reflection for a *B2* atomic order (Aguilar-Ortiz et al. 2016). Between these temperatures the structure was a coexistent dual phase of austenite and martensite. (Rama Rao et al. 2007) used XRD analysis on Ni-Mn-Ga alloys to suggest that the crystal structure is dependent both on the chemical composition and the processing of the alloys. The degree of *L2*₁ order of the alloys $\text{Ni}_{55}\text{Mn}_{20.6}\text{Ga}_{24.4}$, $\text{Ni}_{55}\text{Mn}_{19.6}\text{Ga}_{25.4}$, $\text{Ni}_{53}\text{Mn}_{20.4}\text{Ga}_{26.6}$ and $\text{Ni}_{49.5}\text{Mn}_{24.3}\text{Ga}_{26.2}$ improved after melt-spinning and hence the *B2* to *L2*₁ transformation.

Shown in Figure 27 are XRD patterns of Cu-doped alloys. Figure 27 (a) shows the Rietveld refinement of $\text{Ni}_{50}\text{Mn}_{32.7}\text{Cu}_{1.3}\text{In}_{16}$ and $\text{Ni}_{50}\text{Mn}_{32.4}\text{Cu}_{1.6}\text{In}_{16}$ alloys indicating pure austenite structures with fundamental lattice reflections of (220), (400) and (422). The presence of superstructure reflections at (111), (311) and (331) are an indication of the austenite phase being an ordered Heusler structure (Kaya, M. et al. 2014). Figure 27 (b) shows the room temperature diffraction patterns of $\text{Ni}_{50-x}\text{Cu}_x\text{Mn}_{38}\text{Sn}_{12}$ alloys with *L2*₁ structure for $x = 6$, *10M* martensite for $x = 0, 2$ and coexistent austenite and martensite for $x = 4$ (Jing et al. 2013).

The top panel of Figure 28 (a) shows the XRD plot of $\text{Ni}_{44}\text{Cu}_6\text{Mn}_{39}\text{Sn}_{11}$ alloy (Kaya, Melike & Dincer 2017). The crystal structure of this alloy is indexed to a pure orthorhombic *4O* structure belonging to the space group *Pmma*. The bottom panel shows

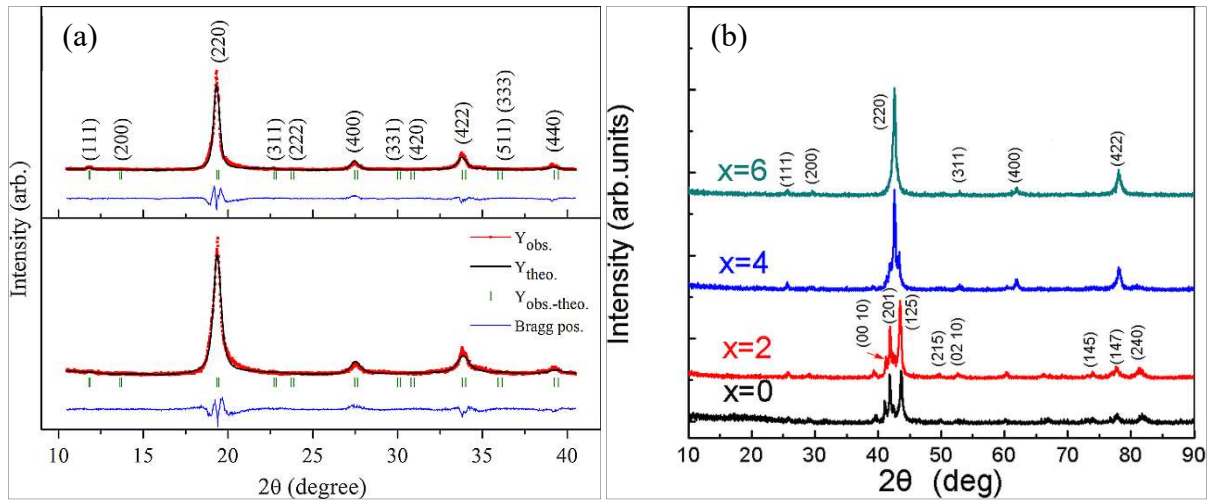


Figure 27. (a) Rietveld refinement patterns of $\text{Ni}_{50}\text{Mn}_{32.7}\text{Cu}_{1.3}\text{In}_{16}$ alloy (top) and $\text{Ni}_{50}\text{Mn}_{32.4}\text{Cu}_{1.6}\text{In}_{16}$ alloy (Kaya, M. et al. 2014); (b) Room temperature XRD patterns of $\text{Ni}_{50-x}\text{Cu}_x\text{Mn}_{38}\text{Sn}_{12}$ ($x=0, 2, 4, 6$) alloys. For $x=0$ and $x=2$, the crystal structures are $10M$ modulated martensitic structures. For $x=6$ the structure is $L2_1$ and for $x=4$ the structure is a coexistent $L2_1$ and $10M$ (Jing et al. 2013).

$\text{Ni}_{43}\text{Cu}_7\text{Mn}_{39}\text{Sn}_{11}$ alloy crystallizing to the $L2_1$ cubic structure in space group $Fm\bar{3}m$ (Kaya, Melike & Dincer 2017). With Cu substituting Ni in these alloys the transition temperatures shift towards lower values. Figure 28 (b) shows the room temperature XRD patterns of $\text{Ni}_{42}\text{Co}_8\text{Mn}_{39}\text{Sn}_{11}$ alloy (Lázpita et al. 2016). The peaks are indexed to an ordered $L2_1$ belonging to the $Fm\bar{3}m$ space group. Additionally fcc- γ is also identified. Small amounts of low-symmetry martensitic phase indexed to orthorhombic crystal structure are also seen.

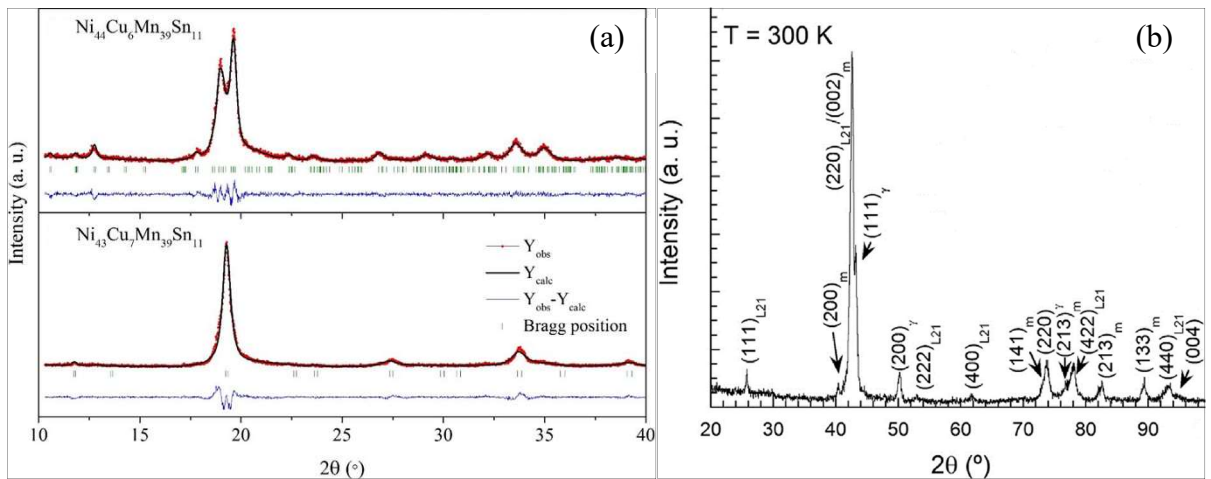


Figure 28. Room temperature XRD diffraction patterns of: (a) $\text{Ni}_{44}\text{Cu}_6\text{Mn}_{39}\text{Sn}_{11}$ alloy (top panel) and $\text{Ni}_{43}\text{Cu}_7\text{Mn}_{39}\text{Sn}_{11}$ alloy (bottom panel) (Kaya, Melike & Dincer 2017); (b) $\text{Ni}_{42}\text{Co}_8\text{Mn}_{39}\text{Sn}_{11}$ alloy (Lázpita et al. 2016).

(Çakır et al. 2015) studied magneto-structural phase transitions and the stability of the different crystallographic structures of $\text{Ni}_{50}\text{Mn}_{50-x}\text{Sn}_x$ alloys under varying temperatures for a broad range of composition $5.1 \leq x \leq 20.3$ ($7.91 \leq e/a \leq 8.34$). Figure 29 (a) to (k) show the temperature dependent diffraction patterns of the alloys. Using superspace approach (Righi et al. 2011), the different modulated phases of martensites are indexed as $5M$ (IC), $7M$ (IC) in addition to $5M$ and $L1_0$ structures for various cooling and warming sequences. IC stands for incommensurate, understood from the additional supplementary vector (modulation vector) necessary to index weak diffraction peaks in diffraction data in the superspace approach (Ahamed Khan et al. 2018). Added to the austenite-to-martensite transformation, intermartensitic transformation³ are observed at lower temperatures in Figure 29 (e), (f) and (i). In Figure 29 (e) an intermartensitic transition changes the $5M$ (IC) martensite to $5M$ (IC) + $L1_0$ mixed martensite on cooling. In Figure 29 (f) similar transformation yielded $5M$ (IC) + $7M$ (IC) mixed martensite on cooling and at further lower temperature intermartensitic transformation resulted in a mixed $7M$ (IC) + $L1_0$ from $7M$ (IC). It has been found that intermartensitic transitions lead to stabilization of the $L1_0$ structure and involve broad hysteresis of up to 100 K. This meant that functional properties of the Heusler alloys will be affected if the temperature of the working material is the below the intermartensitic start temperature (Çakır et al. 2015).

³ Intermartensitic transformations happen when the martensitic phase transforms to other modulated phases at lower temperatures. These are important because reversal back to the original martensitic phase may be difficult and may lead to loss of magnetic shape memory effect (Çakır et al. 2013)

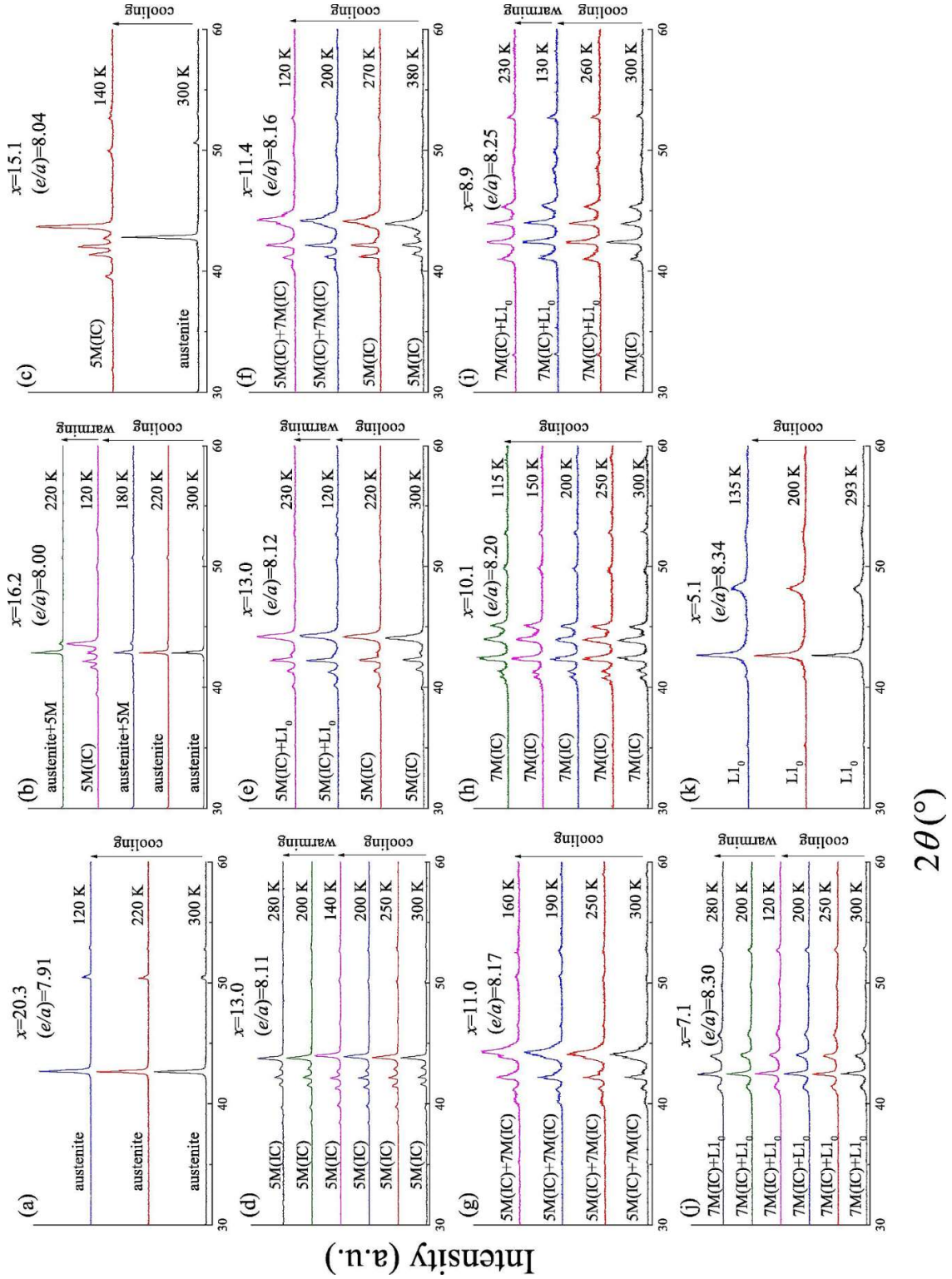


Figure 29. X-ray diffraction patterns shown in the range $30^\circ < 2\theta < 60^\circ$. (a)-(k) show patterns with varying temperature for $x = 20.3, 16.2, 15.1, 13.0, 11.4, 11.0, 10.1, 8.8, 7.1$ and 5.1 respectively (Çakır et al. 2015).

3.2.3.5 Magnetometry

Magnetization measurements are usually carried on a superconducting quantum interference device (SQUID) magnetometer or a vibrating sample magnetometer (VSM) to establish the temperature dependence of magnetization $M(T)$ in applied magnetic fields. The SQUID magnetometer can detect incredibly small magnetic fields. The principle is that in a superconducting ring with one or two weak contacts, the phase difference between the superconducting wave functions is additionally influenced by any magnetic flux through this ring. This magnetic flux is converted into electrical voltage. When a multiferroic alloy sample is moved up and down, it produces an alternating magnetic flux in the superconducting pick-up wire shown. The coil together with the antenna shown in red in Figure 30, transfer the magnetic flux from the sample to the SQUID device shown in blue, where a corresponding voltage is generated which is read in the magnetometer's electronic module (National SQUID Facility).

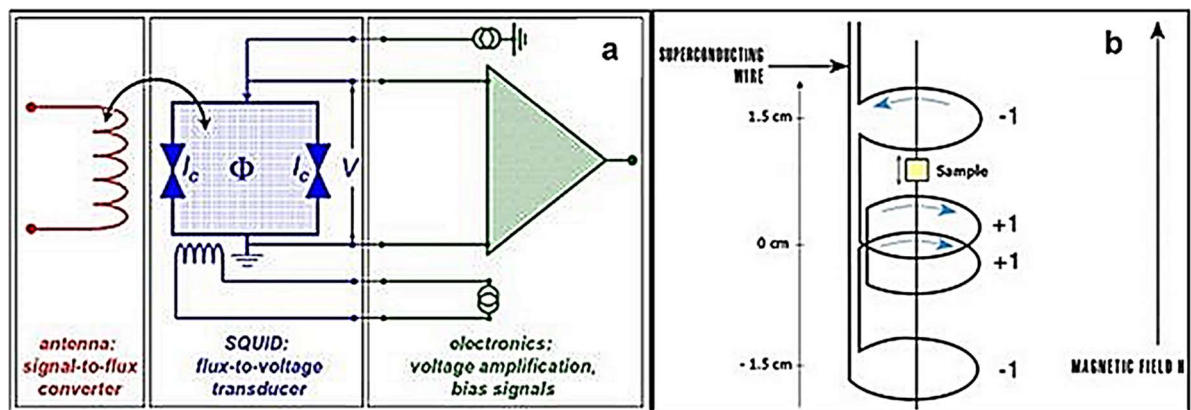


Figure 30. Principle of working of a SQUID magnetometer (National SQUID Facility).

Most of the SQUID magnetometers have a temperature range of $0 K \leq T \leq 400 K$, while measurements up to 700 K are also possible [Ref]. The measurements are done in sequential zero field cooled (ZFC), field cooled (FC) and field heated (FH) protocols. During ZFC, the specimen is cooled from higher temperature to lower temperature without

the application of the magnetic field. The specimen is then heated to higher temperature in the presence of a magnetic field while recording the magnetization values with increasing temperature. With the magnetic field still present the specimen is cooled to lower temperature for FC protocol. The specimen is subsequently heated in the applied magnetic field to a higher temperature for a FH protocol.

Characterization of magnetic behaviour is by determining the M-T and M-H curves. An observed hysteresis in the FC and FH curves is indicative of structural transition while the observed split between the ZFC and FC curves is surmised as the effect of pinning by antiferromagnetic (AF) exchange of the ferromagnetic (FM) matrix. When the Mn-Mn spacing gets smaller due to change in stoichiometry, AF exchange happens giving rise to non-collinear spin structures. These in turn pin the FM domains in different configurations which is the reason for the separation of the FC and ZFC curves (Krenke, Acet, et al. 2005). The magnetic properties are further characterized by measuring the magnetic field dependence of magnetization $M(H)$ in applied fields up to 50 kOe. Examples of magnetic characterization of $\text{Ni}_{50}\text{Mn}_{50-x}\text{Sn}_x$ for $x=15$ (Krenke, Acet, et al. 2005), by superconducting quantum interference device (SQUID) magnetometry are shown in Figures 31 (a) to (d).

From Figure 31 (a) it can be seen the sample with $x=15$ in the $\text{Ni}_{50}\text{Mn}_{50-x}\text{Sn}_x$ alloy system is ferromagnetic (FM) below $T_C^A = 320 \text{ K}$. Figure 31 (b) shows the splitting between the ZFC and FC for $x=18$ and $x=20$. The samples are ferromagnetic down to 190 K, the ferromagnetism decreasing beyond 190 K. In Figure 31 (c) the narrow hysteresis around 190 K is attributed to a first-order structural transition. In the martensitic state the split between ZFC and FC by AF exchange is more pronounced. This can be seen from the ferromagnetic nature of the martensitic state below $M_S = 189 \text{ K}$, in Figure 31 (d).

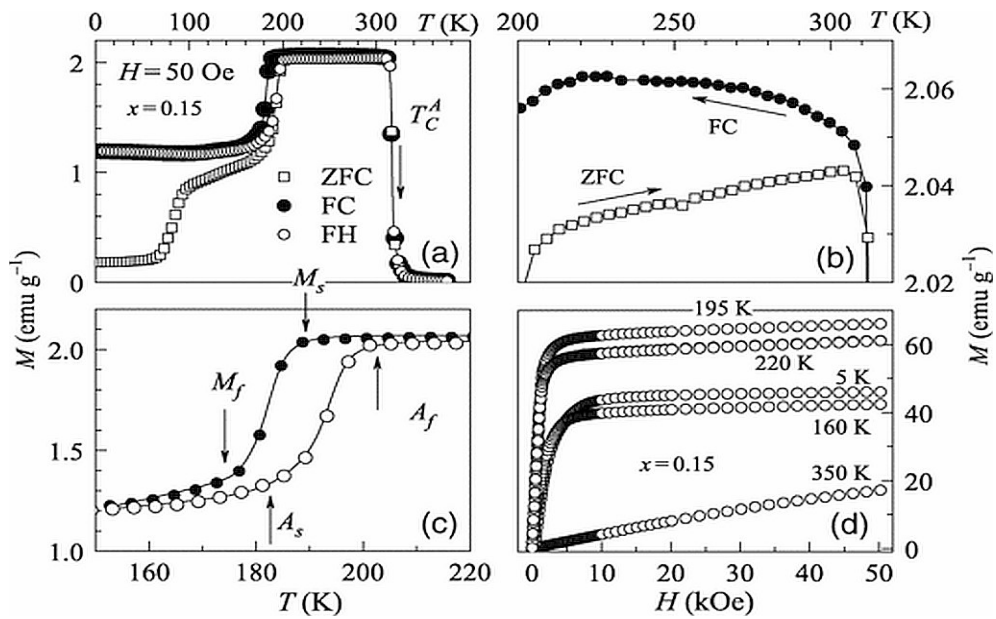


Figure 31. (a) – (d) $M(T)$ and $M(H)$ curves of $\text{Ni}_{0.50}\text{Mn}_{0.35}\text{Sn}_{0.15}$ alloy (Krenke, Acet, et al. 2005)

Figure 32 (a) shows the magnetization vs temperature curves of as-cast, 2 h and 4 weeks annealed $\text{Ni}_{50}\text{Mn}_{37}\text{Sn}_{13}$ alloy (Schlagel, McCallum & Lograsso 2008) in magnetic fields varying from 0 to 5 T. These curves establish the occurrence of magnetostructural transformation besides furnishing information on the effect of annealing on the transformations. In the as-cast alloy a magnetic ordering is observed at around 350 K on cooling from the high temperature austenite region. As it is cooled further the slope of $M(T)$ curve is seen to change abruptly suggesting presence of overlapping transitions or secondary phases. For the 2 h annealed alloy three transitions are evident. The first magnetic ordering occurs at around 325 K. The second is a structural transition at ~ 300 K to martensite with a drop in magnetization by 33%. The third is a magnetic transition of the martensite at 250 K with an overlap between the 2nd and 3rd transitions. The alloy annealed for 4 weeks shows no overlap but clear separation between the structural transformation and magnetic ordering temperature of the martensite. The structural transformation to martensite results in a drop of magnetization to zero and the second magnetic ordering of the martensite occurs at ~ 250 K.

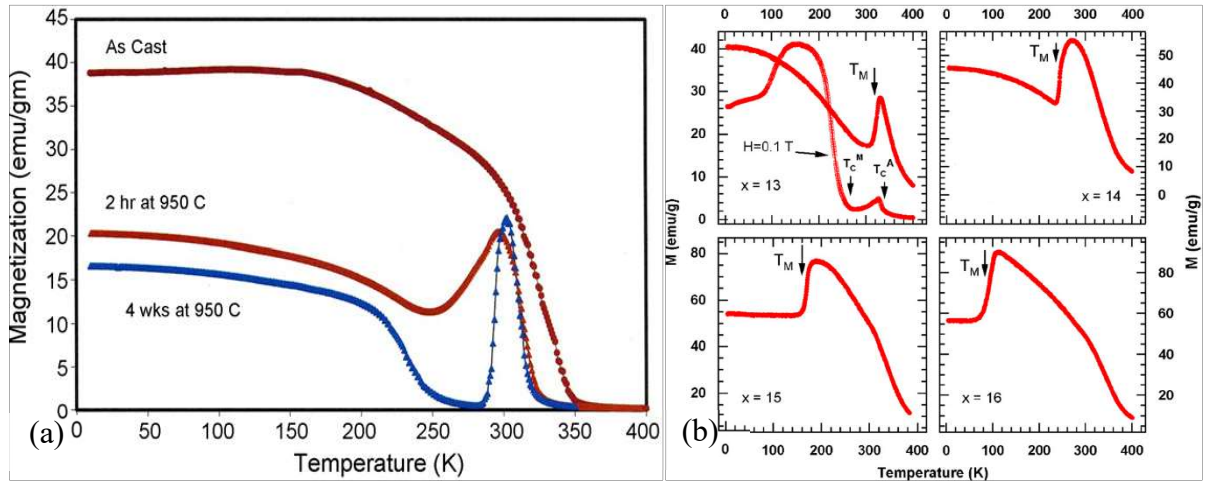


Figure 32. (a) Magnetization as a function of temperature for Ni₅₀Mn₃₇Sn₁₃ alloy in the as-cast condition and annealed at 950 °C for 2h and 4w (Schlagel, McCallum & Lograsso 2008); (b) Magnetization vs Temperature curves of Ni₅₀Mn_{50-x}Sn_x (x = 13, 14, 15 & 16). For x = 13 the magnetization data was measured at 5 T and 0.1 T while for others the applied field was 5 T (Khan et al. 2008).

Figure 32 (b) shows the magnetization vs temperature curves of Ni₅₀Mn_{50-x}Sn_x (x = 13, 14, 15 and 16) alloys. For x = 13, the curve at 5 T resembles the curve for the 2 h annealed alloy of same composition in Figure 32 (a). At H = 0.1 T, the magnetization is seen to increase with temperature. Near 200 K the system approaches the Curie temperature of the martensitic phase T_C^M , with a drop in magnetization. This drop is a result of the system becoming paramagnetic or antiferromagnetic. At near 310 K the transition to paramagnetic state is interrupted by a martensitic transformation to austenitic structure with a corresponding magnetization increase. Finally the system shows purely paramagnetic behaviour as the temperature exceeds the Curie temperature of the austenite state at $T_C^A \approx 350$ K. The martensitic and austenitic structures can be seen to ferromagnetic with separate T_C as shown in Figure 32 (b).

Figure 33 (a) shows the magnetization vs temperature curve under 0.05 T of the alloy Ni₄₅Co₅Mn₃₉Sn₁₁ alloy belonging to the Ni_{50-x}Co_xMn₃₉Sn₁₁ system of alloys (Cong, D.Y., Roth & Schultz 2012). The Curie temperature (T_C) is also determined as the temperature at

which dM/dT shows a minimum in the temperature range $T > A_f$. A Curie transition at ~ 376 K occurs during cooling with a sudden increase in the magnetization. Abrupt changes at ~ 345

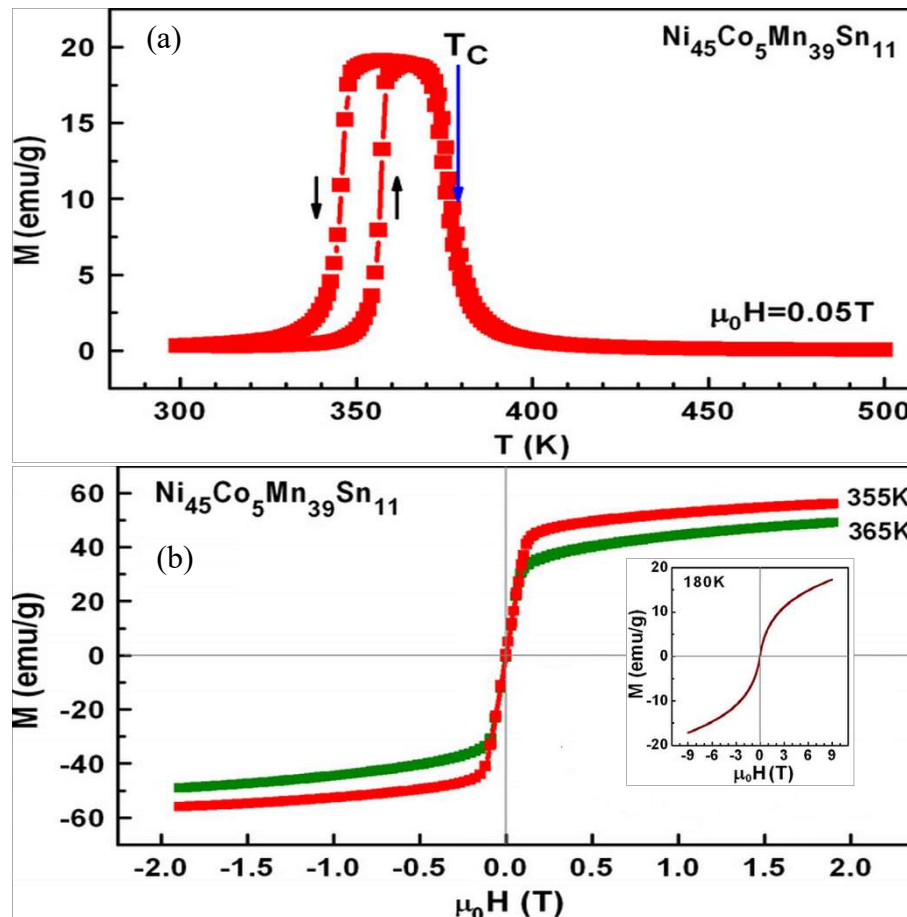


Figure 33. M-T curve under a magnetic field of 0.05 T in the temperature range of 500 - 300 K of $\text{Ni}_{45}\text{Co}_5\text{Mn}_{39}\text{Sn}_{11}$ alloy; (b) M-H curves of the austenite at 355 K and 365 K (below T_C) of $\text{Ni}_{45}\text{Co}_5\text{Mn}_{39}\text{Sn}_{11}$ alloy; (Inset) M-H curve of martensite at 180 K of sigmoid shape (Cong, D.Y., Roth & Schultz 2012).

K and ~ 360 K with corresponding decrease and increase respectively of the magnetization at these temperatures confirm the martensitic and reverse transformations. Figure 33 (b) shows the magnetization vs applied field of austenite at 355 K and 365 K (Cong, D.Y., Roth & Schultz 2012). With the magnetization being high it is clear that the austenite is ferromagnetic below T_C . Shown in the inset of Figure 33 (b) is the magnetization vs applied

field of the martensite at 180 K which is of sigmoid shape with absolutely no hysteresis. Such behaviour is indicative of superparamagnetic behaviour of the martensite.

3.2.4 Effects of microstructure on properties

The most important aspect concerning the magnetostructural effects, microstructures, properties and functions of ferromagnetic Heusler alloys is the composition (Ahamed Khan et al. 2018). $\text{Ni}_{54}\text{Mn}_{20}\text{Ga}_{26}$ thin films prepared by magnetron sputtering demonstrated martensitic phase transformation above room temperature (Shevyrtalov, Miki, et al. 2018) because of a greater extent of hybridization between the excess Ni and Ga in the alloy besides film stress. The effect of composition is not restricted to the prototype Ni-Mn-Ga alloys alone. Metamagnetic shape memory alloys are growing to be technologically significant (Chen, X et al. 2014; Lázpita et al. 2016; Wu et al. 2011) where the stoichiometric composition is varied by tuning the compositions at will with remarkable magnetocaloric effects. To cap it all is the tuning of the composition to draw a perfect austenite-martensite interface with no stressed transition layer which yielded the highest saturation magnetization several orders higher than normally observed (Srivastava, Chen & James 2010). The alloy $\text{Ni}_{45}\text{Co}_5\text{Mn}_{40}\text{Sn}_{10}$ resulting from the tuning was later used in direct energy conversion (Srivastava et al. 2011).

While the crystal structure has a certain effect on the magnetostructural properties, tuning the composition changes it affecting the property being studied. The exact martensitic structure that would evolve for a particular composition and its effect on the properties could not be predicted as there are no rules to predict them. Nevertheless the structure may evolve as cubic – $10M$ – $14M$ – $L1_0$ as seen earlier in accordance with an increasing e/a ratio and temperature (Planes, Mañosa & Acet 2009). In the case of Ga-

doped NiMn alloys, for the structure to be technologically significant the twinning stress has to be minimum for which the lattice distortion, c/a of the martensite has to be minimum. $5M$ and $7M$ martensites were suitable for magnetic-field-induced strain (MFIS) by virtue of the low twinning stress and high anisotropy in them while the non-layered tetragonal $T(L1_0)$ reportedly exhibited high anisotropy and high twinning stress, but not MFIS (Sozinov, Alexei et al. 2003). However addition of small amounts of Co and Cu to NiMnGa yielded a non-modulated structure with an MFIS of 12% (Sozinov, A. et al. 2013).

The differences in the magnetic entropy change (ΔS_m) in off-stoichiometric Ni-Co-Mn-Sn alloys are due changes in composition as seen from arc-melted $Ni_{41}Co_9Mn_{40}Sn_{10}$, $Ni_{43}Co_7Mn_{39}Sn_{11}$ and $Ni_{50}Mn_{34}Co_2Sn_{14}$ alloys and melt-spun $Ni_{48}Co_2Mn_{38}Sn_{12}$ alloy. The composition apparently overrides the crystal structure in the determination of the properties. Interestingly the nature of the transformations too, influences the magnetostructural characteristics (Ahamed Khan et al. 2018). For instance, it may be seen that intermartensitic or martensite-to-martensite transformations yield intermediate structures which may undergo irreversible transformation to b.c.t structures capable of deteriorating the MSM effect (Pérez-Landazábal et al. 2015). This may be partly due to the presence of extended grain boundaries and dislocations (Çakır et al. 2013). Step-like thermoelastic martensite transformation resulting from the compositional segregation in a directionally solidified polycrystalline $Ni_{40.6}Co_{8.5}Mn_{40.9}Sn_{10}$ enhanced the magnetocaloric properties while at the same time widening the working temperature range (Chen, F et al. 2017). Intermartensitic and step-like transformations however are still not clearly understood (Sozinov, Alexei et al. 2003).

Across the martensitic transformation a change in the unit cell volume has a profound effect on the magnetostructural properties, particularly magnetocaloric and also on the

martensitic transformation (Rama Rao et al. 2009; Zheng et al. 2013; Zheng et al. 2014). A volume contraction of -1.31% accounted for a magnetic entropy of 31.9 J/kg K in Ni₄₁Co₉Mn₄₀Sn₁₀ polycrystalline alloy (Huang et al. 2015). Similarly a volume change of 4% accounted for an entropy change of -47.3 J/kg K in Mn-Co-Ge-B alloy (Gschneidner Jr, Mudryk & Pecharsky 2012; Trung et al. 2010). This correlation between the unit cell volume change and structural entropy change with a corresponding magnetic entropy change can be used to predict high-performance magnetocaloric materials from crystallographic data.

The degree of long range $L2_1$ atomic order significantly lowers the transformation entropy change through large shifts in the transformation temperatures in relation to the change in magnetization of the austenite phase (Kustov et al. 2009; Pérez-Sierra, A. M. et al. 2016; Recarte et al. 2012; Sánchez-Alarcos, V. et al. 2012). While $L2_1$ atomic order refers to the fraction of atoms located in the correct sub-lattice of $L2_1$ structure, studies show it can be varied by thermal treatment (Sánchez-Alarcos, Vicente et al. 2014). There are intricate relationships between microstructural factors such as long-range ordering and glassy behaviour coinciding with the arrest of martensitic transformation (Bruno, N. M. et al. 2018). The authors (Bruno, N. M. et al. 2018) show that an unclassified defect quenched in vacancies co-existed with B2 and $L2_1$ long range ordering and led to transformation arrest. Microstructural changes through tuning of stoichiometry also have the effect of increasing the transformation temperatures thus transporting the alloys into the realm of high temperature shape memory alloys (HTSMAs, with temperatures up to 300°C above the standard SMAs such as TiNi with operating temperature of 100°C) (Ahamed Khan et al. 2018). The structure remains cubic $L2_1$ at higher temperatures and transforms to tetragonal upon cooling. Such alloys are useful for applications in automotive and aerospace engines, limited by issues such as brittleness of the alloys. The formation of a ductile γ -

phase with (Ma, Y et al. 2009; Yang, S et al. 2016) or without (Ma, Y et al. 2007) addition of dopants like Co improves the ductility of the alloy, however does not contribute to shape memory effect (SME). The loss of SM/MSM is offset by an improvement in the mechanical properties. The SME is observed to decrease with increasing γ -phase fraction in the combined microstructure of tetragonal martensite and face-centred cubic γ -phase. On the contrary the single-phase martensite with no γ -phase in $\text{Ni}_{54}\text{Mn}_{25}\text{Ga}_{21}$ recorded a good SME. Where there has been an appreciable shape memory effect (SME) in two-phase martensite with γ -phase, it is because the grain size of the γ -phase is smaller with circular morphology brought about by annealing (Yang, S et al. 2016) and thermomechanical treatment of hot rolling (Ma, Y et al. 2009).

Neither the modulation of crystal structure nor the type of magnetic ordering determined the reported giant magnetic field induced strain (Sozinov, Alexei et al. 2003). It was believed that $10M$ or $14M$ modulated martensitic structures with $c/a < 1$ yielded MFIS while non-modulated tetragonal structure with $c/a > 1$ did not. However it has been seen that the mechanism by which field-induced strain occurred is the same irrespective of the modulated structure as in directionally solidified $\text{Ni}_{46}\text{Mn}_{24}\text{Ga}_{22}\text{Co}_4\text{Cu}_4$, $\text{Ni}_{45}\text{Mn}_{23}\text{Ga}_{22}\text{Co}_5\text{Cu}_5$ and $\text{Ni}_{46}\text{Mn}_{22.5}\text{Ga}_{23}\text{Co}_5\text{Cu}_{3.5}$, all of which had $c/a \approx 1.14$ and exhibited near 10% magnetic field-induced strain (Rameš et al. 2018). Also that the magnetic field-induced strain occurred in the martensite phase and did not involve phase transformation.

3.2.5 Heat treatment of ferromagnetic Heusler alloys

The microstructures of the alloys, which wield enormous influence on their magnetostructural properties, are to a great extent dependent on the heat treatment

procedures adopted. Long period annealing achieves structural and chemical homogenization (Schlagel et al. 2008), after which the magnetostructural behaviour is more pronounced. The reasons are understandable because multiphase solidification leads to compositional variations which persist even after short anneals and are capable of annulling the magnetostructural behaviour (Schlagel, McCallum & Lograsso 2008). Annealing of $\text{Ni}_{48}\text{Mn}_{39}\text{In}_{13}$ ribbons caused changes in the atomic ordering and the grain size of the alloy ribbon due to which the transition temperatures and magnetic entropy change increased considerably (Zhao et al. 2010). Low temperature annealing of homogenized samples (1223 K for 4 weeks) of $\text{Ni}_{50}\text{Mn}_{50-x}\text{Sn}_x$ ($x=10-25$) alloys at 773 K caused decomposition to compositions near $x = 1$ and $x = 20$. While one composition would likely exhibit transformation above 700 K, the other exhibited none (Yuhasz et al. 2009; Yuhasz et al. 2010). It was confirmed that the $L2_1$ phase is metastable at 773 K over an intermediate composition range and that transformations below 400 K account for the ferromagnetic shape memory behaviour. The combination of processes and heat treatments also contribute to the microstructure. Heat treated ribbons exhibited ~ 1.7 times larger GS/t (grain size to thickness ratio) than solutionized bulk sample and were more suited for magnetocaloric applications (Bruno, Nickolaus M. et al. 2014). Wheel speed and annealing temperature control grain size, inter-atomic distance, smaller thermal hysteresis and degree of atomic ordering in order to achieve remarkable magnetic properties (Das et al. 2013; Wang, W et al. 2015).

3.2.6 Phase equilibria

Phase diagrams, usually drawn between structural/magnetic phase transition temperatures and the e/a ratio in the case of Heusler alloys, underscore the composition dependence of the transforming phases as in Ni-Mn-Sn alloys (Krenke, Acet, et al. 2005). Phase changes

in transforming material can be represented graphically as phase diagrams. Alloy phase diagrams are useful to metallurgists, materials engineers, and materials scientists in four major areas: (1) development of new alloys for specific applications, (2) fabrication of these alloys into useful configurations, (3) design and control of heat treatment procedures for specific alloys that will produce the required mechanical, physical, and chemical properties, and (4) solving problems that will arise with specific alloys in their performance in commercial applications (Campbell 2012).

Phase diagrams present the relationship between different phases essentially in equilibrium conditions. An exception to equilibrium phases is the presence of metastable phases which decompose extremely slowly even under the most favourable conditions and are at variance with the principles of phase equilibria. Ferromagnetic Heusler alloys exhibit a low-temperature, non-equilibrium metastable state called the magnetic glass, resulting from a kinetic arrest of martensitic transformation under a magnetic field during cooling. The fraction of the arrested austenite persists down to lower temperatures as magnetic glassy state. The applied magnetic field either increases or decreases the kinetic arrest. When the alloy is cooled and heated in differing magnetic fields of H_C and H_W respectively, de-arrest or unfreezing of magnetic glass is possible and a re-entrant transition from the metastable state happens for a critical value of $(H_C - H_W)$ (Lakhani et al. 2012).

Phase diagrams of ternary/quaternary Ni-Mn-Sn alloys are limited in literature. A vertical section of the $Ni_{50}Mn_{50-x}Sn_x$ system ($0 \leq x \leq 50$ at %) in Figure 34 (a) showed $B2$ phase melting congruently at 25at% Sn and going over into the high temperature MnNi (H) phase as the Sn content decreased (Wachtel, Henninger & Predel 1983). From the three-phase ($L+Ni_3Sn+Ni_3Sn_2$) region at 32 at% Sn, single phase Ni_3Sn_2 hexagonal phase formed at lower temperatures. A face-centered cubic γ -region of Mn-Ni system appeared at small Sn

concentrations and a face-centered tetragonal MnNi (T) phase of the CuAuI ($L1_0$) type also existed as a single narrow region.

A similar phase diagram of the $Ni_{50-x}Co_xMn_{39}Sn_{11}$ alloy system in Figure 34 (b) delineates the structural phases and magnetic states in response to compositional variations of element Co (Cong, D.Y., Roth & Schultz 2012). In this diagram with $0 \leq x \leq 4$, the austenite is paramagnetic while martensite is paramagnetic, superparamagnetic (SPM) and

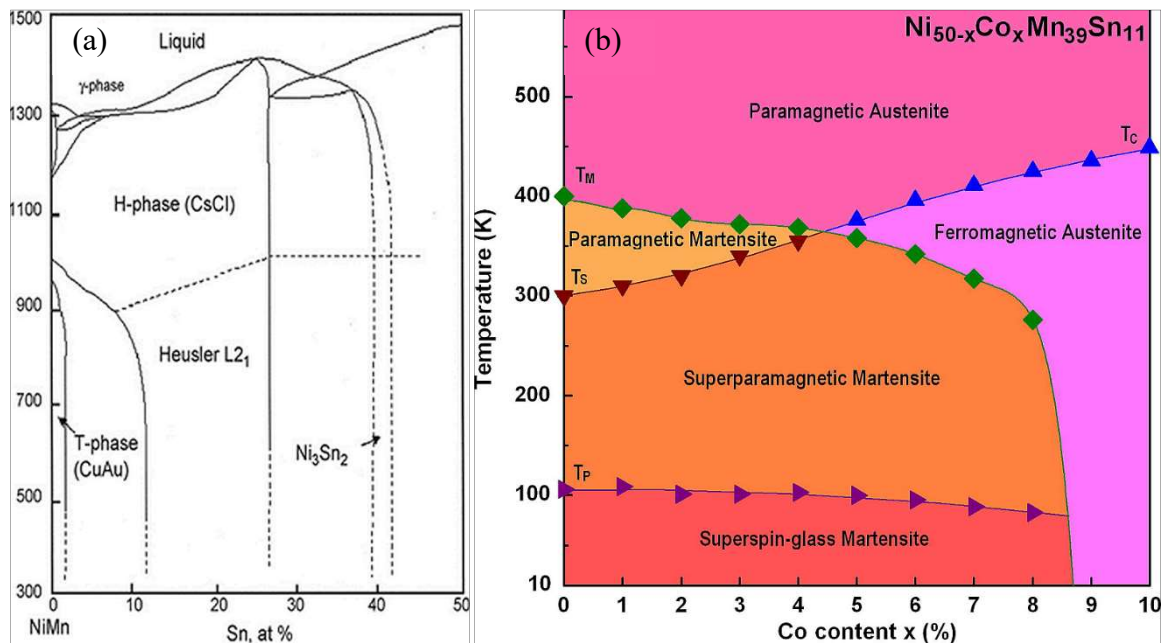


Figure 34. (a) Vertical section of the $Ni_{50}Mn_{50-x}Sn_x$ ($0 \leq x \leq 50$ at%) (Wachtel, Henninger & Predel 1983); (b) Phase diagram of $Ni_{50-x}Co_xMn_{39}Sn_{11}$ ($0 \leq x \leq 10$) alloy system (Cong, D.Y., Roth & Schultz 2012).

superspin glass (SSG) in different temperature ranges during cooling. With $5 \leq x \leq 8$ the austenite is paramagnetic above Curie temperature T_C and ferromagnetic below T_C and the martensite is SPM and SSG in different temperature ranges. For $9 \leq x \leq 10$ the austenite is again paramagnetic above T_C and ferromagnetic below T_C , down to 10 K (Cong, D.Y., Roth & Schultz 2012). SPM refers to the magnetic behaviour with no magnetic hysteresis (zero remanence and coercivity), while SSG has a spin configuration which is random in nature, similar to a paramagnet frozen in time (Sharma, Chattopadhyay & Roy 2007). The phase diagram in Figure 35 of the $Ni_{50}Mn_{50-x}Sn_x$ alloys show the intermartensitic transformation

boundaries with temperatures represented by red triangles (Çakır et al. 2015). The $L1_0$ martensite is at the ground state phase. $5M$ and $7M$ phases act as adaptive phases between $L2_1$ and $L1_0$ structures to compensate the strains occurring during forward and reverse transitions. The concept of adaptive martensite is that modulated martensite is not an equilibrium phase but a nanoscale microstructure of non-modulated (NM) martensite (Niemann et al. 2012). Modulated phases form to minimize elastic energy near the phase boundary by introducing low-energy twin boundaries between lamellae of NM martensite that have widths of a few unit cells (Niemann et al. 2012).

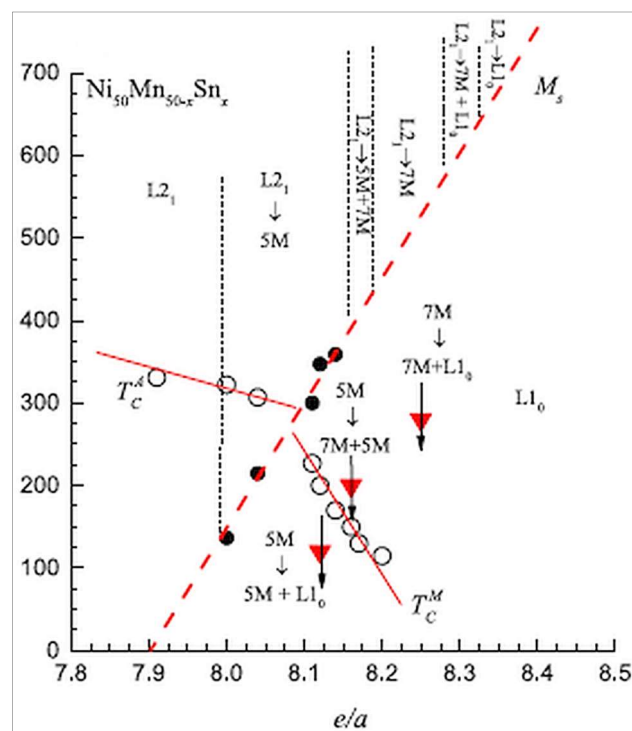


Figure 35. Phase diagram of $\text{Ni}_{50}\text{Mn}_{50-x}\text{Sn}_x$ alloys. Filled circles represent austenite-martensite transition temperatures, open circles correspond to the martensitic and austenitic Curie temperatures. Intermartensitic transition temperatures are shown by red triangles (Çakır et al. 2015).

(Yeldhose 2015) formulated a phase diagram using ThermoCalc software for the quaternary $\text{Ni}_{45}\text{Co}_5\text{Mn}_{40}\text{Sn}_{10}$ alloy, presented in Figure 36. While FCC_L12 and FCC_L12#2 correspond to the cubic austenite, the phase FCC_L10 relates to the non-

modulated $L1_0$ martensite. BCC_B2 is the $B2$ phase with nearest neighbour ordering, characteristic of ferromagnetic Heusler alloys. This phase transforms to austenite at around 750 °C which is in agreement with other works. However (Pérez-Sierra, A.M. et al. 2015) have ruled out $B2$ solidification for the composition being studied. NI3SN_LT corresponds to the low temperature γ -phase while HCP_A3 is the dendritically solidified hexagonal Ni_3Sn_2 structure mentioned in the vertical section of $Ni_{50}Mn_{50-x}Sn_x$ system ($0 \leq x \leq 50$ at %) developed by (Wachtel, Henninger & Predel 1983).

2015.10.27.13.57.02

Ni-Co-Mn-Sn

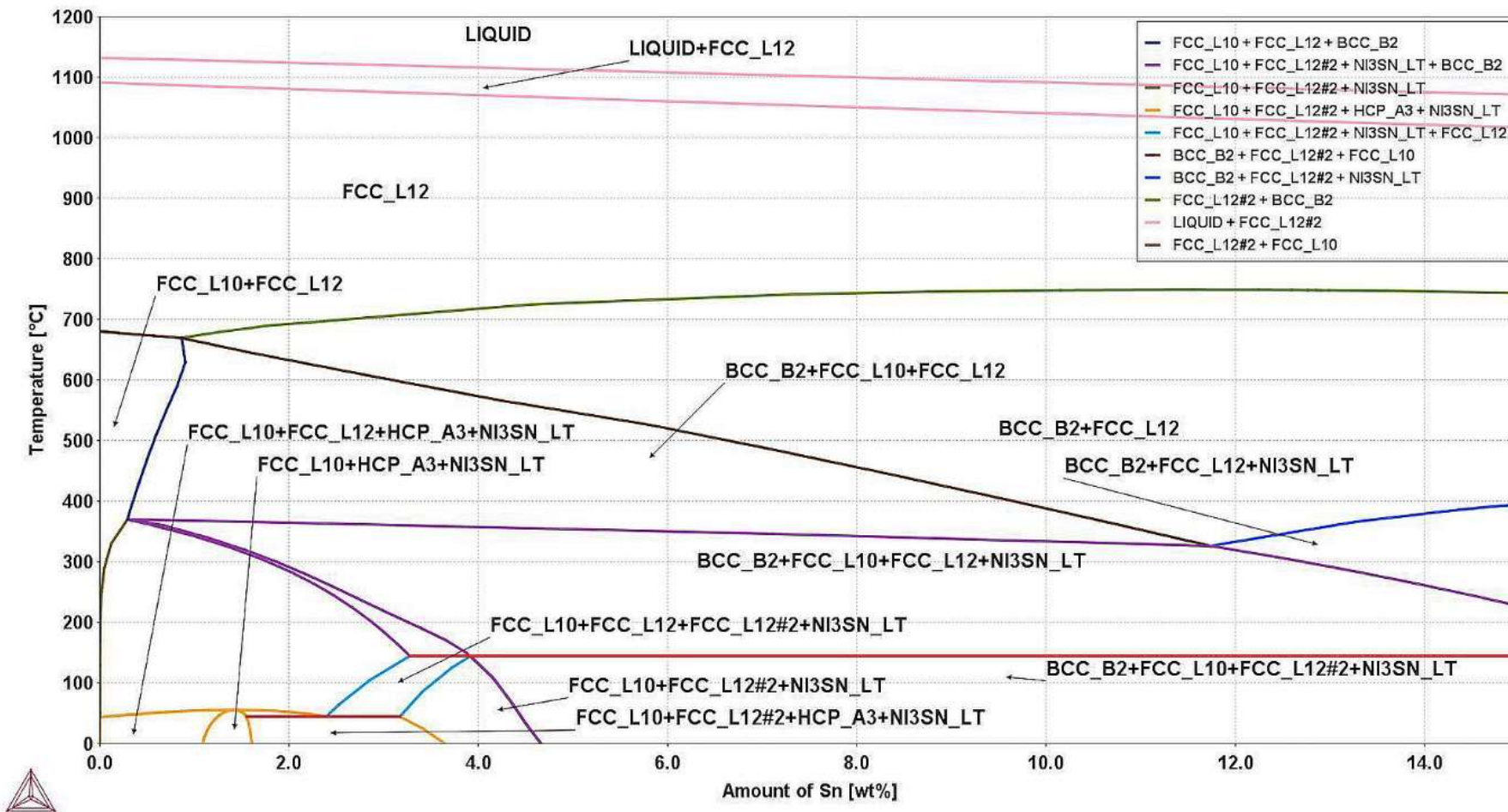


Figure 36. Phase diagram of Ni₄₅Co₅Mn₄₀Sn₁₀ alloy developed using ThermoCalc (Yeldhose 2015).

3.3 Solid Processing

3.3.1 Powder metallurgy – powder production, mixing and consolidation

Solid processing is by powder metallurgy (PM). PM is important for three reasons – economical processing, unique properties and captive processes (Upadhyaya 1996). The basic PM process involves (1) powder production (2) mixing or blending (3) pressing or consolidation and (4) sintering.

Powder production is an important stage of the PM process because the size, shape and texture of powders used in production and the properties of the finished part are dependent on powder production methods. Gas-atomized powders are more regular and spherical than water-atomized which are irregular and contain more oxide impurities. Particularly suited for shape memory materials is gas-atomization because water-atomization produces oxidized particle surfaces which hinder compaction mechanisms and further affect the martensitic transformation and associated properties (Perez-Saez et al. 2000). Blending of different size fractions of powders is needed to control part porosity, aid subsequent sintering (e.g. with use of fine fractions) and facilitate powder compaction (e.g. with use of coarse fractions) (Asthana, Kumar & Dahotre 2006). Blending of elemental powders is advantageous than prealloyed powders. Prealloyed powders are harder, have poor compaction characteristics and poor composition control unlike elemental powders which are best suited for obtaining new alloy compositions.

The mechanical alloying process applied on blended elemental or pre-alloyed powders ensures homogeneity of the starting powders. This process deforms, fractures and cold welds the particles through impact, abrasion, shear and compression. It refines the powder size through impacting the coarse powders entrapped between hardened balls via a process called microforging (Asthana, Kumar & Dahotre 2006). Excellent shape memory properties in

shape memory alloys can then be obtained if the problem of contamination of the powders by mechanical alloying is suitably addressed. Minimizing powder contamination during mechanical alloying may be carried out using methods listed by (Suryanarayana 2001). In the case of Ti-Ni alloys (Terayama & Kyogoku 2010) a short duration milling process turned out to be effective. High duration milling is counter-productive as it can damage microstructure, induce dislocations, nanotwin bands, strain and contamination (Valeanu et al. 2011).

Powder compaction is partial densification of powders through application of external pressure in order to create the part shape. This is carried out either as single-action compaction or double-action compaction depending upon the geometric complexity of the part being produced. The powders are uniaxially pressed in a die by a single punch or by two punches pressing in opposite directions for more uniform densification. Between the first and second pressing strokes, de-airing occurs to remove the entrapped air which otherwise leads to increased spring-back (release of elastic energy stored in the compressed powders during part ejection) and defects in the green parts. It is useful to preheat the die and powder ($\text{Ni}_{50}\text{Ti}_{50-x}\text{Zr}_x$) briefly to a certain temperature preferably in vacuum so that the green density increases before sintering leading to a high final density (Bertheville 2005).

The densification of powders during compaction occurs in three stages (Asthana, Kumar & Dahotre 2006). In stage I, densification is less because the applied pressure is small and only sliding/rearrangement of particles takes place. In stage II, greater densification occurs under much higher applied pressures through deformation and fracture of powder particles because of which porosity is reduced and density is increased. In stage III, higher applied pressures than during stage II do not significantly improve the compact density which is more or less constant. The final process of sintering is dealt elaborately in the following

section.

3.3.1.1 Sintering – pressure-assisted and pressureless

Sintering is a thermal treatment for bonding particles into a coherent, predominantly solid structure via mass transport events that often occur on the atomic scale. The bonding leads to improved strength and lower system energy (German 2014a). Sintering techniques fall into general categories – pressure-assisted and pressureless sintering. The pressure-assisted sintering techniques include hot isostatic pressing, hot pressing and spark sintering that produce high fractional densities by applying temperature and pressure (from 0.1 MPa up to 6 GPa) simultaneously. In the case of hot pressing lower pressures are sufficient for consolidation because resistance to plastic deformation of the powder particles decreases with increase in temperature. Processing parameters such as pressure, temperature, time and working atmosphere are important in hot pressing.

Hot isostatic pressing combines powder compaction and sintering. It is carried out in sheet metal moulds containing powder mixture suspended in a gas (argon) pressure vessel. The temperature and pressure are increased to pre-determined values. The densification is rapid under the combined influence of pressure and temperature. Spark sintering or spark plasma sintering uses electrical energy and mechanical pressure on conductive powder mixtures (occasionally non-conductive powder mixtures as well) to obtain a desired density in the finished component. High frequency AC and DC combined accelerate and augment particle to particle bonding at relatively low pressures resulting in a more uniform part density.

Pressureless sintering on the other hand comprises solid-state and partially liquid phase processes. Single phase sintering and mixed phase sintering such as those applied to form composites, homogenization of mixed powders and activated sintering through the inclusion

of insoluble elements preferentially segregating at the grain boundaries in order to provide a high diffusivity path and lower activation energy barrier are solid-state processes. Homogenization is dissolution of stray second-phase particles at elevated temperatures during heat treatment. Liquid processes involve persistent or transient liquid phases that improve the sintering rate, with the former existing throughout the high temperature portion of the sintering cycle and the latter eventually dissolving into the solid (German 2014a). (Monastyrsky, Odnosum, et al. 2002; Monastyrsky, Van Humbeeck, et al. 2002) reported both solid-state diffusion and transient liquid phase stages in high temperature NiTiZr shape memory alloys sintered conventionally in different gas atmospheres.

There are various stages in sintering beginning with the particle contacts, neck growth or enlargement of individual contacts, further neck growth giving rise to tubular pores and finally the closure of the tubular pores to form spherical pores. The neck formation during the early stages of sintering is as shown in Figure 37.

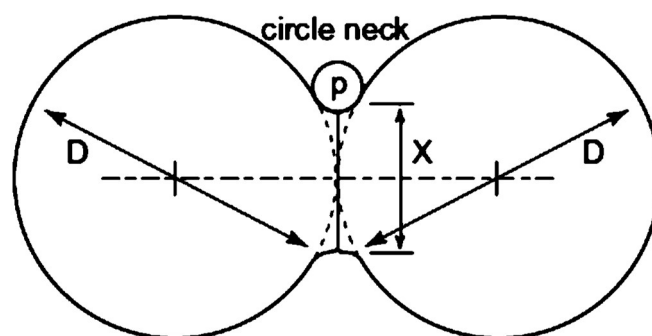


Figure 37. The circle approximation for the neck saddle surface (convex curvature is described by the diameter X while concave curvature is described by the diameter p) enables linkage between neck size and neck volume. A modified geometry with center-center attraction links neck size to sintering shrinkage (German 2014b).

The different sintering stages are clearly represented in Figure 38. The initial stage sintering corresponds to $X/D \leq 0.33$ and the intermediate stage corresponds to $0.33 \leq X/D \leq 0.50$.

Table 2 gives the approximate geometric changes associated with each stage.

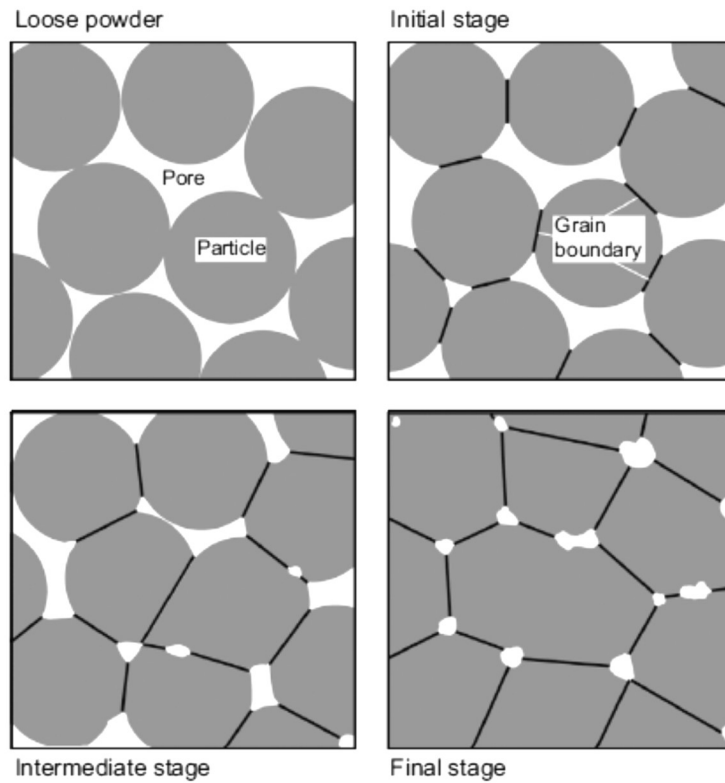


Figure 38. Graphical representation of the sintering stages, assuming the spherical particles start as a loose structure. Neck growth produces densification, round pores, and a strong body. Grain boundaries form at the particle contacts and grow as the necks merge (German 2014b).

Table 2 Geometric changes in the Three Stages of Sintering for Monosize Spheres (German 2014b)

	Initial Stage	Intermediate Stage	Final Stage
Neck size ratio, X/D	< 0.33	0.33 to 0.5	> 0.5
Coordination, N_C	< 7	8 to 12	12 to 14
Density, %	60 to 66	66 to 92	> 92
Shrinkage, $\Delta L/L_0$ %	< 3	3 to 13	> 13
Surface area, S/S_0 %	100 to 50	50 to 10	< 10
Grain size ratio, G/D	≈ 1	> 1	$\gg 1$
Pore size ratio, d/G	< 0.2	Near constant	shrinking

X = neck diameter, D = particle diameter, N_C = coordination number.

$\Delta L/L_0$ = sintering dimensional change over initial size, commonly termed shrinkage.

S = specific surface area, S_0 = initial specific surface area prior to sintering.

G = grain size, G_0 = starting grain size, d = pore diameter.

3.3.1.2 Mechanism of sintering, densification and transport mechanisms

Sintering takes place through diffusional movement of mass toward the neck region facilitated by the sintering force. In the absence of pressure, sintering takes place by surface curvature gradient. The stress associated with a curved surface is approximated on the two sphere initial sintering model, shown in Figure 39, as $\sigma = \gamma \left(\frac{2}{X} - \frac{4D}{X^2} \right)$ where X is the neck diameter and D is the particle diameter, γ denotes surface energy (J/m²) (Xu 2000). In the initial stage when the neck is small, the curvature gradient and hence the stress are quite large resulting in quick neck growth. As neck growth proceeds further the curvature gradient reduces resulting in the relaxation of the driving forces and the process slows down. The mass transport mechanisms during sintering are categorized as adhesion and densification mechanisms.

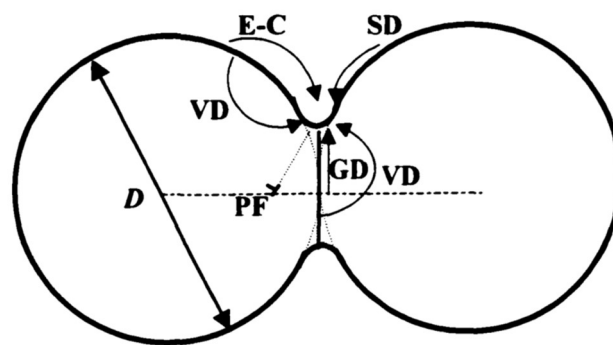


Figure 39. Mass transport paths illustrated in the two sphere sintering model. E-C, evaporation-condensation; SD, surface diffusion; VD, volume diffusion; GD, grain boundary diffusion; PF, plastic flow (Xu 2000).

Surface diffusion, evaporation-condensation and volume diffusion from surface are adhesion mechanisms. Grain boundary diffusion, volume diffusion from grain boundary, viscous flow and plastic flow are densification mechanisms which cause densification by transporting mass.

Surface diffusion – refers to movement of atoms between surface defects such as vacancies, kinks, ledges and adatoms at low temperature when less activation energy is sufficient for

diffusion to occur. It facilitates neck growth however does not cause densification or shrinkage

Evaporation-condensation – occurs due to the difference in vapour pressure between the convex sphere surface and concave neck region causing material from the convex particle surface to deposit at the concave necks between particles. Leads to neck growth, no densification

Volume diffusion – necessarily occurs due to difference in vacancies in the sintering microstructure. Involves movement of vacancies from the particle surface to the neck surface through the particle interior as the temperature is increased (volume diffusion adhesion, no densification). Atoms also move from grain boundaries to neck surface (volume diffusion densification, involves densification).

Grain boundary diffusion – is a densification mechanism. Involves mass flow along grain boundaries and deposition at the bond between particles. The activation energy is intermediate between surface and volume diffusion.

Plastic flow – dislocations move under stress associated with a curved surface. Happens during heating. Plastic flow declines as the dislocation density is decreased during sintering.

Viscous flow – suitable for amorphous materials and not significant for metal powders. Viscous flow can be responsible for densification of alloy powders because they show a semi-solid mixture during supersolidus liquid phase sintering and are densified by viscous flow.

The various mass transport mechanisms discussed above have been accommodated into theoretical models as in the equation given below which predicts variation of neck radius with sintering time. In the initial stage the neck growth is given by a general equation

$$\left(\frac{X}{R}\right)^n = \frac{Bt}{R^m}, \text{ where}$$

n, m depend on the mechanisms of mass transport

X, R neck and particle radii respectively

B constant dependent on material properties, particle geometry and atomic diffusion coefficient, D (Asthana, Kumar & Dahotre 2006).

The values of constants are deduced from various transport mechanisms operative during sintering. It can be seen from the above equation that temperature (due to parameter B related to diffusion coefficient) and particle size (smaller particle size increases sintering rate) influence the sintering rate more than the time of sintering. With finer particles, through enhanced surface and grain boundary diffusion, the neck growth is faster requiring less sintering time or lower sintering temperature.

In the intermediate stage grain growth through movement of grain boundaries occurs during which time the residual pores are either dragged along with the grain boundaries or separated from them to form isolated pores. The pores pin the grain boundaries with some binding energy. At high temperatures in the intermediate stage, the pinning force on the grain boundaries decreases and the driving force for grain boundary mobility increases consequently lowering the density. Thus for enhanced densification grain growth is to be retarded by means of suitable inclusions or using narrow particle size distribution of the starting powders (Asthana, Kumar & Dahotre 2006).

The final stage of sintering is marked by slowed densification, appearance of spherical isolated pores and pore coarsening or Ostwald ripening.

3.3.2 A review of solid processed Heusler alloys

PM could be applied on conventional/ferromagnetic shape memory materials primarily for the compositional control during processing, evolution of fine-grained microstructures and elimination of segregation seen in casting. (Murakami et al. 1981) synthesized (Ni₇₅-

$x\text{Mn}_x\text{Sn}_{25}$) alloys using elemental powders by sintering and reported correlation between phase change and ferromagnetism in them. The structure of these alloys varied from DO_{19} -type hexagonal in the range $x=0\sim 6.5$ at%, DO_3 -type cubic in the range $x=9\sim 15$ at% and $32\sim 47$ at%, and $L2_1$ -type cubic in the range of $x=15\sim 32$ at% at room temperature depending upon Mn content (Murakami et al. 1981). Several powder processing procedures such as pressureless sintering of alloy (Ito, K et al. 2010) and porous alloy (Ito, K et al. 2011) compacts as well as spark plasma sintering (Ito, K et al. 2009) and annealing (Ito, K et al. 2008) of alloy powders of ferromagnetic $\text{Ni}_{43}\text{Co}_7\text{Mn}_{39}\text{Sn}_{11}$ alloy were carried out. The starting material was gas-atomized alloy powder in all experiments. Pressureless sintering of alloy compacts sintered for 12 – 144 h demonstrated two stages in sintering – before and after a sintering time of 100 h, shown in Figure 40. The first stage was characterized by

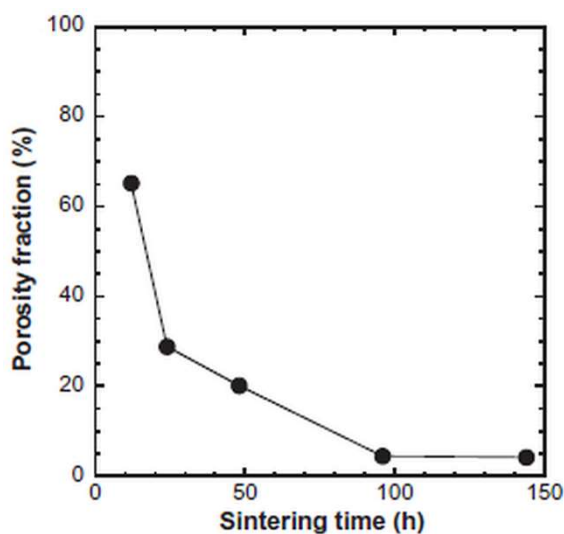


Figure 40. Sintering time dependence of porosity fraction (Ito, K et al. 2010)

formation and growth of necks together with a drastic reduction in porosity content with sintering time. The second stage showed porosity to be independent of sintering time with sluggish densification.

Very recently (Lee et al. 2018) adopted spark plasma sintering (SPS) among other

fabrication methods to fabricate $\text{Co}_{85.5}\text{Sn}_{4.5}\text{Hf}_{10}$ and $\text{Co}_{85.5}\text{Sn}_{4.5}\text{Zr}_{10}$ alloys in order to study the entropy changes caused by phase transformation. Neither elemental nor alloyed powders of Co, Sn, Hf and Zr were used during SPS synthesis. Instead bulk samples of amorphous and crystalline ribbons of the alloys fabricated by melt spinning of arc-melted and suction cast alloys were used. Various processing routes including powder metallurgy employed to process conventional Cu-Al-Ni shape memory alloys have been reviewed (Agrawal & Dube 2018). Mechanical alloying of elemental or pre-alloyed powders followed by sintering, hot isostatic pressing, hot pressing, mechanical working or a combination of these processes and their effects on the shape memory properties of the alloy are discussed in this paper. While nanocrystalline and ultra-fine grained powders could be obtained from mechanical alloying, subsequent sintering alone did not improve either the density or the shape memory properties. Hot pressing instead of sintering eliminated porosity and produced a near-net shape alloy. Additional extrusion resulted in chemical homogeneity with near full density. The use of gas atomized powders before hot pressing or hot isostatic pressing turned out to be expensive however was offset by the desired martensitic transformation temperatures, hysteresis and transformation width obtained. Hot rolling after sintering of Cu-Al-Ni alloy strips on the other hand produced a sub-grain structure permitting stress distribution along grain boundaries because of which substantial plastic deformation occurred before fracture resulting in improved shape memory properties (Agrawal & Dube 2018). Compacted powder preforms of this alloy were sintered at 873 K and hot rolled by reheating the preforms at 1273 K.

Both hot pressing and hot isostatic pressing were found feasible on NiAl shape memory alloys in which the martensitic transformation characteristics were identical to cast alloys in addition to exhibition of superelastic behaviour seen in stress-induced martensite (Kim, YD & Wayman 1990). Hot isostatic pressing of the classic NiTi shape memory alloy, particularly

from prealloyed NiTi powders (Schuller et al. 2003) as also gas-atomized powder of $\text{Cu}_{13.1}\text{Al}_{3.16}\text{Ni}$ (Perez-Saez et al. 2000), yielded not too deviant shape memory characteristics and pseudoelastic effects compared to cast alloys.

Shape memory alloys of TiNi and TiNiCu synthesized through pulse current pressure (spark plasma) sintering produced superior shape memory properties (Terayama & Kyogoku 2010). After nine cycles of shape-memory training two-way shape memory effect was observed. Shape memory training refers to loading in the martensite phase and then heating under no load after unloading completely, while two-way shape memory refers to the decrease in strain during heating and increase in strain during cooling. This two-way shape memory is related to dislocations and coherency strain by precipitation of Ti_3Ni_4 . It is due to the internal stress field formed by the accumulation of dislocations (Terayama & Kyogoku 2010). Spark plasma sintering was applied to prepare porous samples of $\text{Ti}_{50}\text{Ni}_{49.9}\text{Mo}_{0.1}$ and $\text{Ti}_{50}\text{Ni}_{49.7}\text{Mo}_{0.3}$ from gas atomized powders to study how powder size affected transformation temperatures and shape memory properties (Kim, Y-W, Lee & Nam 2013).

Pressure-assisted PM methods are used in order to reduce brittleness so that their suitability for practical applications is enhanced. The brittleness is attributed to four factors a) large elastic anisotropy, b) large grain size, c) large orientation dependence of the transformation strain, and d) grain boundary separation (Perez-Saez et al. 2000). (Ibarra et al. 2004) used mechanical alloying before HIP so that from the resulting compositional homogenisation, desired martensitic transformation temperatures are obtained in Cu-Al-Ni shape memory in addition to an improvement in ductility. (Popa et al. 2017) studied the formation of Ni_2MnSn alloy by solid state reaction from elemental powders, employing a process called mechanosynthesis. After 28 h of planetary ball milling a mixture of Ni_2MnSn – B_2 Heusler alloy (90% wt) and NiMnSn – C_{1b} half Heusler alloy (10% wt) was obtained

(Popa et al. 2017). (Perez-Saez et al. 2000) performed thermomechanical treatment after HIP process to achieve a fracture strain of 12.6% in Cu-Al-Ni alloys. Even ferromagnetic Heusler compositions showed improved ductility after such processes as seen in the case of vacuum hot pressed $\text{Ni}_{50}\text{Mn}_{37.5}\text{Sn}_{12.5-x}\text{In}_x$ ($x = 0, 2, 4, 6$) alloys (Maziarz, W. et al. 2017). At $x = 0$ this alloy with plasticity of about 5% and 2000 MPa strength, showed promise of machinability.

It is seen that even though PM processes offered tremendous advantages and scope for synthesis of conventional/ferromagnetic shape memory materials, their application is only fairly widespread in conventional and sparse in ferromagnetic shape memory alloys. The common cliché through the extant literature pertinent to this work and discussed above is lack of sufficient information on powder processing and characterization of both types of alloys. This offers tremendous scope to employ PM processes on ferromagnetic shape memory alloys and investigate reasons for their neglect.

3.3.3 Magnetostructural effects seen in solid processed alloys

Powder compacts synthesized by pressureless sintering of gas atomized powders of high frequency induction-melted $\text{Ni}_{43}\text{Co}_7\text{Mn}_{39}\text{Sn}_{11}$ alloy exhibited decreasing shape recovery ratio ($R_r = \frac{\varepsilon_r}{\varepsilon_p} \times 100$, where ε_r is the shape memory strain and ε_p the residual strain) for increasing sintering times (Ito, K et al. 2010). The sintering times varied from 12 to 144 h. Its porosity fraction decreased with the increase in the sintering time, from 65% at 12 h to 5% at 144 h. Even though the microstructures in Figure 41 (a), (b) and (c) exhibited single-phase structures, still the shape memory property of the 12 h sintered sample was superior because dense specimens with grains surrounded by neighbouring grains impose constraints during martensitic transformation. There will be restrictions on martensite reorientation in

response to an anisotropic strain build up during the cubic to tetragonal phase transformation. Furthermore, the surrounding grains act as an impediment to strain recovery in dense specimens where there is a plastic accommodation of incompatibilities at the grain boundaries.

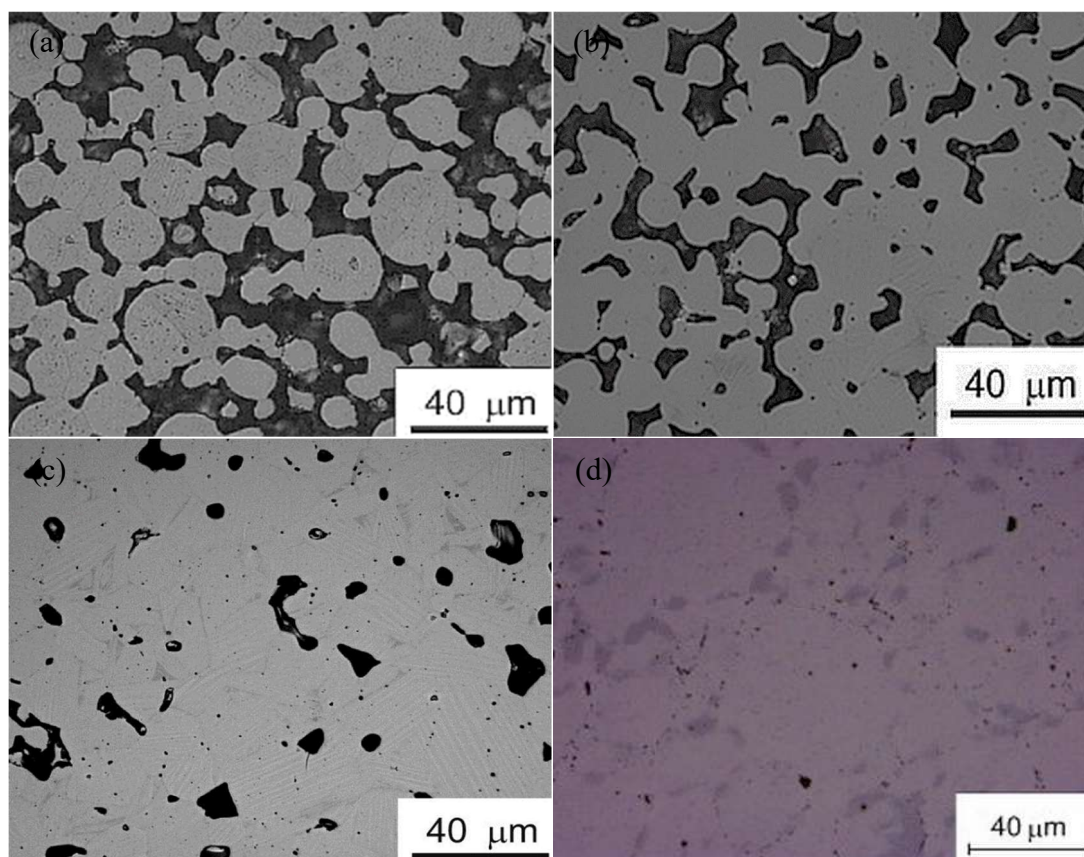


Figure 41. Porous sample sintered for: (a) 12 h; (b) 96 h; (c) 144 h (Ito, K et al. 2010); (d) sample synthesized by spark plasma sintering (Ito, K et al. 2009).

The same alloy powder after synthesis by SPS at 1173 K under 50 MPa for 15 min, exhibited enhanced ductility reportedly due to the reduction in grain size and introduction of ductile *fcc* precipitates because of which the grain boundaries are strengthened. An imperfect shape recovery corresponding to 48% of the residual strain resulted because the sintered microstructure contained the second phase (Ito, K et al. 2009). The microstructure of the SPS alloy is shown in Figure 41 (d). Concentrations of a precipitate phase rich in Co were observed. The compositional inhomogeneity due to the presence of a second phase and

contamination by the graphite die during the spark process resulted in an imperfect shape memory effect.

The magnetic field-induced strain in the case of a porous compact of $\text{Ni}_{43}\text{Co}_7\text{Mn}_{39}\text{Sn}_{11}$ alloy (Ito, K et al. 2011) was better than the SPS synthesized alloy (Ito, K et al. 2009) of the same composition. At 320 K with the application of magnetic field up to 8 T, the recovered strain was 0.84% corresponding to a shape recovery ratio of 43%. In the SPS alloy the shape recovery ratio corresponded to 18% which was 2.5 times less than the porous compact. The SPS sample exhibited gradual transformation and hence a large transformation interval. This is attributed to the compositional inhomogeneity by carbon contamination and by internal stresses from surrounding grains. Magnetization measurements indicated negative shifts in the recorded transformation temperatures at two different magnetic fields of 0.05 T and 7 T, suggesting the stabilization of the austenitic phase by the magnetic field. A kinetic arrest phenomenon is believed to be the reason for the difference in magnetization between heating and cooling curves at 150 K.

The high shape recovery ratio in the powder compacts with high porosity fraction provided a basis for selectively introducing porosity in the samples in order that their properties are improved. Solid state replication was attempted on $\text{Ni}_{43}\text{Co}_7\text{Mn}_{39}\text{Sn}_{11}$ powders in which the powders were blended with ammonium bicarbonate space holders with a particle size distribution between 350 and 500 μm . Magnetization measurements are shown to be identical to an ideally heat-treated baseline specimen (Monroe et al. 2012). (López-García et al. 2018) performed annealing at different temperatures of 573 K, 773 K and 873 K on a mechanically milled $\text{Ni}_{50}\text{Mn}_{35}\text{Sn}_{15}$ alloy and found that relaxation due to annealing brought about recovery of martensitic transformation and enhancement of magnetism. The density of non-magnetic inclusions (defects) and their stress field decreased leading to an increased saturation magnetization and lower martensitic transformation temperature. An important

finding is that with the transformation temperature fixed by the composition, thermomechanical treatments are the best way to improve the functional properties (López-García et al. 2018).

The advantages of PM methods in terms of composition control, easier mixing of elemental powders than alloyed powders which have poor compaction characteristics and are also harder and the cost-effectiveness of the process are strong reasons to explore the PM route of synthesis of ferromagnetic Heusler alloys. In doing so the observations that PM processing resulted in incomplete martensitic transformation (Ito, K et al. 2008) or evolved secondary phases (Ito, K et al. 2009) which are detrimental to the magnetostructural transformation and properties are to be given careful consideration.

3.3.4 Characterization of solid processed alloys

The characterization of PM fabricated Heusler alloys is based on the same techniques employed for liquid processed alloys as briefly discussed in the following with DSC, XRD and microscopical analysis as the main tools. (Maziarz, W. et al. 2017) characterized the microstructure of the $\text{Ni}_{50}\text{Mn}_{37.5}\text{Sn}_{12.5-x}\text{In}_x$ ($x = 0, 2, 4, 6$ at%) synthesized by vacuum hot pressing. Room temperature X-ray diffraction patterns of $\text{Ni}_{50}\text{Mn}_{37.5}\text{Sn}_{12.5-x}\text{In}_x$ ($x = 0, 2, 4, 6, 8$) alloy powders in Figure 42 indicate that at $x = 0$ and $x = 2$ the structure is coexistent $L2_1$ and $4O$ which however changes to a single phase at higher concentrations. It is $4O$ at $x = 4$ and $10M$ at $x = 6$.

Based on the X-ray diffraction patterns in Figure 5 and with the help of scanning transmission electron micrograph high angle angular dark field (STEM-HAADF) image in Figure 43 (a) which has an atomic number contrast it was pointed out that the microstructure consisted of equiaxed grains of austenite and martensite of size $\sim 2 \mu\text{m}$. This grain size

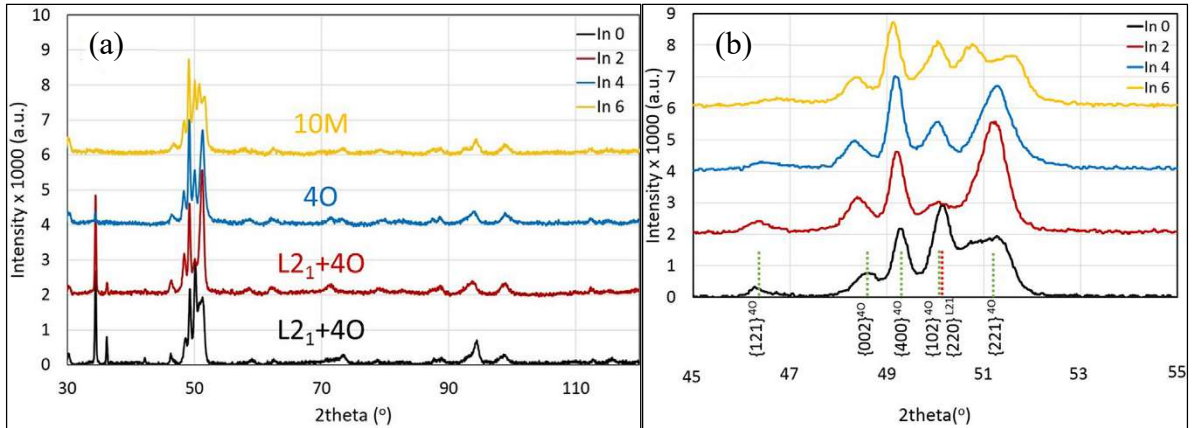


Figure 42. X-Ray diffraction patterns of sintered alloys in 2theta range a) 30 – 115°; (b) 45 – 55°.(Maziarz, W. et al. 2017).

refinement was the reason for the 5% plasticity and 2000 MPa strength observed in this alloy. Dislocations within the austenite grain, whose existence is related to factors such as order of $L2_1$ phase, location at antiphase boundaries, stress induced dislocations during sintering or incompatibility between austenite and martensite crystal structures are shown in in Figure 43 (b). The structure of 4O modulated martensite is shown in Figure 43 (c).

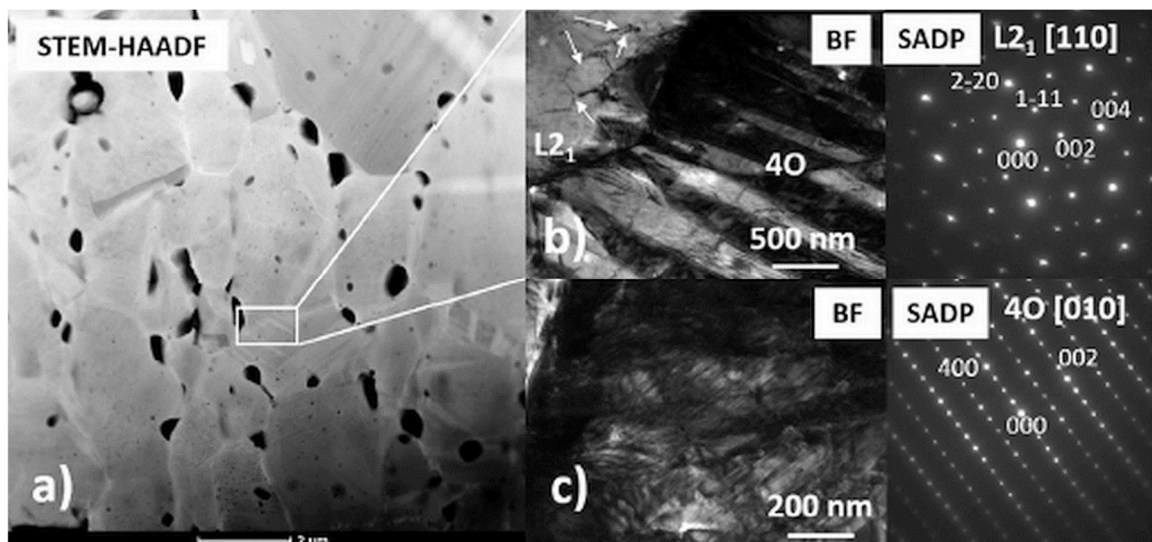


Figure 43. Set of TEM microstructures consist of (a) STEM-HAADF image; (b) and (c) bright field images and corresponding selected area diffraction patterns of In0 sintered sample (Maziarz, W. et al. 2017).

The thermomagnetization curves measured at field heating (FH) and field cooling (FC) protocols together with superimposed DSC curves in the same temperature range of $\text{Ni}_{50}\text{Mn}_{37.5}\text{Sn}_{12.5-x}\text{In}_x$ alloy powder compare the temperatures of magnetostructural transformations directly shown in Figure 44. The difference in magnetization between the alloys $\text{Ni}_{50}\text{Mn}_{37.5}\text{Sn}_{12.5-x}\text{In}_x$ and $\text{Ni}_{50}\text{Mn}_{37.5}\text{Sn}_{12.5-x}\text{In}_x$ is explained by the difference in the relative proximity and essentially overlap between the MT temperature and T_C^A (Maziarz, W. et al. 2017).

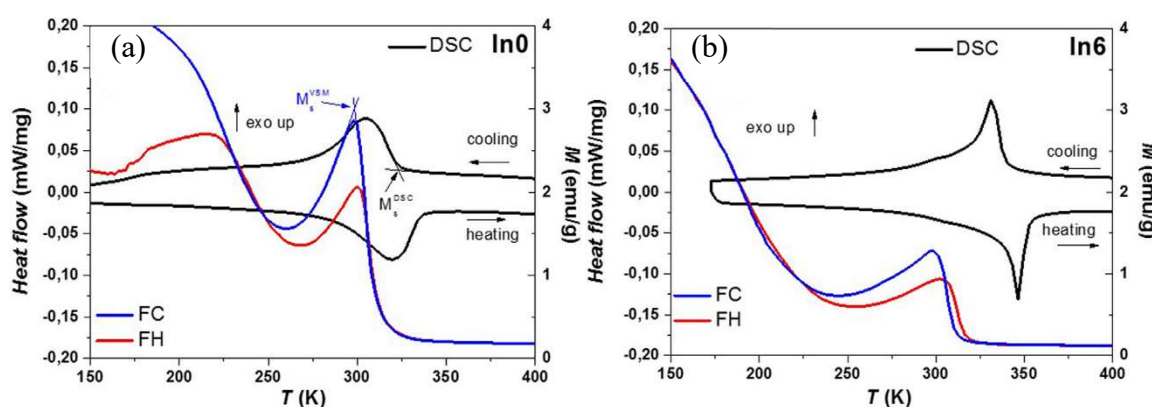


Figure 44. Thermo-magnetization curves measured at low magnetic field (100 Oe) during field cooling (FC) and field heating (FH) with superimposed DSC curves in the same temperature range for a) In0 and b) In5 sintered samples (Maziarz, W. et al. 2017).

3.4 Summary

A clear and cohesive review of NiMn-based ferromagnetic Heusler alloys from fundamental concepts to their technological significance through synthesis and characterization is presented. In the absence of adequate literature on synthesis and characterization of PM alloys, available literature on liquid processed alloys is to be examined. Comparisons can be made between the liquid processed and PM alloys in aspects governing the synthesis and characterization to draw conclusions about the microstructure and effect of microstructure on the magnetostructural properties. However there can be limits as liquid and solid

processing procedures are different. Liquid processing ensures compositional homogeneity necessary for phase transformation and associated magnetostructural properties. Sintering on the other hand is a thermal treatment that bonds particles through diffusion. The more effective the diffusion the more effective is the sintering and hence compositional homogeneity. This can be seen in the different microstructures obtained after each process. PM microstructures may possess porosity, intermediate phases or even small amounts of unsintered compositions. In spite of this PM microstructures can exhibit a diffusionless martensitic transformation at the transformation temperature and well-defined martensitic lath structures at room temperature similar to a cast alloy. The differences in the magnetic behaviour of liquid processed and PM alloys could then be related to the structure of the formed martensite. If the structures are the same other microstructural aspects may possibly influence the magnetic behaviour.

This research on employing conventional pressure-less sintering to fabricate ferromagnetic Heusler alloys and characterize them was driven by the amazing reversible phase transformation in the singular $\text{Ni}_{45}\text{Co}_5\text{Mn}_{40}\text{Sn}_{10}$ alloy enabling it to be used for the conversion of low grade heat into electricity. As a high potential energy material, this and other ferromagnetic Heusler alloys of multifunctional significance need be synthesized through cost-effective alternatives to casting. The fact that solid processing has been sparsely applied in the synthesis of ferromagnetic Heusler materials provided the impetus. Synthesis of just a handful of alloys using alloyed not elemental powders, opened up vistas to employ elemental powders which are more advantageous.

The scope for employing powder metallurgy is vast in terms of characterization using different solid processes, process parameters governing the synthesis, transport properties of the alloys, magnetostructural transformations and microstructural characteristics. The

objectives as stated in section 1.3 are narrowed down to study the feasibility of conventional press and sinter method on elemental powders and the effects of process parameters on the transformations and microstructural characteristics of the sintered alloys.

4 Materials and Experimental Procedure

The various experimental methods with which the multiferroic NiMn-based quaternary Heusler alloys were synthesized and characterized are detailed in this chapter. Powder characterization which includes particle size and size distribution was first carried out. Fabrication of samples using conventional press and sinter, hot pressing and spark plasma sintering is detailed in the following sections. All the different characterization procedures employed on the samples are elaborated in sections that follow. While a part of the experimental procedure has been published (Chapter 5) and included in Chapter 6, it has been endeavoured to avoid duplication of text and data in this chapter except where necessary.

4.1 Powder characterization – particle size and distribution

Commercial purity elemental powders of nickel, manganese, cobalt, tin and a mixture of tin and copper (2.5 wt %) were used. The as-received elemental powders were first characterized for particle size, distribution and morphology.

The particle size and distribution were measured on a Mastersizer 2000 from Malvern Instruments (now Malvern PANalytical), UK, working on the principle of Mie scattering which refers to the elastic scattering of light by particles with diameter comparable to the wavelength of incident light. Mie theory allows completely accurate results over a large size range on the assumption that the particles are spherical. However the refractive indices for the material and medium must be known and the absorption part of the refractive index must be known or estimated. The Mastersizer 2000, picture shown in Figure 45, uses laser scattering by particles suspended in a fluid medium with a size range of 0.02 to 2000 μm .

For the powders used in this work the dispersant is distilled water with a refractive index of 1.33. A small quantity of individual powders (1 – 2 g) was dispersed in the medium and the measurements were saved on a computer. Reports of particle size measurement were later generated using the proprietary software of the manufacturer of the equipment.



Figure 45. Mastersizer 2000 used in particle size analysis

$D(v, 0.1)$, $D(v, 0.5)$, $D(v, 0.9)$, $D[3,2]$ and $D[4,3]$ values of the powder sizes are tabulated in Table 3. $D(v, 0.1)$ is the size of the particle below which 10% of the sample lies and $D(v, 0.9)$ refers to the size below which 90% of the sample lies. $D(v, 0.5)$ is the size at which 50% of the sample is smaller and 50% is larger. This value is also known as the Mass Median Diameter (MMD) or the median of volume distribution. $D[4,3]$ is the Volume Weighted Mean of mass moment mean diameter. $D[3,2]$ is the Surface Weighted Mean, also known as the Surface Area Moment Mean Diameter or Sauter mean.

Figure 46, reproduced from (Ahamed et al. 2018) in Chapter 5, shows the particle size distribution of the constituent powders including the Sn-Cu mixture. Additionally the distribution of Sn powder alone is also shown. The particle sizes range from 8 μm for Co to 32 μm for the Sn-Cu mixture. All particle sizes are less than 20 μm except for Sn-Cu powder.

The inset of Figure 46 shows the morphology of tin powder (without Cu) used in this work.

Table 3 Particle sizes of different powders

Powder	Ni/ μm	Mn/ μm	Sn/ μm	Sn-Cu/ μm	Co/nm
Volumetric mean/D[4,3]	13.83	20.58	23.43	37.24	52.53
Surface mean/D[3,2]	8.94	10.07	14.92	21.13	6.01
D (v, 0.1)	5.06	4.38	8.94	10.28	3.40
D (v, 0.5)	11.52	16.91	19.14	31.8	8.05
D (v, 0.9)	25.3	41.77	36.2	71.59	18.79

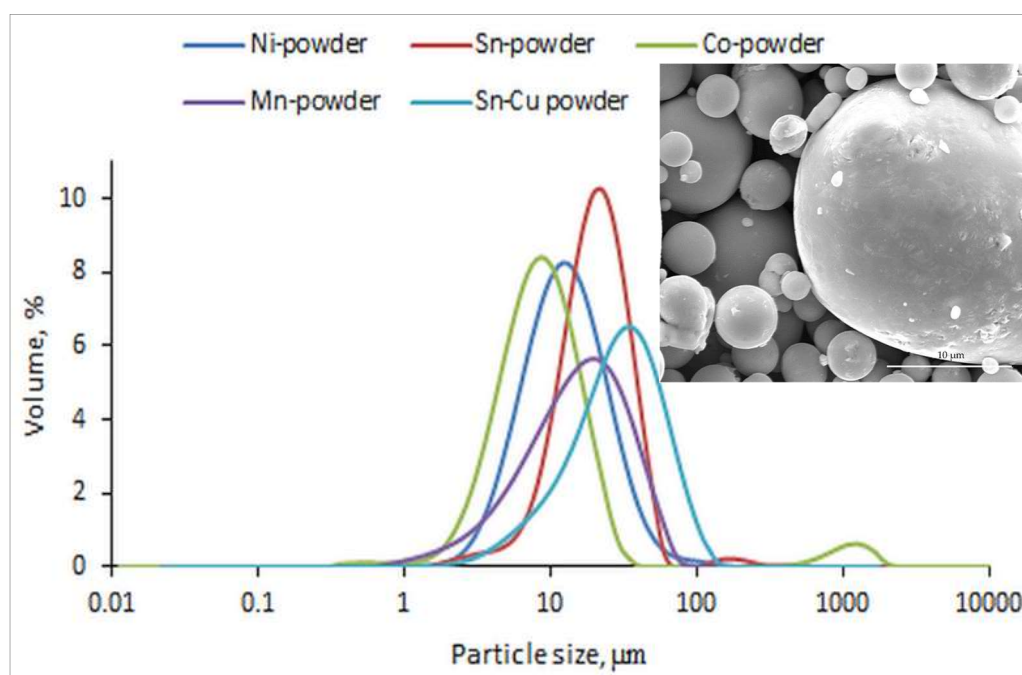


Figure 46. Particle size distribution of constituent powders (reproduced from (Ahamed et al. 2018)) and (inset) SEM micrograph of Sn powder.

A similar procedure was adopted to determine the size and size distribution of Ni, Ti and Zr powders used in the powder processing of high temperature Ni-Ti-Zr alloys (Monastyrsky, Odnosum, et al. 2002). The analysis was carried out on a Coulter laser scattering particles sizes analyser. Another method of determining powder particle sizes is

through use of software on BSE images of powders that go into the alloy, as done on pre-alloyed, melt-spun and milled $\text{Ni}_{50}\text{Mn}_{37.5}\text{Sn}_{12.5-x}\text{In}_x$ ($x = 0, 2, 4, 6$) powders, using Gata DigitalMicrograph software (Maziarz, Wojciech et al. 2016; Maziarz, W. et al. 2017).

4.2 Fabrication processing

4.2.1 Powder mixing and compaction

The powders were then used to prepare the samples. Two compositions were prepared - $\text{Ni}_{45}\text{Co}_5\text{Mn}_{40}\text{Sn}_{10}$ (at%) and $\text{Ni}_{45}\text{Co}_5\text{Mn}_{40}(\text{Sn,Cu})_{10}$ (at%) by carefully weighing to atomic composition. To the powders was added 0.5 to 1% A-wax (Acrawax; N, N' Ethylene Bisstearamide) for lubrication. The composition of powders were then sealed in a clean, degreased and sealed cylindrical stainless steel mixing tube with 5 mm diameter steel balls and rotated at 120 rpm for 1 -2 hrs. An approximate ball to powder ratio of 4:1 was used. Compaction for densification of powders through uniaxial pressing in a die by a double acting punch was carried out in a manner similar to (Jabur, Al-Haidary & Al-Hasani 2013; Valeanu et al. 2011) who used uniaxial cold compaction in tool steel dies to prepare green compacts of Ni-Ti and $\text{Ti}_{50}\text{Ni}_{30}\text{Cu}_{20}$ shape memory alloys at compaction pressures ranging from 300 to 800 MPa. The mixed powders were filled in a tool steel die 11 mm in diameter and closed with a punch. The powder was then compacted by pressing in a Mohr & Federhaff universal testing machine with a maximum capacity of 200 kN. The compacting loads were 70 KN (184 MPa) and 80 KN (210 MPa). The compacting pressure was applied for 30 to 45 s for all samples before it was released. After ejection from the mould the compacts measured 11 mm in diameter and up to 10 mm in length. Figure 47 (a) shows the picture of the die and punch. Figure 47 (b) shows a pair of green and sintered compacts.

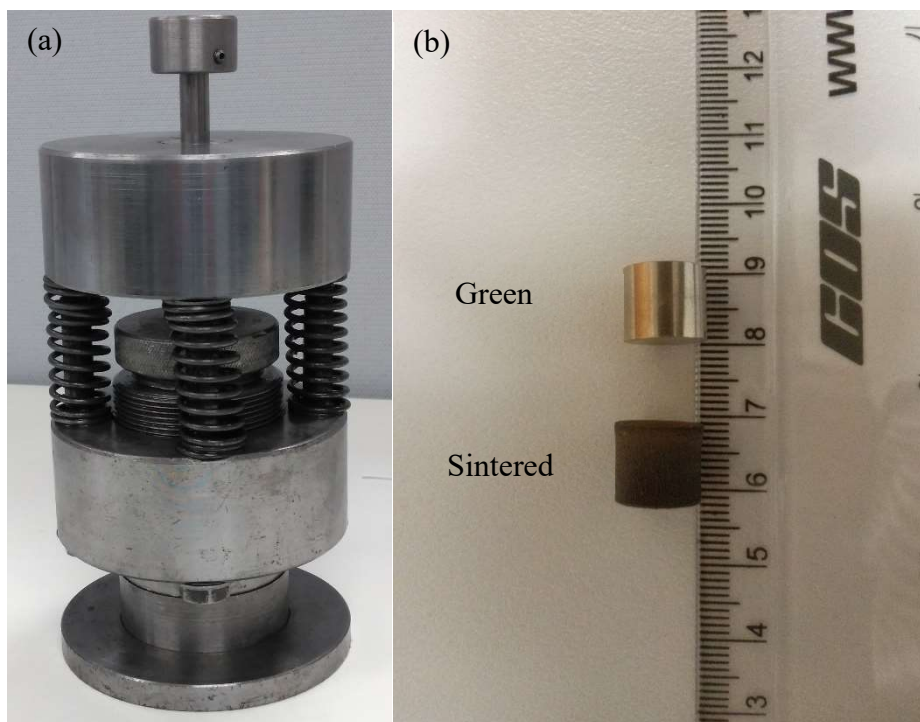


Figure 47. (a) Die and punch; (b) a pair of green and sintered compacts

4.2.2 Pressureless sintering in Ar atmosphere

The sintering procedure briefly explained in Chapter 5 is elaborated in this section. The compacts were then sintered in a Henan Andy high temperature tube furnace (AY-TF-80-175). The maximum working temperature of the furnace is 1650 °C with a maximum heating/cooling rate of 3 °C/min above 1200 °C and 5 °C/min below 1200 °C. The size of the high purity cylindrical alumina tube is 70 mm ID and 1000 mm length. The tube chamber is heated by 1800 grade MoSi₂ heating elements. The central heating zone of 150 mm is calibrated to be at the maximum temperature where the set (programmed) temperature and temperature from thermocouple synchronize. The alloy samples are placed in alumina boat-crucibles and pushed into the central heating zone from one end of the tube. The alumina tube is sealed tightly, with a narrow tubing providing a vent for the argon gas and fumes generated during the heating to escape into the atmosphere. Pure industrial argon (061 G2) is passed through the other end of the tube in order to prevent oxidation. The furnace also has a vacuum rotary pump to create vacuum (max. 10⁻² torr.) in the tube before introducing

argon. The samples were sealed-off in silica tubes at argon-partial pressure and heated at 950 °C and 1050 °C for 24 h, 72 h and 144 h. Table 4 shows the processing conditions of the different alloys. X-ray analysis on sintered powders of Ti, Ni and Zr in argon and nitrogen atmospheres revealed that, based on the reflections in the X-ray spectrum, argon was best suited for sintering because a number of phases, intermetallic compounds and nitrides formed during sintering in nitrogen atmosphere (Monastyrsky, Odnosum, et al. 2002).

Table 4. Processing conditions used for the preparation of the alloy samples

Sample ID	Sample Composition	Compaction pressure/MPa	Holding time/h	Temperature/°C	
1050a2C	Ni ₄₅ Co ₅ Mn ₄₀ (Sn,Cu)	184	24	1050	
950a2Cu		184	24	950	
S950a1	Ni ₄₅ Co ₅ Mn ₄₀ Sn ₁₀	184	12	950	
S950a2		184	24	950	
S1050a1		184	12	1050	
S1050a2		184	24	1050	
S950b1		210	12	950	
S950b2		210	24	950	
S1050b1		210	12	1050	
S1050b2		210	24	1050	
S950a3		Ni ₄₅ Co ₅ Mn ₄₀ Sn ₁₀	184	72	950
S950a4			184	144	950
S1050a3	184		72	1050	
S1050a4	184		144	1050	
S950b3	210		72	950	
S950b4	210		144	950	
S1050b3	210		72	1050	
S1050b4	210		144	1050	

4.3 Density measurements

The densities of the green and sintered compacts were determined in accordance with Archimedes principle using a custom-built density measuring apparatus. The measured densities can be used for the determination of porosity%. (Jabur, Al-Haidary & Al-Hasani

2013) determined the densities and porosity% Ni-Ti shape memory alloys prepared by powder metallurgy using the expression $Porosity\% = \left[1 - \left(\frac{\rho_T}{\rho_0}\right)\right] \times 100$

where ρ_T is the actual density of the sample calculated by dividing the weight (measured with a balance) by volume; ρ_0 is the theoretical density calculated as

$$\rho_0 = [\rho_0^{Ni} \times (at\% Ni)] + [\rho_0^{Ti} \times (at\% Ti)] + [\rho_0^{additive} \times (at\% additive)]$$

where ρ_0^{Ni} , ρ_0^{Ti} and $\rho_0^{additive}$ are the theoretical densities of the Ni, Ti and additives such as Cr and Al used in their work.

In this work the theoretical densities of $Ni_{45}Co_5Mn_{40}Sn_{10}$ and $Ni_{45}Co_5Mn_{40}(Sn,Cu)_{10}$ compositions were determined as given above. The %theoretical density values instead of %porosity were used for analysis.

4.4 Metallography

Thin sections of the samples were cut using Struers slow speed diamond saw for the different characterization analyses to be carried out. The cut sections of the samples were hot mounted on 25 mm mounts using Struers Citopress-5 hot mounting equipment. The equipment has two attachments for preparing 25 mm and 30 mm diameter mounts. ‘Multifast’ resin was used. The heating temperature was 180 °C and applied pressure 30 MPa. The heating and cooling cycles were programmed for 3 and 2 min respectively. Subsequently the mounts were metallographically polished on a Struers Tegramin-25 automatic polisher (Chapter 5) with a variable disc speed of 40 – 600 rpm and variable specimen mover head speed of 50 – 150 rpm (clockwise and counter-clockwise). The specimen holder on the specimen mover head can accommodate six specimens. A new method specific to polishing of multiferroic material samples was created in the single specimen methods module. This method specified the different mounting resins, suspensions, lubricants, direction of rotation of both the disc and mover, the force at which the specimens are held, the rate of dosing of the suspension and

the time of polishing. Grinding and polishing was carried out sequentially, as shown in Table 3, on various resin mounts with appropriate dosing suspensions to obtain a good surface finish on the samples.

Table 5. Table shows the metallographic preparation for microstructural analysis

Step	Plane Grinding	Diamond Polishing			Oxide Polishing
Surface	MD-Piano™ 200/500/1200	MD- Allegro™	MD-Dur™	MD-Nap™	MD- Chem™
Suspension		DiaP. All/Lar. 9	DiaP. Dur3	DiaP. Nap-B1	OP-U
Rpm		150	150	150	150
Force (N)		25	20	20	20
Time (min)		7	4	4	4

For microstructural examination using optical and electron microscopy the polished samples are suitably etched. Metallographic etchants reveal microstructural details which cannot be observed on the as-polished sample. The details include grain size, segregation, shape, size and distribution of the phases and inclusions. Different etchants are used on ferromagnetic Heusler alloys – Oberhoffer solution (1 g CuCl₂, 30 g FeCl₃, 0.5 g SnCl₂, 42 ml HCl, 500 ml H₂O and 500 ml C₂H₅OH) (Krenke, Acet, et al. 2005), Kalling’s reagent (50% HCl, 50% CH₃OH, 2-5 g CuCl₂), Nital or other etchants which may include 99 ml C₂H₅OH + 2 ml HNO₃ + 5 g FeCl₃ (Yang, S, Wang & Liu 2012). For the present work Kalling’s reagent (Ahamed et al. 2018) and Nital were used through swabbing on the surface for 1 – 2 min.

4.5 Hardness measurements

Microhardness measurements were carried out on a LECO Microhardness Tester LM

700 AT with Vickers indenter. All measurements were recorded for an applied load of 500 g and 15 s dwell time. A majority of the ferromagnetic shape memory alloys have been characterized only for their magnetostructural transformations and properties. Mechanical properties such as hardness of the alloys are usually not determined or discussed. However in the case of $\text{Ni}_{50}\text{Mn}_{37.5}\text{Sn}_{12.5-x}\text{In}_x$ ($x = 0, 2, 4, 6$) alloys the microhardness of the ribbons which were pulverized and milled to obtain powders were determined at an applied load of 0.49 N. This was done in order to understand the effect of composition on the hardness which was evident from its decrease as the In content increased (Maziarz, W. et al. 2017).

4.6 Differential scanning calorimetry

Differential scanning calorimetry experiments were first performed on very small quantities of all sintered samples. The experiments were carried out on a Mettler-Toledo TGA/DSC 2 equipment. This equipment has a maximum temperature of 1600 °C, balance capacity of up to 1 g including the weight of sample and two crucibles and a balance resolution of 1 µg. Three types of gases – purge, protective and reactive gases are used. Purge gases are either air, oxygen, carbon dioxide, or an inert gas such as nitrogen used in the furnace. Protective gas is nitrogen flowing continuously at the rate of at least 20 ml/min up to 54 ml/min used for the balance. Reactive gases are used when required. Heating and cooling methods specifying the minimum and maximum temperatures and the heating/cooling rates are first created using the ‘Routine Editor’ of the ‘STARe’ software associated with the equipment. For experiments in this work the heating method was specified with a minimum temperature of 25 °C, a maximum temperature of 650 °C and a heating rate of 5 °C/min. The cooling method was specified with starting temperature of 650 °C, ending temperature of 25 °C and a cooling rate of 5 °C/min. After the sample is placed inside the furnace, it is closed and the experiment is started. The results are evaluated on the ‘Evaluation Window’ of the STARe

software. The enthalpy changes (ΔH) around the phase transformation are calculated from DSC data using the software.

4.7 Microstructural analysis

4.7.1 X-ray diffraction

To understand the microstructure better, X-ray diffraction studies were carried out on Rigaku MiniFlex 600 diffractometer. This diffractometer is a benchtop machine capable of crystalline phase identification and quantification, determination of % crystallinity, crystallite size and strain, lattice parameter refinement, Rietveld refinement and molecular structure. The advanced PDXL powder diffraction software associated with the equipment uses a fundamental parameter method (FP) for accurate peak calculation. Phase identification of the different phases present in the microstructure is done using Crystallography Open Database (COD) and JCPDS of International Center for Diffraction Data (ICDD). The patterns were obtained using Cu-K α radiation with a wavelength of 1.5406 Å. For the quinary samples diffraction studies were carried out as detailed in Chapter 5. This diffractometer at School of Mechanical Engineering, University of New South Wales, is a multipurpose diffractometer suitable for all sample types such as powders, thin films, nanomaterials, etc. and uses an advanced search-match HighScore software.

In order to offset the difficulty in the exact search-match of phases in the ferromagnetic Heusler alloy discussed in this work, the peaks were indexed in accordance with the space groups to which the phases belonged. Different cubic, orthorhombic/monoclinic, tetragonal structures etc. corresponding to the austenite, martensite and other phases were identified.

4.7.2 Optical microscopy

Microstructural examination was carried out using optical and electron microscopy. The optical microscope used was a Zeiss Axio Imager.M2m from Carl Zeiss Microscopy GmbH with a range of different contrasting techniques. The samples can be examined in brightfield, darkfield, differential interference contrast (DIC), circular differential interference contrast (C-DIC), polarization or fluorescence using reflected light.

The microscope is equipped with AxioVision 4.9.1 software with specialized modules for image acquisition, processing and analysis. Various phases present in the microstructure are determined using the Multiphase module. The software necessitates the creation of a materials analysis archive for storing and managing data including test specifications necessary for phase analysis. Phases are determined based on both the size of the individual particles of a phase as well as the percentage of area they represent. Optical microscopy was used to differentiate the microstructures between the as-atomized and annealed powders (Ito, K et al. 2008) as well as conventionally sintered, porous and SPS sintered alloy of composition $\text{Ni}_{43}\text{Co}_7\text{Mn}_{39}\text{Sn}_{11}$ (Ito, K et al. 2010; Ito, K et al. 2011; Ito, K et al. 2009). Besides identifying the phases in the microstructures, it also allows the determination of phases and porosity contents using the associated image analysis software of the equipment.

4.7.3 Scanning electron microscopy

The microstructure examination in this work was carried out using scanning electron microscopy. Both secondary electron (SE) and backscattered electron (BSE) images were obtained from FESEM (Quanta 450 FEG, USA) microscope. A beam probe size of 5 nm at an accelerating potential (voltage) of 20 kV was used. The compositions of the alloy were determined through spectrometry (EDS), using TEAM software associated with the system. All three formats of the X-ray signal used in composition analysis such as spectrum, line scan

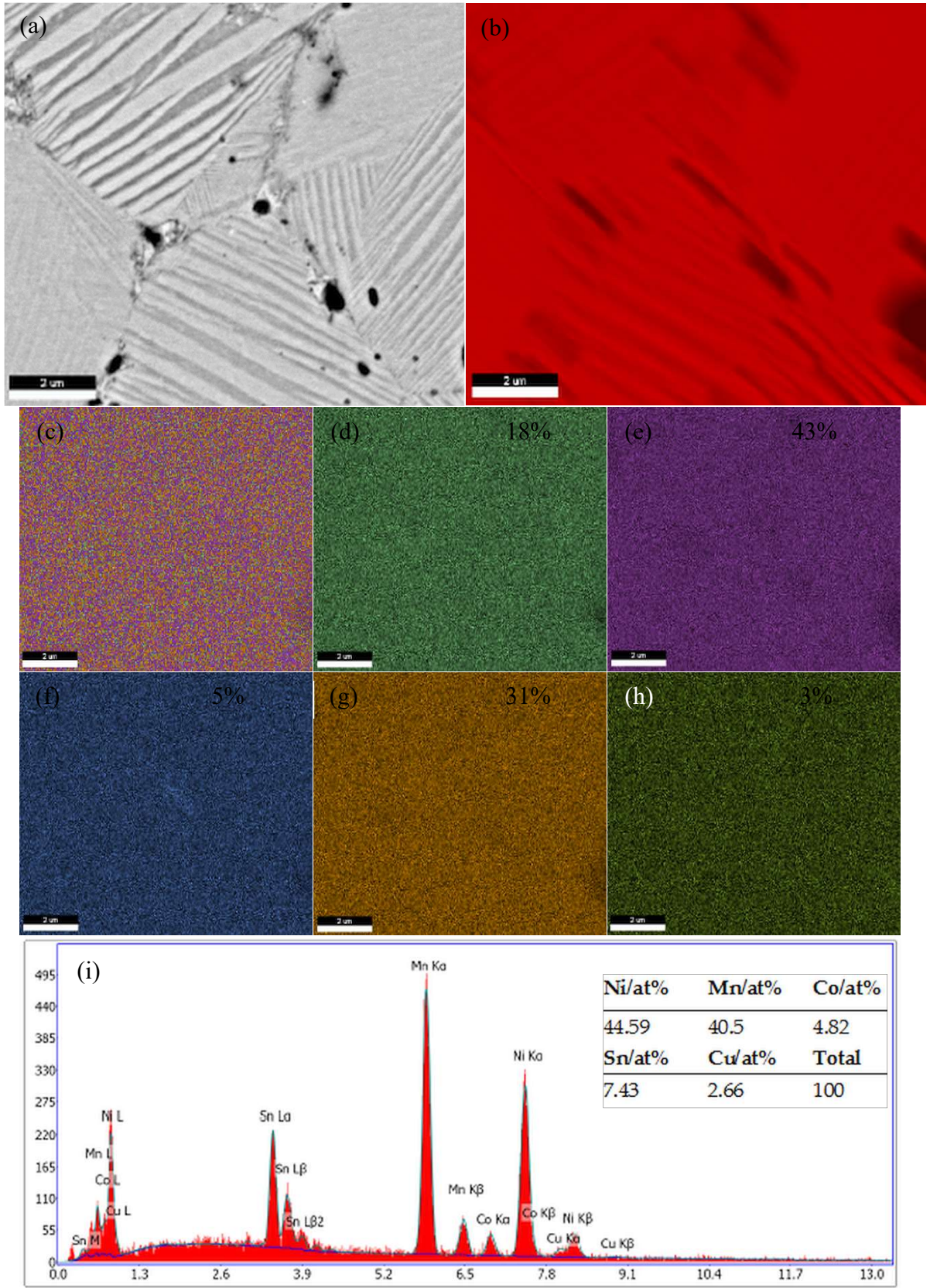


Figure 48. (a) BSE image of sample 1 (refer Table 2); (b) Compositional map of phase MnK/NiK/SnL/CoK; (c) Element overlay; (d) to (h) Elemental distribution of Sn, Mn, Co, Ni and Cu respectively; (i) and (inset) Composition of phase shown in red in (b).

and chemical concentration map (X-ray map) have been used. An example of the composition map for a region of sample 1 (refer Table 4) is shown in Figure 48. BSE image of the microstructure mapped is shown in Figure 48 (a) and the live map of composition is seen in Figure 48 (b). Figure 48 (c) shows the elemental overlay. Figure 48 (d) to (h) are the elemental maps and Figure 48 (i) (and inset) is the EDS compositional analysis.

4.7.4 Transmission electron microscopy

The use of a high resolution (0.10 nm) CM200 FEG transmission electron microscope operating at 200 kV for examining the structure of martensite and the application of dual-beam focused ion beam system (DB-FIB, XT, Nova Nanolab 200) for the preparation TEM thin foil samples are mentioned in Chapter 5. The DB-FIB system has the electron and ion columns separated by an angle of 52° between them such that both the beams are concentrated on the same region of interest. TEM samples are very precisely and rapidly prepared by DB-FIB using the ‘lift-out’ approach from among the two approaches discussed in (Munroe 2009). After deposition of the protective metal layer (Pt) on the region of interest, a series of mills were performed on the DB-FIB to prepare an electron transparent membrane of thickness $\sim 1000 - 2000 \text{ \AA}$. The transparent lamella was removed from the milled trench using a micromanipulator and placed on a carbon-coated Cu grid. Alternatively TEM specimens can also be prepared through jet polishing using an electrolyte (Maziarz, Wojciech et al. 2016; Maziarz, W. et al. 2017) or through mechanical polishing followed by ion milling (Valeanu et al. 2011).

4.7.5 Electron probe microanalysis (EPMA)

More accurately the compositions of a few of the samples synthesized at different conditions were determined through wavelength dispersive spectrometry (WDS) routines on an EPMA

microscope were carried out. CAMECA SXFive electron probe microanalysis machine with advanced WDS spectrometers for accurate analysis of trace and light elements was used.

4.7.6 Magnetization measurements

Magnetization measurements were carried out using the Quantum Design Magnetic Property Measurement System (MPMS3) magnetometer with a 7 T magnet and magnetic field control with $\leq 10^{-8}$ emu sensitivity. DC scan mode was employed for a continuous plotting of the M-T (Magnetization-Temperature) diagram. Standard zero-field-cooled (ZFC), field-cooled (FC) and field-heated (FH) protocols were followed to determine the M-T curves of the samples. The ZFC protocol consisted of heating the sample to 400 K at $H = 0$, cooling to 2 K and then measuring M-T with $H = 100$ Oe. The FC protocol consisted of heating the sample to 400 K and applying 7 T field in order for the samples to be magnetized and then cooling to 2 K in an applied field of 100 Oe. The M-T is then measured with $H = 100$ Oe. AC susceptibility mode was employed to determine the AC susceptibility of the samples at different temperatures. M-H curves were determined using a vibrating sample magnetometer (VSM) under a maximum applied field of 18 kOe.

In order to further explain magnetometry, an example is presented here from literature. The M-T, DSC and M-H curves of $\text{Ni}_{45}\text{Co}_5\text{Mn}_{40}\text{Sn}_{10}$ ferromagnetic Heusler alloy is shown in Figure 7 (Srivastava et al. 2011). The properties seen in the curves are the properties desired in ferromagnetic Heusler alloys for them to be multifunctional. It can be seen from Figure 49 (a) that at an applied field of 1 T, the magnetization suddenly increases from less than 10 emu/cm^3 in the martensite phase to more than 1100 emu/cm^3 in the austenite phase (Srivastava et al. 2011). Figure 49 (c) indicates that the structure of the alloy has a small volume fraction of ferromagnetic particles in an antiferromagnetic matrix due to a pinning

effect of non-collinear or antiferromagnetic structures in the ferromagnetic domain. Despite the saturation magnetization being very high (1100 emu/cm^3), the susceptibility of the austenite is determined as $\chi_0 = 2.3 \text{ emu/cm}^3\text{Oe}$ near $H = 0$, indicating that the austenite is magnetically soft, shown in Figure 49 (d). The DSC plot is shown in Figure 49 (b). The thermal hysteresis from the hysteresis plot is determined as 6°C ($A_f - M_s$). This low thermal hysteresis and high value of saturation magnetization is any material scientist's delight and is dependent on the composition of the alloy.

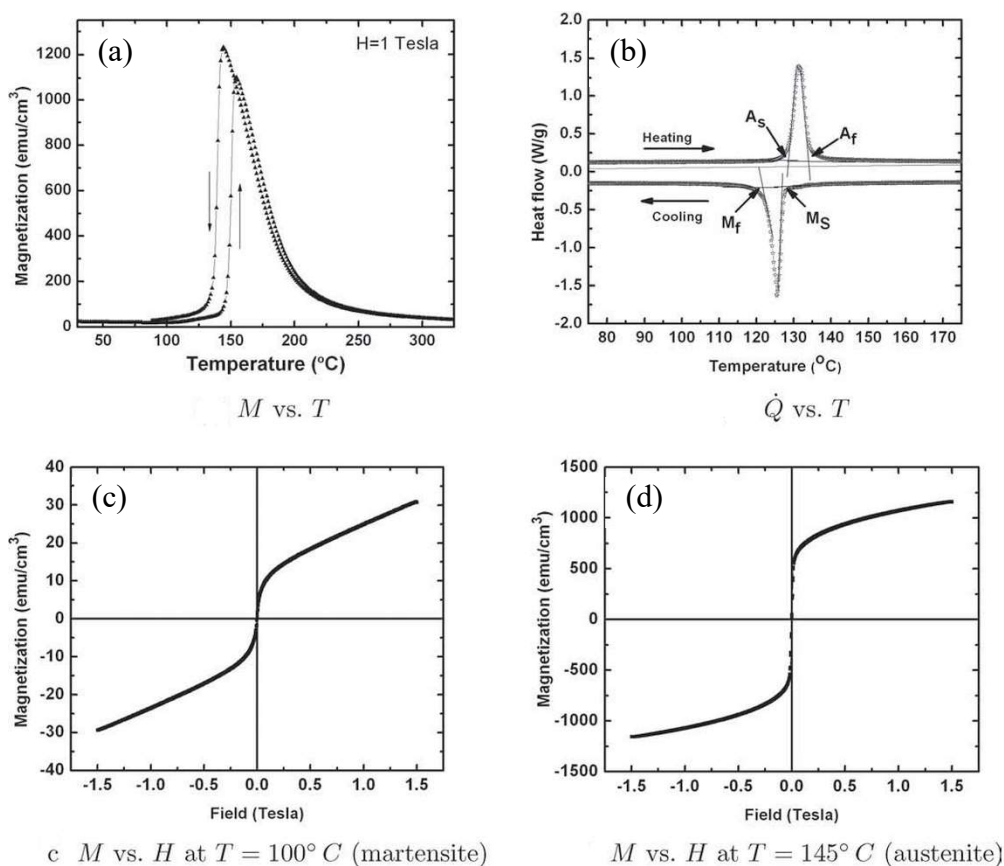


Figure 49. $\text{Ni}_{45}\text{Co}_5\text{Mn}_{40}\text{Sn}_{10}$ alloy (a) M - T under 1 T field; (b) DSC plot; (c) M - H curve of martensite; (d) M - H curve of austenite (Srivastava et al. 2011).

5 Powder processing and characterisation of a quinary Ni-Mn-Co-Sn-Cu Heusler alloy

Riaz Ahamed^a, Reza Ghomashchi^a, Zonghan Xie^a, Lei Chen^a, Paul Munroe^b, Song Xu^b

^a School of Mechanical Engineering, The University of Adelaide, Adelaide, SA 5005

^b School of Materials Science and Engineering, University of New South Wales, Sydney, NSW 2052

Powder Technology 2018, 324, 69-75.

Statement of Authorship

Title of Paper	Powder Processing and characterisation of a quinary Ni-Mn-Co-Sn-Cu Heusler alloy
Publication Status	<input checked="" type="checkbox"/> Published <input type="checkbox"/> Accepted for Publication <input type="checkbox"/> Submitted for Publication <input type="checkbox"/> Unpublished and Unsubmitted work written in manuscript style
Publication Details	Ahamed, R, Ghomashchi, R, Xie, Z, Chen, L, Munroe, P & Xu, S 2018, 'Powder processing and characterisation of a quinary Ni-Mn-Co-Sn-Cu Heusler alloy', <i>Powder Technology</i> , vol. 324, pp. 69-75.

Principal Author

Name of Principal Author (Candidate)	Riaz Ahamed Ahamed Khan		
Contribution to the Paper	I was responsible for the design and conduct of experiments and tests which included powder characterization, compact preparation, sintering, metallography, DSC and microscopy (optical and SEM). Tests like XRD and TEM were carried out externally at UNSW. Wrote the first draft of the manuscript and incorporated and addressed all comments/suggestions by other authors. Interpretation of results was primarily my responsibility.		
Overall percentage (%)	85%		
Certification:	This paper reports on original research I conducted during the period of my Higher Degree by Research candidature and is not subject to any obligations or contractual agreements with a third party that would constrain its inclusion in this thesis. I am the primary author of this paper.		
Signature	<table border="1"> <tr> <td>Date</td> <td>21/6/19</td> </tr> </table>	Date	21/6/19
Date	21/6/19		

Co-Author Contributions

By signing the Statement of Authorship, each author certifies that:

- i. the candidate's stated contribution to the publication is accurate (as detailed above);
- ii. permission is granted for the candidate to include the publication in the thesis; and
- iii. the sum of all co-author contributions is equal to 100% less the candidate's stated contribution.

Name of Co-Author	Lei Chen		
Contribution to the Paper	Supervising development of work, evaluating methods and theories, helping with experimental setup and evaluating manuscript.		
Signature	<table border="1"> <tr> <td>Date</td> <td>21/06/19</td> </tr> </table>	Date	21/06/19
Date	21/06/19		

Name of Co-Author	Reza Ghomashchi		
Contribution to the Paper	Supervising development of work, evaluating methods and theories, helping with experimental setup and evaluating and editing the manuscript.		
Signature	<table border="1"> <tr> <td>Date</td> <td>28/5/2019</td> </tr> </table>	Date	28/5/2019
Date	28/5/2019		

Name of Co-Author	Zonghan Xie		
Contribution to the Paper	Supervising development of work, evaluating methods and theories, helping with experimental setup and evaluating manuscript.		
Signature		Date	2019-06-21

Name of Co-Author	Paul Munroe		
Contribution to the Paper	Assisted in analysis of TEM data in the paper and in editing drafts prior to submission		
Signature		Date	29/12/18

Name of Co-Author	Song Xu		
Contribution to the Paper	TEM & XRD Data in the paper		
Signature		Date	8/1/2019



Powder processing and characterisation of a quinary Ni-Mn-Co-Sn-Cu Heusler alloy



Riaz Ahamed^{a,*}, Reza Ghomashchi^a, Zonghan Xie^a, Lei Chen^{a,*}, Paul Munroe^b, Song Xu^b

^a School of Mechanical Engineering, University of Adelaide, Adelaide, SA 5005, Australia

^b School of Materials Science and Engineering, University of New South Wales, Sydney, NSW 2052, Australia

ARTICLE INFO

Article history:

Received 31 May 2017

Received in revised form 14 September 2017

Accepted 3 October 2017

Available online 10 October 2017

Keywords:

Heusler alloys
Powder processing
Microstructure
Martensite
Magnetic behaviour

ABSTRACT

Ni-Co-Mn-Sn-Cu alloys were sintered from elemental powders at a temperature of 1050 °C for 24 h. The resulting microstructures and physical properties were characterised by differential scanning calorimetry, X-ray diffraction, optical/electron microscopy and SQUID magnetometry. The use of the alloys in energy conversion was satisfactorily tested. The new alloys exhibited a distinct martensitic transformation when cooled to room temperature. The presence of Cu in the powders moved the transformation temperature toward a higher value. The findings of this study demonstrate that the powder processing could be used to replace time-consuming arc/induction melting process in the development of high performance Heusler alloys at a lower cost.

© 2017 Elsevier B.V. All rights reserved.

1. Introduction

Heusler alloys have attracted considerable interest due to their multiferoic attributes [1]. Often described as X_2YZ (X, Y – transition metals and Z – main group element), these alloys usually possess two of three ferroic characteristics – ferromagnetism, ferroelectricity and ferroelasticity, making them attractive functional materials for various applications [2]. What makes them multiferoic and therefore multifunctional is a phase transformation from austenite (at high temperatures) to martensite (at low temperatures) that occurs at a temperature below their Curie temperatures. This is also accompanied by a magnetic transition that changes the magnetic order of the phases [3]. For Heusler alloys martensitic transformation can occur over a range of temperature [4–7]. It can also be induced by the application of a magnetic field. The application of magnetic field may reduce martensite starting temperature and therefore cause reverse martensitic transformation by forming the high temperature ferromagnetic phase. Both structural and magnetic properties become strongly coupled to one another, giving rise to properties such as magnetic shape memory effect [8], magneto-caloric effect [9–11], magneto-resistance [7,12] and direct conversion of heat into electricity [13].

Quite important in the study of Heusler alloys is the difference in magnetisation between the martensitic and austenitic phases, the larger the gap is, the better it is for driving structural transformation by application of magnetic fields. The field induced reverse martensitic

transformation adds further to the functionality of the materials such as a large inverse magneto-caloric effect, giant strain and giant magneto-resistivity [14]. The alloy chemistry and atomic arrangement within crystal structure play an important role in phase transformation and resultant magnetization. A large difference in magnetisation between the phases is realised by the addition of Co to the Ni-Mn-Sn alloy [14] to replace Ni or Mn. Since Co has a higher magnetic moment than Ni [15], substitution of Ni with Co lowers the martensitic transformation temperature (M_s), while at the same time increases the Curie temperature (T_c). On the other hand, substitution by Co for Mn increases both M_s and T_c [16]. Addition of other elements such as Cu, too, has the effect of changing the martensitic transformation temperature depending on whether it is substituted for Ni or Mn [17,18]. For example, the substitution of Cu for Mn in $Ni_{50}Mn_{34}In_{16}$ ($Ni_{50}Mn_{34-x}Cu_xIn_{16}$) showed an increase in martensitic transition temperature along with a drop in Curie temperature [19]. However addition of Cu has not been shown to bring about a large difference in magnetisation between phases as Co does [17,18].

It is common to synthesize Heusler alloys by arc/induction-melting of high purity elements in a controlled environment. The alloy casts are usually remelted over several times to improve homogeneity and reheated and kept at high temperatures (normally 80% of the melting point) for up to several days before quenching in ice water [20]. The rationale behind such prolonged treatment is to ensure a uniform distribution of constituent elements and the formation of fully martensitic structure at room temperature. Another technique used is to prepare the alloy ribbons by melt-spinning through a rapid solidification process. While the melt-spinning could bring about advantages

* Corresponding authors.

E-mail address: riazahamed.ahamedkhan@adelaide.edu.au (R. Ahamed).

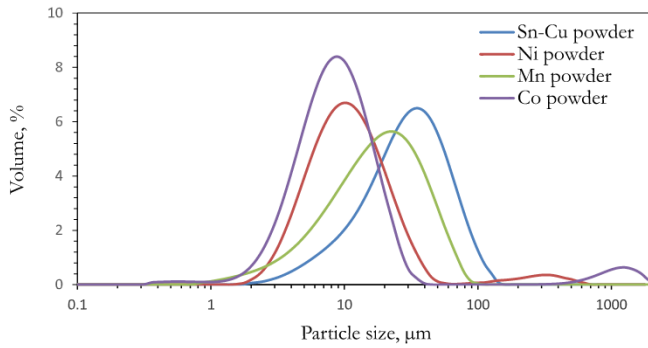


Fig. 1. Particle size distribution of constituent powders.

Table 1
Powder particle size.

Powder	Ni/ μm	Mn/ μm	Sn-Cu/ μm	Co/nm
Volumetric mean/D [4,3]	23.8	20.6	37.2	4029 (Z-Ave)

like increased solid solubility limits and refinement of microstructure [21], it is difficult to prepare bulk materials and limits its application.

Powder metallurgy (P/M) is relatively simple material processing technique, where alloy composition can be tailored for specific

application with minimum waste. Although the P/M process has been employed for fabrication of conventional shape memory alloys [22–28], it has been less common in the synthesis of ferromagnetic shape memory (Heusler) alloys. Furthermore, very few P/M fabrications reported in the literature used costly alloy powders rather than simple elemental powders. For example, spark plasma sintering (SPS), pressure-less sintering (PLS) and solid state replication were used to consolidate alloy powders of $\text{Ni}_{43}\text{Co}_7\text{Mn}_{39}\text{Sn}_{11}$, to explore the martensitic and magnetic properties usually found in cast alloys [29–31]. One advantage of P/M route is the control of porosity, which affects the ductility and shape recovery (memory) characteristics of these alloys [31].

Since no report can be found on the synthesis of Heusler materials by P/M using elemental powders, there is a practical need to explore the P/M routes in fabricating high performance Heusler alloys at low costs. This work reports on powder processing, microstructural development including phase transformation, magnetisation behaviour and the energy conversion function of quinary Ni-Mn-Co-Sn-Cu alloys prepared using elemental powders. The advantage of this method is discussed when compared to alloys prepared by melting.

2. Experimental procedure and sample preparation

The powder mixture was prepared with a starting stoichiometric composition of $\text{Ni}_{45}\text{Mn}_{40}\text{Co}_5\text{Sn}_{10}$ [13] reported for cast alloy that exhibited attractive martensitic and magnetic behaviour. Commercial purity elemental powders of nickel, manganese, cobalt and a mixture

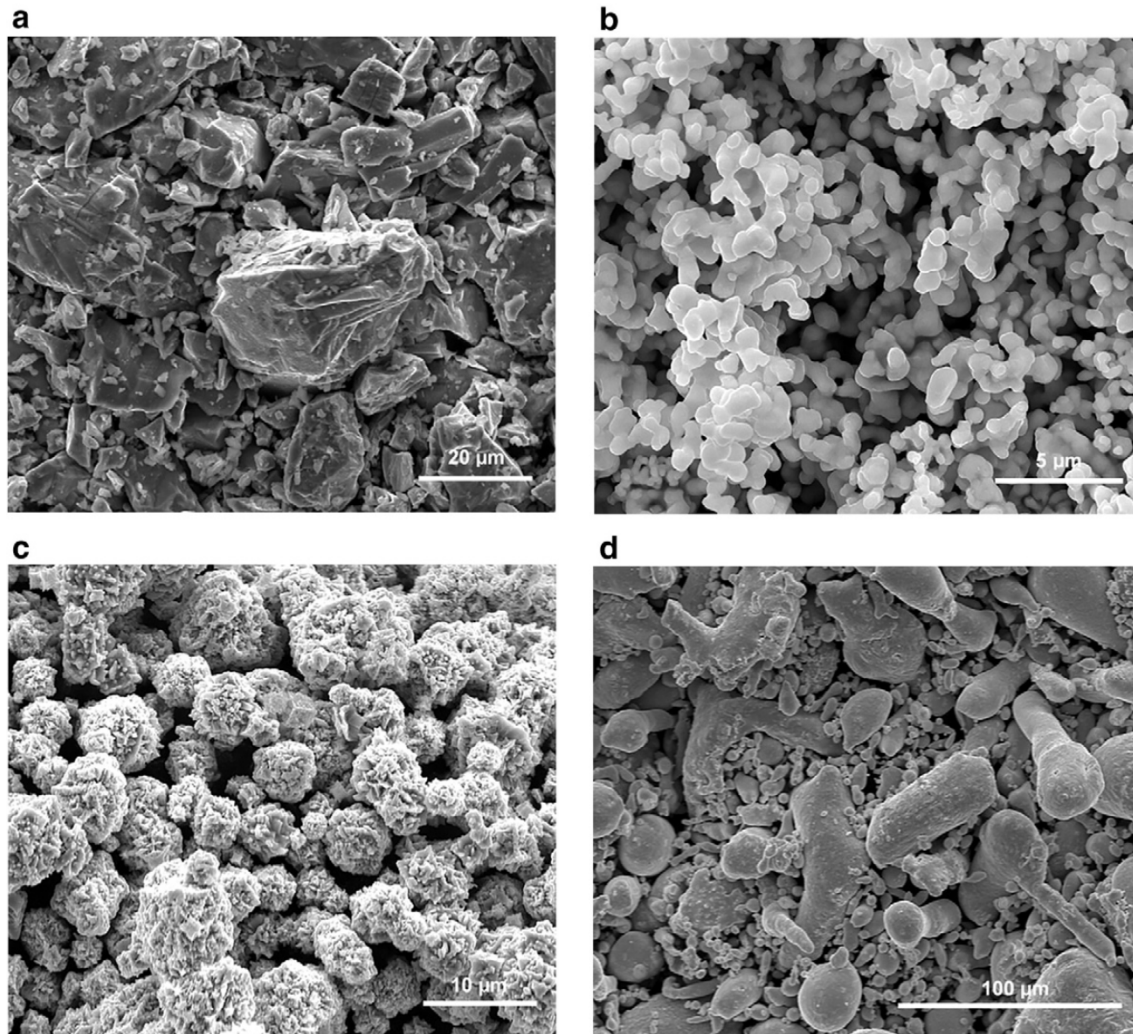


Fig. 2. SEM micrographs to show the morphology of (a) Mn (b) Co (c) Ni and (d) Sn-Cu powders.

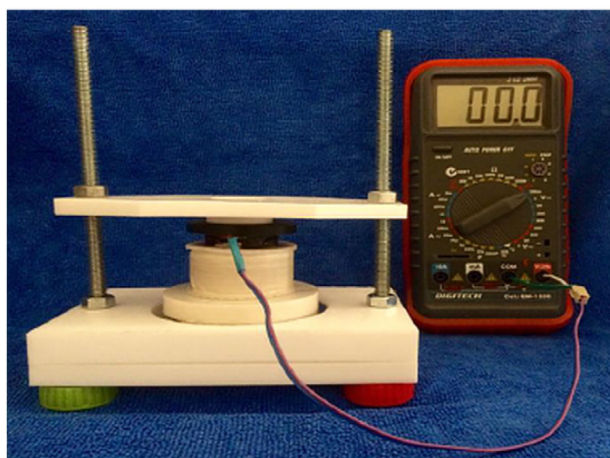


Fig. 3. Device used for energy conversion test.

Table 2
Specifications of coils.

Coil	Turns	Wire diameter/mm	Outside diameter/mm	Inside diameter/mm	Height of coil/mm
Copper	4000	0.15	38	16	26
Copper	8000	0.15	38	19	20

of tin and copper (2.5 wt.%) were used. The size distribution of the as-received elemental powders is given in Fig. 1 analysed using laser diffraction particle size analyser (Mastersizer 2000, Malvern Instruments, UK). The mean size for all powders is given in Table 1. The SEM micrographs in Fig. 2 provide an indication of powder morphology and size including some degree of agglomeration of the elemental powders.

The powders were carefully weighed and blended with an organic binder in a cylindrical mixer for 3 h to render a good mixing. Following the mixing, the powders were compacted in a double action press at a maximum load of 70 kN to produce cylindrical compacts of 11 mm diameter. The green compacts were sintered at 1050 °C for 24 h in a high temperature resistance heating tube furnace using an Ar atmosphere. The compacts were first heated at a heating rate of 5 °C/min to

400 °C, held for 30 min to burn off the binder and then ramped up to the sintering temperatures at the same rate.

For the microstructural analysis of as-sintered alloys, samples were cut using a slow speed diamond saw with surfaces prepared using an automatic polisher (Tegramin-25, Struers, Denmark). The etchant used was Kalling's reagent (50 ml HCl, 50 ml CH₃OH and 2–5 g CuCl₂). The microstructure and composition of the as-sintered samples were evaluated using FESEM (Quanta 450 FEG, USA) and electron microprobe (SXFive, CAMECA, France) with both EDS and WDS attachments. The formation of phases was confirmed by XRD (PANalytical Empyrean) using Cu-K α radiation. The microstructure of the as-sintered specimens was also investigated by a transmission electron microscope (FEG-TEM, Philips CM200) operating at 200 KV. The samples used for TEM observation were prepared by a dual-beam focused ion beam system (FIB, XT Nova Nanolab 200), using a sample preparation method described elsewhere [32].

The phase transformation temperatures were measured using differential scanning calorimeter (Mettler-Toledo TGA/DSC) within the temperature range of 20–400 °C at heating and cooling rates of 5 °C/min. The magnetisation behaviour of the alloys was studied within a temperature range of 0–400 K under an applied magnetic field of 100 Oe using a superconducting quantum interference device (SQUID) magnetometer. Standard zero-field-cooled (ZFC), field-cooled (FC) and field-heated protocols were followed.

To demonstrate the ability of the alloy in energy conversion, a custom-made device was built as shown in Fig. 3 [33]. The underlying principle of the experimental set-up is based on the fundamental dipolar relationship between magnetization M , magnetic induction B and magnetic field H given by $B = H + 4\pi M$. Phase transformation in the alloy is expected to induce a non-zero dB/dt on which Faraday's law $curl E = \frac{1}{c} \frac{dB}{dt}$ can be applied. A neodymium permanent magnet of 70 mm diameter and 15 mm thickness was used. Two coils of copper were used whose specifications are shown in Table 2. A digital multimeter was used to measure the voltage. Temperature changes were recorded using a thermal imager targeting the top of the coil. IRBIS3 Plus was used to analyse the images from the imager. The sample was heated to 400 °C and then cooled differently using water and ice packs.

3. Results and discussion

The volumetric mean diameter D [4,3] values of nickel, manganese powders and tin-copper mixture are $\sim 23 \mu\text{m}$, $\sim 20 \mu\text{m}$ and $\sim 37 \mu\text{m}$

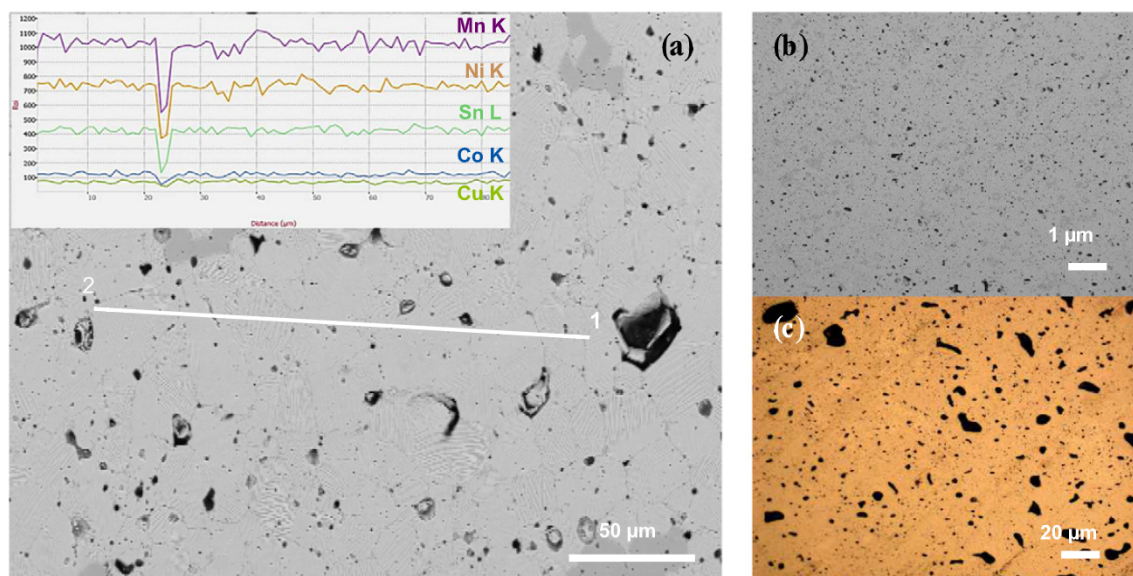


Fig. 4. (a) Inset shows an EDS line scan between points 1 & 2 (main panel) showing uniform distribution of constituent elements (b) SEM and (c) optical micrographs of the as-sintered specimen showing the distribution and morphology of the pores.

Table 3
Microprobe analysis of alloy composition of the as-sintered specimens.

Ni/at.%	Mn/at.%	Co/at.%	Sn/at.%	Cu/at.%	Total
44.3	40.4	5.2	7.7	2.4	100

Table 4
Composition of micro-constituents determined by EDS.

	Ni/at.%	Co/at.%	Mn/at.%	Sn/at.%	Cu/at.%	Total
Martensitic grains	44.4	5.1	40.9	7.5	2.2	100
Spongy phase	43.8	5.1	37.8	10.2	3.2	100
Dark grey intermetallics	43.9	11.0	41.0	1.1	2.9	100

respectively. The Z-average value of cobalt powder is $\sim 4 \mu\text{m}$. As expected, there is some degree of agglomeration of constituent powders that may affect the density of green compacts. The green density averaged around 70% of the theoretical density for the applied pressure of $\sim 735 \text{ MPa}$. The measured density of the sintered specimens was around 90% of the theoretical density after being kept for 24 h at $1050 \text{ }^\circ\text{C}$. An EDS line scan shown in inset, between points 1 and 2 in the main panel of Fig. 4(a), confirms a uniform distribution of Mn, Ni, Co and Sn within the bulk alloy. The increased density is an indication of an effective diffusion amongst the particles of the constituent powders that helped close down the pores in between, Fig. 4(b) & (c). The microprobe analysis of the as-sintered specimens, as shown in Table 3, confirmed the alloy sample composition matches the design very well.

3.1. Microstructure

The optical and SEM micrographs of Fig. 5 provide a detailed view of the microstructural features in the sintered alloys. The formation of 'grains' or colonies bearing a clear martensitic morphology can be clearly seen in Fig. 5(a). The backscatter electron micrographs in

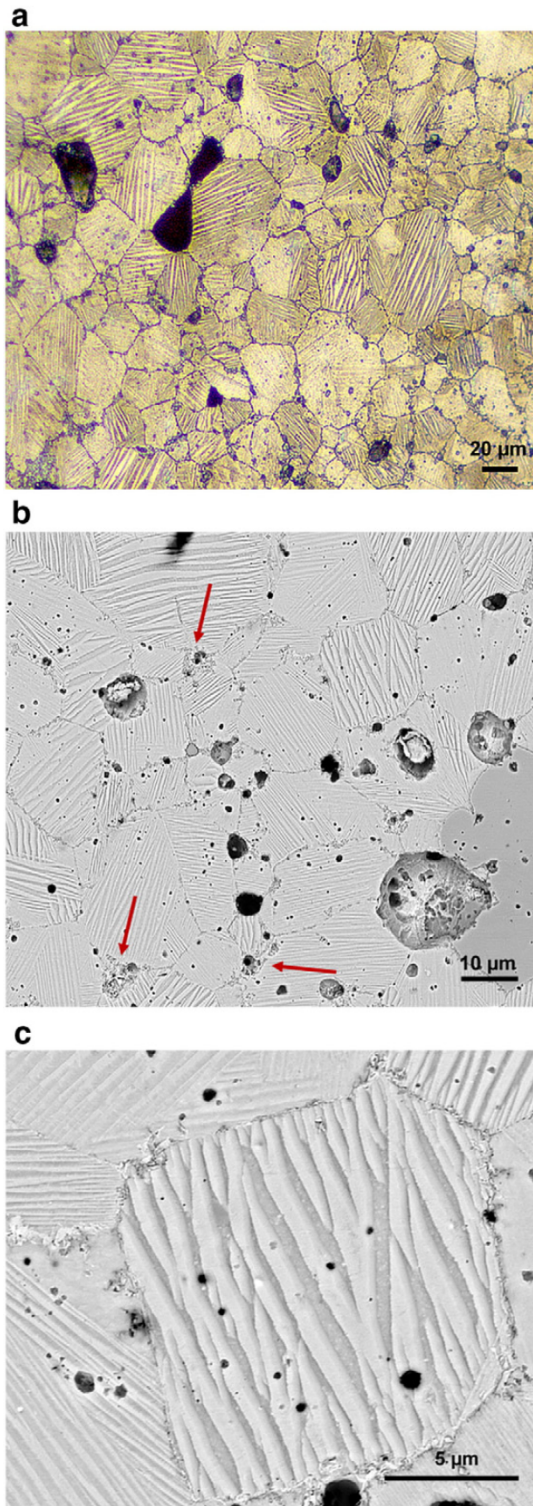


Fig. 5. Optical and backscatter electron micrographs to show the development of Heusler alloy synthesis.

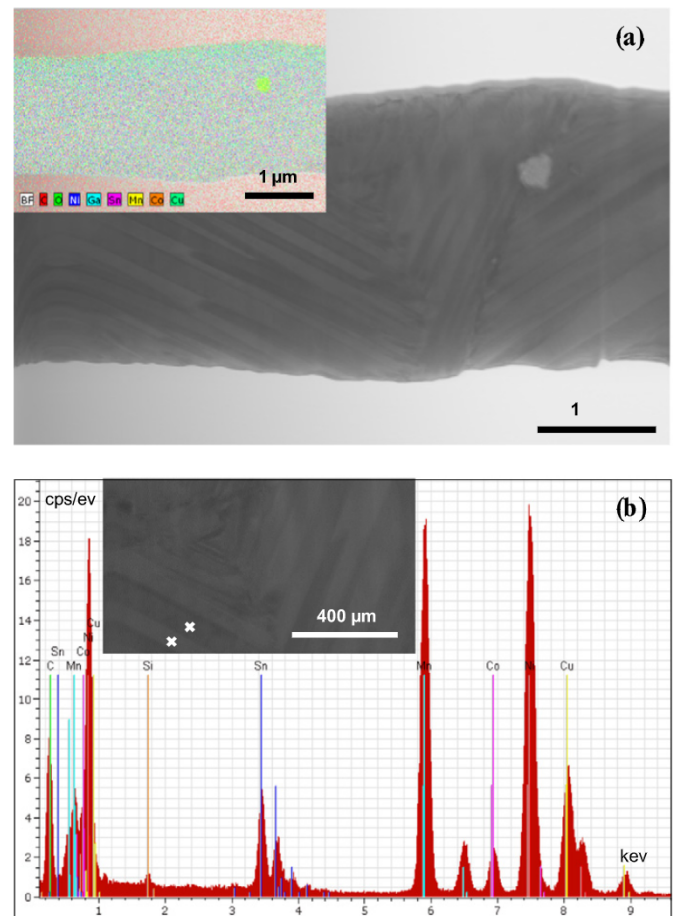


Fig. 6. TEM and compositional map of the as-sintered specimen (a) Martensite grains. Inset shows the map of constituent elements. The presence of Ga is due to ion sputtering during TEM specimen preparation (b) EDS spectrum of marked points on the martensitic laths within the grains, shown in inset.

Fig. 5(b) & (c), reveal the presence of the martensitic grains along with a bulky dark grey phase that have the distinct feature of intermetallics, both phase compositions are summarised in Table 4. In addition, a small number of little spongy-like phase, shown by red arrows in

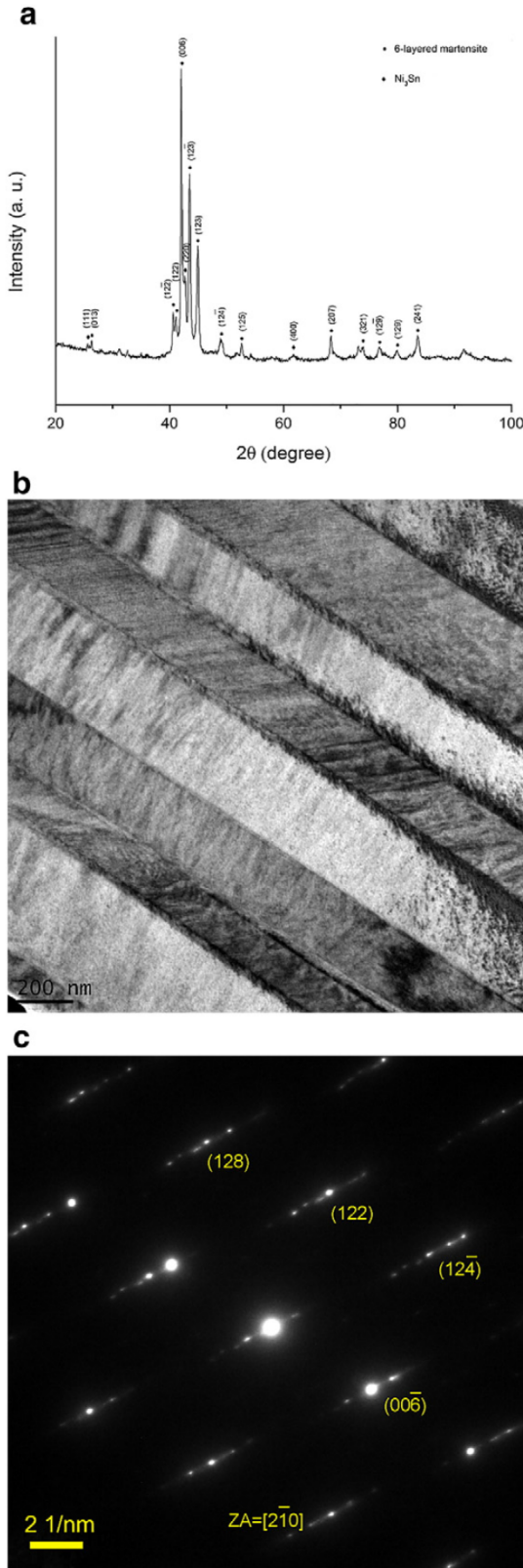


Fig. 7. (a) XRD spectrum of the alloy showing a 6-layered martensite structure and Ni₃Sn phase (b) Bright field TEM image of martensite phase (c) SAED pattern revealing 6-layered martensite.

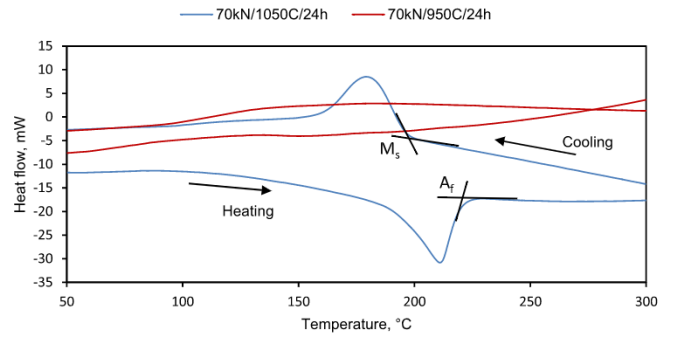


Fig. 8. DSC curves of the alloys sintered at two different temperatures.

Table 5
Phase transformation temperatures.

Alloy	Processing condition	A _s /°C	A _f /°C	M _s /°C	M _f /°C
1	70/1050/24	188	225	199	159
2	70/950/24	–	–	–	–

Fig. 5(b), was detected near the pores, whose composition is also given in Table 4. The spongy phase appears to be Sn-rich, while the bulky dark grey phase is rich in Co with a trace amount of Sn in solution. The formation of the spongy phase may be due to that the low melting point Sn flowed through the green compact at the early stage of sintering and accumulated within the pores. Dark regions which are rich in Co may have resulted from the agglomeration of Co particles, which had the smallest particle size, probably due to inadequate mixing. However, it is quite clear that more than 95% of the region is made of martensite phase as seen in Fig. 5(a).

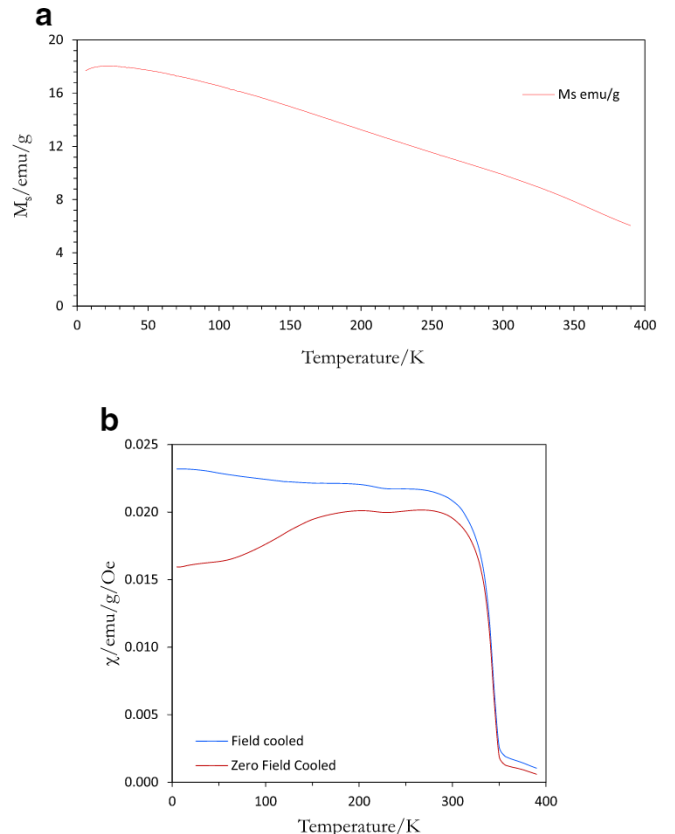


Fig. 9. (a) Temperature vs Magnetisation (b) Temperature vs ac susceptibility curves of the new alloy.

Table 6
Test data for evaluation of voltage generation.

Test start temperature/°C	Method of cooling	Measured voltage/mV	Specimen diameter/mm	Specimen thickness/mm	Turns of coil
200	Wet pack	0	10	6	4000
220	Wet pack	0.1	10	6	8000
250	Wet pack	0.2	10	2	8000
310	Wet pack	0.4	10	2	8000
335	Ice pack	0.6	10	2	8000

Furthermore, TEM studies were carried out to examine compositional variations across the martensitic laths and also provide information on the degree of homogeneity across entire grains. The main panel of Fig. 6(a) shows a twinned structure with martensitic laths evenly distributed. The compositional map of the thin section which confirms the uniform distribution of alloy elements is seen in the inset of Fig. 6(a). An EDS spectrum is shown in Fig. 6(b) for the points marked in the inset of Fig. 6(b).

The indication of martensite formation shows the potential of the P/M for the synthesis of Heusler alloys. To identify the martensitic structure and other phases which may form, XRD analysis of the specimen is shown in Fig. 7(a), in which the peaks are indexed to a six-layered martensite structure and an intermetallic compound, Ni₃Sn. Corresponding bright field TEM image of the heavily twinned martensite is shown in Fig. 7(b) and the SAED pattern of the martensite is shown in Fig. 7(c). The presence of five satellite spots between principal reflections is consistent with the six-layered structure [34].

3.2. Thermal characterisation

The results of DSC measurements carried out to determine the structural transformation temperatures of the alloys are shown in Fig. 8. Exothermic and endothermic peaks are seen corresponding to

the forward and reverse martensitic transformation. There are however no peaks seen for alloys sintered at 950 °C shown in brown colour. This indicates that the sintering temperature (950 °C) is not adequate to induce reactions which may cause martensitic transformation to occur. For the alloys sintered at 1050 °C the austenite start and finish (A_s and A_f , A_f shown) temperatures, as well as the martensitic start and finish temperatures (M_s and M_f , M_s shown), are given in Table 5. A thermal hysteresis of ~25 °C is observed. The transformation temperatures are higher when compared to the cast alloys [13], probably due to the presence of Cu in the alloys [35,36].

3.3. Magnetisation behaviour

The magnetic transition of the new alloys was characterised from saturation magnetisation (M_s) and ac susceptibility (χ) vs temperature (T) measurements using standard protocols in a biased field of 100 Oe in the temperature range of 0–400 K. As seen from Fig. 9 a) the magnetisation begins to increase at a temperature in the vicinity of 400 K to ~17 emu/g at 0 K. The Curie temperature could not be clearly established. However it could be inferred that using susceptibility measurements shown in Fig. 9(b) there is a transition from paramagnetic to ferromagnetic behaviour at ~360 K. It is obvious that the martensitic transformation and magnetic transition temperatures are different when compared to the cast alloy in [13]. The decrease in magnetic transition temperatures may be due to the effect of the applied magnetic field which has the effect of decreasing the magnetic transition temperatures in Ni_{50-x}Co_xMn₃₉Sn₁₁ multifunctional alloys when $5 < x < 8$ [35]. The separation seen between the zero field-cooled and the field-cooled curves may be attributed to the pinning of ferromagnetic domains in different orientations by anti-ferromagnetic exchanges resulting from changes in Mn–Mn spacing introduced by the addition of Sn atoms as suggested in [36]. This may be a further indication that the new alloy sintered has the typical characteristics of a Heusler alloy.

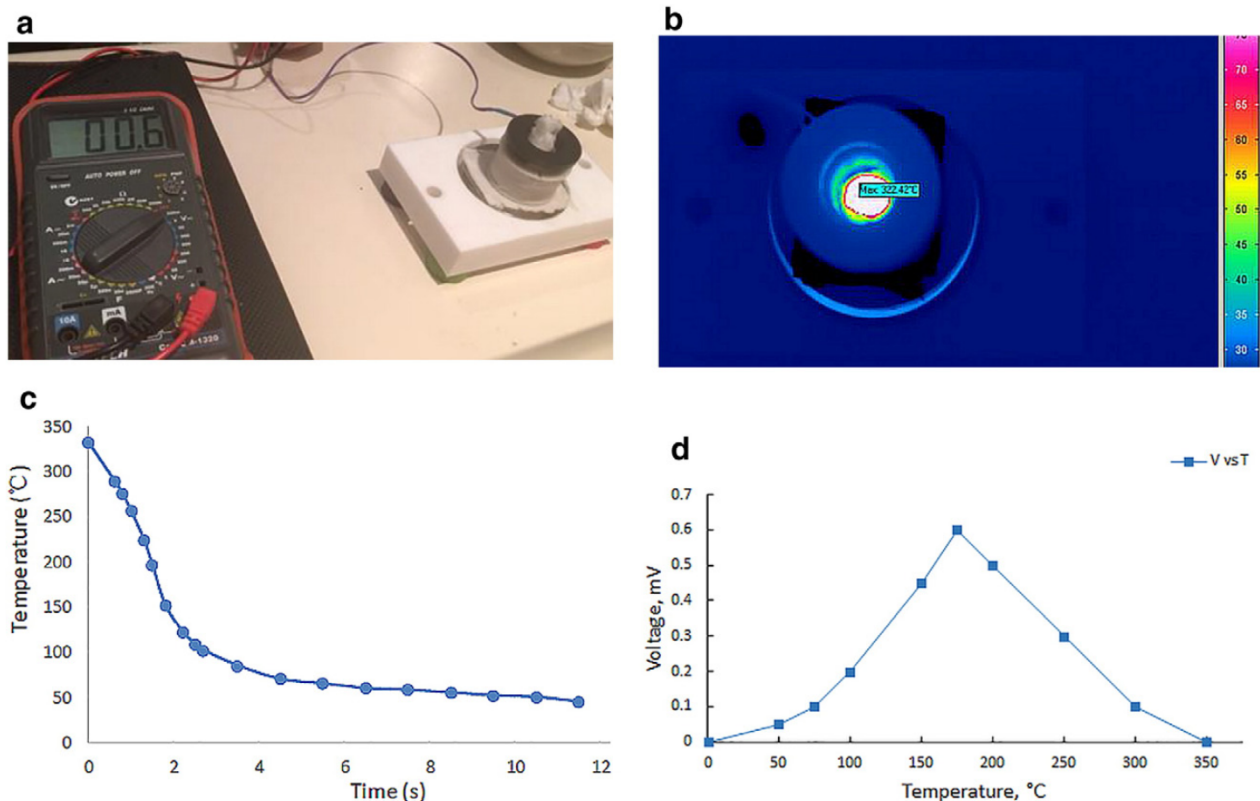


Fig. 10. a) Voltage recorded at the condition of maximum voltage generation b) temperature of sample recorded by the thermal imaging system c) rate of cooling of specimen and d) variation of voltage with temperature for the condition shown in a).

3.4. Evaluation of voltage generation

To reveal the energy conversion function of the developed alloy, the electrical voltage generated by the alloy as it cooled from elevated temperatures, was measured and displayed in Table 6. The samples were heated in a furnace to above 400 °C and then immediately transferred into the coil. The start temperature listed in the table is the actual temperature at which the voltage measurement was started after the samples were transferred from the furnace and cooled by momentarily placing them on wet and ice packs. From elemental calculations using the methods discussed in [37] the specimen thickness and number of turns in coil were determined. It can be seen from Table 6 that the condition of maximum voltage generation was when the sample was rapidly cooled using an ice pack. This is because higher cooling rates as in rapid quenching have a greater influence on the martensitic transformation. The sample thickness was 2 mm and the number of turns in the coil was 8000 at this condition. Fig. 10(a) shows the condition of maximum voltage generation in which a voltage of 0.6 mV was recorded. Fig. 10(b) shows the temperature of the sample as recorded by the thermal imaging system. The rate at which the sample cooled down to room temperature upon ice cooling, measured separately, is seen in Fig. 10(c). The drop in temperature was quite abrupt with the temperature dropping nearly 200 °C in 2 s. The variation of voltage generated with temperature for the condition of maximum voltage generation is shown in Fig. 10(d). The temperature at which the maximum voltage was recorded was 175 °C.

4. Conclusions

The Ni-Co-Mn-Sn-Cu quinary alloy was prepared by simple powder metallurgy route in this study. The new findings can be summarised as follows.

1. Synthesis of Ni-Mn based Heusler alloys by powder processing using elemental powders is feasible. A sintering temperature of 1050 °C is sufficient for diffusion to occur leading to desired structural transformations. The room temperature microstructure appeared to be a six-layered martensite.
2. The addition of Cu shifted the structural transformation temperature to a higher value, compared to the cast alloys.
3. Magnetic transition from paramagnetic to ferromagnetic occurs at around 360 K (~90 °C) when a magnetic field of 100 Oe is applied.
4. A voltage of 0.6 mV was generated at a temperature of 175 °C with the sample thickness being 2 mm.

Acknowledgements

The authors are grateful to the staff at Adelaide Microscopy for assistance of SEM & EPMA, Dr. Robert Woodward and Dr. Peter Metaxas at the University of Western Australia for assistance of SQUID magnetic measurements.

References

- [1] V. Srivastava, K.P. Bhatti, Ferromagnetic shape memory Heusler alloys, in: Hardev Singh Virk, W. Kleeman (Eds.), *Ferroics and Multiferroics*, vol. 189, Trans Tech Publications Ltd, Switzerland 2012, p. 189.
- [2] R.D. James, Z. Zhang, A way to search for multiferroic materials with “unlikely” combinations of physical properties, in: L. Manosa, A. Planes, A. Saxena (Eds.), *Magnetism and Structure in Functional Materials*, Springer, New York 2005, p. 159.
- [3] S.B. Roy, *J. Phys. Condens. Matter* (2013) 25.
- [4] A. Planes, *Physics* (2010) 3.
- [5] Y. Sutou, Y. Imano, N. Koeda, T. Omori, R. Kainuma, K. Ishida, K. Oikawa, *Appl. Phys. Lett.* 85 (2004) 4358.
- [6] S. Aksoy, T. Krenke, M. Acet, E.F. Wassermann, X. Moya, L. Manosa, A. Planes, *Appl. Phys. Lett.* 91 (2007).
- [7] J.M. Barandiaran, V.A. Chernenko, P. Lazpita, J. Gutierrez, J. Feuchtwanger, *Phys. Rev. B* 80 (2009).
- [8] K. Ullakko, J.K. Huang, C. Kantner, R.C. O’Handley, V.V. Kokorin, *Appl. Phys. Lett.* 69 (1996) 1966.
- [9] L. Pareti, M. Solzi, F. Albertini, A. Paoluzi, *Eur. Phys. J. B* 32 (2003) 303.
- [10] J. Marcos, A. Planes, L. Manosa, F. Casanova, X. Batlle, A. Labarta, B. Martinez, *Phys. Rev. B* 66 (2002).
- [11] T. Krenke, E. Duman, M. Acet, E.F. Wasserman, X. Moya, L. Manosa, A. Planes, E. Suard, B. Ouladdiaf, *Phys. Rev. B* 75 (2007).
- [12] K. Koyama, S. Okamoto, T. Watanabe, T. Kanomata, R. Kainuma, W. Ito, K. Oikawa, K. Ishida, *Appl. Phys. Lett.* 89 (2006).
- [13] V. Srivastava, X. Chen, R.D. James, *Appl. Phys. Lett.* 97 (2010).
- [14] J-m. Cao, C-l. Tan, X-h. Tian, Q-c. Li, E-j. Guo, L-p. Wang, Y-j. Cao, *Trans. Nonferrous Metals Soc. China* 24 (2014) 1053.
- [15] X. Chen, V.B. Naik, R. Mahendiran, R.V. Ramanujan, *J. Alloys Compd.* 618 (2014) 187.
- [16] F. Chen, Y.X. Tong, X.L. Lu, B. Tian, L. Li, Y.F. Zheng, *J. Mater. Eng. Perform.* 21 (2012) 2508.
- [17] C. Jing, Y.J. Yang, Z. Li, X.L. Wang, B.J. Kang, S.X. Cao, J.C. Zhang, J. Zhu, B. Lu, *J. Appl. Phys.* 113 (2013) 173902.
- [18] P.O. Castillo-Villa, L. Manosa, A. Planes, D.E. Soto-Parra, J.L. Sanchez-Llamazares, H. Flores-Zuniga, C. Frontera, *J. Appl. Phys.* 113 (2013).
- [19] M. Kaya, S. Yildirim, E. Yüziak, I. Dincer, R. Ellialtioglu, Y. Elerman, *J. Magn. Magn. Mater.* 368 (2014) 191.
- [20] T. Graf, C. Felser, S.S.P. Parkin, *Prog. Solid State Chem.* 39 (2011) 1.
- [21] C. Suryanarayana, Rapid solidification processing, in: P. Veyssi re, K.H.J. Buschow, R.W. Cahn, M.C. Flemings, B. Ilshner, E.J. Kramer, S. Mahajan (Eds.), *Encyclopedia of Materials: Science and Technology*, Second Edition Elsevier, Oxford 2002, p. 1.
- [22] G.E. Monastyrsky, V. Odnosum, J. Van Humbeeck, V.I. Kolomytsev, Y.N. Koval, *Intermetallics* 10 (2002) 95.
- [23] G.E. Monastyrsky, J. Van Humbeeck, V.I. Kolomytsev, Y.N. Koval, *Intermetallics* 10 (2002) 613.
- [24] S.K. Vajpai, R.K. Dube, P. Chatterjee, S. Sangal, *Metall. Mater. Trans. A Phys. Metall. Mater. Sci.* 43 (2012) 2484.
- [25] R.B. Perez-Saez, V. Recarte, M.L. No, O.A. Ruano, J.J. San, *Adv. Eng. Mater.* 2 (2000) 49.
- [26] A. Ibarra, P.P. Rodriguez, V. Recarte, J.I. Perez-Landazabal, M.L. No, *J. San Juan, Mater. Sci. Eng. A* 370 (2004) 492.
- [27] Y-W Kim, Y-S Chung, E Choi, T-H. Nam, *Microstructure and Shape Memory Characteristics of Powder-Metallurgical-Processed Ti-Ni-Cu Alloys*, vol. 43, Springer Boston, 101 Philip Drive, Assinippi Park, Norwell, MA 02061, United States, 2012 2932.
- [28] M. Valeanu, M. Lucaci, A.D. Crisan, M. Sofronie, L. Leonat, V. Kuncser, *J. Alloys Compd.* 509 (2011) 4495.
- [29] K. Ito, W. Ito, R.Y. Umetsu, I. Karaman, K. Ishida, R. Kainuma, *Scr. Mater.* 63 (2010) 1236.
- [30] K. Ito, W. Ito, R.Y. Umetsu, S. Tajima, H. Kawaura, R. Kainuma, K. Ishida, *Scr. Mater.* 61 (2009) 504.
- [31] J.A. Monroe, J. Cruz-Perez, C. Yegin, I. Karaman, A.B. Geltmacher, R.K. Everett, R. Kainuma, *Scr. Mater.* 67 (2012) 116.
- [32] P.R. Munroe, *Mater. Charact.* 60 (2009) 2.
- [33] T. Zhou, Y. Guo, *Waste Heat Harvesting Using Multiferroic Alloys*, University of Adelaide, Australia, 2015.
- [34] L. Righi, P. Lazpita, J. Gutierrez, J.M. Barandiaran, V.A. Chernenko, G. Calestani, *Scr. Mater.* 62 (2010) 383.
- [35] D.Y. Cong, S. Roth, L. Schultz, *Acta Mater.* 60 (2012) 5335.
- [36] T. Krenke, M. Acet, E.F. Wasserman, X. Moya, L. Manosa, A. Planes, *Phys. Rev. B* 72 (2005).
- [37] V. Srivastava, Y. Song, K. Bhatti, R.D. James, *Adv. Energy Mater.* 1 (2011) 97.

6 Powder metallurgy synthesis of Heusler alloys: Effects of Process Parameters

Riaz Ahamed^a, Reza Ghomashchi^a, Zonghan Xie^a and Lei Chen^a

^a School of Mechanical Engineering, The University of Adelaide, Adelaide, SA 5005

Materials 2019, 12(10), 1596.

Statement of Authorship

Title of Paper	Powder Metallurgy Synthesis of Heusler Alloys: Effects of Process Parameters
Publication Status	<input checked="" type="checkbox"/> Published <input type="checkbox"/> Accepted for Publication <input type="checkbox"/> Submitted for Publication <input type="checkbox"/> Unpublished and Unsubmitted work written in manuscript style
Publication Details	Ahamed, R, Ghomashchi, R, Xie, Z., Chen, L 2019, 'Powder Metallurgy Synthesis of Heusler Alloys: Effects of Process Parameters', <i>Materials</i> , vol. 12, 1596.

Principal Author

Name of Principal Author (Candidate)	Riaz Ahamed Ahamed Khan				
Contribution to the Paper	I was responsible for the design and conduct of experiments and tests which included powder characterization, compact preparation, sintering, metallography, DSC and microscopy (optical and SEM). A few XRD and magnetization tests were carried out overseas. Wrote the first draft of the manuscript and incorporated and addressed all comments/suggestions by other authors. Interpretation of results was primarily my responsibility.				
Overall percentage (%)	85%				
Certification:	This paper reports on original research I conducted during the period of my Higher Degree by Research candidature and is not subject to any obligations or contractual agreements with a third party that would constrain its inclusion in this thesis. I am the primary author of this paper.				
Signature	<table border="1" style="width: 100%;"> <tr> <td style="width: 80%;"></td> <td style="width: 20%;">Date</td> </tr> <tr> <td></td> <td>21/6/19</td> </tr> </table>		Date		21/6/19
	Date				
	21/6/19				

Co-Author Contributions

By signing the Statement of Authorship, each author certifies that:

- i. the candidate's stated contribution to the publication is accurate (as detailed above);
- ii. permission is granted for the candidate to include the publication in the thesis; and
- iii. the sum of all co-author contributions is equal to 100% less the candidate's stated contribution.

Name of Co-Author	Lei Chen				
Contribution to the Paper	Supervising development of work, evaluating methods and theories, helping with experimental setup and evaluating manuscript.				
Signature	<table border="1" style="width: 100%;"> <tr> <td style="width: 80%;"></td> <td style="width: 20%;">Date</td> </tr> <tr> <td></td> <td>21/06/19</td> </tr> </table>		Date		21/06/19
	Date				
	21/06/19				

Name of Co-Author	Reza Ghomashchi				
Contribution to the Paper	Supervising development of work, evaluating methods and theories, helping with experimental setup and evaluating and editing the manuscript.				
Signature	<table border="1" style="width: 100%;"> <tr> <td style="width: 80%;"></td> <td style="width: 20%;">Date</td> </tr> <tr> <td></td> <td>28/5/2019</td> </tr> </table>		Date		28/5/2019
	Date				
	28/5/2019				

Name of Co-Author	Zonghan Xie		
Contribution to the Paper	Supervising development of work, evaluating methods and theories, helping with experimental setup and evaluating manuscript.		
Signature		Date	2019-06-21

Article

Powder Metallurgy Synthesis of Heusler Alloys: Effects of Process Parameters

Riaz Ahamed *, Reza Ghomashchi, Zonghan Xie and Lei Chen 

School of Mechanical Engineering, University of Adelaide, Adelaide, SA 5005, Australia;

reza.ghomashchi@adelaide.edu.au (R.G.); zonghan.xie@adelaide.edu.au (Z.X.); lei.chen@adelaide.edu.au (L.C.)

* Correspondence: riazahamed.ahamedkhan@adelaide.edu.au

Received: 22 April 2019; Accepted: 13 May 2019; Published: 15 May 2019



Abstract: $\text{Ni}_{45}\text{Co}_5\text{Mn}_{40}\text{Sn}_{10}$ Heusler alloy was fabricated with elemental powders, using a powder processing route of press and sinter, in place of vacuum induction melting or arc melting route. The effects of process parameters, such as compaction load, sintering time, and temperature, on the transformation characteristics and microstructures of the alloy were investigated. While the effect of compaction pressure was not significant, those of sintering time and temperature are important in causing or annulling martensitic transformation, which is characteristic of Heusler alloys. The processing condition of 1050 °C/24 h was identified to be favorable in producing ferromagnetic Heusler alloy. Longer durations of sintering resulted in an increased γ -phase fraction, which acts as an impediment to the structural transformation.

Keywords: Heusler alloy; powder processing; process parameters; microstructure; martensite

1. Introduction

Ni–Mn–X (X – Ga, Sn, In, Sb)-based ferromagnetic Heusler alloys are multifunctional materials on account of their multiferroic nature [1]. This has its origin in a couple of remarkable and reversible solid-state transformations, viz., the primary martensitic phase transformation and the secondary magnetic transition. While the former transforms the parent cubic $L2_1$ austenite to modulated orthorhombic/non-modulated tetragonal martensite, the latter changes the magnetic order of the phases from ferromagnetic austenite to anti-ferromagnetic/paramagnetic martensite [2]. The reversibility of the transformations is uniquely identified with a shape memory effect (SME), either magnetic (MSME) or metamagnetic (MMSME). In the former, strain recovery is by martensitic twin variants reorientation under an applied field as in Ni–Mn–Ga alloys [3], while in the latter, it is by a field-induced reverse transformation from the martensite phase back to parent austenite phase, as in other Ga-free alloys (e.g., $\text{Ni}_{50}\text{Mn}_{34}\text{In}_{16}$) [3]. MSME [4] and other effects of magnetocaloric [5–8], magneto-resistance [9,10], exchange bias [11], and direct conversion of heat into electricity [12] are interconnected [2], which explains the multifunctional behavior.

These alloys are usually synthesized by liquid processing, followed by annealing. Examples of Heusler alloys prepared by arc/induction melting and characterized for their remarkable magnetostructural properties include compositions in the $\text{Ni}_{50}\text{Mn}_{50-x}\text{Sn}_x$ system (composition rewritten) with large inverse entropy change, leading to a large inverse magnetocaloric effect [6], $\text{Ni}_{41}\text{Co}_9\text{Mn}_{40}\text{Sn}_{10}$ with large magnetic entropy change and magnetoresistance [5], compositions in the $\text{Ni}_{50}\text{Mn}_{50-y}\text{X}_y$ (X = In, Sn, Sb) system with magnetic shape memory [13], $\text{Ni}_{43}\text{Co}_7\text{Mn}_{39}\text{Sn}_{11}$ with magnetic field-induced shape recovery by reverse phase transformation [14], and $\text{Ni}_{45}\text{Co}_5\text{Mn}_{40}\text{Sn}_{10}$ for potential energy conversion [15]. Other alloys, such as $\text{Ni}_{50}\text{Mn}_{37}\text{Sn}_{13}$ [16], compositions in the $\text{Ni}_{50}\text{Mn}_{50-x}\text{Sn}_x$ system (composition rewritten) [17], $\text{Ni}_{42}\text{Co}_8\text{Mn}_{39}\text{Sn}_{11}$ [18], compositions in the $\text{Ni}_{50}\text{Mn}_{50-x}\text{Sn}_x$ system [19], and Ni–Co–Mn–Sn alloy [20] synthesized by liquid processing, deal with microstructural aspects,

such as the effect of compositional variations on microstructure in response to heat treatments, crystal structures of austenite and martensite, determination of crystallographic phases, and stability of different crystallographic structures under varying temperatures and solidification microstructures respectively. Carried out under controlled conditions of a vacuum (10^{-4} bar), an inert atmosphere (argon) with/without the addition of suitable oxygen getter materials, such as Ta or Ti to prevent oxidation [21], arc/melting ensures compositional homogeneity, resulting in a stable single phase $L2_1$ structure. Melt-spinning [22–26] produces highly textured samples with controlled austenitic grain size, suitable for practical applications. In a process in which the alloy melt stream is allowed to solidify rapidly on a fast-rotating (10 m/s to 60 m/s) substrate wheel, the wheel speeds which are an indication of the solidified foil thickness and its solidification rate, influence the magnetostructural phase transformations and characteristics of the alloys [27]. Directional solidification results in chemical segregation or a composition gradient with a control over the transformation temperatures. Bridgman–Stockbarger [28] and Czochralski [29] techniques of directional solidification have been used for preparing single crystals of the alloys.

Solid processing by conventional powder metallurgy (P/M) has been used in a limited manner with alloy powders [30–33] with properties identical to or less than the bulk material. The use of elemental powders in a conventional compaction/sintering procedure has been attempted in the synthesis of a quinary Ni–Co–Mn–Sn–Cu alloy [34]. The transformational characteristics and the observed microstructure of the sintered quinary alloy are similar to cast alloy, thereby offering scope for further investigation. Given that good compositional control can be obtained with the use of elemental powders, the P/M route warrants further study to fabricate high performance Heusler alloys at low costs. This paper endeavors to elucidate the effects of the conventional powder metallurgy parameters, such as compaction load, sintering time, and temperature, upon the transformation characteristics and microstructural features of a quaternary $Ni_{45}Co_5Mn_{40}Sn_{10}$ Heusler alloy.

2. Materials and Methods

Quaternary $Ni_{45}Mn_{40}Co_5Sn_{10}$ alloys were prepared using the P/M technique from commercial purity elemental powders of nickel, manganese, cobalt, and tin. The particle size and distribution were measured on a Mastersizer 2000 (Malvern Panalytical, Worcestershire, UK) laser diffraction particle size analyzer. $D(v,0.5)$ sizes of the powders are tabulated in Table 1. $D(v,0.5)$ refers to the size at which 50% of the sizes are smaller and 50% are larger.

Table 1. Particle sizes of different powders.

	Ni (μm)	Mn (μm)	Sn (μm)	Co (μm)
$D(v,0.5)$	11.52	16.91	19.14	8.05

The individual powders were carefully weighed to atomic composition. About 0.5 to 1% A-wax (Acrawax; N, N' Ethylene Bisstearamide) was added for lubrication. The powders were sealed in a clean cylindrical steel tube and mixed at 120 rpm for approximately 2 h with 5 mm diameter balls at an approximate ball to powder ratio of 4:1. They were then compacted into 11 mm diameter cylindrical compacts, using a tool steel die and punch on a Mohr and Federhaff universal testing machine with a maximum capacity of 200 kN. The green compacts were sintered in a high-temperature tube furnace (70 mm ID and a heating zone of 150 mm) by sealing them off inside silica tubes at argon-partial pressure at a heating rate of 5 °C/min. Table 2 shows the prepared samples and corresponding processing conditions. All samples were furnace cooled (furnace turned off after desired sintering time) to room temperature.

Table 2. Processing conditions of the alloy samples.

Sample ID	Compaction Pressure (MPa)	Holding Time (h)	Temperature (°C)
S950a1	184	12	950
S950a2	184	24	950
S1050a1	184	12	1050
S1050a2	184	24	1050
S950b1	210	12	950
S950b2	210	24	950
S1050b1	210	12	1050
S1050b2	210	24	1050
S1050a3	184	72	1050
S1050a4	184	144	1050
S1050b3	210	72	1050
S1050b4	210	144	1050

The densities of the green and sintered compacts were determined in accordance with the Archimedes principle, using a custom-built density measuring apparatus. Phase transformation temperatures were determined through differential scanning calorimetry (DSC), using a TGA/DSC 2 equipment (Mettler-Toledo AG, Schwerzenbach, Switzerland) differential scanning calorimeter within the temperature range of 25–400 °C. Heating and cooling rates of 5 °C/min were followed in the heating and cooling routines. The enthalpy changes (ΔH) around the phase transformation were calculated from DSC data, using the ‘STARe’ software (Version 9.30, Mettler-Toledo AG, Schwerzenbach, Switzerland) associated with the equipment. Metallographic procedures were similar to those applied on the quinary alloy samples described elsewhere. A LECO LM 700 AT Microhardness Tester (LECO, Saint Joseph, MI, USA) with Vickers indenter with an applied load of 500 g for 15 s dwell time was used for microhardness measurements. Examination of microstructures was carried out on an Environmental SEM (Quanta FEG 450, Hillsboro, OR, USA) scanning electron microscope, equipped with an energy dispersive spectroscopy (EDS) attachment for composition determination. A Rigaku MiniFlex 600 X-ray diffractometer (XRD) (Rigaku, Akishima-shi, Tokyo, Japan) was used for phase determination. All the patterns were obtained using Cu-K α radiation with a wavelength of 1.5406 Å. Additionally, XRD and M–H curves of the samples were obtained from another laboratory for the purpose of verification of our results.

3. Results and Discussion

The actual compositions of the samples were measured using EDS and listed in Table 2. The compositions are not too deviant from the starting composition of Ni₄₅Co₅Mn₄₀Sn₁₀, except for slight variations in Sn and Mn. This confirms that the powder metallurgy route can also be employed to synthesize Heusler alloys.

3.1. Density and Hardness

The theoretical density of the quaternary alloy was determined as 8.02 g/cm³. The measured densities of the quaternary alloy samples are expressed as percentages of the theoretical density (% theoretical density). The % theoretical densities and the microhardness values of the conventionally sintered alloys, sintered for 12 h and 24 h, are plotted in Figures 1 and 2. The variation in the % theoretical densities is around 77% for S950a1, S950a2, S950b1, and S950b2 alloys, as seen in Figure 1a,b, while it is around 89% for S1050a1, S1050a2, S1050b1, and S1050b2 alloys, shown in Figure 2a,b. The percentage of porosity of samples sintered at 950 °C is approximately 23%, while that of alloys sintered at 1050 °C is approximately 11%. Figure 2 shows that longer sintering times and higher temperatures are desirable for effective sintering and reduction in porosity. Microhardness variations of the alloys also reveal that specimens sintered at 1050 °C (S1050 alloys) have higher hardness values

varying from 260 HV to 290 HV, while alloys sintered at 950 °C (S950 alloys) have relatively lower hardness values varying from 140 HV to 175 HV. In all of them, the microhardness is seen to be increasing with the sintering duration. The effect of compaction load is not as significant. The measured densities of the quaternary S1050a3, S1050a4, S1050b3, and S1050b4 alloys expressed as percentages of the theoretical density are plotted in Figure 3. After 144 h, the % density is approximately 96%.

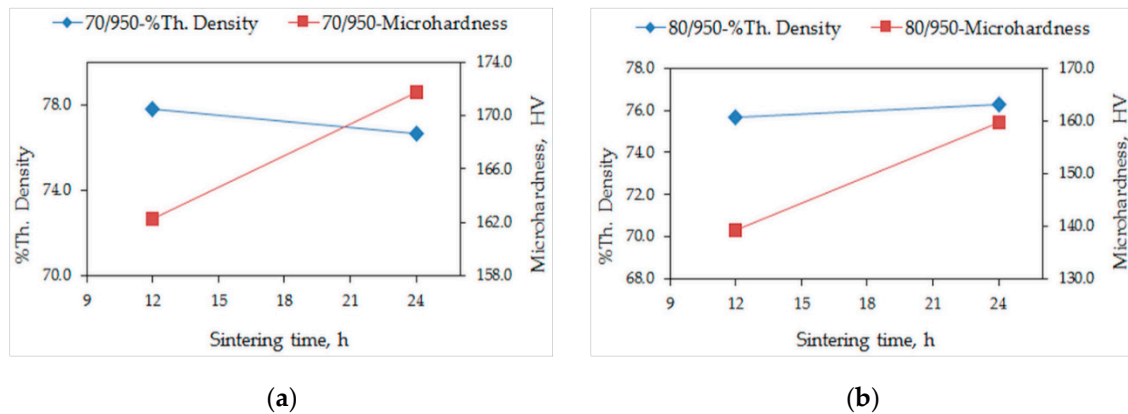


Figure 1. Variation of % theoretical density and microhardness with sintering time of: (a) S950a1, S950a2; (b) S950b1, S950b2.

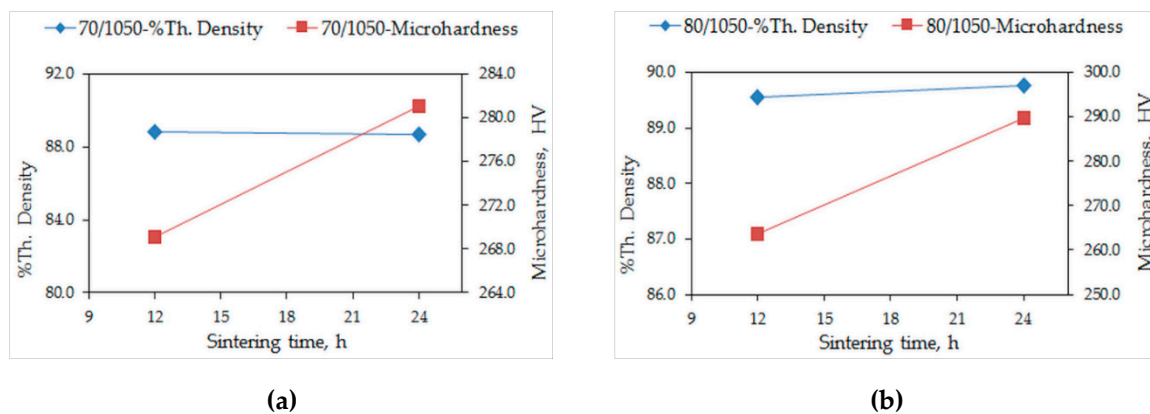


Figure 2. Variation of % theoretical density and microhardness with sintering time of: (a) S1050a1, S1050a2 and (b) S1050b1, S1050b2.

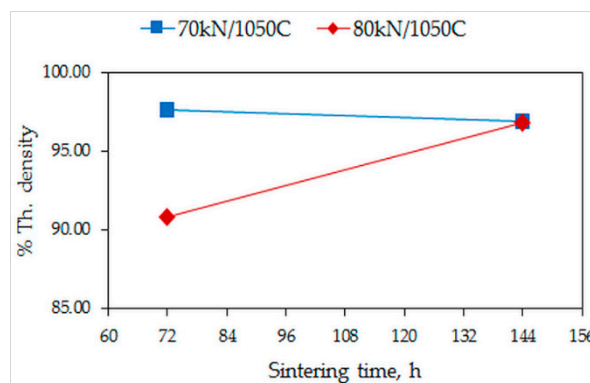


Figure 3. Variation of % theoretical density with sintering time of quaternary alloys S1050a3, S1050a4, S1050b3, and S1050b4.

SEM micrographs of S950a2, S950b2, S1050a2, and S1050b2 alloys, sintered for 24 h, are shown in Figure 4. It can be seen that the alloys sintered at 950 °C show a poor microstructure with large amounts

of porosity, as in Figure 4a,b. On the other hand, alloys sintered at 1050 °C show microstructures that are indicative of the occurrence of effective sintering in them, as in Figure 4c,d. Although more than one phase seemed to appear, the porosity is less in these alloys. The porosities of the alloys are in agreement with the measured densities discussed earlier. It becomes clear that higher temperatures are necessary for effective diffusion between powder particles. The effect of compaction is observed to be less significant. The compositions of the alloys listed in Table 2 are identical to the starting composition, with the Ni and Co values being nearly equal. However, alloys S950a1, S950a2, S950b1, and S950b2 have less Sn and more Mn. This may be attributed to the sintering temperature being insufficient for effective diffusion of the powder particles to attain homogeneity. As a result, the microstructures seen in Figure 4a,b show high levels of porosity. Alloys S1050a1, S1050a2, S1050b1, and S1050b2 also have less Sn and more Mn. However, the difference is about half the difference seen in S950a1, S950a2, S950b1, and S950b2 alloys. The sintering temperature and duration of sintering seemed to have favored increased diffusion, thereby reducing the inhomogeneity. This can be seen from the reduced porosity in the microstructures in Figure 4c,d and also from the measured densities.

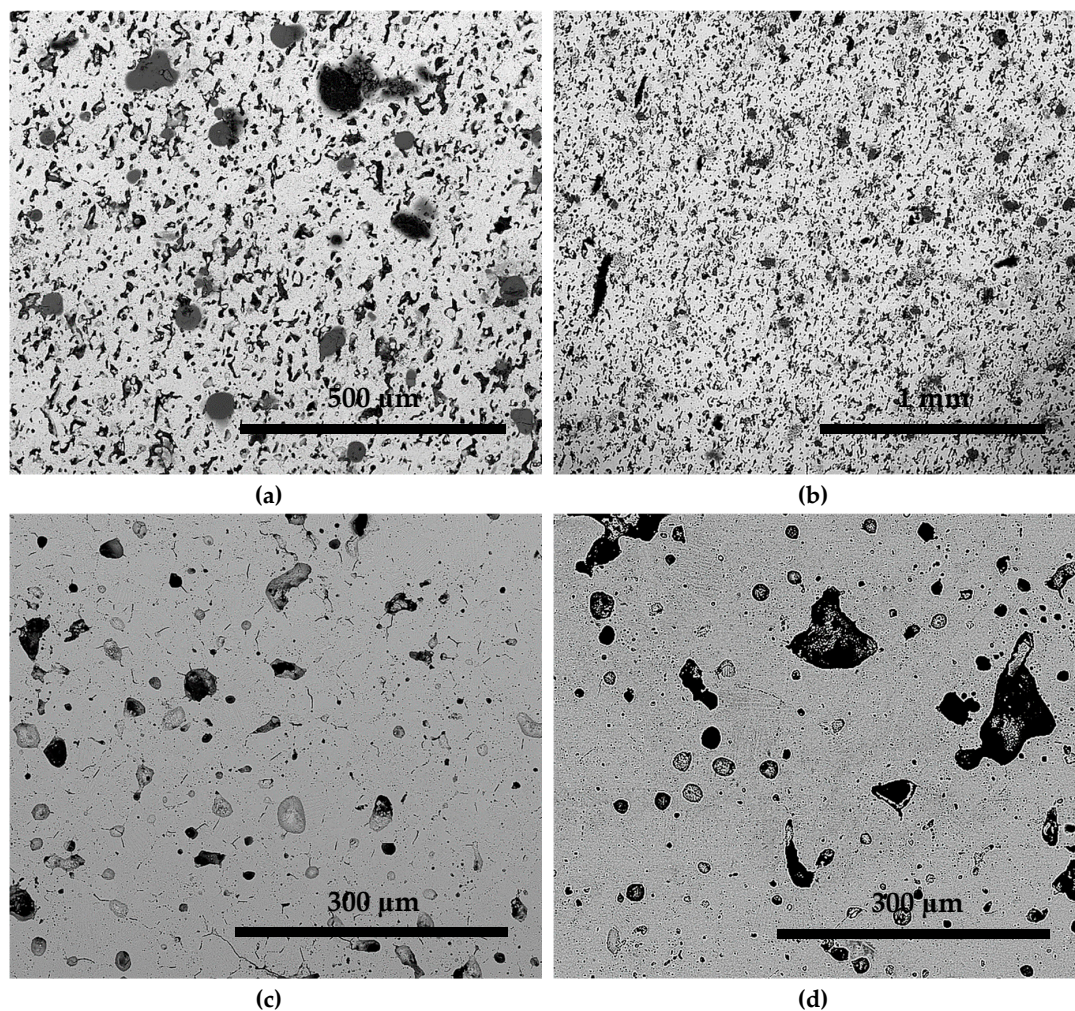


Figure 4. BSE images of samples: (a) S950a2; (b) S950b2; (c) S1050a2; and (d) S1050b2.

SEM micrographs of S1050a3 and S1050b4 alloys shown in Figure 5 suggest melting has occurred at an extended duration of sintering (72 and 144 h, respectively) resulting in a dendritic structure. The microstructures in Figure 5a,b show the light gray cells surrounded with a two phase mixture of light and dark gray regions, with porosity (black) being minimal. In Figure 5b of the sample sintered for 144 h, the progress of powder particle interaction is seen, with interparticle regions

becoming more developed and the large light gray cells coarsened and smoothed off when compared to Figure 4a. The composition of S1050a3 is close to the starting composition with a small variation in Sn. However, when the sintering time increases to 144 h, the difference between Mn and Sn expands, which is an indication that more Sn has been removed from the powder mixture, S1050b4 and S1050a4. The reduction in the level of tin may be attributed to the tin moving into the pores, due to the capillarity effect, as Sn has a very low melting point (232 °C) and is expected to have very low viscosity at the sintering temperature.

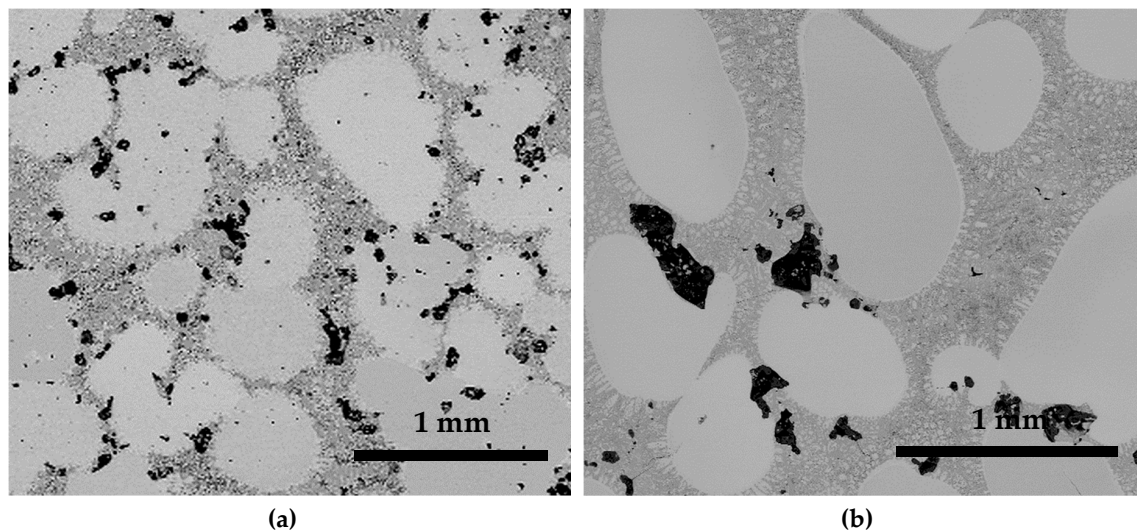


Figure 5. BSE images of samples: (a) S1050a3 and (b) S1050b4.

3.2. Differential Scanning Microscopy

Differential scanning calorimetry (DSC) measurements were obtained from identical heating and cooling cycles for all the samples. The austenite start (A_S), finish (A_F), and peak (A_P), martensite start (M_S), finish (M_F), and peak (M_P), martensitic transformation $(A_S + M_F)/2$, thermal hysteresis ($A_F - M_S$) temperatures, and enthalpy changes around phase transformation (ΔH) of the samples are presented in Table 3. These temperatures are also suitably identified in the DSC curves shown below in Figure 6. The enthalpy changes (ΔH) around the phase transformation are calculated from DSC data.

Table 3. Composition of the alloys obtained from EDS.

Sample ID	Ni (at %)	Mn (at %)	Co (at %)	Sn (at %)	Total
S950a1	44.7	42.8	5.3	7.2	100.0
S950a2	45.8	41.1	5.1	7.9	100.0
S1050a1	44.8	41.8	5.4	8.0	100.0
S1050a2	45.9	39.9	4.6	9.5	100.0
S950b1	45.0	42.2	5.1	7.7	100.0
S950b2	45.2	42.0	4.9	7.8	100.0
S1050b1	44.9	41.0	5.0	8.9	100.0
S1050b2	45.2	40.8	5.1	8.9	100.0
S1050a3	45.8	40.3	5.0	8.9	100.0
S1050a4	44.9	41.6	5.6	7.8	100.0
S1050b3	45.3	40.9	5.9	7.7	100.0
S1050b4	44.6	42.7	5.8	6.9	100.0

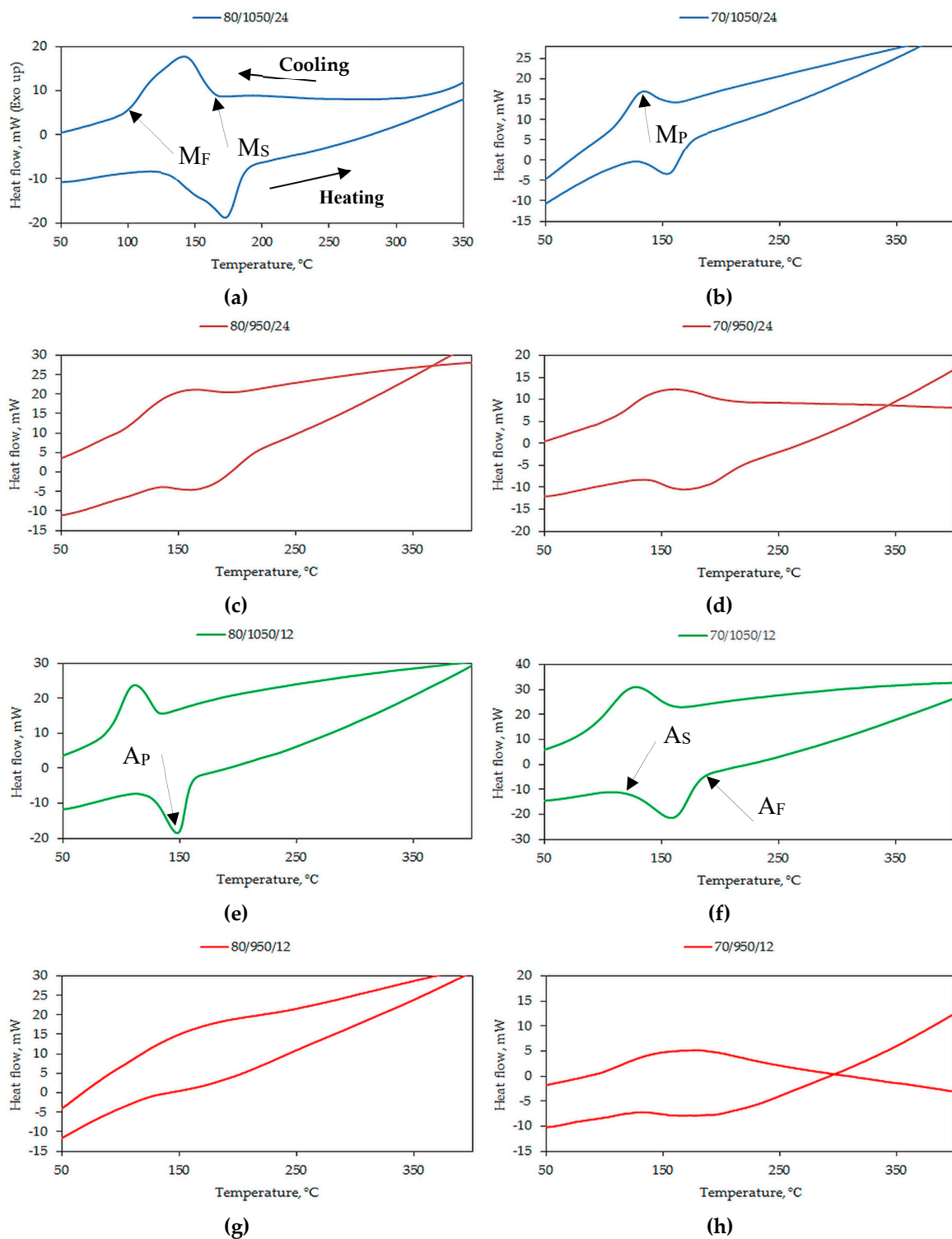


Figure 6. DSC curves of: (a) S1050b2; (b) S1050a2; (c) S950b2; (d) S950a2; (e) S1050b1; (f) S1050a1; (g) S950b1; and (h) S950a1.

Exothermic peaks corresponding to austenite–martensite transformation (cooling) and endothermic peaks corresponding to a reverse martensite–austenite transformation (heating) seen on the DSC curves indicate the occurrence of forward and reverse martensitic transformation, while the absence of peaks is not indicative of martensitic transformation. The effects of temperature and time on the phase transformations are to be examined. A sintering temperature of 950 °C resulted in an

incomplete martensitic transformation in which the transformation and hysteresis temperatures could not be decisively determined. This can be seen in samples S950a1 and S950b1 in Figure 6h,g, respectively, wherein the sintering duration of 12 h also does not favor a complete transformation sequence. On the contrary, both forward and reverse martensitic transformation sequences are discerned in samples S950b2 and S9502 in Figure 6c,d, sintered at 950 °C for 24 h. The transformation and hysteresis temperatures determined for these samples appear to be an aberration as the peaks are not sharp and narrow. It is conjectured that even a longer sintering duration at an insufficient sintering temperature could result in an inhomogeneity or, more likely, the incomplete synthesis of phases with large changes in the stoichiometry. Martensitic transformation is dependent on the composition and thermal events associated with it increase in sharpness and intensity upon additional annealing [35]. Quenching after annealing completes the formation of martensite. It can be seen that fast heating/cooling freezes the calorimetric response of the samples in terms of both the transition temperature and enthalpies [36].

In samples S1050a1 and S1050b1, compacted at different pressures but sintered at 1050 °C and 12 h, the transformation temperatures are 103 °C and 107 °C, respectively. These are seen in Figure 6f,e. The temperatures are lower than 125 °C, obtained for the cast alloy [15]. In samples S1050b2 and S1050a2, seen in Figure 6a,b, the transformation temperatures are not very different from those reported in [12,15], because the sintering time for these samples was 24 h. Sintering temperature and duration of sintering are important. Figure 7 shows the DSC curves of samples S1050a3 and S1050a4. It can be seen that these samples record no martensitic transformation. The lack of martensitic transformation is due to the formation of other phases, which are explained in detail in the next section.

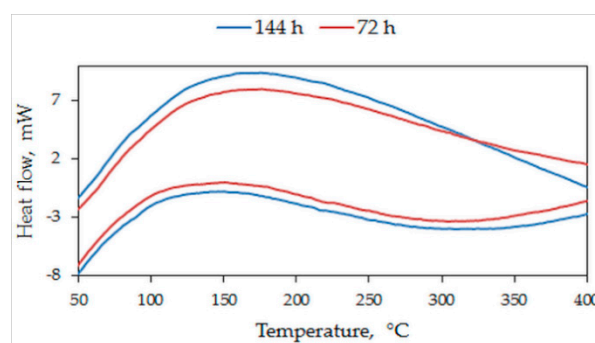


Figure 7. DSC curves of: Samples S1050a3 and S1050a4.

3.3. Microstructure Analysis

Figure 8a shows the BSE micrograph of alloy S1050a1 and Figure 8b shows that of alloy S1050a2. Both structures show martensitic grains with “lath” structures clearly seen. The average grain size determined by the intercept method is 13.95 μm and 10.97 μm , respectively. The structures are predominantly single phase, labelled as martensite. However, in S1050a2, additional dark gray regions are seen. S1050b1 has martensitic and non-martensitic regions with an average grain size of 14.57 μm , seen in Figure 8c, while S1050b2, seen in Figure 8d, has a similar microstructure to S1050a2, with an average grain size of 8.28 μm . The decrease in grain size with increasing sintering time does not go with the well-accepted concept that further diffusion will bring about coarsening, i.e., larger grain size. As will be discussed later, this is due to reactions at the grain boundaries, which tend to consume part of the grains, resulting in reduction of grain size, in contradiction to popular belief. Martensitic and non-martensitic regions, along with the dark gray phases, are identified on the micrographs. The compositions of the phases seen in Figure 8 are presented in Table 4. The composition of the dark gray region in all samples shows an increased Co content and only traces of Sn. These dark gray regions with excess Co are identified as γ -phase and the non-martensitic regions are identified as $L2_1$ /martensite, in accordance with literature [20]. The non-martensitic phase is actually the $L2_1$ austenite, which transforms to martensite upon cooling. From Table 4, it can be seen that the compositions of martensitic and non-martensitic regions are nearly similar.

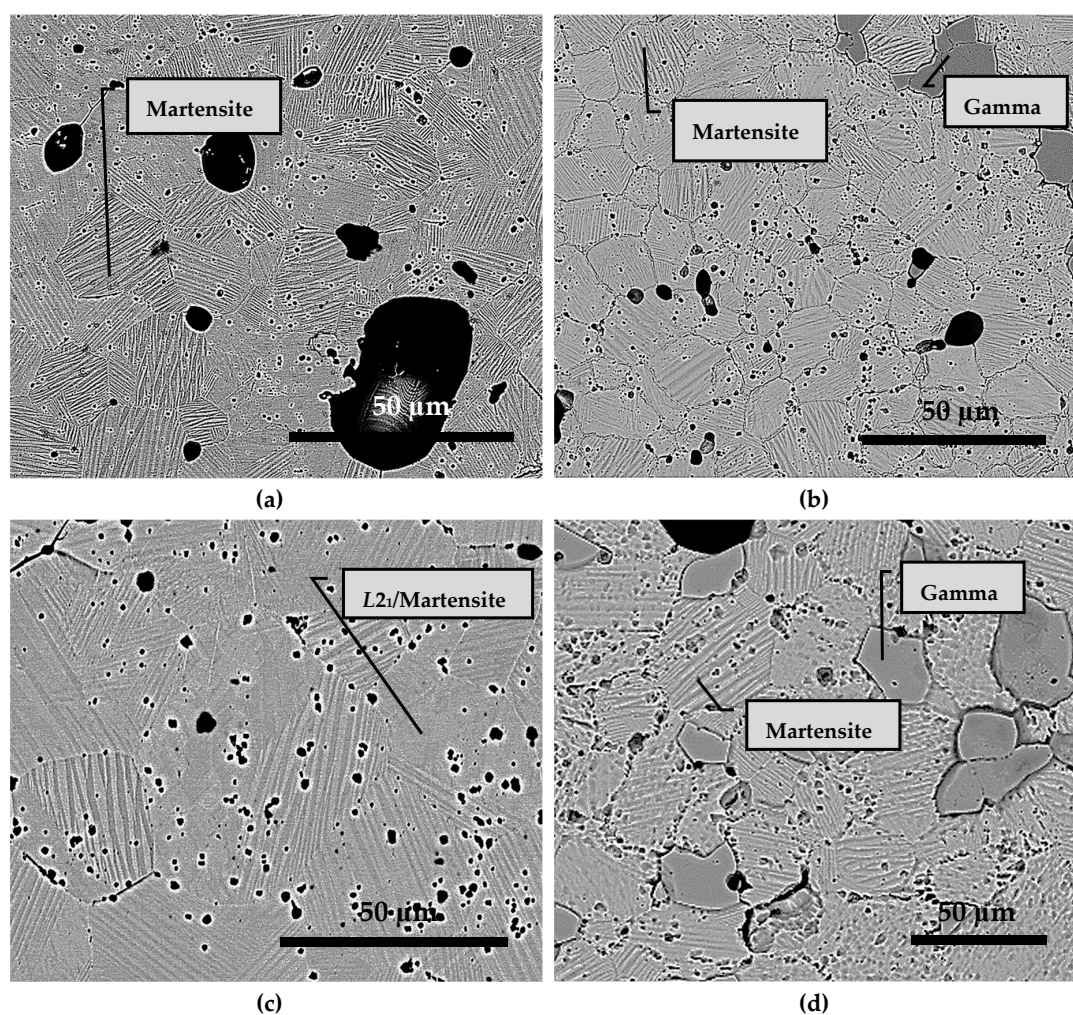


Figure 8. BSE micrographs of $\text{Ni}_{45}\text{Co}_5\text{Mn}_{40}\text{Sn}_{10}$ alloy: (a) S1050a1; (b) S1050a2; (c) S1050b1; and (d) S1050b2.

Table 4. Transformation and hysteresis temperatures obtained from differential scanning calorimetry (DSC).

Sample ID	A_S (°C)	A_F (°C)	A_P (°C)	M_S (°C)	M_F (°C)	M_P (°C)	$(A_S + M_F)/2$ (°C)	$(A_F - M_S)$ (°C)	$\Delta H/\text{Jg}^{-1}$	
									Heat	Cool
S950a1	135	—	—	—	103	—	—	—	—	—
S950a2	140	215	175	210	105	156	123	5	20.08	33.75
S1050a1	120	182	160	155	85	125	103	27	26.45	25.60
S1050a2	130	175	157	158	109	135	120	17	12.75	13.89
S950b1	132	—	—	—	—	—	—	—	—	—
S950b2	130	220	170	205	100	155	115	15	19.42	22.66
S1050b1	125	160	148	132	88	112	107	28	22.27	19.56
S1050b2	130	187	174	168	100	140	115	19	32.17	34.29
S1050a3	—	—	—	—	—	—	—	—	—	—
S1050a4	—	—	—	—	—	—	—	—	—	—

Figure 9 shows the back scattered electron (BSE) micrograph of S1050a3 alloy and the EDS spectra of different regions in it. Figure 10 shows the micrograph of S1050b4 alloy along with the EDS spectra. The compositions of the phases represented by the regions are included in Table 5. Of identical regions, the compositions are fairly uniform. The microstructures can be seen to resemble a cast structure when melting and solidification takes place. In addition to non-martensitic light gray cells, the inter-cell structure comprises three regions—martensitic structure having a faint lath morphology, predominantly forming at the periphery of the inter-cell region, light gray of a similar feature to that

of cells, and dark gray regions having a bulky morphology. It is seen from Figures 9 and 10 that the light gray phase within the inter-cell regions is transformed to bulky dark gray phase. In S1050a2 and S1050b2 samples, sintered for 24 h, the presence of dark gray phase is less and the microstructures resemble a predominantly martensitic structure, as seen in Figure 8b,d respectively. In samples S1050a3 and S1050b4, sintered for 72h and 144 h, the dark gray regions identified as γ -phase earlier are present in large measure, as seen from Figures 9 and 10 and also from Figure 5a,b. The compositions of the phases are included in Table 6. The volume fraction of the γ -phase is more in S1050b4 when compared to S1050a3, which means that increased amounts of γ -phase have stabilized at 144 h of sintering. This is because phases with excess Co stabilize at higher temperatures beyond 950 °C [20]. Thus, with dark gray regions stabilizing in the phase boundaries, relegation of martensite to the boundaries by the light regions occurs because the γ -phase acts as a heat sink for the martensite, which usually forms through a shear and diffusionless mechanism during quenching. The alloys being furnace-cooled underwent an incomplete martensitic transformation with the martensite confined only to the boundary region adjoining the γ -phase. This, together with the formation of the γ -phase, accounts for the absence of distinct martensitic transformation peaks in the DSC graphs.

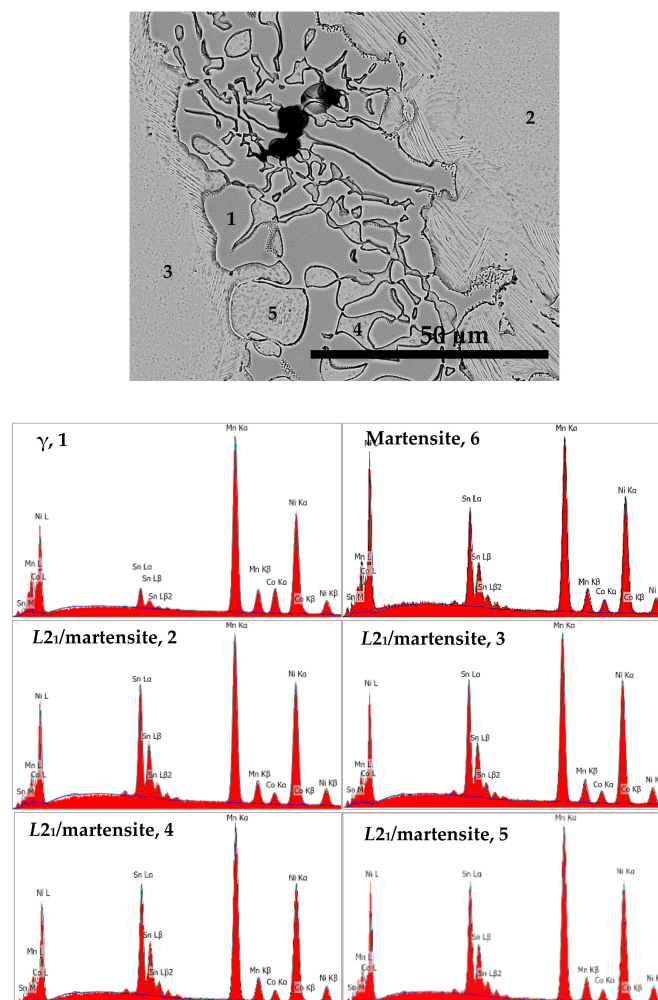


Figure 9. BSE micrograph and EDS spectra of different regions seen in S1050a3.

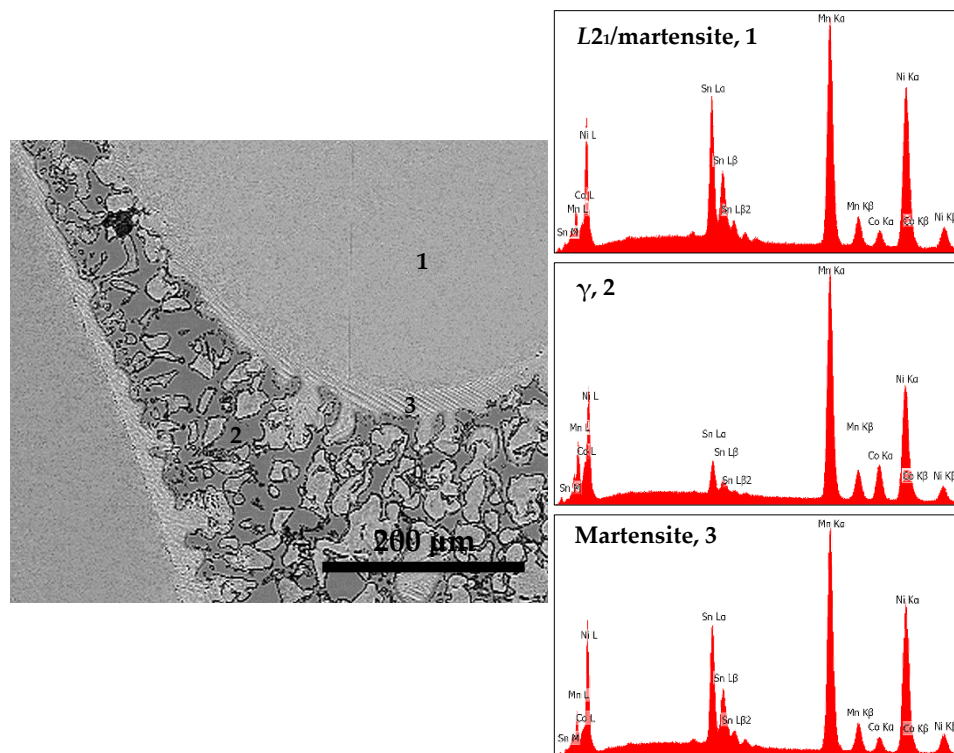


Figure 10. BSE micrograph and EDS spectra of different regions seen in S1050b4.

Table 5. Composition of regions in the microstructures of the S1050a1, S1050a2, S1050b1, and S1050b2.

Sample ID	Ni (at %)	Mn (at %)	Co (at %)	Sn (at %)	Total	In Figure
S1050a1	45.2	40.8	5.1	8.9	100.0	8a: Martensite
S1050a2	45.6	40.4	5.4	8.7	100.0	8b: Martensite
S1050a2	44.9	41.9	11.1	2.1	100.0	8b: γ -phase
S1050b1	45.0	41.7	5.1	8.2	100.0	8c: Martensite
S1050b1	45.5	41.1	4.6	8.8	100.0	8c: Non-martensite
S1050b2	45.0	41.0	5.1	8.9	100.0	8d: Martensite
S1050b2	42.3	45.2	11.3	1.2	100.0	8d: γ -phase

Table 6. Composition of regions in the microstructures of the S1050a3 and S1050b4.

Sample ID	Ni (at %)	Mn (at %)	Co (at %)	Sn (at %)	Total	In Figure
S1050a3	46.0	40.2	4.4	9.4	100.0	9: Martensite, 6
S1050a3	44.6	43.7	9.6	2.1	100.0	9: γ -phase, 1
S1050a3	46.9	38.3	3.9	10.9	100.0	9: L_{21} /martensite, 2
S1050a3	46.9	38.1	4.0	11.0	100.0	9: L_{21} /martensite, 3
S1050a3	45.9	40.0	3.7	10.4	100.0	9: L_{21} /martensite, 4
S1050a3	45.7	39.6	4.0	10.7	100.0	9: L_{21} /martensite, 5
S1050b4	46.6	39.2	4.5	9.7	100.0	10: L_{21} /martensite, 1
S1050b4	40.3	45.4	11.6	2.7	100.0	10: γ -phase, 2
S1050b4	45.9	40.9	4.6	8.6	100.0	10: Martensite, 3

Shown in Figure 11 is the microstructure of S1050a4 at high magnification. This sample is sintered for 144 h. A lamellar structure can be seen within the γ -phase (dark gray regions) at the grain boundaries. The composition of lamellae alternately corresponds to L_{21} /martensite (light gray) and γ -phase (dark gray) regions. This is akin to a eutectoid L_{21} and γ -phase precipitating from D_{03} phase in a solid state [20]. The D_{03} phase has higher Sn content, while in S1050a4, no such phase is seen. From the microstructure shown in Figure 11, it can be deduced that the non-martensitic light gray region, since D_{03} is absent, formed the eutectoid structure. Another characteristic of Heusler alloys is that a $B2$ – L_{21} order–disorder transition occurs at around 500–800 °C, however the compositions of

the alloys in [20] do not favor such a transition. Therefore, the B2–L2₁ order-disorder transition is not a characteristic in the powder processed alloys being discussed in this work.

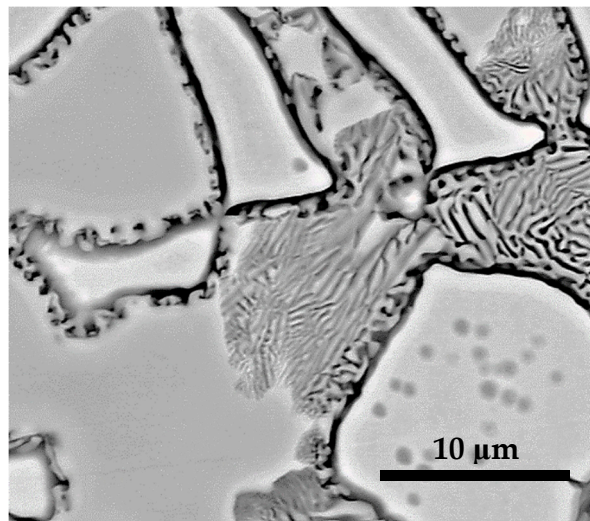


Figure 11. BSE micrographs of S1050a4 higher magnification.

From the composition map of alloy S1050a3 shown in Figure 12b, it can be seen that 63% of the area is light region (red) and 36% contains the dark region (γ -phase), light region, and the eutectoid region (blue). Sample S1050b4, sintered at 144 h, also exhibited around 62% of light region and 37% of light, dark, and eutectoid regions (not shown). Figure 13a shows the BSE micrograph of alloy S1050a3. This also has large light grey regions relegating the martensitic and dark grey regions to and in between the grain boundaries.

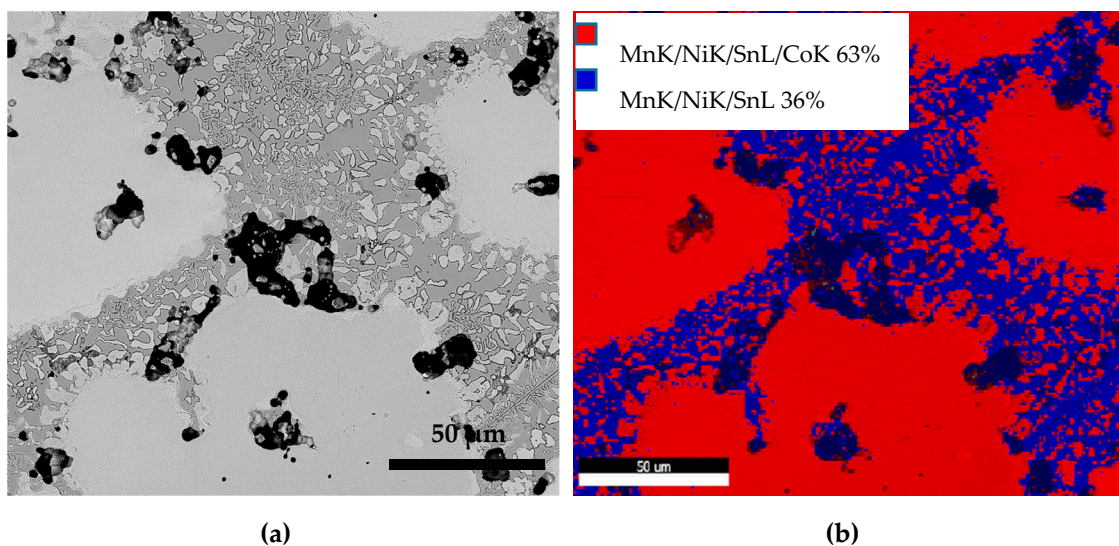


Figure 12. (a) BSE micrograph of S1050a3 and (b) compositional map of the microstructure.

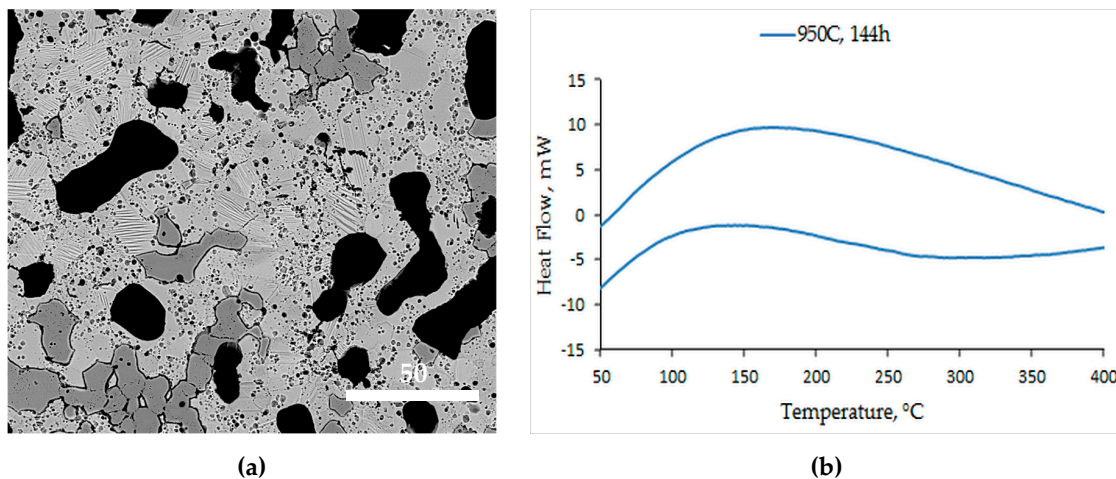


Figure 13. (a) BSE micrograph of S950b4 and (b) DSC curve of S950b4.

The microstructure of alloy S950b4 is shown in Figure 13a. Seen in this microstructure are martensitic, non-martensitic, and dark gray regions, as in any other alloy. The average grain size is 6.95 μm . While the martensitic lath structures are as in S1050a2 and S1050b2, the presence of pores and γ -regions is fairly appreciable. The DSC (Figure 13b) of this alloy does not clearly define any phase transformation, even though the microstructure exhibits martensite. This is because both the structural and compositional homogeneity are not attained in the alloy, in spite of having been sintered for 144 h at 950 $^{\circ}\text{C}$.

Figure 14a,b shows the room temperature diffraction patterns of the quaternary samples S1050a2 and S1050a1, sintered at 24 h and 12 h, respectively. The inset in Figure 14b shows 2 theta values from 40 to 45 degrees. The spectrum in Figure 14a was indexed to Heusler $L2_1$ (space group $Fm\bar{3}m$) in addition to a single peak indexed to monoclinic (6M) phase (space group $C12/m1$), typed in red. The spectrum in Figure 14b was indexed to Heusler $L2_1$ (space group $Fm\bar{3}m$, lattice parameter $a = 6.0250 \text{ \AA}$) and monoclinic (6M) phases (space group $C12/m1$, lattice parameters: $a = 12.2000 \text{ \AA}$, $b = 4.0550 \text{ \AA}$, $c = 5.2150 \text{ \AA}$, $\beta = 105.03^{\circ}$). Monoclinic reflections are typed in red letters. The coexistence of austenite and martensite in the as-cast $\text{Ni}_{50}\text{Mn}_{37}\text{Sn}_{13}$ alloys has been reported [37]. The room temperature XRD patterns of alloy S1050b4, S1050a3, S950b4, and S950b3 are shown in Figure 15. They point to the presence of austenite/ $L2_1$ phase (light gray regions in all microstructures) and γ -phase (dark gray), denoted by (220). The γ -phase is seen in all the samples. S950b4 shows the structure is largely six-layered martensite, coexistent with austenite. Additionally, there is a weak reflection, specific to $D0_3$ phase, which is absent in samples sintered at 1050 $^{\circ}\text{C}$.

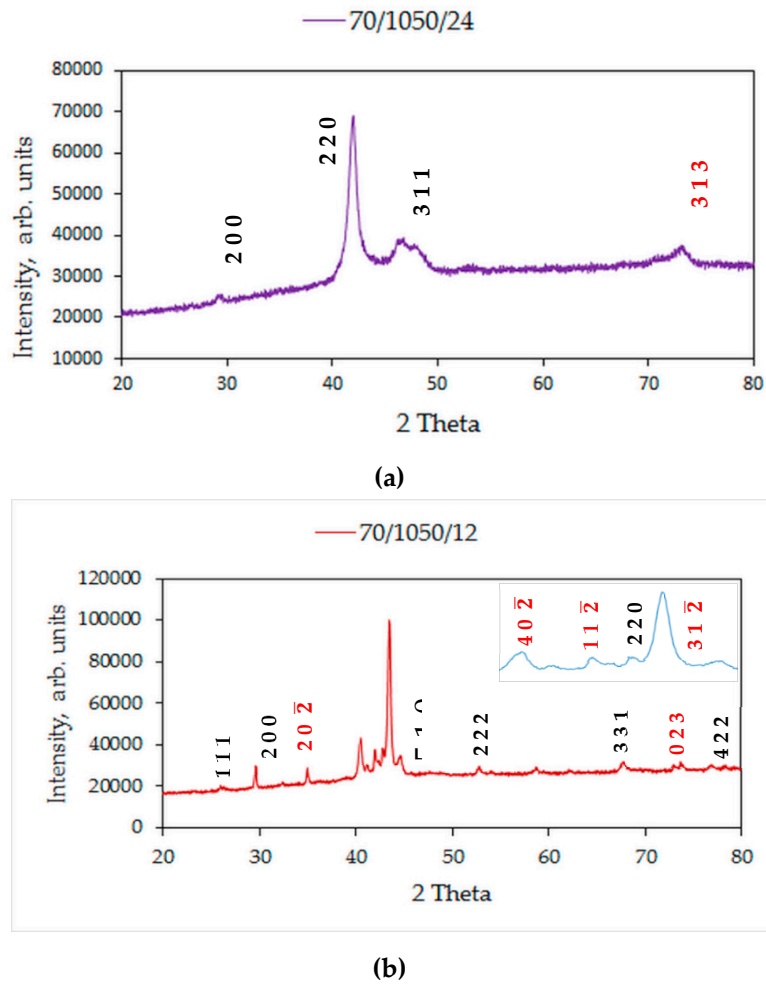


Figure 14. XRD patterns of: (a) S1050a2 and (b) S1050a1.

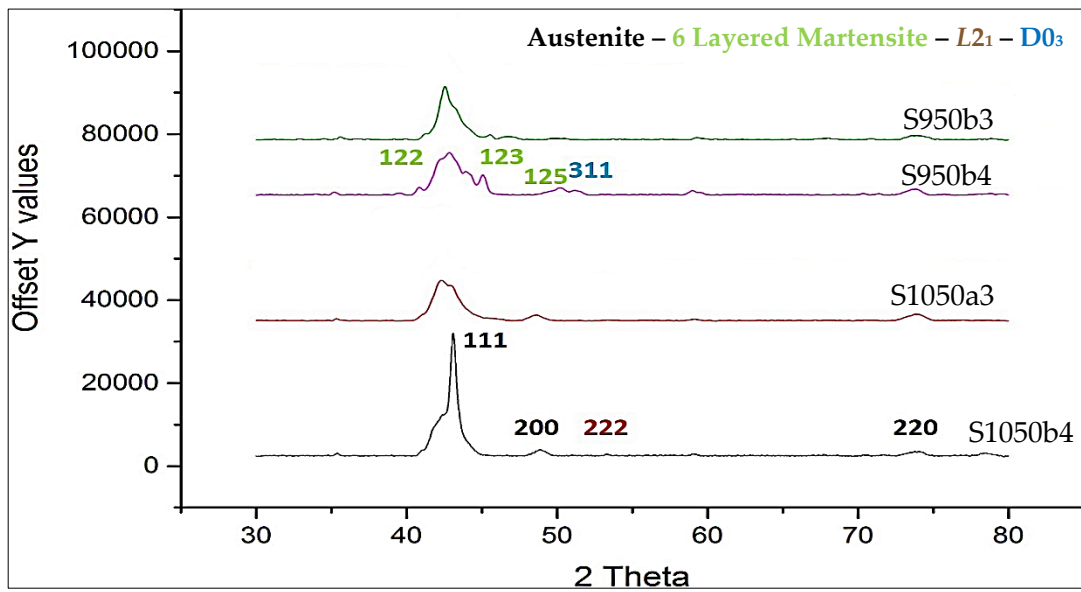


Figure 15. XRD patterns of S1050b4, S1050a3, S950b4, and S950b3.

3.4. Magnetization Measurements

Figure 16a,b shows the M–H curves of samples S1050b4 and S1050b3, sintered at 1050 °C for 144 h and 72 h, respectively. The measurements were carried out at room temperature. The magnetic parameters determined from the measurements are shown in Table 7, including S950b4 (M–H curve not shown). All the samples tested for magnetization are soft magnets, seen from the low values of remanence, coercivity, and squareness.

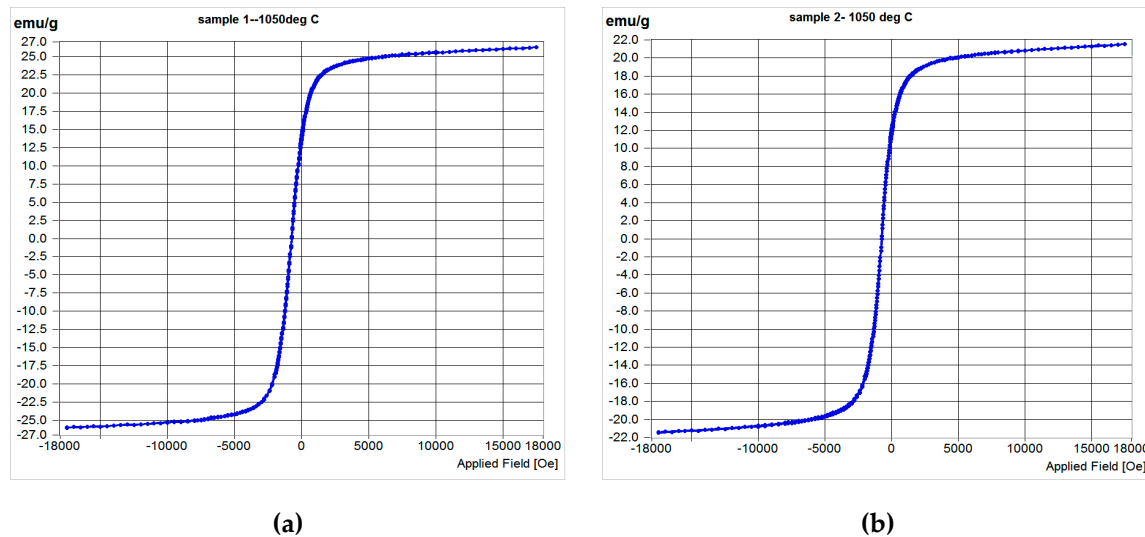


Figure 16. M–H curves of samples: (a) S1050b4; (b) S1050b3.

Table 7. Magnetic parameters of samples S1050b4 and S1050b3.

Sample	Coercivity, H _C Oe	Remanence, M _R emu/g	Saturation magnetization, M _S emu/g	Squareness, M _R /M _S
S1050b4	4.64	0.09654	26.148	0.532
S1050b3	6.596	0.12719	21.483	0.552
S950b4	7.623	0.1566	12.34	0.593

4. Conclusions

The effects of the sintering parameters on the transformation characteristics and microstructure of a Ni₄₅Co₅Mn₄₀Sn₁₀ alloy synthesized using pressureless powder metallurgy were studied. The findings are summarized as follows:

1. Synthesis of Ni–Co–Mn–Sn Heusler alloys by powder processing using elemental powders is feasible;
2. The effect of compaction pressure on the magnetostructural characteristics is not as significant;
3. A higher sintering temperature of 1050 °C enables adequate sintering to occur, demonstrated by the decrease of the porosity and the increase of hardness;
4. Sintering at 1050 °C results in a predominantly single phase L₂₁ structure and a small fraction of γ-phase. At a lesser duration of 12/24 h, the γ-phase is less and at a higher duration of 72/144 h, it stabilizes to around 36% of the alloy composition;
5. At 72/144 h, the L₂₁ solidified again into L₂₁ and γ-phase in a eutectoid process;
6. A slightly lower process temperature of 950 °C did not ensure adequate diffusion and sintering and, consequently, no martensitic transformation, essential for magnetostructural applications. However, after 144 h, the microstructure had clear martensitic grains with grain refinement. Still, no martensitic transformation was recorded, due to the persistence of inhomogeneity;

7. A processing condition of 1050 °C/24 h is favorable for synthesizing ferromagnetic Ni–Co–Mn–Sn alloys. A secondary thermomechanical procedure is necessary for the elimination of the γ -phase that masks magnetostructural behaviour.

Author Contributions: Supervision, R.G., Z.X., and L.C.; Writing—original draft, R.A.

Funding: This research received no external funding.

Acknowledgments: The authors are grateful to Adelaide Microscopy for SEM & EPMA analysis. They are also grateful to Ashish Garg and Nitin Kumar Sharma, IIT Kanpur, India, for the XRD and magnetization test results. Zonghan Xie acknowledges the support from the Australian Research Council Discovery projects.

Conflicts of Interest: The authors declare no conflict of interest.

References

1. Srivastava, V.; Bhatti, K.P. Ferromagnetic shape memory Heusler alloys. In *Ferroids and Multiferroids*; Hardev, S.V., Kleeman, W., Eds.; Trans Tech Publications Ltd.: Pfaffikon, Switzerland, 2012; Volume 189, pp. 189–208.
2. Planes, A.; Mañosa, L.; Acet, M. Magnetocaloric effect and its relation to shape-memory properties in ferromagnetic Heusler alloys. *J. Phys. Condens. Matter* **2009**, *21*, 233201. [[CrossRef](#)] [[PubMed](#)]
3. Krenke, T.; Aksoy, S.; Duman, E.; Acet, M.; Moya, X.; Manosa, L.; Planes, A. Hysteresis effects in the magnetic-field-induced reverse martensitic transition in magnetic shape-memory alloys. *J. Appl. Phys.* **2010**, *108*, 043914. [[CrossRef](#)]
4. Ullakko, K.; Huang, J.K.; Kantner, C.; O’Handley, R.C.; Kokorin, V.V. Large magnetic-field-induced strains in Ni₂MnGa single crystals. *Appl. Phys. Lett.* **1996**, *69*, 1965–1968. [[CrossRef](#)]
5. Huang, L.; Cong, D.Y.; Ma, L.; Nie, Z.H.; Wang, M.G.; Wang, Z.L.; Suo, H.L.; Ren, Y.; Wang, Y.D. Large magnetic entropy change and magnetoresistance in a Ni₄₁Co₉Mn₄₀Sn₁₀ magnetic shape memory alloy. *J. Alloy Compd.* **2015**, *647*, 1081–1085. [[CrossRef](#)]
6. Krenke, T.; Duman, E.; Acet, M.; Wassermann, E.F.; Moya, X.; Manosa, L.; Planes, A. Inverse magnetocaloric effect in ferromagnetic Ni–Mn–Sn alloys. *Nat. Mater.* **2005**, *4*, 450–454. [[CrossRef](#)] [[PubMed](#)]
7. Moya, X.; Manosa, L.; Planes, A.; Krenke, T.; Duman, E.; Wassermann, E.F. Calorimetric study of the inverse magnetocaloric effect in ferromagnetic Ni–Mn–Sn. *J. Magn. Magn. Mater.* **2007**, *316*, e572–e574. [[CrossRef](#)]
8. Pérez-Sierra, A.M.; Bruno, N.M.; Pons, J.; Cesari, E.; Karaman, I. Atomic order and martensitic transformation entropy change in Ni–Co–Mn–In metamagnetic shape memory alloys. *Scr. Mater.* **2016**, *110*, 61–64. [[CrossRef](#)]
9. Barandiaran, J.M.; Chernenko, V.A.; Lazpita, P.; Gutierrez, J.; Feuchtwanger, J. Effect of martensitic transformation and magnetic field on transport properties of Ni–Mn–Ga and Ni–Fe–Ga Heusler alloys. *Phys. Rev. B* **2009**, *80*, 104404. [[CrossRef](#)]
10. Koyama, K.; Okamoto, S.; Watanabe, T.; Kanomata, T.; Kainuma, R.; Ito, W.; Oikawa, K.; Ishida, K. Observation of large magnetoresistance of magnetic Heusler alloy Ni₅₀Mn₃₆Sn₁₄ in high magnetic fields. *Appl. Phys. Lett.* **2006**, *89*, 182510. [[CrossRef](#)]
11. Sanchez, T.; Sato Turtelli, R.; Grossinger, R.; Sanchez, M.L.; Santos, J.D.; Rosa, W.O.; Prida, V.M.; Escoda, L.; Sunol, J.J.; Koledov, V.; et al. Exchange bias behavior in Ni_{50.0}Mn_{35.5}In_{14.5} ribbons annealed at different temperatures. *J. Magn. Magn. Mater.* **2012**, *324*, 3535–3537. [[CrossRef](#)]
12. Srivastava, V.; Chen, X.; James, R.D. Hysteresis and unusual magnetic properties in the singular Heusler alloy Ni₄₅Co₅Mn₄₀Sn₁₀. *Appl. Phys. Lett.* **2010**, *97*, 014101. [[CrossRef](#)]
13. Sutou, Y.; Imano, Y.; Koeda, N.; Omori, T.; Kainuma, R.; Ishida, K.; Oikawa, K. Magnetic and martensitic transformations of NiMnX (X = In, Sn, Sb) ferromagnetic shape memory alloys. *Appl. Phys. Lett.* **2004**, *85*, 4358–4360. [[CrossRef](#)]
14. Kainuma, R.; Imano, Y.; Ito, W.; Sutou, Y.; Morito, H.; Okamoto, S.; Kitakami, O.; Oikawa, K.; Fujita, A.; Kanomata, T.; et al. Magnetic-field-induced shape recovery by reverse phase transformation. *Nature* **2006**, *439*, 957–960. [[CrossRef](#)] [[PubMed](#)]
15. Srivastava, V.; Song, Y.; Bhatti, K.; James, R.D. The direct conversion of heat to electricity using multiferroic alloys. *Adv. Energy Mater.* **2011**, *1*, 97–104. [[CrossRef](#)]
16. Schlagel, D.L.; McCallum, R.W.; Lograsso, T.A. Influence of solidification microstructure on the magnetic properties of Ni–Mn–Sn Heusler alloys. *J. Alloy Compd.* **2008**, *463*, 38–46. [[CrossRef](#)]

17. Krenke, T.; Acet, M.; Wasserman, E.F.; Moya, X.; Manosa, L.; Planes, A. Martensitic transitions and nature of ferromagnetism in the austenitic and martensitic states of Ni-Mn-Sn alloys. *Phys. Rev. B* **2005**, *72*. [[CrossRef](#)]
18. Lázpita, P.; Sasmaz, M.; Cesari, E.; Barandiarán, J.M.; Gutiérrez, J.; Chernenko, V.A. Martensitic transformation and magnetic field induced effects in Ni₄₂Co₈Mn₃₉Sn₁₁ metamagnetic shape memory alloy. *Acta Mater.* **2016**, *109*, 170–176. [[CrossRef](#)]
19. Çakır, A.; Righi, L.; Albertini, F.; Acet, M.; Farle, M. Intermartensitic transitions and phase stability in Ni₅₀Mn_{50-x}Sn_x Heusler alloys. *Acta Mater.* **2015**, *99*, 140–149. [[CrossRef](#)]
20. Pérez-Sierra, A.M.; Pons, J.; Santamarta, R.; Vermaut, P.; Ochín, P. Solidification process and effect of thermal treatments on Ni-Co-Mn-Sn metamagnetic shape memory alloys. *Acta Mater.* **2015**, *93*, 164–174. [[CrossRef](#)]
21. Graf, T.; Felser, C.; Parkin, S.S.P. Simple rules for the understanding of Heusler compounds. *Prog. Solid State Chem.* **2011**, *39*, 1–50. [[CrossRef](#)]
22. Chen, X.; Naik, V.B.; Mahendiran, R.; Ramanujan, R.V. Optimization of Ni-Co-Mn-Sn Heusler alloy composition for near room temperature magnetic cooling. *J. Alloy Compd.* **2014**, *618*, 187–191. [[CrossRef](#)]
23. Bruno, N.M.; Yegin, C.; Karaman, I.; Chen, J.-H.; Ross, J.H.; Liu, J.; Li, J. The effect of heat treatments on Ni₄₃Mn₄₂Co₄Sn₁₁ meta-magnetic shape memory alloys for magnetic refrigeration. *Acta Mater.* **2014**, *74*, 66–84. [[CrossRef](#)]
24. Das, R.; Saravanan, P.; Arvindha Babu, D.; Perumal, A.; Srinivasan, A. Influence of solidification rate and heat treatment on magnetic refrigerant properties of melt spun Ni₅₁Mn₃₄In₁₄Si₁ ribbons. *J. Magn. Magn. Mater.* **2013**, *344*, 152–157. [[CrossRef](#)]
25. Sanchez Llamazares, J.L.; Sanchez, T.; Santos, J.D.; Prez, M.J.; Sanchez, M.L.; Hernando, B.; Escoda, L.; Sunol, J.J.; Varga, R. Martensitic phase transformation in rapidly solidified Mn₅₀Ni₄₀In₁₀ alloy ribbons. *Appl. Phys. Lett.* **2008**, *92*, 012513. [[CrossRef](#)]
26. Rajkumar, D.M.; Rao, N.V.R.; Muthu, S.E.; Arumugam, S.; Raja, M.M.; Suresh, K.G. Effect of Fe on the Martensitic Transition, Magnetic and Magnetocaloric Properties in Ni-Mn-In Melt-spun Ribbons. *Def. Sci. J.* **2016**, *66*, 403–412. [[CrossRef](#)]
27. Ma, S.C.; Shih, C.W.; Liu, J.; Yuan, J.H.; Lee, S.Y.; Lee, Y.I.; Chang, H.W.; Chang, W.C. Wheel speed-dependent martensitic transformation and magnetocaloric effect in Ni-Co-Mn-Sn ferromagnetic shape memory alloy ribbons. *Acta Mater.* **2015**, *90*, 292–302. [[CrossRef](#)]
28. Chen, F.; Tong, Y.X.; Li, L.; Sánchez Llamazares, J.L.; Sánchez-Valdés, C.F.; Müllner, P. The effect of step-like martensitic transformation on the magnetic entropy change of Ni_{40.6}Co_{8.5}Mn_{40.9}Sn₁₀ unidirectional crystal grown with the Bridgman-Stockbarger technique. *J. Alloy Compd.* **2017**, *691*, 269–274. [[CrossRef](#)]
29. Laudise, R.A.; Sunder, W.A.; O'Bryan, H.M.; Carlson, D.J.; Witt, A.F. Czochralski growth of single crystals of Ni_{3-x}Mn_xSn. *J. Cryst. Growth* **1992**, *118*, 277–286. [[CrossRef](#)]
30. Ito, K.; Ito, W.; Umetsu, R.Y.; Tajima, S.; Kawaura, H.; Kainuma, R.; Ishida, K. Metamagnetic shape memory effect in polycrystalline NiCoMnSn alloy fabricated by spark plasma sintering. *Scr. Mater.* **2009**, *61*, 504–507. [[CrossRef](#)]
31. Ito, K.; Ito, W.; Umetsu, R.Y.; Karaman, I.; Ishida, K.; Kainuma, R. Mechanical and shape memory properties of Ni₄₃Co₇Mn₃₉Sn₁₁ alloy compacts fabricated by pressureless sintering. *Scr. Mater.* **2010**, *63*, 1236–1239. [[CrossRef](#)]
32. Ito, K.; Ito, W.; Umetsu, R.Y.; Nagasako, M.; Kainuma, R.; Fujita, A.; Oikawa, K.; Ishida, K. Martensitic transformation in NiCoMnSn metamagnetic shape memory alloy powders. *Mater. Trans.* **2008**, *49*, 1915–1918. [[CrossRef](#)]
33. Monroe, J.A.; Cruz-Perez, J.; Yegin, C.; Karaman, I.; Geltmacher, A.B.; Everett, R.K.; Kainuma, R. Magnetic response of porous NiCoMnSn metamagnetic shape memory alloys fabricated using solid-state replication. *Scr. Mater.* **2012**, *67*, 116–119. [[CrossRef](#)]
34. Ahamed, R.; Ghomashchi, R.; Xie, Z.; Chen, L.; Munroe, P.; Xu, S. Powder processing and characterisation of a quinary Ni-Mn-Co-Sn-Cu Heusler alloy. *Powder Technol.* **2018**, *324*, 69–75. [[CrossRef](#)]
35. Yuhasz, W.M.; Schlagel, D.L.; Xing, Q.; Dennis, K.W.; McCallum, R.W.; Lograsso, T.A. Influence of annealing and phase decomposition on the magnetostructural transitions in Ni₅₀Mn₃₉Sn₁₁. *J. Appl. Phys.* **2009**, *105*, 07A921. [[CrossRef](#)]

36. Nespoli, A.; Biffi, C.A.; Villa, E.; Tuissi, A. Effect of heating/cooling rate on martensitic transformation of NiMnGa-Co high temperature ferromagnetic shape memory alloys. *J. Alloy Compd.* **2017**, *690*, 478–484. [[CrossRef](#)]
37. Zheng, H.; Wang, W.; Xue, S.; Zhai, Q.; Frenzel, J.; Luo, Z. Composition-dependent crystal structure and martensitic transformation in Heusler Ni-Mn-Sn alloys. *Acta Mater.* **2013**, *61*, 4648–4656. [[CrossRef](#)]



© 2019 by the authors. Licensee MDPI, Basel, Switzerland. This article is an open access article distributed under the terms and conditions of the Creative Commons Attribution (CC BY) license (<http://creativecommons.org/licenses/by/4.0/>).

7 Conclusions

Powder metallurgy synthesis of ferromagnetic quaternary Ni-Co-Mn-Sn and quinary Ni-Co-Mn-(Sn, Cu) Heusler alloys was carried out using elemental powders with the objectives of examining the feasibility of the PM process and the effects of process parameters such as compaction pressure, sintering temperature and sintering duration on the magnetostructural properties of the alloys. The process employed was conventional pressure-less sintering on an important composition with a potential for energy generation from low-heat waste heat, namely the off-stoichiometric $\text{Ni}_{45}\text{Co}_5\text{Mn}_{40}\text{Sn}_{10}$ quaternary Heusler alloy and $\text{Ni}_{45}\text{Co}_5\text{Mn}_{40}(\text{Sn,Cu})_{10}$ quinary alloy. The first conventional sintering experiments were carried out on the quinary alloy at two different temperatures of 950 °C and 1050 °C at two different times of 12 h and 24 h. The alloy was compacted at 184 MPa pressure. Compositional homogeneity was important in these alloys for martensitic transformation and magnetostructural behaviour to occur. In order to attain compositional homogenization extended sintering durations of 72 h and 144 h at the same temperatures were employed during the second experiments on the quaternary alloy in addition to 12 and 24 h. The usual characterization procedures detailed in Chapter 4 for these kinds of alloys were carried out. The findings are summarised as follows:

Quinary alloy:

- Of the two temperatures selected for synthesis, 950 °C did not cause satisfactory sintering. The composition was not homogeneous, the microstructure reflected greater porosity and martensitic transformation did not occur as seen from the DSC analysis.

- The second temperature of 1050 °C favoured satisfactory sintering showing decreased porosity and increased hardness. The microstructure resembled a cast microstructure with a more uniform distribution of the constituent elements and a fairly rich room temperature martensitic structure. The presence of second phase such as γ -phase was minimal.
- A processing condition of 1050 °C/24 h yielded good results in terms of magnetostructural transformation and behaviour. At this processing condition the quinary alloy exhibited a 6M modulated martensite at room temperature.
- The presence of Cu in the quinary alloy shifted the transformation temperatures to a higher value compared to the cast alloy. In Heusler alloys of this type the addition of Cu increases or decreases the transformation temperatures depending on whether it substitutes Mn or Ni respectively.
- Paramagnetic to ferromagnetic transition occurred in this alloy at around 360 K under an applied magnetic field of 100 Oe.
- A voltage generation of 0.6 mV at a temperature of 175 °C by sample of thickness 2 mm. The equipment used for custom-built using a neodymium permanent magnet of 70 mm diameter and two copper coils with 4000 and 8000 turns. This demonstrated the efficacy of conventional pressure-less sintering using elemental powders.

Quaternary alloy:

- In quaternary alloys the higher sintering durations at the sintering temperature of 1050 °C resulted in the reduction of porosity. At 24 h the porosity was around 11% and at 144 h the porosity was around 4%.
- From an examination of the microhardness of alloys sintered at 12 h and 24 h at both sintering temperatures, the microhardness was seen to increase with increasing duration. At 950 °C the variation in microhardness was from 140 to 175 HV. At 1050

°C the variation in microhardness was from 260 to 290 HV. This variation was nearly identical for alloys compacted at both the compacting loads indicating that the effect of compaction load is not as significant.

- The microstructures of the alloy samples compacted at both 184 and 210 MPa and sintered at 1050 °C for 12 and 24 h showed a decrease in grain size with increasing sintering time which was in contradiction to the well-accepted concept of coarsening as diffusion progresses with sintering. This is attributed to reactions at the grain boundaries and formation of γ -phase which tend to consume parts of the grains with martensitic structure resulting in reduction of grain size martensitic phase.
- In the case of quaternary alloys sintering at 1050 °C resulted in a predominantly single phase $L2_1$ structure and a small fraction of γ -phase. At lesser duration of 12/24 h the γ -phase is less and at higher duration of 72/144 h the γ -phase stabilizes to higher amounts of the alloy phases concentration.
- The microstructures of alloy samples compacted at both 184 and 210 MPa and sintered at 1050 °C for 72 and 144 h alloys resembled cast alloys with melting and solidification having occurred. Three regions corresponding to as many phases were seen – non-martensitic light gray, martensitic (lath morphology) and dark gray (γ -phase).
- The non-martensitic light gray region related to $L2_1$ /martensite phase which is actually austenite transforming to martensite upon cooling.
- The martensite is seen relegated to the boundaries probably because the alloys were furnace cooled and not cold water quenched. With quenching the martensite forms through a shear and diffusionless mechanism, however in these alloys it formed at the boundaries with the γ -phase which acted as a heat sink.
- In comparison no melting is seen S950b4 alloy sintered at 950 °C for 144 h. The microstructure however has the same three phases of non-martensitic light gray,

martensitic and dark gray regions in addition to enlarged pores. No martensitic transformation is recorded from DSC which meant that the transformation is incomplete.

- DSC analysis of samples compacted at both 184 and 210 MPa and sintered at 1050 °C for 72 and 144 h showed that the martensitic transformation was incomplete with the curves showing no sharp exothermic/endothemic peaks and consequently no minimal thermal hysteresis.
- Room temperature magnetization tests revealed a ferromagnetic phase although it is seen as a soft magnet from the low values of remanence, coercivity and squareness.

7.1 Significance of this study and future work

Significance:

Ferromagnetic Heusler alloys which have not been synthesized through PM route using elemental powders have been fabricated and characterized through PM route using elemental powders. This study thus established the feasibility of employing the press and sinter method of synthesis using elemental powders. Merely stating that the alloys were powder processed is an understatement because this study has opened up enormous opportunities for conducting a whole range of studies on solid processed ferromagnetic Heusler alloys that have been predominantly carried out on liquid processed alloys.

The results and insights gained from this study are vital for the development and application of a new generation of ferromagnetic Heusler alloys via solid processing.

Future work:

Suggestions for future work include elimination of secondary phases which annul magnetostructural behaviour through heat-treatment of as-sintered samples at low

temperatures, and grain refinement through extensive use of pressure-assisted sintering procedures such as vacuum hot pressing and spark plasma sintering and evaluating all the magnetostructural properties such as shape memory, magnetic entropy change, magnetoresistance etc. Many NiMn-based alloys with reportedly remarkable properties could be used for the purpose. Use of powders of differing sizes such as micron, sub-micron and nano on the magnetostructural effects could be investigated. The exact relationship between the modulated structures and the magnetostructural effects could also be investigated by modeling approaches.

8 References

Agrawal, A & Dube, RK 2018, 'Methods of fabricating Cu-Al-Ni shape memory alloys', *Journal of Alloys and Compounds*, vol. 750, pp. 235-247.

Aguilar-Ortiz, CO, Soto-Parra, D, Álvarez-Alonso, P, Lázpita, P, Salazar, D, Castillo-Villa, PO, Flores-Zúñiga, H & Chernenko, VA 2016, 'Influence of Fe doping and magnetic field on martensitic transition in Ni-Mn-Sn melt-spun ribbons', *Acta Materialia*, vol. 107, pp. 9-16.

Ahamed Khan, R, Ghomashchi, R, Xie, Z & Chen, L 2018, 'Ferromagnetic Shape Memory Heusler Materials: Synthesis, Microstructure Characterization and Magnetostructural Properties', *Materials*, vol. 11, no. 6, p. 988.

Ahamed, R, Ghomashchi, R, Xie, Z, Chen, L, Munroe, P & Xu, S 2018, 'Powder processing and characterisation of a quinary Ni-Mn-Co-Sn-Cu Heusler alloy', *Powder Technology*, vol. 324, pp. 69-75.

Aksoy, S, Acet, M, Wassermann, EF, Krenke, T, Moya, X, Manosa, L, Planes, A & P. Deen, P 2009, 'Structural properties and magnetic interactions in martensitic Ni-Mn-Sb alloys', *Philosophical Magazine*, vol. 89, no. 22-24, pp. 2093-2109.

Anandh 2009, 'Vacuum Induction Melting Unit', viewed 30 June 2017, <<http://home.iitk.ac.in/~anandh/lab/Induction%20Melting%20Unit2.pdf>>.

Ashby, M, Shercliff, H & Cebon, D 2007, *Materials : Engineering, Science, Processing and Design*, Elsevier Science & Technology, Oxford, United Kingdom.

Asthana, R, Kumar, A & Dahotre, NB 2006, '3 - Powder Metallurgy and Ceramic Forming', in R Asthana, A Kumar & NB Dahotre (eds), *Materials Processing and Manufacturing Science*, Academic Press, Burlington, pp. 167-245.

Bertheville, B 2005, 'Powder metallurgical processing of ternary Ni₅₀Ti_{50-x}Zr_x (x = 5, 10 at.%) alloys', *Journal of Alloys and Compounds*, vol. 398, no. 1-2, pp. 94-99.

Bhadeshia, HKDH 2001, 'Martensitic Transformation', in Patrick Veysseyre, KHJ Buschow, RW Cahn, MC Flemings, B Ilchner, EJ Kramer & S Mahajan (eds), *Encyclopedia of Materials: Science and Technology (Second Edition)*, Elsevier, Oxford, pp. 5203-5206.

Bruno, NM, Salas, D, Wang, S, Roshchin, IV, Santamarta, R, Arroyave, R, Duong, T, Chumlyakov, YI & Karaman, I 2018, 'On the microstructural origins of martensitic

transformation arrest in a NiCoMnIn magnetic shape memory alloy', *Acta Materialia*, vol. 142, pp. 95-106.

Bruno, NM, Yegin, C, Karaman, I, Chen, J-H, Ross, JH, Liu, J & Li, J 2014, 'The effect of heat treatments on Ni₄₃Mn₄₂Co₄Sn₁₁ meta-magnetic shape memory alloys for magnetic refrigeration', *Acta Materialia*, vol. 74, pp. 66-84.

Caballero-Flores, R, González-Legarreta, L, Rosa, WO, Sánchez, T, Prida, VM, Escoda, L, Suñol, JJ, Batdalov, AB, Aliev, AM, Koledov, VV, Shavrov, VG & Hernando, B 2015, 'Magnetocaloric effect, magnetostructural and magnetic phase transformations in Ni_{50.3}Mn_{36.5}Sn_{13.2} Heusler alloy ribbons', *Journal of Alloys and Compounds*, vol. 629, pp. 332-342.

Cai, W, Feng, Y, Sui, JH, Gao, ZY & Dong, GF 2008, 'Microstructure and martensitic transformation behavior of the Ni₅₀Mn₃₆In₁₄ melt-spun ribbons', *Scripta Materialia*, vol. 58, no. 10, pp. 830-833.

Çakır, A, Righi, L, Albertini, F, Acet, M & Farle, M 2015, 'Intermartensitic transitions and phase stability in Ni₅₀Mn_{50-x}Sn_x Heusler alloys', *Acta Materialia*, vol. 99, pp. 140-149.

Çakır, A, Righi, L, Albertini, F, Acet, M, Farle, M & Aktürk, S 2013, 'Extended investigation of intermartensitic transitions in Ni-Mn-Ga magnetic shape memory alloys: A detailed phase diagram determination', *Journal of Applied Physics*, vol. 114, no. 18, p. 183912.

CAMECA, *Introduction to EPMA*, viewed 26 October 2018, <<https://www.cameca.com/products/epma/technique>>.

Campbell, FC 2012, *Phase Diagrams : Understanding the Basics*, A S M International, Materials Park, United States.

Chen, F, Tong, YX, Huang, YJ, Tian, B, Li, L & Zheng, YF 2013, 'Suppression of gamma phase in Ni₃₈Co₁₂Mn₄₁Sn₉ alloy by melt spinning and its effect on martensitic transformation and magnetic properties', *Intermetallics*, vol. 36, pp. 81-85.

Chen, F, Tong, YX, Li, L, Sánchez Llamazares, JL, Sánchez-Valdés, CF & Müllner, P 2017, 'The effect of step-like martensitic transformation on the magnetic entropy change of Ni_{40.6}Co_{8.5}Mn_{40.9}Sn₁₀ unidirectional crystal grown with the Bridgman-Stockbarger technique', *Journal of Alloys and Compounds*, vol. 691, pp. 269-274.

Chen, X, Naik, VB, Mahendiran, R & Ramanujan, RV 2014, 'Optimization of Ni-Co-Mn-Sn Heusler alloy composition for near room temperature magnetic cooling', *Journal of Alloys and Compounds*, vol. 618, pp. 187-191.

Cong, DY, Huang, L, Hardy, V, Bourgault, D, Sun, XM, Nie, ZH, Wang, MG, Ren, Y, Entel, P & Wang, YD 2018, 'Low-field-actuated giant magnetocaloric effect and excellent mechanical properties in a NiMn-based multiferroic alloy', *Acta Materialia*, vol. 146, pp. 142-151.

Cong, DY, Roth, S & Schultz, L 2012, 'Magnetic properties and structural transformations in Ni-Co-Mn-Sn multifunctional alloys', *Acta Materialia*, vol. 60, no. 13-14, pp. 5335-5351.

Cong, DY, Wang, S, Wang, YD, Ren, Y, Zuo, L & Esling, C 2008, 'Martensitic and magnetic transformation in Ni-Mn-Ga-Co ferromagnetic shape memory alloys', *Materials Science and Engineering A*, vol. 473, no. 1-2, pp. 213-218.

Das, R, Saravanan, P, Arvindha Babu, D, Perumal, A & Srinivasan, A 2013, 'Influence of solidification rate and heat treatment on magnetic refrigerant properties of melt spun Ni₅₁Mn₃₄In₁₄Si₁ ribbons', *Journal of Magnetism and Magnetic Materials*, vol. 344, no. 0, pp. 152-157.

Delville, R, Schryvers, D, Zhang, Z & James, RD 2009, 'Transmission electron microscopy investigation of microstructures in low-hysteresis alloys with special lattice parameters', *Scripta Materialia*, vol. 60, no. 5, pp. 293-296.

Devi, P, Mejía, CS, Zavareh, MG, Dubey, KK, Kushwaha, P, Skourski, Y, Felser, C, Nicklas, M & Singh, S 2019, 'Improved magnetostructural and magnetocaloric reversibility in magnetic Ni-Mn-In shape-memory Heusler alloy by optimizing the geometric compatibility condition', *Physical Review Materials*, vol. 3, no. 6, p. 062401.

Dubenko, I, Quetz, A, Pandey, S, Aryal, A, Eubank, M, Rodionov, I, Prudnikov, V, Granovsky, A, Lahderanta, E, Samanta, T, Saleheen, A, Stadler, S & Ali, N 2015, 'Multifunctional properties related to magnetostructural transitions in ternary and quaternary Heusler alloys', *Journal of Magnetism and Magnetic Materials*, vol. 383, pp. 186-189.

Eerenstein, W, Mathur, ND & Scott, JF 2006, 'Multiferroic and magnetoelectric materials', *Nature*, vol. 442, p. 759.

Famodu, OO, Hattrick-Simpers, J, Aronova, M, Chang, K-S, Murakami, M, Wuttig, M, Okazaki, T, Furuya, Y, Knauss, LA, Bendersky, LA, Biancaniello, FS & Takeuchi, I 2004, 'Combinatorial Investigation of Ferromagnetic Shape-Memory Alloys in the Ni-Mn-Al Ternary System Using a Composition Spread Technique', *Materials Transactions*, vol. 45, no. 2, pp. 173-177.

Franco, V, Bl'azquez, JS, Ingale, B & Conde, A 2012, 'The magnetocaloric effect and magnetic refrigeration near room temperature: materials and models', *Annual Review of Materials Research*, vol. 42, pp. 305-342.

Gao, B, Shen, J, Hu, FX, Wang, J, Sun, JR & Shen, BG 2009, 'Magnetic properties and magnetic entropy change in Heusler alloys $\text{Ni}_{50}\text{Mn}_{35-x}\text{Cu}_x\text{Sn}_{15}$ ', *Applied Physics A*, vol. 97, no. 2, pp. 443-447.

German, RM 2014a, 'Chapter One - Introduction', in RM German (ed.), *Sintering: from Empirical Observations to Scientific Principles*, Butterworth-Heinemann, Boston, pp. 1-12.

German, RM 2014b, 'Chapter Six - Geometric Trajectories during Sintering', in RM German (ed.), *Sintering: from Empirical Observations to Scientific Principles*, Butterworth-Heinemann, Boston, pp. 141-181.

Graf, T, Felser, C & Parkin, SSP 2011, 'Simple rules for the understanding of Heusler compounds', *Progress in Solid State Chemistry*, vol. 39, pp. 1-50.

Gschneidner Jr, KA, Mudryk, Y & Pecharsky, VK 2012, 'On the nature of the magnetocaloric effect of the first-order magnetostructural transition', *Scripta Materialia*, vol. 67, no. 6, pp. 572-577.

Haritha, L, Gangadhar Reddy, G, Ramakanth, A, Ghatak, SK & Nolting, W 2010, 'Interplay of magnetic order and Jahn–Teller distortion in a model with strongly correlated electrons system', *Physica B*, vol. 405, pp. 1701-1705.

Hooshmand Zaferani, S, Ghomashchi, R & Vashae, D 2019, 'Strategies for engineering phonon transport in Heusler thermoelectric compounds', *Renewable and Sustainable Energy Reviews*, vol. 112, pp. 158-169.

Hu, F-x, Shen, B-g & Sun, J-r 2000, 'Magnetic entropy change in $\text{Ni}_{51.5}\text{Mn}_{22.7}\text{Ga}_{25.8}$ alloy', *Applied Physics Letters*, vol. 76, no. 23, pp. 3460-3462.

Huang, L, Cong, DY, Ma, L, Nie, ZH, Wang, MG, Wang, ZL, Suo, HL, Ren, Y & Wang, YD 2015, 'Large magnetic entropy change and magnetoresistance in a $\text{Ni}_{41}\text{Co}_9\text{Mn}_{40}\text{Sn}_{10}$ magnetic shape memory alloy', *Journal of Alloys and Compounds*, vol. 647, pp. 1081-1085.

Huang, L, Cong, DY, Suo, HL & Wang, YD 2014, 'Giant magnetic refrigeration capacity near room temperature in $\text{Ni}_{40}\text{Co}_{10}\text{Mn}_{40}\text{Sn}_{10}$ multifunctional alloy', *Applied Physics Letters*, vol. 104, no. 132407.

Ibarra, A, Rodriguez, PP, Recarte, V, Perez-Landazabal, JI, No, ML & San Juan, J 2004, 'Internal friction behaviour during martensitic transformation in shape memory alloys processed by powder metallurgy', *Materials Science and Engineering A*, vol. 370, no. 1-2, pp. 492-496.

Inoue, K, Enami, K, Yamaguchi, Y, Ohoyama, K, Morii, Y, Matsuoka, Y & Inoue, K 2000, 'Magnetic-field-induced martensitic transformation in Ni₂MnGa-based alloys', *Journal of the Physical Society of Japan*, vol. 69, no. 11, pp. 3485-3488.

Inoue, K, Yamaguchi, Y, Ohoyama, K, Note, R & Enami, K 2002, 'Martensitic and magnetic transformations of Ni₂MnGa-based shape-memory alloys', *Applied Physics A: Materials Science and Processing*, vol. 74, no. SUPPL.II, pp. S1061-S1065.

Ito, K, Ito, W, Umetsu, RY, Karaman, I, Ishida, K & Kainuma, R 2010, 'Mechanical and shape memory properties of Ni₄₃Co₇Mn₃₉Sn₁₁ alloy compacts fabricated by pressureless sintering', *Scripta Materialia*, vol. 63, no. 12, pp. 1236-1239.

Ito, K, Ito, W, Umetsu, RY, Karaman, I, Ishida, K & Kainuma, R 2011, 'Metamagnetic shape memory effect in porous Ni₄₃Co₇Mn₃₉Sn₁₁ alloy compacts fabricated by pressureless sintering', *Materials Transactions*, vol. 52, no. 12, pp. 2270-2273.

Ito, K, Ito, W, Umetsu, RY, Nagasako, M, Kainuma, R, Fujita, A, Oikawa, K & Ishida, K 2008, 'Martensitic transformation in NiCoMnSn metamagnetic shape memory alloy powders', *Materials Transactions*, vol. 49, no. 8, pp. 1915-1918.

Ito, K, Ito, W, Umetsu, RY, Tajima, S, Kawaura, H, Kainuma, R & Ishida, K 2009, 'Metamagnetic shape memory effect in polycrystalline NiCoMnSn alloy fabricated by spark plasma sintering', *Scripta Materialia*, vol. 61, no. 5, pp. 504-507.

Ito, W, Imano, Y, Kainuma, R, Sutou, Y, Oikawa, K & Ishida, K 2007, 'Martensitic and magnetic transformation behaviors in Heusler-type NiMnIn and NiCoMnIn metamagnetic shape memory alloys', *Metallurgical and Materials Transactions A*, vol. 38, pp. 759-766.

Jabur, AS, Al-Haidary, JT & Al-Hasani, ES 2013, 'Characterization of Ni-Ti shape memory alloys prepared by powder metallurgy', *Journal of Alloys and Compounds*, vol. 578, pp. 136-142.

James, RD & Zhang, Z 2005, 'A way to search for multiferroic materials with "unlikely" combinations of physical properties', in L Manosa, A Planes & A Saxena (eds), *Magnetism and structure in functional materials*, Springer, New York.

Jing, C, Yang, YJ, Li, Z, Wang, XL, Kang, BJ, Cao, SX, Zhang, JC, Zhu, J & Lu, B 2013, 'Tuning martensitic transformation and large magnetoresistance in

Ni_{50-x}Cu_xMn₃₈Sn₁₂ Heusler alloys', *Journal of Applied Physics*, vol. 113, no. 17, p. 173902.

Kainuma, R, Imano, Y, Ito, W, Morito, H, Sutou, Y, Oikawa, K, Fujita, A, Ishida, K, Okamoto, S, Kitakami, O & Kanomata, T 2006, 'Metamagnetic shape memory effect in a Heusler-type Ni₄₃Co₇Mn₃₉Sn₁₁ polycrystalline alloy', *Applied Physics Letters*, vol. 88, no. 192513.

Kainuma, R, Imano, Y, Ito, W, Sutou, Y, Morito, H, Okamoto, S, Kitakami, O, Oikawa, K, Fujita, A, Kanomata, T & Ishida, K 2006, 'Magnetic-field-induced shape recovery by reverse phase transformation', *Nature*, vol. 439, no. 7079, pp. 957-960.

Karaman, I, Basaran, B, Karaca, HE, Karsilayan, AI & Chumlyakov, YI 2007, 'Energy harvesting using martensite variant reorientation mechanism in a NiMnGa magnetic shape memory alloy', *Appl. Phys. Lett.*, vol. 90, no. 172505.

Kaya, M & Dincer, I 2017, 'Magnetic and magnetocaloric properties of Ni_{50-x}Cu_xMn₃₉Sn₁₁ alloys', *Solid State Communications*, vol. 267, pp. 10-13.

Kaya, M, Yildirim, S, Yüzüak, E, Dincer, I, Ellialtioglu, R & Elerman, Y 2014, 'The effect of the substitution of Cu for Mn on magnetic and magnetocaloric properties of Ni₅₀Mn₃₄In₁₆', *Journal of Magnetism and Magnetic Materials*, vol. 368, pp. 191-197.

Khan, M, Pathak, AK, Paudel, MR, Dubenko, I, Stadler, S & Ali, N 2008, 'Magnetoresistance and field-induced structural transitions in Ni₅₀Mn_{50-x}Sn_x Heusler alloys', *Journal of Magnetism and Magnetic Materials*, vol. 320, no. 3-4, pp. L21-L25.

Kim, Y-W, Chung, Y-S, Choi, E & Nam, T-H 2012, 'Microstructure and shape memory characteristics of powder-metallurgical-processed Ti-Ni-Cu alloys', *Metallurgical and Materials Transactions A*, vol. 43, pp. 2932-2938.

Kim, Y-W, Lee, Y-J & Nam, T-H 2013, 'Shape memory characteristics of Ti-Ni-Mo alloys sintered by sparks plasma sintering', *Journal of Alloys and Compounds*, vol. 577, no. SUPPL. 1, pp. S205-S209.

Kim, Y, Kim, EJ, Choi, K, Han, WB, Kim, H-S, Shon, Y & Yoon, CS 2014, 'Room-temperature magnetocaloric effect of Ni-Co-Mn-Al Heusler alloys', *Journal of Alloys and Compounds*, vol. 616, pp. 66-70.

Kim, YD & Wayman, CM 1990, 'Shape memory effect in powder metallurgy NiAl alloys', *Scripta metallurgica et materialia*, vol. 24, no. 2, pp. 245-250.

- Krenke, T, Acet, M, Wasserman, EF, Moya, X, Manosa, L & Planes, A 2005, 'Martensitic transitions and nature of ferromagnetism in the austenitic and martensitic states of Ni-Mn-Sn alloys', *Physical Review B*, vol. 72, no. 014412.
- Krenke, T, Duman, E, Acet, M, Moya, X, Manosa, L & Planes, A 2007, 'Effect of Co and Fe on the inverse magnetocaloric properties of Ni-Mn-Sn', *Journal of Applied Physics*, vol. 102, no. 3.
- Krenke, T, Duman, E, Acet, M, Wasserman, EF, Moya, X, Manosa, L, Planes, A, Suard, E & Ouladdiaf, B 2007, 'Magnetic superelasticity and inverse magnetocaloric effect in Ni-Mn-In', *Physical Review B*, vol. 75, no. 104414.
- Krenke, T, Duman, E, Acet, M, Wassermann, EF, Moya, X, Manosa, L & Planes, A 2005, 'Inverse magnetocaloric effect in ferromagnetic Ni-Mn-Sn alloys', *Nature Materials*, vol. 4, no. 6, pp. 450-454.
- Kustov, S, Corró, ML, Pons, J & Cesari, E 2009, 'Entropy change and effect of magnetic field on martensitic transformation in a metamagnetic Ni-Co-Mn-In shape memory alloy', *Applied Physics Letters*, vol. 94, no. 19, p. 191901.
- Lakhani, A, Banerjee, A, Chaddah, P, Chen, X & Ramanujan, RV 2012, 'Magnetic glass in shape memory alloy: Ni₄₅Co₅Mn₃₈Sn₁₂', *Journal of Physics Condensed Matter*, vol. 24, no. 38.
- Larin, VS, Torcunov, AV, Zhukov, A, González, J, Vazquez, M & Panina, L 2002, 'Preparation and properties of glass-coated microwires', *Journal of Magnetism and Magnetic Materials*, vol. 249, no. 1, pp. 39-45.
- Laudise, RA, Sunder, WA, O'Bryan, HM, Carlson, DJ & Witt, AF 1992, 'Czochralski growth of single crystals of Ni_{3-x}Mn_xSn', *Journal of Crystal Growth*, vol. 118, no. 3, pp. 277-286.
- Lázpita, P, Sasmaz, M, Cesari, E, Barandiarán, JM, Gutiérrez, J & Chernenko, VA 2016, 'Martensitic transformation and magnetic field induced effects in Ni₄₂Co₈Mn₃₉Sn₁₁ metamagnetic shape memory alloy', *Acta Materialia*, vol. 109, pp. 170-176.
- Lee, AY, Kim, SY, Oh, HR, Kim, HA, Kim, YD & Lee, MH 2018, 'Effect of synthesis methods on magnetocaloric properties of Co-based Heusler-type alloys', *Materials Science and Engineering: B*, vol. 231, pp. 98-104.
- Lei, CH, Li, LJ, Shu, YC & Li, JY 2010, 'Austenite-martensite interface in shape memory alloys', *Applied Physics Letters*, vol. 96, no. 141910.

Liu, Z, Wu, Z, Yang, H, Liu, Y, Wang, W, Ma, X & Wu, G 2011, 'Martensitic transformation and magnetic properties in ferromagnetic shape memory alloy Ni₄₃Mn₄₆Sn_{11-x}Si_x', *Intermetallics*, vol. 19, no. 10, pp. 1605-1611.

Llamazares, JLS, Sanchez, T, Santos, JD, Pérez, MJ, Sanchez, ML, Hernando, B, Escoda, L, Suñol, JJ & Varga, R 2008, 'Martensitic phase transformation in rapidly solidified Mn₅₀Ni₄₀In₁₀ alloy ribbons', *Applied Physics Letters*, vol. 92, no. 012513.

López-García, J, Unzueta, I, Sánchez-Alarcos, V, Recarte, V, Pérez-Landazábal, JI, Rodríguez-Velamazán, JA, García, JA & Plazaola, F 2018, 'Correlation between defects and magneto-structural properties in Ni-Mn-Sn metamagnetic shape memory alloys', *Intermetallics*, vol. 94, pp. 133-137.

Ma, SC, Shih, CW, Liu, J, Yuan, JH, Lee, SY, Lee, YI, Chang, HW & Chang, WC 2015, 'Wheel speed-dependent martensitic transformation and magnetocaloric effect in Ni-Co-Mn-Sn ferromagnetic shape memory alloy ribbons', *Acta Materialia*, vol. 90, pp. 292-302.

Ma, Y, Jiang, C, Li, Y, Xu, H, Wang, C & Liu, X 2007, 'Study of Ni_{50+x}Mn₂₅Ga_{25-x} (x=2–11) as high-temperature shape-memory alloys', *Acta Materialia*, vol. 55, no. 5, pp. 1533-1541.

Ma, Y, Yang, S, Liu, Y & Liu, X 2009, 'The ductility and shape-memory properties of Ni-Mn-Co-Ga high-temperature shape-memory alloys', *Acta Materialia*, vol. 57, no. 11, pp. 3232-3241.

Maziarz, W, Czaja, P, Szczerba, MJ, Lityń'ska-Dobrzyń'ska, L, Czeppe, T & Dutkiewicz, J 2014, 'Influence of Ni/Mn concentration ratio on microstructure and martensitic transformation in melt spun Ni–Mn–Sn Heusler alloy ribbons', *Journal of the Mechanics and Physics of Solids*.

Maziarz, W, Wójcik, A, Czaja, P, Żywczak, A, Jan, D, Hawełek, Ł & Cesari, E 2016, 'Magneto-structural transformations in Ni₅₀Mn_{37.5}Sn_{12.5-x}In_x Heusler powders', *Journal of Magnetism and Magnetic Materials*, vol. 412, pp. 123-131.

Maziarz, W, Wójcik, A, Grzegorek, J, Żywczak, A, Czaja, P, Szczerba, MJ, Dutkiewicz, J & Cesari, E 2017, 'Microstructure, magneto-structural transformations and mechanical properties of Ni₅₀Mn_{37.5}Sn_{12.5-x}In_x (x=0, 2, 4, 6 % at.) metamagnetic shape memory alloys sintered by vacuum hot pressing', *Journal of Alloys and Compounds*, vol. 715, pp. 445-453.

McDowell, DL, Panchal, JH, Choi, H-J, Seepersad, CC, Allen, JK & Mistree, F 2010, 'Chapter 1 - Integrated Material, Product, and Process Design—A New Frontier in Engineering Systems Design', in DL McDowell, JH Panchal, H-J Choi, CC Seepersad,

- JK Allen & F Mistree (eds), *Integrated Design of Multiscale, Multifunctional Materials and Products*, Butterworth-Heinemann, Boston, pp. 1-22.
- Monastyrsky, GE, Odnosum, V, Van Humbeeck, J, Kolomytsev, VI & Koval, YN 2002, 'Powder metallurgical processing of Ni–Ti–Zr alloys undergoing martensitic transformation: part I', *Intermetallics*, vol. 10, pp. 95-103.
- Monastyrsky, GE, Van Humbeeck, J, Kolomytsev, VI & Koval, YN 2002, 'Powder metallurgical processing of Ni–Ti–Zr alloys undergoing martensitic transformation—part II', *Intermetallics*, vol. 10, pp. 613-624.
- Monroe, JA, Cruz-Perez, J, Yegin, C, Karaman, I, Geltmacher, AB, Everett, RK & Kainuma, R 2012, 'Magnetic response of porous NiCoMnSn metamagnetic shape memory alloys fabricated using solid-state replication', *Scripta Materialia*, vol. 67, no. 1, pp. 116-119.
- Muddle, BC & Nie, JF 2001, 'Martensite', in Patrick Veyssi re, KHJ Buschow, RW Cahn, MC Flemings, B Ilchner, EJ Kramer & S Mahajan (eds), *Encyclopedia of Materials: Science and Technology (Second Edition)*, Elsevier, Oxford, pp. 5189-5193.
- Munroe, PR 2009, 'The application of focused ion beam microscopy in the material sciences', *Materials Characterization*, vol. 60, no. 1, pp. 2-13.
- Murakami, Y, Watanabe, Y, Kanaizuka, T & Kachi, S 1981, 'Magnetic properties and phase change of Ni_{3-y}Mn_ySn alloy', *Transactions of the Japan Institute of Metals*, vol. 22, no. 8, pp. 551-557.
- Murray, SJ, Marioni, M, Allen, SM, O'Handley, RC & Lograsso, TA 2000, '6% magnetic-field-induced strain by twin-boundary motion in ferromagnetic Ni-Mn-Ga', *Applied Physics Letters*, vol. 77, no. 6, pp. 886-888.
- National SQUID Facility, IITD, *What is Superconducting Quantum Interface Device (SQUID)?*, viewed 01 March 2015 <http://squid.iitd.ernet.in/Basic_Literature.htm>.
- Niemann, R, R b ler, UK, Gruner, ME, Heczko, O, Schultz, L & F hler, S 2012, 'The Role of Adaptive Martensite in Magnetic Shape Memory Alloys', *Advanced Engineering Materials*, vol. 14, no. 8, pp. 562-581.
- Oikawa, K, Tanaka, Y, Sutou, Y, Omori, T, Fenghua, L, Kainuma, R & Ishida, K 2006, 'Effects of aging and Co addition on martensitic and magnetic transitions in Ni-Al-Fe β -based shape memory alloys', *ISIJ International*, vol. 46, no. 9, pp. 1287-1291.
- Otsuka, K & Kakeshita, T 2002, 'Science and technology of shape memory materials: new developments', *MRS Bulletin*, vol. 27.

Pareti, L, Solzi, M, Albertini, F & Paoluzi, A 2003, 'Giant entropy change at the co-occurrence of structural and magnetic transitions in the Ni_{2.19}Mn_{0.81}Ga Heusler alloy', *The European Physics Journal B*, vol. 32, pp. 303-307.

Pecharsky, VK & Gschneidner, KA, Jr. 1997, 'Giant magnetocaloric effect in Gd₅(Si₂Ge₂)', *Physical Review Letters*, vol. 78, no. 23, pp. 4494-4497.

Pérez-Landazábal, JI, Lambri, OA, Bonifacich, FG, Sánchez-Alarcos, V, Recarte, V & Tarditti, F 2015, 'Influence of defects on the irreversible phase transition in Fe–Pd ferromagnetic shape memory alloys', *Acta Materialia*, vol. 86, no. , pp. 110-117.

Perez-Saez, RB, Recarte, V, No, ML, Ruano, OA & San, JJ 2000, 'Advanced shape memory alloys processed by powder metallurgy', *Advanced Engineering Materials*, vol. 2, no. 1-2, pp. 49-53.

Pérez-Sierra, AM, Bruno, NM, Pons, J, Cesari, E & Karaman, I 2016, 'Atomic order and martensitic transformation entropy change in Ni–Co–Mn–In metamagnetic shape memory alloys', *Scripta Materialia*, vol. 110, pp. 61-64.

Pérez-Sierra, AM, Pons, J, Santamarta, R, Vermaut, P & Ochin, P 2015, 'Solidification process and effect of thermal treatments on Ni–Co–Mn–Sn metamagnetic shape memory alloys', *Acta Materialia*, vol. 93, pp. 164-174.

Planes, A, Mañosa, L & Acet, M 2009, 'Magnetocaloric effect and its relation to shape-memory properties in ferromagnetic Heusler alloys', *Journal of Physics: Condensed Matter*, vol. 21, no. 233201.

Planes, A, Manosa, L & Acet, M 2013, 'Recent Progress and future perspectives in magnetic and metamagnetic shape-memory Heusler alloys', *Materials Science Forum*, vol. 738-739, pp. 391-399.

Popa, F, Chicinaş, HF, Marinca, TF & Chicinaş, I 2017, 'Influence of mechanical alloying and heat treatment processing on the Ni₂MnSn Heusler alloy structure', *Journal of Alloys and Compounds*, vol. 716, pp. 137-143.

Rama Rao, NV, Gopalan, R, Chandrasekaran, V & Suresh, KG 2009, 'Phase coexistence, microstructure and magnetism in Ni-Mn-Sb alloys', *Journal of Physics D: Applied Physics*, vol. 42, no. 6.

Rama Rao, NV, Gopalan, R, Chandrasekaran, V & Suresh, KG 2010, 'Large low-field inverse magnetocaloric effect near room temperature in Ni_{50-x}Mn_{37+x}In₁₃ Heusler alloys', *Applied Physics A: Materials Science and Processing*, vol. 99, no. 1, pp. 265-270.

Rama Rao, NV, Gopalan, R, Manivel Raja, M, Arout Chelvane, J, Majumdar, B & Chandrasekaran, V 2007, 'Magneto-structural transformation studies in melt-spun Ni-Mn-Ga ribbons', *Scripta Materialia*, vol. 56, no. 5, pp. 405-408.

Rameš, M, Heczko, O, Sozinov, A, Ullakko, K & Straka, L 2018, 'Magnetic properties of Ni-Mn-Ga-Co-Cu tetragonal martensites exhibiting magnetic shape memory effect', *Scripta Materialia*, vol. 142, pp. 61-65.

Rao, NVR, Gopalan, R, Chandrasekaran, V & Suresh, KG 2009, 'Microstructure, magnetic properties and magnetocaloric effect in melt-spun Ni-Mn-Ga ribbons', *Journal of Alloys and Compounds*, vol. 478, no. 1-2, pp. 59-62.

Recarte, V, Pérez-Landazábal, JI, Sánchez-Alarcos, V & Rodríguez-Velamazán, JA 2012, 'Dependence of the martensitic transformation and magnetic transition on the atomic order in Ni-Mn-In metamagnetic shape memory alloys', *Acta Materialia*, vol. 60, no. 5, pp. 1937-1945.

Righi, L, Albertini, F, Fabbrici, S & Paoluzi, A 2011, 'Crystal structures of modulated martensitic phases of FSM Heusler alloys', in VA Chernenko (ed.), *Advances in Magnetic Shape Memory Materials*, vol. 684, Trans Tech Publications Ltd, Switzerland, pp. 105-116.

Roy, SB 2013, 'First order magneto-structural phase transition and associated multifunctional properties in magnetic solids', *Journal of Physics Condensed Matter*, vol. 25, no. 183201.

Sánchez-Alarcos, V, Recarte, V, Pérez-Landazábal, J, Cesari, E & Rodríguez-Velamazán, J 2014, 'Long-Range Atomic Order and Entropy Change at the Martensitic Transformation in a Ni-Mn-In-Co Metamagnetic Shape Memory Alloy', *Entropy*, vol. 16, no. 5, p. 2756.

Sánchez-Alarcos, V, Recarte, V, Pérez-Landazábal, JI, Gómez-Polo, C & Rodríguez-Velamazán, JA 2012, 'Role of magnetism on the martensitic transformation in Ni-Mn-based magnetic shape memory alloys', *Acta Materialia*, vol. 60, no. 2, pp. 459-468.

Santos, JD, Sanchez, T, Alvarez, P, Sanchez, ML, Llamazares, JLS, Hernando, B, Escoda, L, Sunol, JJ & Varga, R 2008, 'Microstructure and magnetic properties of Ni₅₀Mn₃₇Sn₁₃ Heusler alloy ribbons', *Journal of Applied Physics*, vol. 103, no. 7.

Schlagel, DL, McCallum, RW & Lograsso, TA 2008, 'Influence of solidification microstructure on the magnetic properties of Ni-Mn-Sn Heusler alloys', *Journal of Alloys and Compounds*, vol. 463, pp. 38-46.

- Schlagel, DL, Yuhasz, WM, Dennis, KW, McCallum, RW & Lograsso, TA 2008, 'Temperature dependence of the field-induced phase transformation in Ni₅₀Mn₃₇Sn₁₃', *Scripta Materialia*, vol. 59, pp. 1083-1086.
- Schuller, E, Hamed, OA, Bram, M, Sebold, D, Buchkremer, HP & Stover, D 2003, 'Hot isostatic pressing (HIP) of elemental powder mixtures and prealloyed powder for NiTi shape memory parts', *Advanced Engineering Materials*, vol. 5, no. 12, pp. 918-924.
- Seguí, C, Pons, J & Cesari, E 2007, 'Effect of atomic ordering on the phase transformations in Ni–Mn–Ga shape memory alloys', *Acta Materialia*, vol. 55, no. 5, pp. 1649-1655.
- Sharma, VK, Chattopadhyay, MK & Roy, SB 2007, 'Kinetic arrest of the first order austenite to martensite phase transition in Ni₅₀Mn₃₄In₁₆: dc magnetization studies', *Physical Review B*, vol. 76, no. 14, p. 140401.
- Shevyrtalov, S, Miki, H, Ohtsuka, M, Grunin, A, Lyatun, I, Mashirov, A, Seredina, M, Khovaylo, V & Rodionova, V 2018, 'Martensitic transformation in polycrystalline substrate-constrained and freestanding Ni-Mn-Ga films with Ni and Ga excess', *Journal of Alloys and Compounds*, vol. 741, pp. 1098-1104.
- Shevyrtalov, S, Zhukov, A, Lyatun, I, Medvedeva, S, Miki, H, Zhukova, V & Rodionova, V 2018, 'Martensitic transformation behavior of Ni_{2.44}Mn_{0.48}Ga_{1.08} thin glass-coated microwire', *Journal of Alloys and Compounds*, vol. 745, pp. 217-221.
- Smith, A, Bahl, CRH, Bjørk, R, Engelbrecht, K, Nielsen, KK & Pryds, N 2012, 'Materials Challenges for High Performance Magnetocaloric Refrigeration Devices', *Advanced Energy Materials*, vol. 2, no. 11, pp. 1288-1318.
- Song, Y, Chen, X, Dabade, V, Shield, TW & James, RD 2013, 'Enhanced reversibility and unusual microstructure of a phase-transforming material', *Nature*, vol. 502, pp. 85-88.
- Sozinov, A, Lanska, N, Soroka, A & Zou, W 2013, '12% magnetic field-induced strain in Ni-Mn-Ga-based non-modulated martensite', *Applied Physics Letters*, vol. 102, no. 2, p. 021902.
- Sozinov, A, Likhachev, AA, Lanska, N, Soderberg, O, Ullakko, K & Lindroos, VK 2003, 'Effect of crystal structure on magnetic-field-induced strain in Ni-Mn-Ga', in DC Lagoudas (ed.), *Smart Structures and Materials 2003: Active Materials: Behavior and Mechanics, Proceedings of SPIE*, vol. 5053, pp. 586-594.

- Sozinov, A, Likhachev, AA, Lanska, N, Ullakko, K & Lindroos, VK 2002, 'Crystal structure, magnetic anisotropy, and mechanical properties of seven-layered martensite in Ni-Mn-Ga', in CS Lynch (ed.), *Smart Structures and Materials 2002: Active Materials: Behavior and Mechanics, Proceedings of SPIE*, vol. 4699, pp. 195-205.
- Spaldin, NA, Cheong, S-W & Ramesh, R 2010, 'Multiferroics: Past, present, and future', *Physics Today*, vol. 63, no. 10, pp. 38-43.
- Srivastava, V, Chen, X & James, RD 2010, 'Hysteresis and unusual magnetic properties in the singular Heusler alloy Ni₄₅Co₅Mn₄₀Sn₁₀', *Applied Physics Letters*, vol. 97, no. 014101.
- Srivastava, V, Song, Y, Bhatti, K & James, RD 2011, 'The direct conversion of heat to electricity using multiferroic alloys', *Advanced Energy Materials*, vol. 1, no. 1, pp. 97-104.
- Sun, XM, Cong, DY, Li, Z, Zhang, YL, Chen, Z, Ren, Y, Liss, KD, Ma, ZY, Li, RG, Qu, YH, Yang, Z, Wang, L & Wang, YD 2019, 'Manipulation of magnetostructural transition and realization of prominent multifunctional magnetoresponse properties in NiCoMnIn alloys', *Physical Review Materials*, vol. 3, no. 3, p. 034404.
- Suryanarayana, C 2001, 'Mechanical alloying and milling', *Progress in Materials Science*, vol. 46, no. 1, pp. 1-184.
- Suryanarayana, C 2002, 'Rapid Solidification Processing', in P Veyssi re, KHJ Buschow, RW Cahn, MC Flemings, B Ilchner, EJ Kramer & S Mahajan (eds), *Encyclopedia of Materials: Science and Technology (Second Edition)*, Elsevier, Oxford, pp. 1-10.
- Sutou, Y, Imano, Y, Koeda, N, Omori, T, Kainuma, R, Ishida, K & Oikawa, K 2004, 'Magnetic and martensitic transformations of NiMnX (X=In, Sn, Sb) ferromagnetic shape memory alloys', *Applied Physics Letters*, vol. 85, no. 19, pp. 4358-4360.
- Takeuchi, I, Famodu, OO, Read, JC, Aronova, MA, Chang, KS, Craciunescu, C, Lofland, SE, Wuttig, M, Wellstood, FC, Knauss, L & Orozco, A 2003, 'Identification of novel compositions of ferromagnetic shape-memory alloys using composition spreads', *Nature Materials*, vol. 2, p. 180.
- Terayama, A & Kyogoku, H 2010, 'Shape memory characteristics of the P/M-processed Ti-Ni-Cu alloys', *Materials Science and Engineering: A*, vol. 527, no. 21-22, pp. 5484-5491.
- Tickle, R & James, RD 1999, 'Magnetic and magnetomechanical properties of Ni₂MnGa', *Journal of Magnetism and Magnetic Materials*, vol. 195, no. 3, pp. 627-638.

Trung, NT, Zhang, L, Caron, L, Buschow, KHJ & Brück, E 2010, 'Giant magnetocaloric effects by tailoring the phase transitions', *Applied Physics Letters*, vol. 96, no. 17, p. 172504.

Ullakko, K, Huang, JK, Kantner, C, O'Handley, RC & Kokorin, VV 1996, 'Large magnetic-field-induced strains in Ni₂MnGa single crystals', *Applied Physics Letters*, vol. 69, no. 13, pp. 1965-1968.

Upadhyaya, GS 1996, *Powder Metallurgy Technology*, Cambridge International Science Publishing, Cambridge, United Kingdom.

Valeanu, M, Lucaci, M, Crisan, AD, Sofronie, M, Leonat, L & Kuncser, V 2011, 'Martensitic transformation of Ti₅₀Ni₃₀Cu₂₀ alloy prepared by powder metallurgy', *Journal of Alloys and Compounds*, vol. 509, no. 13, pp. 4495-4498.

Wachtel, E, Henninger, F & Predel, B 1983, 'Constitution and magnetic properties of Ni-Mn-Sn alloys - solid and liquid state', *Journal of Magnetism and Magnetic Materials*, vol. 38, pp. 305-315.

Wang, W, Li, H, Ren, J, Fu, J, Zhai, Q, Luo, Z & Zheng, H 2015, 'Enhanced magnetocaloric properties in annealed Heusler Ni-Mn-Sn ribbons', *Journal of Magnetism and Magnetic Materials*, vol. 374, pp. 153-156.

Wang, W, Yu, J, Zhai, Q, Luo, Z & Zheng, H 2013, 'Origin of retarded martensitic transformation in Heusler Ni-Mn-Sn melt-spun ribbons', *Intermetallics*, vol. 42, no. , pp. 126-129.

Wang, ZL, Cong, DY, Nie, ZH, Gao, J, Liu, W & Wang, YD 2012, 'The suppression and recovery of martensitic transformation in a Ni-Co-Mn-In magnetic shape memory alloy', *Journal of Alloys and Compounds*, vol. 511, no. 1, pp. 41-44.

Wu, Z, Liu, Z, Yang, H, Liu, Y & Wu, G 2011, 'Effect of Co addition on martensitic phase transformation and magnetic properties of Mn₅₀Ni_{40-x}In₁₀Co_x polycrystalline alloys', *Intermetallics*, vol. 19, no. 12, pp. 1839-1848.

Xu, X 2000, 'Densification, microstructure and strength evolution in sintering', PhD thesis, Pennsylvania State University, Pennsylvania.

Yang, LH, Zhang, H, Hu, FX, Sun, JR, Pan, LQ & Shen, BG 2014, 'Magnetocaloric effect and martensitic transition in Ni₅₀Mn_{36-x}Co_xSn₁₄', *Journal of Alloys and Compounds*, vol. 588, pp. 46-48.

- Yang, S, Wang, C & Liu, X 2012, 'Phase equilibria and composition dependence of martensitic transformation in Ni-Mn-Ga ternary system', *Intermetallics*, vol. 25, pp. 101-108.
- Yang, S, Wang, C, Shi, Z, Wang, J, Zhang, J, Huang, Y & Liu, X 2016, 'Microstructure, martensitic transformation, mechanical and shape memory properties of Ni-Co-Mn-In high-temperature shape memory alloys under different heat treatments', *Materials Science and Engineering: A*, vol. 655, pp. 204-211.
- Yeldhose, AM 2015, 'Thermodynamic property analysis of multiferroic alloys', School of Mechanical Engineering, Masters by coursework thesis, University of Adelaide, Adelaide, Australia.
- Yu, J-K, Li, H-W, Zhai, Q-J, Fu, J-X, Luo, Z-P & Zheng, H-X 2014, 'Crystal structure and formation mechanism of the secondary phase in Heusler Ni-Mn-Sn-Co materials', *Advances in Manufacturing*, vol. 2, no. 4, pp. 353-357.
- Yuhasz, WM, Schlagel, DL, Xing, Q, Dennis, KW, McCallum, RW & Lograsso, TA 2009, 'Influence of annealing and phase decomposition on the magnetostructural transitions in Ni₅₀Mn₃₉Sn₁₁', *Journal of Applied Physics*, vol. 105, no. 7.
- Yuhasz, WM, Schlagel, DL, Xing, Q, McCallum, RW & Lograsso, TA 2010, 'Metastability of ferromagnetic Ni-Mn-Sn Heusler alloys', *Journal of Alloys and Compounds*, vol. 492, no. 1-2, pp. 681-684.
- Zhang, K, Tan, C, Zhao, W, Guo, E & Tian, X 2019, 'Computation-Guided Design of Ni-Mn-Sn Ferromagnetic Shape Memory Alloy with Giant Magnetocaloric Effect and Excellent Mechanical Properties and High Working Temperature via Multielement Doping', *ACS Applied Materials & Interfaces*, vol. 11, no. 38, pp. 34827-34840.
- Zhao, XG, Hsieh, CC, Lai, JH, Cheng, XJ, Chang, WC, Cui, WB, Liu, W & Zhang, ZD 2010, 'Effects of annealing on the magnetic entropy change and exchange bias behavior in melt-spun Ni-Mn-In ribbons', *Scripta Materialia*, vol. 63, no. 2, pp. 250-253.
- Zheng, H, Wang, W, Xue, S, Zhai, Q, Frenzel, J & Luo, Z 2013, 'Composition-dependent crystal structure and martensitic transformation in Heusler Ni-Mn-Sn alloys', *Acta Materialia*, vol. 61, pp. 4648-4656.
- Zheng, H, Wang, W, Yu, J, Zhai, Q & Luo, Z 2014, 'Martensitic transformation in melt-spun Heusler Ni-Mn-Sn-Co ribbons', *Journal of Materials Research*, vol. 29, no. 7, pp. 880-886.

Zhukov, A, Rodionova, V, Ilyn, M, Aliev, AM, Varga, R, Michalik, S, Aronin, A, Abrosimova, G, Kiselev, A, Ipatov, M & Zhukova, V 2013, 'Magnetic properties and magnetocaloric effect in Heusler-type glass-coated NiMnGa microwires', *Journal of Alloys and Compounds*, vol. 575, pp. 73-79.

9 Appendix 1

Ferromagnetic Shape Memory Heusler Materials: Synthesis, Microstructure Characterization and Magnetostructural Properties.

Riaz Ahamed Ahamed Khan^a, Reza Ghomashchi^a, Zonghan Xie^{a,b} and Lei Chen^a

^a School of Mechanical Engineering, The University of Adelaide, Adelaide, SA 5005

^b School of Engineering, Edith Cowan University, Joondalup WA 6027

Materials 2018, 11 (6), 988.

A comprehensive review about the physics, chemistry, materials science and metallurgical aspects of ferromagnetic NiMnX (X = group IIIA-VA elements) Heusler alloys that might be of interdisciplinary interest, is presented in this section. More importantly, different methods of synthesis, characterization and effects of microstructure on the magnetostructural properties of these alloys are given. Concepts presented here will equip researchers with a background knowledge necessary to carry out meaningful research in this field. For instance one might be drawn to idea that martensitic transformation in these alloys is driven by a band Jahn-Teller effect and magnetostructural coupling responsible for the multiferroic nature occurs through an indirect oscillatory Ruderman-Kittel-Kasuya-Yosida (RKKY) exchange interaction. Basic information about the crystal structure such as Wyckoff atomic positions and their relationship to the magnetic behaviour is understood from close neighbours Mn-Mn at 4a positions coupling ferromagnetically and those at 4a-4b positions coupling antiferromagnetically. Or the idea that martensitic transformation could be isothermal or athermal depending on the kinetics could be interesting. In isothermal transformation the amount of martensite formed depends on both time and temperature. In athermal transformation it is dependent only on temperature, with both transformations influencing

the electronic state of the alloys. Isothermal nature of transformations can be established through differential scanning calorimetry (DSC).

Various methods of synthesis of NiMn-based Heusler alloys are elaborated with their merits and demerits. Liquid processing techniques include arc/induction melting and casting, rapid solidification by melt-spinning, directional solidification using Bridgman-Stockbarger and Czochralski techniques, Taylor-Ulitovsky method of fabricating glass-coated microwires and hot-forging and rolling. Solid processing techniques of pressure-less sintering, spark plasma sintering and solid-state replication using pre-alloyed atomized powders of constituent elements can be employed. Combinatorial material synthesis and composition-spread methods of materials design as well as the geometrical non-linear theory of martensite (GNLTM) solutions to alloy design that ensure high levels of reversibility of phase transformation greatly help in alloy development and application. Of particular interest are the microstructural effects on the magnetostructural properties of the alloys. Microstructural factors such as composition, crystal structure changing according to the e/a ratio, unit cell volume, degree of long-range $L2_1$ atomic ordering and the presence of additional phases such as the γ -phase have a profound influence on the transformation temperatures and the magnetostructural properties of the alloys.

Section 3.2.4 of this thesis draws considerably from this review article. The primary intent of this review and Chapters 2 and 3, in the absence of literature on PM alloys with elemental powders, is to provide a platform to look for comparisons between solid processed and liquid processed alloys.

Statement of Authorship

Title of Paper	Ferromagnetic Shape Memory Heusler Materials: Synthesis, Microstructure Characterization and Magnetostructural Properties
Publication Status	<input checked="" type="checkbox"/> Published <input type="checkbox"/> Accepted for Publication <input type="checkbox"/> Submitted for Publication <input type="checkbox"/> Unpublished and Unsubmitted work written in manuscript style
Publication Details	Ahamed, R, Ghomashchi, R, Xie, Z., Chen, L 2018, 'Powder Metallurgy Synthesis of Heusler Alloys: Effects of Process Parameters', <i>Materials</i> , vol. 11, 988.

Principal Author

Name of Principal Author (Candidate)	Riaz Ahamed Ahamed Khan				
Contribution to the Paper	I was responsible for the literature review required for the work, and conducting of experiments discussed in the paper. Wrote the first draft of the manuscript and incorporated and addressed all comments/suggestions by other authors in subsequent revisions. Interpretation of results was primarily my responsibility.				
Overall percentage (%)	85%				
Certification:	This paper reports on original research I conducted during the period of my Higher Degree by Research candidature and is not subject to any obligations or contractual agreements with a third party that would constrain its inclusion in this thesis. I am the primary author of this paper.				
Signature	<table border="1" style="width: 100%;"> <tr> <td style="width: 80%;"></td> <td style="width: 20%;">Date</td> </tr> <tr> <td></td> <td>21/6/19</td> </tr> </table>		Date		21/6/19
	Date				
	21/6/19				

Co-Author Contributions

By signing the Statement of Authorship, each author certifies that:

- i. the candidate's stated contribution to the publication is accurate (as detailed above);
- ii. permission is granted for the candidate to include the publication in the thesis; and
- iii. the sum of all co-author contributions is equal to 100% less the candidate's stated contribution.


Name of Co-Author	Lei Chen				
Contribution to the Paper	Supervising development of work, evaluating methods and theories, helping with experimental setup and evaluating manuscript.				
Signature	<table border="1" style="width: 100%;"> <tr> <td style="width: 80%;"></td> <td style="width: 20%;">Date</td> </tr> <tr> <td></td> <td>21/06/19</td> </tr> </table>		Date		21/06/19
	Date				
	21/06/19				

Name of Co-Author	Reza Ghomashchi				
Contribution to the Paper	Supervising development of work, evaluating methods and theories, helping with experimental setup and evaluating and editing the manuscript.				
Signature	<table border="1" style="width: 100%;"> <tr> <td style="width: 80%;"></td> <td style="width: 20%;">Date</td> </tr> <tr> <td></td> <td>25/6/2019</td> </tr> </table>		Date		25/6/2019
	Date				
	25/6/2019				

Name of Co-Author	Zonghan Xie		
Contribution to the Paper	Supervising development of work, evaluating methods and theories, helping with experimental setup and evaluating manuscript.		
Signature		Date	25/06/19

Review

Ferromagnetic Shape Memory Heusler Materials: Synthesis, Microstructure Characterization and Magnetostructural Properties

Riaz Ahamed Ahamed Khan ^{1,*}, Reza Ghomashchi ^{1,*}, Zonghan Xie ^{1,2} and Lei Chen ¹ 

¹ School of Mechanical Engineering, University of Adelaide, Adelaide 5005, Australia; zonghan.xie@adelaide.edu.au (Z.X.); lei.chen@adelaide.edu.au (L.C.)

² School of Engineering, Edith Cowan University, Joondalup WA 6027, Australia

* Correspondence: riazahamed.ahamedkhan@adelaide.edu.au (R.A.A.K.); reza.ghomashchi@adelaide.edu.au (R.G.); Tel.: +61-8-8313-4713 (R.A.A.K.)

Received: 1 May 2018; Accepted: 8 June 2018; Published: 11 June 2018



Abstract: An overview of the processing, characterization and magnetostructural properties of ferromagnetic NiMnX (X = group IIIA–VA elements) Heusler alloys is presented. This type of alloy is multiferroic—exhibits more than one ferroic property—and is hence multifunctional. Examples of how different synthesis procedures influence the magnetostructural characteristics of these alloys are shown. Significant microstructural factors, such as the crystal structure, atomic ordering, volume of unit cell, grain size and others, which have a bearing on the properties, have been reviewed. An overriding factor is the composition which, through its tuning, affects the martensitic and magnetic transitions, the transformation temperatures, microstructures and, consequently, the magnetostructural effects.

Keywords: Heusler alloys; martensitic transformation; magnetic/metamagnetic shape memory; magnetocaloric; liquid and solid processing; microstructure

1. Introduction

The term multiferroic refers to the simultaneous exhibit of multiple ferroic behaviors of ferromagnetism, ferroelectricity and ferroelasticity in materials. Each is characterized by the presence of a distinct hysteresis loop when switched magnetically, electrically or mechanically. Various factors, such as chemistry, symmetry, conductivity (conductor/insulator), mechanical distortion, etc., do not place any constraint on a material being multiferroic. Multiferroic behavior can therefore be engineered by bringing about a coexistence of phases with unlikely properties [1]. Several conditions, such as (a) phase boundary between phases, (b) phase transformation by application of fields or stresses, (c) sufficiently fast kinetics of transformation and (d) reversibility, are to be satisfied. Martensitic transformation in materials by virtue of being diffusionless could be a basis for the realization of multiferroic behavior. With reversibility and compatibility between phases ensured by tuning the composition, the ferroic orderings can be combined [1] with a large potential for applications. Heusler materials (e.g., Cu₂MnAl: magnetic even though constituent elements are nonmagnetic, TiNiSn: semiconducting even though constituent elements are metals), discovered by Fritz Heusler in 1903, are multiferroic by martensitic phase transformation. Multiferroic effects in NiMnX (X = group IIIA–VA elements) Heusler materials [2] form the subject matter of this overview paper. Prominent effects seen in them are magnetic/metamagnetic shape memory (MSM/MMSM), magnetocaloric (MC) and direct energy conversion.

The terms MSM/MMSM are all-pervading in the discussion of these materials. Martensitic transformation renders variants in the product (martensite) phase, which possesses magnetic domains

below the Curie point. Upon the application of a magnetic field and given a strong magnetic anisotropy of the material, the martensitic variants rotate to bring their easy axes in the direction of the applied field by utilizing the difference in their Zeeman energy levels in a manner similar to rearrangement by twin boundary motion under an applied stress [2]. Heating to above the austenite finish temperature reverts the product phase back to the parent phase and the large deformation from the application of magnetic field can be recovered. This is magnetic shape memory effect. Early research on magnetic field-induced strain (MFIS) in single crystals of Ni₂MnGa alloys through twin boundary motion was reported in [3–7]. It has been found that necessary conditions for large MFIS are a low twinning stress (σ_{tw}) and a high energy of magnetic anisotropy [8]. The magnetic field-controlled strain response ϵ (MSM) is supposedly equal to the maximum strain $\epsilon_0 = (1 - c/a)$, c and a are lattice parameters for tetragonal crystal structure) allowed by twinning when the magnetic anisotropy energy density $K > \epsilon_0 \sigma_{tw}$ ($\epsilon_0 \sigma_{tw}$ —mechanical driving force) [8]. Metamagnetic shape memory effect, observed in off-stoichiometric Ga-free alloys, on the other hand, refers to the recoverability upon heating of large strains obtained when a reverse martensitic transformation from the product phase to parent phase is induced by the application of a magnetic field, with emphasis on the reverse transformation from martensite to austenite [9–12].

Magnetocaloric effect is given as the change in entropy induced by the applied magnetic field, measured by calorimetric measurements or from magnetization isotherms. Typically, it is quantified by an adiabatic temperature change or an isothermal entropy change occurring on the application or removal of an external magnetic field. The product of the changes in isothermal field-induced entropy (ΔS) and the adiabatic field-induced temperature (ΔT), $|\Delta S \Delta T|$, is maximum when the magnetization change at the transition is maximum for an optimal composition in ferromagnetic Heusler alloys [13]. Interest in magnetocaloric materials was triggered by the discovery of a giant magnetocaloric effect (GMCE) in Gd₅(Si₂Ge₂) around room temperature [14]. Research on MCE in NiMnX alloys followed later on, with the NiMnGa system most studied [15–18]. The observed large isothermal entropy change is broken up into the magnetic and structural entropy changes arising out of the spin-lattice coupling [2,19], occurring at the point where the martensitic transformation temperature and the magnetic transition temperature are close to one another [20]. A positive value of entropy change is termed as inverse effect and is related to the magnetocrystalline anisotropy of the martensitic phase. The inverse effect is more pronounced when the difference between the martensitic transition and Curie temperatures is an appreciable value. Conversely, a negative entropy change is termed conventional effect, and the change from inverse to conventional occurs as the martensitic transformation temperature approaches the Curie temperature at higher values of applied field [20,21]. Alloys such as Ni_{0.50}Mn_{0.50-x}Sn_x, Ni₅₀Mn₃₅Sn₁₅ and Ni₅₀Mn_{33.66}Cr_{0.34}In₁₆, which have been reported to exhibit inverse/conventional magnetocaloric/giant magnetocaloric effects, are reported in [10,22,23]. Polycrystalline Ni₄₅Mn₄₃CrSn₁₁ alloy exhibited large inverse magnetocaloric effect with magnetic and total entropy changes of 35 J/kgK and 39.7 J/kgK, respectively [24].

The direct conversion of thermal energy (waste heat) to electricity is a more recent phenomenon, exhibited by a singular quaternary ferromagnetic Heusler alloy. A sudden and large thermally induced change in magnetization in a biased magnetic field initiated by phase transition was utilized to generate a voltage of 0.6 mV. This is using the fundamental dipolar relationship between magnetization M , magnetic induction (magnetic flux density) B and magnetic field H , given by $B = H + 4\pi M$ and Faraday's law $\text{curl} E = \frac{1}{c} \frac{dB}{dt}$ based on the premise that the magnetostructural transformation essentially induces a non-zero dB/dt [25]. This phenomenon, as envisaged by the researchers, could be taken to the stage of actual application, with the alloy having the potential to be used for harvesting energy from low waste heat sources of the order of less than 200 °C [25].

For all intents and purposes, the synthesis and microstructures play a vital role in the functionality of these materials. There are a large number of alloys prepared in this class of materials, evidenced by the number of publications appearing in ISI Web of Science each year [26]. Additionally, review articles have been published on MSM/MMSM materials [13] and magnetocaloric materials [2,20,27].

Particular to MCE, research is also being carried out on using materials with reduced dimensions, such as thin films, ribbons and microwires [28]. Even though there is a vast amount of literature about multiferroic materials proportionate to the growing interest in them, a review of how the synthesis procedures and microstructures influence their magnetostructural properties would be appropriate. This article mostly restricts itself to NiMn-based MSM/MMSM and MC materials, since it will be impossible to summarize the data of a large number of publications on a whole range of ferromagnetic alloy systems, most of which just report a new composition with an enhanced magnetostructural characteristic. This article is written with intent of providing enough information to the uninitiated researchers in order that they can meaningfully channelize their research and contribute their might toward extending the realm of these multiferroic materials from experimental to actual application.

The first section of this article deals with the fundamental concepts necessary for the understanding of the concept of multiferroic behavior in materials. The second section of this article deals with the fundamental concepts necessary for the understanding of the concept of multiferroic behavior in materials. The third section covers the synthesis and characterization procedures employed on these class of materials, with some inputs to design. The fourth section looks into how the magnetostructural characteristics of various ferromagnetic Heusler alloys are influenced by microstructural features.

2. Fundamental Concepts

2.1. Crystal Structures of Austenite and Martensite

The austenite structure in ferromagnetic Ni-Mn-X ($X = \text{Sn, Sb, In, Ga}$) alloy systems is of $L2_1$ atomic order [2,29]. The cubic $L2_1$ (space group $F\bar{4}3m$) structure has four interpenetrating face-centered cubic (fcc) sublattices. The crystal sites are designated as A (0, 0, 0), B (1/2, 1/2, 1/2), C (1/4, 1/4, 1/4) and D (3/4, 3/4, 3/4) in Wyckoff notations, which indicate positions of atoms in a crystal. Generally, in X_2YZ Heusler alloys, the X atoms occupy (A, C) sites, Y atoms occupy B sites and the main group element Z occupies the D sites. Between X and Y, the one which has a higher number of valence electrons occupies the (A, C) sites and the one with fewer valence electrons occupies the B site. In some alloys, an order–disorder phase transition ($L2_1$ –B2) occurs, transforming the nonequilibrium B2 to a more stable $L2_1$ phase. This sometimes causes confusion in distinguishing the two phases correctly from electron diffraction studies, as the atomic scattering is similar. The $B2'$ structure has Y/Z atoms occupying A positions and X atoms occupying B positions and exhibits a first neighbor ordering, while $L2_1$ exhibits a second neighbor ordering [30]. The austenitic structure is $L2_1$ at room temperature in the case of quaternary Heusler alloys with the stoichiometry defined by 1:1:1:1. Wyckoff atomic positions 4a (0, 0, 0), 4b (1/2, 1/2, 1/2), 4c (1/4, 1/4, 1/4) and 4d (3/4, 3/4, 3/4) are occupied by Z, Y, X and X', respectively, in $XX'YZ$ alloys ($X = \text{Ni}$, $X' = \text{Co}$, $Y = \text{Mn}$ and $Z = \text{main group element}$) [31]. As in ternary alloys, in quaternary alloys, B2-type structural disorder appears with variation of the Z element, particularly Al.

The martensite structure varies from a body-centered tetragonal (with $c/a < 1$) and is modulated along the $\langle 100 \rangle$ crystallographic direction of $L2_1$ lattice for stoichiometric alloys to layered 5M or 7M structures, or even unmodulated body-centered tetragonal ($L1_0$, with $c/a > 1$) for compositions different from stoichiometric. The martensite structure also varies with the dopant and its concentration. It is interesting to note that depending on the temperature of martensitic transformation M_s , the martensite is five-layered for both stoichiometric and off-stoichiometric compositions below M_s , five- or seven-layered near M_s and seven-layered/10M/unmodulated above M_s [30]. The $L2_1$ structure of austenite [32] is shown in Figure 1a. The 5M (also referred to as 10M) and 7M (also referred to as 14M) modulated structures of martensite are shown in Figure 1b. Martensitic structures can even coexist in the same composition, e.g., 6M and 10M [9] and 10M and 14M [33]. The different stacking sequences of the martensite are evaluated on the basis of the 2M structure, which has a unique lattice correspondence with the $L1_0$ structure [34].

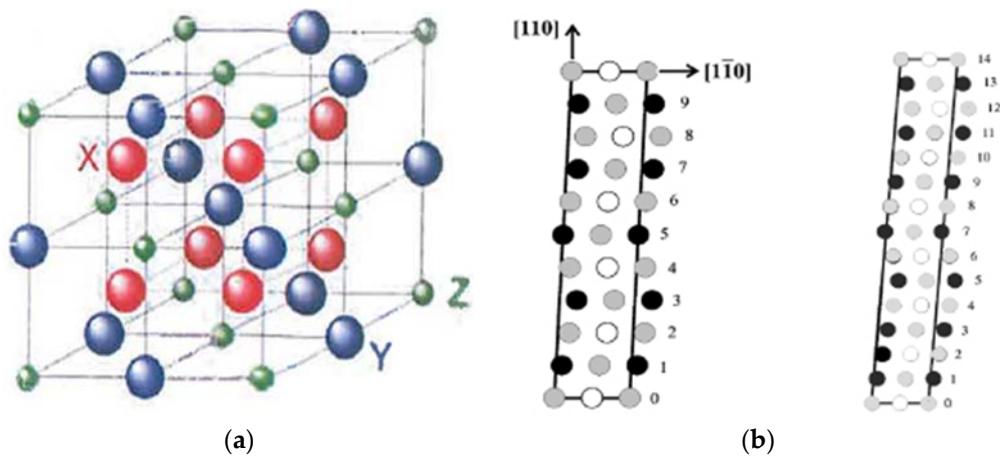


Figure 1. (a) The $L2_1$ structure representing the crystalline structure of austenite [32], with copyright permission from © Trans Tech Publications; (b) the 5M and 7M modulated structures of martensite. Light grey—X, white—Y, black—Z [2], with copyright permission from © IOP Publishing.

The structural modulations of the martensite are periodic stacking faults of atomic planes along determined crystallographic directions, seen as extra reflections in XRD and TEM characterization [35]. These reflections enable the modulations to be represented as nM , indicating n -fold modulation, where $n = s + 1$ (s ' being the satellite spots lying between main spots) is the number of unit cells that constitute the superstructure, as in 5M, 6M, 7M, 10M and 12M martensite with 5, 6, 7, 10 and 12 unit cells, seen in Figure 2a. On the other hand, the Zhdanov notation identifies the modulation of martensitic structures as a series of numbers indicating the atomic layers in a periodic shift corresponding to the fundamental lattice vector, with the minus sign indicating the opposite shift and the suffix indicating the number of zigzag motifs which make up the crystal lattice, shown in Figure 2b. However, the incommensurateness associated with the structure is best described by the $(3 + 1)$ superspace approach. An additional supplementary vector (modulation vector) is used to index the weak diffraction peaks seen in the diffraction data. The generic diffraction vector H becomes

$$H = ha^* + kb^* + lc^* + mq$$

where $q = \alpha a^* + \beta b^* + \gamma c^*$.

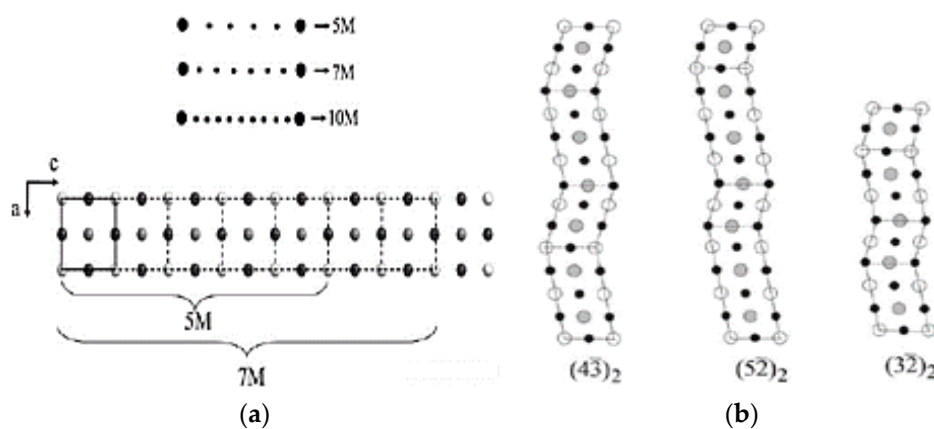


Figure 2. (a) Graphical representation of the $nM = s + 1$ relationship; (b) three examples of Zhdanov sequences of martensitic layered surfaces—7M and 5M modulations [35], with copyright permission from © Trans Tech.

Each Bragg reflection has four indices $hklm$ corresponding to a^* , b^* , c^* (conventional lattice) and q . When coefficients α , β and γ correspond to a rational number, the modulation is commensurate, and when they correspond to an irrational number, the modulation is incommensurate, requiring the introduction of superspace [35].

2.2. Magnetostructural Coupling and Magnetic Behavior

The mechanism of magnetostructural coupling in Heusler materials is very startling. Physicists and materials scientists have used density functional theory (DFT), ab initio methods and several approximations of DFT, such as the Perdew, Burke and Ernzerhof (PBE) functional, to understand magnetostructural coupling and determine the underlying principles which govern it. The magnetic ordering is reported to occur through an indirect oscillatory Ruderman–Kittel–Kasuya–Yosida (RKKY) exchange interaction [13,19], since there is no direct overlap between neighboring magnetic electrons. This magnetic ordering induces a hybridization of the electronic states through band Jahn–Teller (J–T) effect [36,37], which influences the martensitic transformation. In Heusler alloys, the magnetic moments are localized at the d states of Mn atoms. These localized moments overlap to cause ferromagnetic ordering. However, the shortest distance between Mn–Mn atoms is ~ 4.2 Å, which is insufficient for a direct overlap of the localized moments. Therefore, spin polarization of conduction electrons induced by the localized moments indirectly link the actual localized moments to create either a ferromagnetic/antiferromagnetic order [13]. Mn–Mn pairs at 4a (0, 0, 0) positions couple ferromagnetically and close neighbors Mn–Mn pairs at 4a–4b (0, 0, 0–1/2, 1/2, 1/2) positions couple antiferromagnetically. The martensitic transformation itself is known to occur in Heusler alloys at off-stoichiometric compositions. The magnetic moments from local distortions evident from shorter Ni–Mn bond distances cause hybridization between the Mn(d) and Ni(d) states at or near Fermi level and influence the martensitic transformation. In NiMnGa alloys, the hybridization is between spin-down $3d$ electrons of Ni and $4p$ electrons of Ga.

The magnetic order state of martensite is paramagnetic, mixed ferro-antiferromagnetic or even ferromagnetic. At lower temperatures, ferro- and antiferromagnetic components show up, leading to a complex state that is dependent on the doping element. Cong et al. reported martensite as paramagnetic, superparamagnetic (SPM) and superspin glass (SSG) in different temperature ranges during cooling [38] for compositions $0 \leq x \leq 8$ in the $\text{Ni}_{50-x}\text{Co}_x\text{Mn}_{39}\text{Sn}_{11}$ alloy system. SPM refers to the magnetic behavior with no magnetic hysteresis (zero remanence and coercivity). Its $M(H)$ curve fits the Langevin model given as

$$M(H) = N\bar{\mu}L(\xi) + \chi_0H$$

where $L(\xi) = \coth(\xi) - \frac{1}{\xi}$ is the Langevin function, $\xi = \mu_0\bar{\mu}H/k_B T$, χ_0 is the magnetic susceptibility, $\bar{\mu}$ is the average magnetic moment, μ_0 is the vacuum permeability, N is the cluster density of SPM clusters and k_B is the Boltzmann constant. SSG has a spin-configuration which is random in nature, similar to a paramagnet frozen in time [39]. SPM and SSG behaviors are understood from magnetic susceptibility measurements at lower temperatures and at different frequencies. SSG behavior is further explored from aging, rejuvenation and memory experiments conducted on a magnetometer. More information on the details of the experiments can be read in [38]. Additionally, the spin glass state occurs when the crystallite size is less than a critical value of 10 nm, with its morphology comprising a combination of small grains (<10 nm) and nanograins (~ 100 nm), as seen in electrodeposited Ni–Fe permalloy films [40,41]. Magnetic configurations in quaternary alloys are in accordance with the occupancy of the fourth element [42].

The formation of SSG or magnetic glass state is linked to isothermal transformation, wherein the austenite–martensite transformation is arrested when held isothermally in high magnetic fields. The knowledge of the kinetics of transformation becomes therefore necessary. Based on transformation kinetics, martensitic transformation is classified as either isothermal or athermal [43,44]. While in the former the amount of martensite formed depends on both time and temperature, in the latter it is dependent only on temperature, with both transformations influencing the electronic state of

ferromagnetic Heusler alloys [45]. The description of athermal transformation is contrary to thermally activated transitions, wherein the relaxation from a metastable state occurs due to thermal fluctuations. Attention is drawn to the fact that martensitic transformation occurs through a cooperative movement of a large number of atoms at intersonic speeds (speeds exceeding the materials shear wave velocity), implied from a report on twin motion being faster than the speed of sound [46]. The compositions of the product and parent phases are the same, which serves to exclude time-dependence of the transformation. The kinetics changes from isothermal to athermal in the presence of high magnetic fields [47]. From an analysis of Fe-Ni-Mn alloys, Kakeshita et al. proposed a model to explain the natures of both transformations [45]. Assuming that martensitic transformation may start when a minimum size of a cluster of particles is formed and simultaneously excited in the austenite, the model accounts for the presence or absence of a C-curve in the time-temperature-transformation (TTT) diagrams of isothermal and athermal transformations, respectively, by considering the temperature dependence of Gibbs chemical free energies, $\Delta G(T)$, of austenite and martensite (see Figure 3), in which isothermal transformation of the alloy formed an asymmetric C-curve, with the time required to form 0.1% volume fraction of martensite being different on the higher and lower temperature sides. Lee et al. also confirmed the formation of a C-curve in the TTT diagram of an $\text{Ni}_{45}\text{Co}_5\text{Mn}_{36.5}\text{In}_{13.5}$ alloy [48].

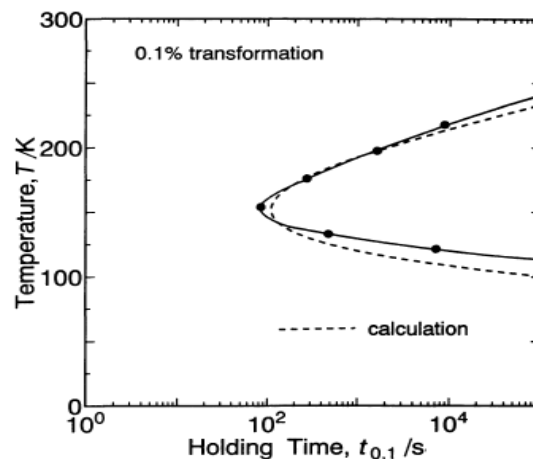


Figure 3. Time-temperature-transformation (TTT) diagram of the isothermal martensitic transformation in Fe-Ni-Mn alloy. Thick lines with closed circles represent measured values and dotted lines represent calculated values [45], with copyright permission from © JIM.

Several studies on isothermal/athermal martensitic transformation have been reported [49,50]. The kinetic arrest of martensitic transformation under a magnetic field during cooling and the subsequent increase in the amount of martensite phase during heating under zero magnetic field is attributed to the low mobility of the habit plane between austenite and martensite phases [51]. Thermomagnetization, electrical resistivity and X-ray structural analysis studies confirm the kinetic arrest phenomenon (incomplete transformation), in which the kinetics of the martensitic transition (first order) gets disrupted. The resulting low-temperature phase, which is not in an equilibrium state, has both fractions of the transformed stable martensite and metastable high-temperature austenite phases. The metastable state is referred to as magnetic glass, with the applied magnetic field either increasing or decreasing the kinetic arrest. This leads to the condition that when the alloy is cooled and heated in differing magnetic fields (H_C and H_W) [52], the de-arrest or unfreezing of magnetic glass happens and a re-entrant transition (reverse magnetic transition) happens for a critical value of (H_C and H_W).

3. Methods of Synthesis and Characterization

It is pertinent that the design aspects of an alloy system are known. Different ways of design are discussed which are central to synthesis and characterization of ferromagnetic Heusler alloys. An important characteristic of ferromagnetic Heusler materials is the reversibility of martensitic transformation that holds the key to the realization of coexistent phases with different electromagnetic properties [1]. Moreover, as the transformations are composition-dependent, tailoring the composition suitably will enhance the reversibility of the martensitic transformation such that switching between coexistent phases (austenite and martensite) occurs cyclically without any diminishing of properties, electromagnetic in particular. Mathematical conditions called cofactor conditions, adapted from the geometric nonlinear theory of martensite (GNLTM), provide a definite way to design highly functional alloys [53]. The geometrical conditions satisfy the premise that there should be no stressed transition layer between switching phases for the realization of least thermal hysteresis and enhanced reversibility.

The GNLTM solutions, as such, correspond to the twinning volume fractions, f and $1 - f$ [53]. When $f = 0$ or $f = 1$, the absence of an elastic transition layer between the austenite and the single variant martensite interface is possible when the middle eigenvalue λ_2 of a transformation stretch matrix 'U' (3×3 , obtained from X-ray measurements of lattice parameters and knowledge of space groups of the two phases) takes a value 1. For other volume fractions given by $0 \leq f \leq 1$, two additional conditions corresponding to different twin types are to be satisfied. The volume fraction of the twin variants can then be continuously varied, while at the same time keeping the low-elastic-energy interface with austenite [53]. Using these conditions on the basic $\text{Ni}_{50}\text{Mn}_{50-x}\text{Sn}_x$ alloy system, a composition $\text{Ni}_{45}\text{Co}_5\text{Mn}_{40}\text{Sn}_{10}$ was perfected with unusual magnetostructural properties [54]. The efficacy of the compatibility conditions have been proved experimentally in Zn-Au-Cu [53], Ti-Ni-Pd [55] alloys and used in modeling the austenite–martensite interface in shape memory materials [56].

Another approach to synthesis of ferromagnetic Heusler materials is by the combinatorial approach, which accelerates the discovery and optimization of known and new materials by combining efficient synthesis of a large number of different material compositions and high-throughput property screening methods to delineate composition–structure–property relationships and hence identify compositions with desired properties [57]. Combinatorial materials synthesis combined with GNLTM will certainly help in accelerated discovery of new and highly multifunctional Heusler alloys. More about combinatorial materials synthesis is detailed in Section 3.1.

It is possible to predict compositions having room temperature martensitic transformations or martensitic structures through the determination of the valence electron concentration per atom, written as the e/a ratio. An e/a value of 7.6 favored room temperature martensitic transformations [58]. The structure changed from cubic–10M–14M–L1₀ in accordance with an increasing e/a ratio and temperature [2], as shown in Figure 4.

The e/a ratio is calculated as concentration-weighted average of the valence (s, p and d) electrons using the expression

$$\frac{e}{a} = f_{\text{Ni}}e^{\text{Ni}} + f_{\text{Mn}}e^{\text{Mn}} + f_{\text{X}}e^{\text{X}} + f_{\text{Z}}e^{\text{Z}}$$

where f_{Ni} , f_{Mn} , f_{X} , f_{Z} represent the atomic fractions of the elements, e^{Ni} , e^{Mn} , e^{X} , e^{Z} are the corresponding numbers of valence electrons and, X, Z represent the third and fourth elements of a quaternary alloy, respectively.

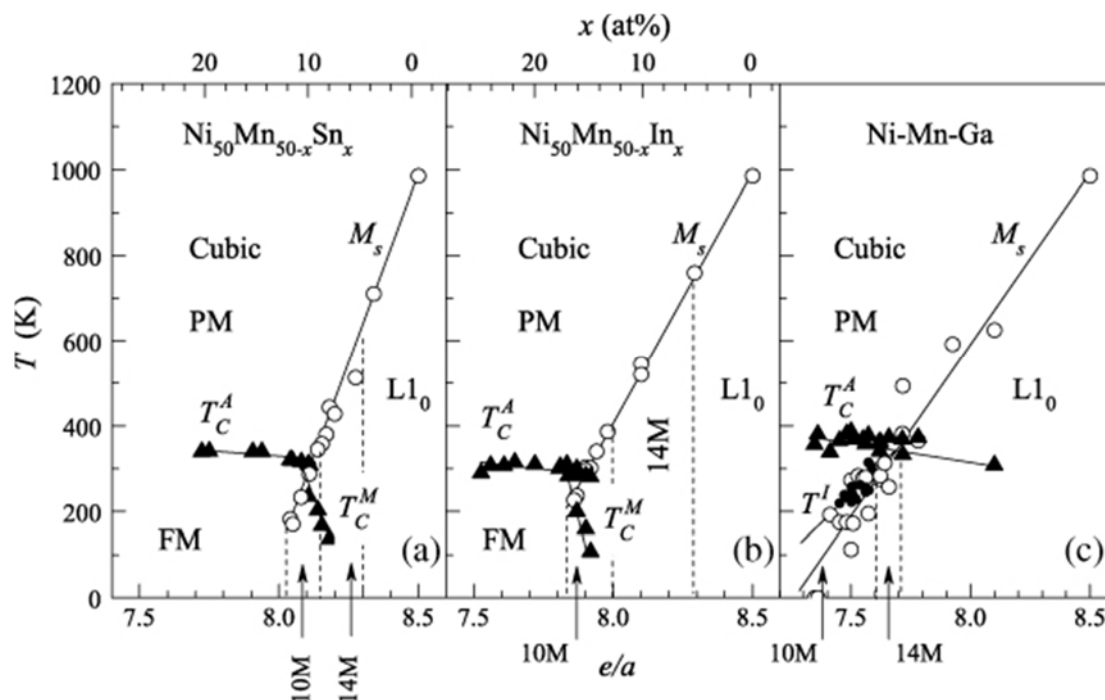


Figure 4. The magnetic and structural phase diagram of Ni-Mn-Z Heusler alloys with Z as: (a) Sn; (b) In; (c) Ga. The triangles and circles correspond to the magnetic and martensitic transformation temperatures, respectively. The regions corresponding to the different structures are separated by discontinuous lines [2], with copyright permission from © IOP Publishing.

Phase equilibria information about Ni–Mn-based alloys, which would equip researchers in alloy development, is scarce. The work by Yang et al. in consolidating the phase equilibria of the Ni–Mn–Ga system, using the equilibrium compositions obtained from the diffusion couples and two-phase alloys, highlights critical compositions favoring near room temperature martensitic transformations as those with e/a of 7.6 [58]. A similar work on Ni–Mn–In alloy system confirmed a single β phase region existing over a composition range of 0–20 atom % In, in addition to the martensite [59]. Microstructure observation with magnetic colloid (Magnetic colloid refers to a technique of observation of magnetic structures smaller than 100 nm. Ferrofluids with magnetic particles like Fe_3O_4 , $\gamma\text{-Fe}_2\text{O}_3$ or metallic particles of iron, nickel or cobalt having 10–15 nm diameter dispersed in water or an inorganic liquid are used for imaging the fields of magnetization. The particles in the ferrofluid interact by magnetic forces and by electrostatic and van der Waals forces. The liquid is usually dried up or rinsed, leaving the colloid particles to form Bitter patterns, after F. Bitter) [60] yielded a critical boundary between the ferromagnetic and paramagnetic phases spread over a wide composition range from the Ni-rich region to the Mn-rich region.

However an isothermal section of the Ni–Mn–In ternary phase diagram at 773 K showed a host of single, two- and three-phase regions [61] with no bearing on the martensitic and magnetic behavior. A vertical section of the $\text{Ni}_{50}\text{Mn}_{50-x}\text{Sn}_x$ system ($0 \leq x \leq 50$ atom %) drawn from magnetic susceptibility measurements and saturation magnetization vs. temperature, structural and X-ray investigations also identifies different low- and high-temperature phases as also a face-centered cubic γ phase at small Sn concentrations [62]. Martensitic structures formed after annealing at high temperatures followed by quenching in water for Sn content from 0 to 11 atom %. Phase diagrams showing both high- and low-temperature regions of $\text{Ni}_{50-x}\text{Co}_x\text{Mn}_{39}\text{Sn}_{11}$ quaternary Heusler system enhance the understanding of the composition and temperature-dependent functional properties and associated physical phenomena [38], shown in Figure 5.

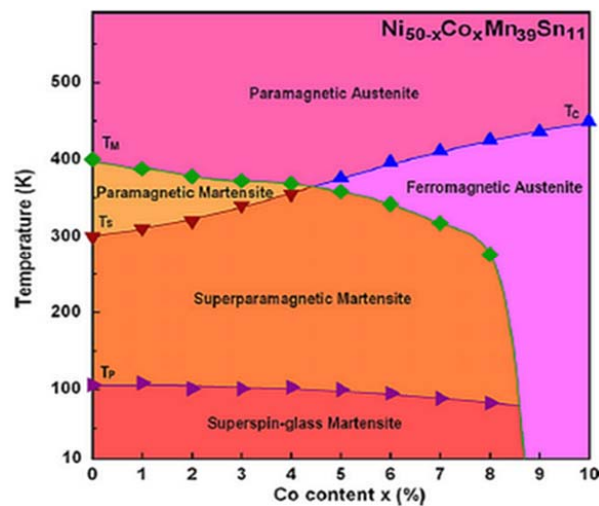


Figure 5. Phase diagram of $\text{Ni}_{50-x}\text{Co}_x\text{Mn}_{39}\text{Sn}_{11}$ ($0 \leq x \leq 10$) alloy system [38], with copyright permission from © Elsevier.

3.1. Synthesis

Ferromagnetic Heusler materials are synthesized through both liquid and solid processing routes. The commonly employed processing route is melting and casting [63]. The techniques include arc/induction melting under controlled conditions and rapid solidification by melt spinning. Directional solidification using Bridgman–Stockbarger [64] and Czochralski [65] techniques also have been used. Solid processing is by powder metallurgy (P/M) using alloy [66] and elemental [67] powders. Sintering techniques include pressureless sintering [68,69], spark plasma [70] and solid-state replication to obtain a porous alloy sample [71].

Liquid processing route has been predominantly applied in synthesizing the Heusler alloys primarily because of the compositional homogeneity obtained after several rounds of remelting. The alloys are melted, turned over and remelted in arc or induction melting furnaces, either in vacuum or an inert atmosphere. The arc melting furnace uses an electric arc struck between an electrode (tungsten) and the metal mix placed in crucibles for melting where temperatures in excess of $2500\text{ }^\circ\text{C}$ can be reached. Induction melting, on the other hand, combines the advantages of a controlled atmosphere and control of the melting process, where heating is by eddy currents from an induction coil with no direct contact between the metal and coil. The process capability is defined by temperatures of up to $2000\text{ }^\circ\text{C}$ that can be reached [72].

Liquid processing yielded multiphase microstructures, as can be seen from the investigations by several researchers. $L2_1$ /martensite, DO_3 and γ (disordered fcc) phases were observed in the as-cast microstructures of various Ni-Co-Mn-Sn alloys [73], shown in Figure 6a,b. Cong et al. reported the presence of unidentified second-phase particles, even after annealing in quaternary $\text{Ni}_{50-x}\text{Co}_x\text{Mn}_{39}\text{Sn}_{11}$ alloy system for $x = 9$ $x = 10$ [73]. Ni-Mn-Sn alloys solidified as multiphase microstructures, which affected both the phase stability of the $L2_1$ phase and martensitic transformation [74]. Cubic DO_3 , $L2_1$ and hexagonal DO_{19} phases were reported in $\text{Ni}_{75-x}\text{Mn}_x\text{Sn}_{25}$ ($0 \leq x \leq 40$) alloys [75]. The multiphase microstructures, however, changed to single-phase microstructures upon annealing. The vertical section of the phase diagram of the $\text{Ni}_{50}\text{Mn}_{50-x}\text{Sn}_x$ ($0 \leq x \leq 50$) alloy system in Figure 6c shows the as-solidified alloy changing to a single-phase structure [62]. If the compositional variations are still seen, it is because chemical variations require longer annealing treatments than the time scale for structural conversion.

Since phase transformations in ferromagnetic Heusler alloys are highly composition-dependent, it is necessary that chemical variations are equilibrated over extended time scales through long annealing treatments and not limited to shorter time scales used for structural conversion in order

that compositional homogeneity is achieved [76]. The magnetic and structural transitions then become distinct. Figure 7a shows the as-cast structure of $\text{Ni}_{50}\text{Mn}_{37}\text{Sn}_{13}$ ternary alloy which exhibited multiphase microstructure, which changed to single-phase microstructure rapidly upon annealing. Figure 7b shows of the sample annealed at 950 °C for 72 h, during which the compositional variations were eliminated. Extended annealing periods of up to 4 weeks sharpened the thermal peak of martensitic transformation, shown in Figure 7c, which was a result of homogenization occurring through the duration of annealing [76].

Another dimension to synthesis of polycrystalline magnetic shape memory alloys is the application of directional solidification to prepare highly oriented alloys [64]. These alloys exhibit a large pseudoelastic recovery besides chemical segregation, or a composition gradient due to which changes in transformation temperatures are obtainable. Czochralski and Bridgman–Stockbarger techniques are the two widely employed techniques of directional solidification for synthesizing ferromagnetic shape memory alloys. The Bridgman–Stockbarger method has a high-temperature zone, an adiabatic loss zone and a low-temperature zone. While Czochralski technique is known for its relatively high growth rate, modified Bridgman–Stockbarger technique employs gradient freezing, which requires no translation of either the crucible or furnace, and temperature gradient is affected through programmed control of the multiple heat zones in the furnace. A schematic of the Bridgman–Stockbarger method [77] is shown in Figure 8.

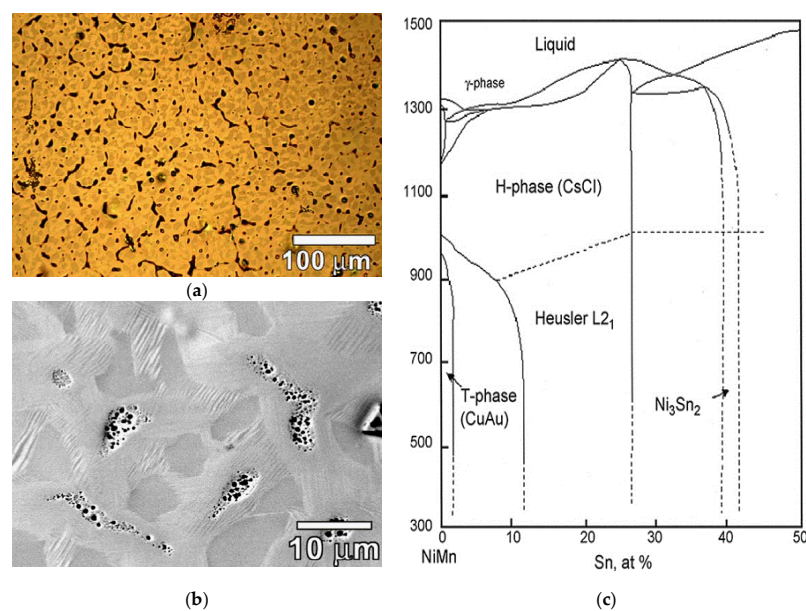


Figure 6. (a) Optical micrograph of as-cast $\text{Ni}_{44.5}\text{Co}_{5.5}\text{Mn}_{39.5}\text{Sn}_{10.5}$ alloy [73], with copyright permission from © Elsevier; (b) SEM micrograph of the as-cast alloy [73], with copyright permission from © Elsevier; (c) vertical section of phase diagram [62], with copyright permission from © Elsevier BV.

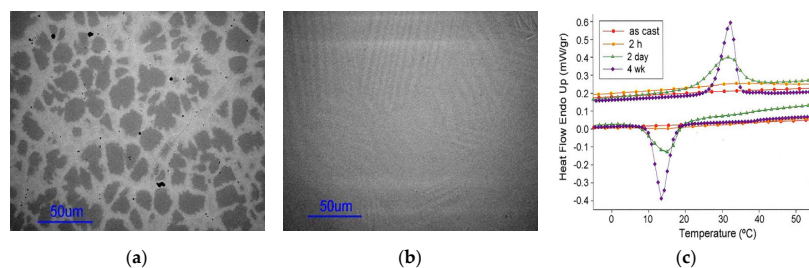


Figure 7. (a) As-cast; (b) heat-treated for 72 h; (c) differential scanning calorimetry (DSC) data showing the effect of heat treatment [76], with copyright permission from © Elsevier BV.

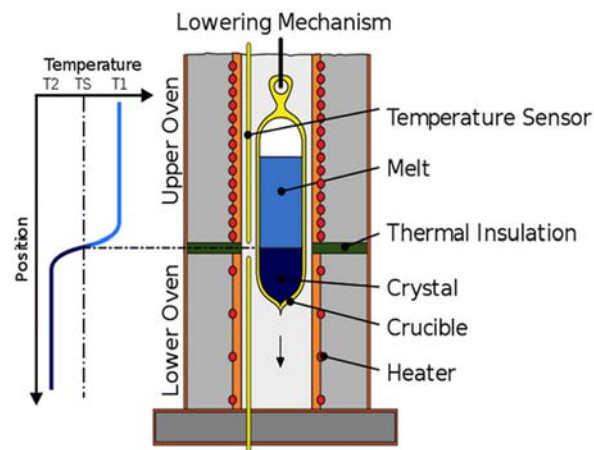


Figure 8. Schematic of the Bridgman–Stockbarger method [77].

A unidirectional crystal of $\text{Ni}_{40.6}\text{Co}_{8.5}\text{Mn}_{40.9}\text{Sn}_{10}$ grown using Bridgman–Stockbarger technique [64] yielded a microstructure which had no secondary γ phase precipitate, as seen in Figure 9a. The resulting compositional segregation with an increase in Ni, Sn and decrease in Mn, Co, as shown in Figure 9b, induced a steplike martensitic transformation, shown in Figure 9c, which broadened the working temperature range for magnetic entropy [64]. The magnetic entropy change and refrigeration capacity were better than those in $\text{Ni}_{40}\text{Co}_{10}\text{Mn}_{40}\text{Sn}_{10}$ [78], $\text{Gd}_5\text{Ge}_2\text{Si}_2$ [79] and $\text{Ni}_{50}\text{Mn}_{36}\text{Sn}_{14}$ [80] alloys, reported for their exceptional magnetocaloric properties. The functional properties of magnetic shape memory alloys are usually best seen in single crystals, as in [81].

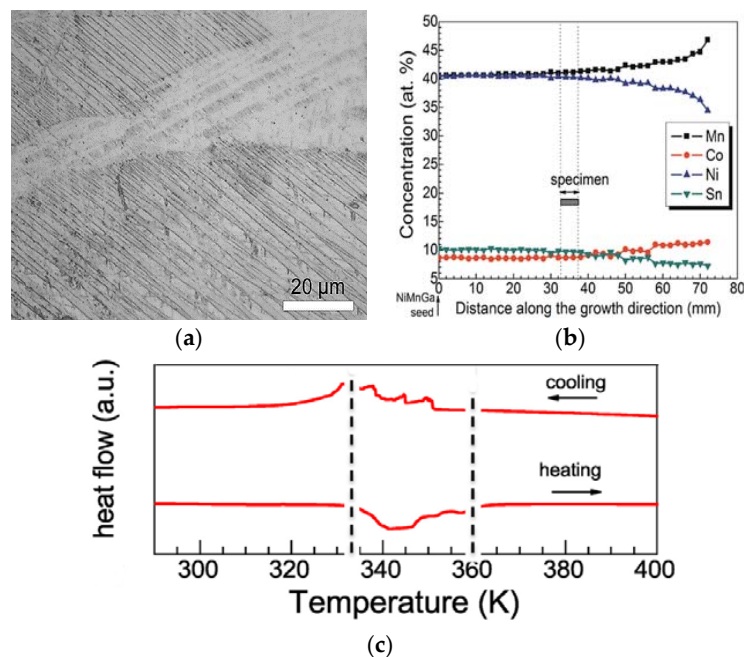


Figure 9. (a) Microstructure of directionally solidified alloy; (b) composition profile along the growth direction; (c) DSC curves across the structural transition [64], with copyright permission from © Elsevier BV.

Other synthesis methods which have been used on ferromagnetic shape memory alloys are hot-forging and rolling, where the resultant strong textures and large in-plane plastic flow anisotropy are attributed to the rearrangement of martensitic variants during the thermomechanical

processes [82–84]. The Taylor–Ulitsky method of fabricating glass-coated microwires [85] is increasingly being applied on MCE materials [86–90]. The process, which has a capability of up to 10,000 m of continuous microwire, consists of induction heating a few grams of the master alloy in a borosilicate glass tube. As the alloy is melted, the glass tube softens around the molten alloy droplet, from which a glass capillary is drawn out with the alloy filling the capillary and forming a microwire. The microwire has the glass shell surrounding the alloy (metal) core. The formation of the core is limited by the initial amount of master alloy and its microstructure is dependent on the rate of cooling [85] as it is wound on a receiving coil. The microstructure of as-cast microwire of $\text{Ni}_{49.5}\text{Mn}_{25.4}\text{Ga}_{25.1}$ was seen to consist of two phases—tetragonal $I4/mmm$ and cubic $Fm3m$ [86], which, after annealing, turned into single phase favoring martensitic transformation.

Rapid solidification processing with solidification rates ranging from $10^2 \text{ K}\cdot\text{s}^{-1}$ to $10^{14} \text{ K}\cdot\text{s}^{-1}$ [91] has been a very useful method for preparing ferromagnetic Heusler alloys. The characteristics of rapid solidification processing are extension of solid solubility limits, microstructural refinement and formation of nonequilibrium phases, such as metastable intermediate phases, metallic glasses and quasicrystalline phases with crystallographically forbidden 5-fold, 10-fold and other symmetries [91]. The discussion about crystallographically forbidden lattices is beyond the scope of this overview, even though such microstructures are not reported in Ni–Mn-based Heusler alloys as they transform to modulated, commensurate/incommensurate $6M$, $10M$, $14M$, $4O$ or $L1_0$ martensitic structures. Crystallographically forbidden lattices in conventional shape memory materials, such as Cu–Al–Ni [92] and Cu–Zn–Al [93] alloys, modify the normal $2H$ (orthorhombic) microstructure of the martensite.

Melt-spinning as a rapid solidification technique is gaining wide acceptance in synthesizing Heusler alloys [94–96] for varying reasons, such as obtaining textured samples suitable for practical utilization as sensors, actuators and magnetocaloric materials which optimize the heat transfer in a refrigeration unit [97–99]. Furthermore, it lends credence to the fact that the processing methods can tailor the functional attributes of Heusler alloys by controlling the lattice parameters, interatomic distance, degree of atomic ordering and microstructure. It is primarily employed to control the grain size of the austenite phase. This is because the martensitic transition can occur only when the austenite grain size is bigger than the martensite plate [100]. Also, homogeneity in terms of grain size and elemental composition is achieved by melt spinning [100]. Another reason for using melt spinning is that it favors avoidance of prolonged annealing.

Synthesis by melt spinning is by allowing the alloy melt stream jet to solidify rapidly on a fast-rotating and thermally conducting substrate to produce a continuous strip or ribbon of the alloy up to 500 mm in width [91]. Wheel speed, nozzle size, ejection pressure and material of the rotating substrate (wheel) are some of the parameters which influence the process. Typical wheel speeds vary from 10 m/s to 60 m/s and the substrate is usually copper. Melt spinning has the effect of eliminating the secondary γ phase in $\text{Ni}_{38}\text{Co}_{12}\text{Mn}_{41}\text{Sn}_{19}$ alloy as a result of which an enhancement of magnetocaloric properties equivalent to the bulk alloy was observed [101]. The effective refrigeration capacity (RC_{eff}) values of ~ 48.8 and 47.8 J/kg were obtained for as-spun ribbons and annealed ribbons prepared at 15 m/s and 25 m/s, respectively [99]. The MCE characteristics of as-cast and annealed melt-spun $\text{Ni}_{50}\text{Mn}_{35}\text{In}_{14.5}\text{B}_{0.5}$ alloy ribbons, in which the isoelectronic B is substituted for In, were identical to the bulk alloy. A relative cooling power of 150 J/kg for annealed ribbons was reported [102].

Solid processing using P/M has also been applied to synthesize both conventional [103–108] and ferromagnetic shape memory materials [66–71], although its application has been widespread in the former category. Apart from the application of P/M in conventional shape memory materials, its observed benefits have been the ability to obtain the desired martensitic transformation temperatures, transformation width (range) and hysteresis, as in Cu–Al–Ni [109], drop in transformation temperatures, as in Ti–Ni–Cu [110] and, more importantly, significant reduction in the number of secondary phases using vapor phase calciothermic reduction (VPCR) in solid-state sintering of $\text{Ni}_{50}\text{Ti}_{50-x}\text{Zr}_x$ [111].

Synthesis of ferromagnetic Heusler alloys by P/M is often not the preferred choice of processing because it resulted in incomplete martensitic transformation [66] or evolved secondary phases [70], which are detrimental to the magnetostructural transformation and properties. Nevertheless, application of P/M in the case of ferromagnetic Heusler alloys opens opportunities for interested researchers. With pressureless sintering of porous samples of $\text{Ni}_{43}\text{Co}_7\text{Mn}_{39}\text{Sn}_{11}$ alloy powders at 1173 K, the porosity fraction decreased with the increase in the sintering time, from 65% at 12 h to 5% at 144 h [68]. Even though the microstructures in Figure 10a,b exhibited single-phase structures, still the shape memory property of the 12 h sintered sample was superior because dense specimens with grains surrounded by neighboring grains impose constraints during martensitic transformation. The microstructure of the same alloy composition sintered by spark plasma sintering is shown in Figure 10c. Concentrations of a precipitate phase rich in Co were observed. The compositional inhomogeneity due to the presence of a second phase and contamination by the graphite die during the spark process resulted in an imperfect shape memory effect [70].

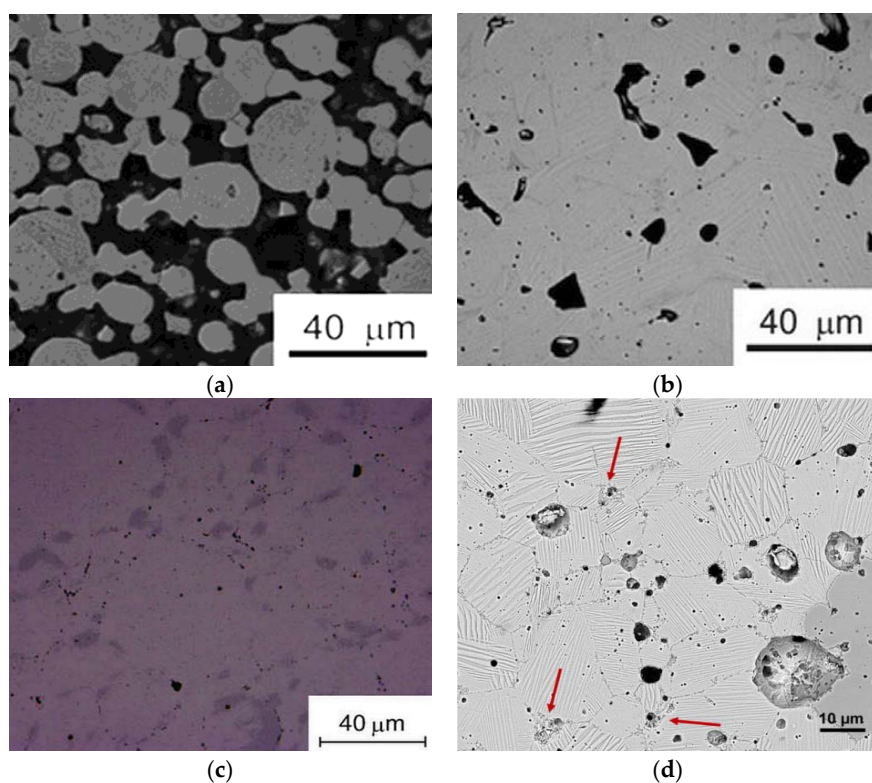


Figure 10. Porous sample sintered for: (a) 12 h; (b) 144 h [68], with copyright permission from © Pergamon; (c) sample synthesized by spark plasma sintering [70], with copyright permission from © Pergamon; (d) microstructure of the quinary alloy synthesized by powder metallurgy (P/M) [67], with copyright permission from © Elsevier S.A.

It is well known that P/M methods are advantageous in terms of composition control. Furthermore, use of elemental powders instead of alloy powders can ensure substantial composition control while, at the same time, making P/M processes more cost-effective. Elemental powders, in addition, are easier to mix than alloy powders, which are harder and with poor compaction characteristics. Synthesis and characterization of a quinary Ni-Co-Mn-(Sn,Cu) alloy from elemental powders using P/M amply demonstrated the usefulness of the solid state processing method [67]. The alloy exhibited martensitic transformation, 6M martensite and magnetic field-induced transformation, seen in Figure 10d. However, analogous to the spark plasma sintered sample [70], the addition of a fifth element to the quaternary alloy, the existence of a multiphase microstructure

(shown by red arrows) and grain growth affected the magnetostructural characteristics, which were reflected in the saturation magnetization not being similar to the bulk alloy. Thus, for solid state processing to become the preferred choice of synthesis of ferromagnetic shape memory alloys, compositional homogeneity through elimination of second phases by secondary heat treatment and inhibiting grain growth by secondary thermomechanical treatments are critical for identical magnetostructural characteristics, as in bulk alloys, to be apparent.

In the combinatorial approach of materials synthesis, a large number of different materials are synthesized by advanced fabrication methods on a single substrate under identical conditions and are subsequently screened for properties by parallel or fast sequential methods of high-throughput characterization. Combinatorial thin-film fabrication methods include physical vapor deposition, chemical vapor deposition, ion implantation and other continuous/discrete composition methods. Automated energy dispersive spectroscopy, X-ray diffraction, focused ion beam machining for TEM investigation and temperature-dependent magnetoelectronic property measurement are some of the high-throughput characterization techniques. Critical reviews of the combinatorial thin-film materials science [57] and combinatorial approaches for the high-throughput characterization of mechanical properties [112] add to the understanding.

Composition-spread method, which is a continuous composition technique of thin-film synthesis based on co-deposition, is the most common synthesis method employed on shape memory and ferromagnetic shape memory materials. The schematic of the technique is shown in Figure 11.

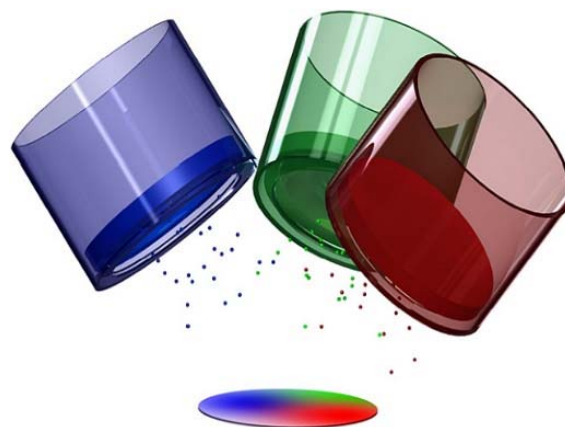


Figure 11. Schematic of the composition-spread method with three vapor sources [57], with copyright permission from © Elsevier S.A.

This system is capable of sequential sputtering with six magnetron cathodes arranged along a movable arm sequentially depositing layered films on a substrate. Four computer-controlled shutters move during the deposition to create wedge-shaped thickness gradients across the substrate [113].

Phase transformation characteristics of conventional shape memory alloys systems Ti-Ni-Cu and Ti-Ni-Pd for microactuator applications were investigated using composition-spread technique and high-throughput characterization by cantilever deflection methods and automated measurements [113,114]. With GNLTM, a combinatorial approach in ternary Ni-Ti-Cu and Ni-Ti-Pd systems [115], as well as in quaternary Ti-Ni-Cu-Pd shape memory alloy systems [116], yielded alloy compositions with thermal hysteresis width ($\Delta T = A_f - M_s$) converging to zero, close to $\lambda_2 = 1$. Figure 12a shows thermal hysteresis width values on a pseudoternary Ni-Cu-Pd phase diagram, which itself is a projection of the quaternary composition tetrahedron with Ti content limited to 47–67 atom %. Compositions with near-zero ΔT are shown in blue. Figure 12b shows ΔT vs. λ_2 plots of various ternary and quaternary alloy compositions, with the ΔT values converging to zero for quaternary compositions close to $\lambda_2 = 1$.

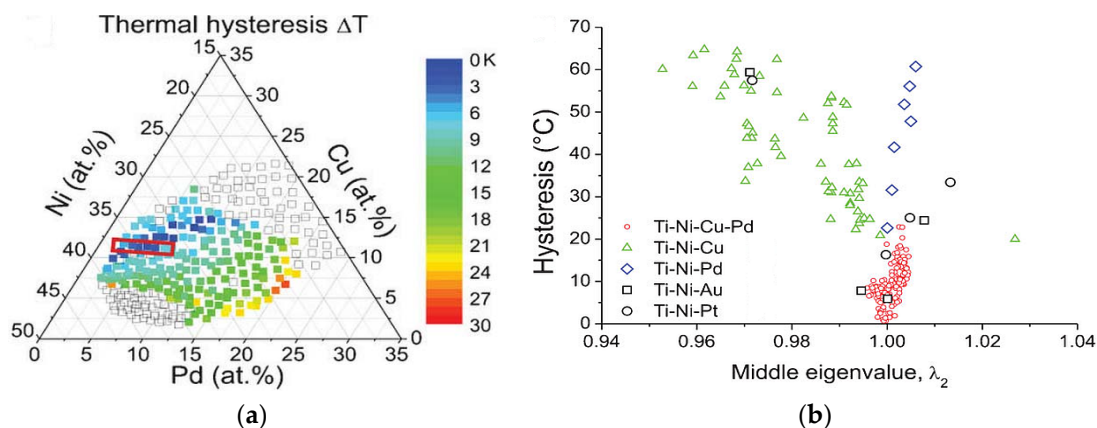


Figure 12. (a) ΔT values on a pseudoternary projection of the quaternary composition tetrahedron with the red box highlighting compositions for which ΔT approached zero; (b) thermal hysteresis values in Ti–Ni-based ternary and quaternary shape memory alloys [116], with copyright permission from © IOP Publishing.

Thin-film composition-spreads deposited on micromachined arrays of cantilevers were screened using scanning superconducting quantum interference device (SQUID) microscope and X-ray microdiffractometer to map the functional phase diagram of the Ni–Mn–Ga ferromagnetic shape memory alloy system [117]. Figure 13a shows the Ni–Mn–Ni₂Ga₃ spread deposited on the cantilever library. Figure 13b shows the functional diagram, with the hatched region comprising compositions with average e/a ratio of 7.3–7.8, dotted line surrounding the region of reversible martensites and the red region having the highest magnetization in the yellow ferromagnetic region. A similar study was conducted on Ni–Mn–Al alloy system, where it was seen that both ferromagnetic and shape memory properties coexisted [118]. High-throughput screening using nanoindentation was performed on Ni–Mn–Al thin-film composition spreads to delineate martensitic regions, which were found to have low elastic modulus and hardness [119].

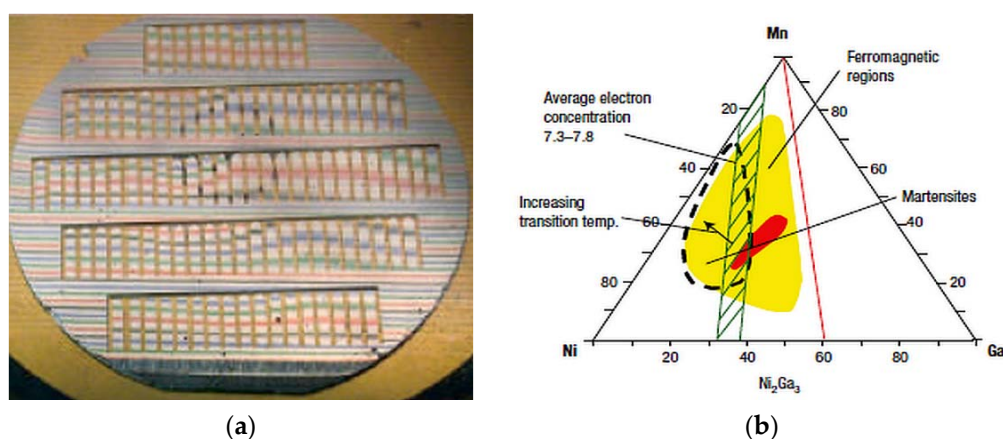


Figure 13. (a) Photograph of the cantilever library; (b) functional phase diagram of the Ni–Mn–Ni₂Ga₃ alloy system [117], with copyright permission from © Nature Publishing Group.

3.2. Characterization

In this section, we discuss how the different techniques of characterization have contributed to the understanding of several issues concerning magnetostructural behavior in ferromagnetic Heusler alloys from physical and metallurgical perspectives.

Differential scanning calorimetry (DSC) is a technique of thermal analysis which measures, depending on whether heat is absorbed or liberated, the enthalpy of phase transformation in a structurally transforming material as a function of time and temperature. It is often the first step in the characterization sequence, used for the determination of the martensitic and magnetic transition temperatures, heat flow curves, thermal hysteresis and enthalpy/entropy changes in ferromagnetic Heusler alloys [120–123]. Compositional dependence of martensitic transformation [124], progressive evolution of the martensitic transformation behavior in response to increasing Co content in $\text{Mn}_{50}\text{Ni}_{40-x}\text{In}_{10}\text{Co}_x$ [125] and the mechanism of suppression and recovery of martensitic transformation in NiCoMnIn alloys fabricated under nonequilibrium conditions [126] have been established using DSC. The suppression occurs when dendrite-like precipitates hinder the martensitic transformation [126].

An irreversible transformation of face-centered tetragonal (f.c.t) martensite to a body-centered martensite (b.c.t) at low temperature in a martensite-to-martensite transformation in Fe–Pd alloys has been captured using DSC [127]. Subsequent aging treatments stabilize the f.c.t martensite at low temperatures, which again has been determined using DSC [127]. The isothermal (time-dependent) nature of martensitic transformations was observed from elaborate interrupted forward and reverse transformation sequences carried out using DSC [50]. The transformation behavior of $\text{Ni}_{43}\text{Co}_7\text{Mn}_{41}\text{Sn}_9$ alloy after a full transformation cycle is shown in Figure 14a, and during interrupted cooling in Figure 14b–l. The interrupted transformation is shown as comprising two stages—part P1 (austenite) to M1 (martensite), and the remaining part P2 (austenite) to M2 (martensite) later during the interrupted process.

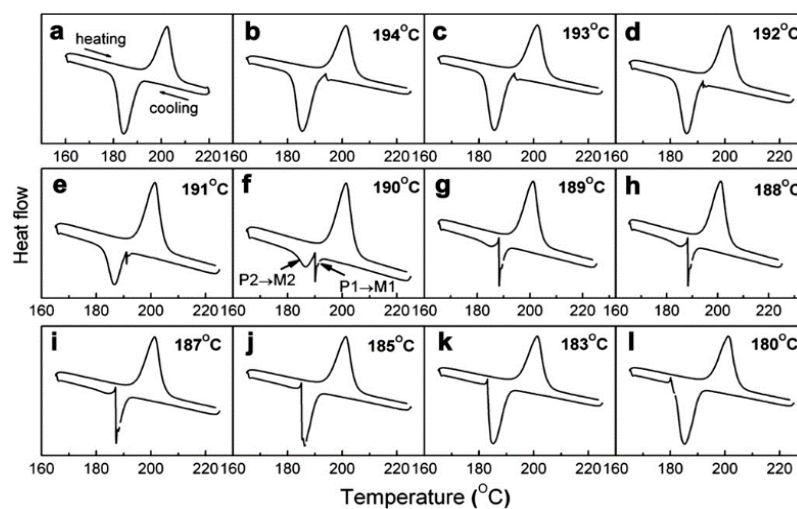


Figure 14. DSC curves of the transformation behavior of the $\text{Ni}_{43}\text{Co}_7\text{Mn}_{41}\text{Sn}_9$ alloy measured: (a) after a full transformation cycle (b–l) and during interrupted cooling [50], with copyright permission from © Elsevier Ltd.

Figure 15 shows the latent heat values of P1–M1, P2–M2, total latent heat and reverse latent heat after interrupted cooling as a function of amount of M1 formed. Not shown is a similar interrupted heating process. From both the sequences it was seen that the transformations continued to completion (ΔQ_R constant in all interrupted cycles in Figure 15) demonstrating the time-dependence of austenite–martensite transformation at finite cooling rates [50]. However, the authors refute the findings that the time-dependent sequences of the transformations are just “artefacts” in which the latent heats of transformation dissipate by “inertia” continuation during thermal equilibration, which again are due to metallurgical causes. Identical experiments on NiTi and NiCoMnIn alloys [128] evaluate the latent heats, shown in Figure 16, of transformation in a supposedly thermal inertia-driven isothermal behavior.

Microscopy, including in situ microscopy and diffraction techniques, provides insight into the field-induced effects in both real and reciprocal space, respectively. Metallurgical samples are usually examined in reflection because the conduction electrons render metals opaque to visible light [129] and, consequently, the contrast seen in optical micrographs is topological. The characterization of martensitic structures as $L1_0$, $14M$, $10M$ and $L2_1$ for $x = 0.05, 0.10, 0.13$ and 0.25 , respectively, in $Ni_{0.50}Mn_{0.50-x}Sn_x$ alloys [130] and/or multiphase microstructures in $Ni_{45}Co_5Mn_{40}Sn_{10}$, $Ni_{44.5}Co_{5.5}Mn_{39.5}Sn_{10.5}$ and $Ni_{43}Co_7Mn_{39}Sn_{11}$ alloys, which included an fcc γ -phase representing decreases in Ni and Sn and increases in Mn and Co in both as-cast and annealed samples [73], are examples wherein optical microscopy has been put into good use.

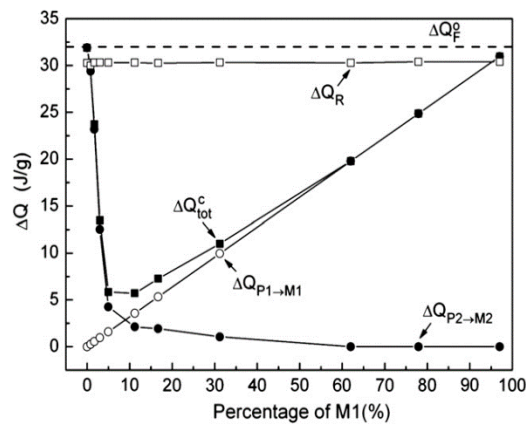


Figure 15. The absolute value of latent heat of P1–M1 and P2–M2, total latent heat and the reverse latent heat after interrupted cooling as a function of M1 percentage [50], with copyright permission from © Nature Publishing Group.

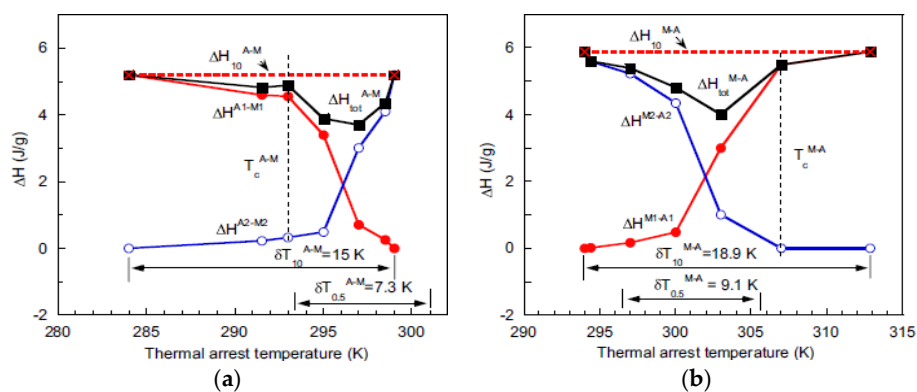


Figure 16. Absolute values of latent heat determined by interrupted measurement at different stages during: (a) forward and; (b) reverse $L2_1$ -orthorhombic martensitic transformation in $Ni_{43}Co_7Mn_{39}In_{11}$ at a cooling/heating rate of 10 K/min [128], with copyright permission from © Elsevier Ltd.

In situ optical microscopy conducted on $Ni_{45}Co_5Mn_{36.7}In_{13.3}$ alloys studies the magnetic field-induced transformation (MFIT) and heating-induced martensitic transformation (HIMT), also known as kinetic arrest (KA) [131]. During the field-induced transformation from martensite to parent phase, the parent phase freezes upon removal of the applied field and the reappearance of martensite phase is not until the sample is heated. A high-speed microscopic imaging system (HSMIS) capable of in situ microscopic examination under a pulsed high magnetic field and at extremely low temperatures [132] has been used in this study. Figure 17 shows how the parent phase freezes when the magnetic field became zero and unfreezes upon heating to 180 K, giving rise to heating-induced martensitic transformation.

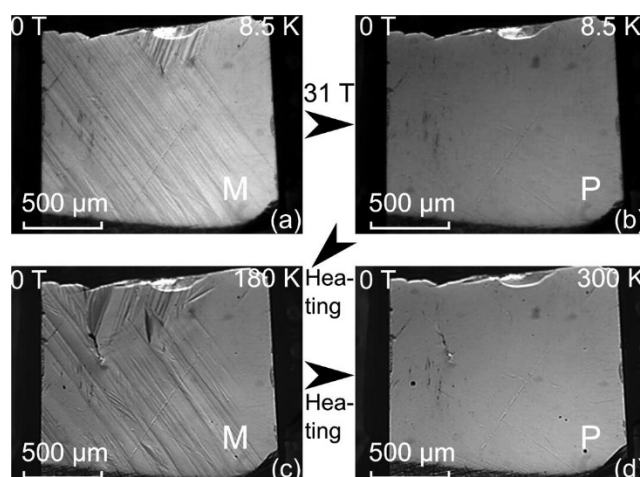


Figure 17. Micrographs: (a) before and (b) after a 31 T pulsed magnetic field application at 8.5 K. Parent phase (P—*austenite*) was arrested even when the magnetic field became zero in (b); (c) *martensite* phase obtained at 180 K out of an abnormal heating-induced transformation; (d) the *martensite* phase eventually transferred back to parent phase when further heated to 300 K [131], with copyright permission from © Pergamon.

X-ray and neutron diffraction techniques measure in reciprocal space and provide an understanding of the typical states of identical entities, such as *martensitic* twin variants. The diffraction spectrum from a crystalline material during X-ray diffraction testing can be represented by the Bragg condition $\lambda = 2d\sin\theta$, where λ is the wavelength of the incident wave, d is the interplanar lattice spacing and θ is half the angle between the incident and the scattered beam. The distance d between planes is a function of the Miller indices of the planes and the lattice parameters of the crystal lattice [133]. With a polychromatic incident beam, individual Bragg reflections from lattice planes with same interplanar spacing of d are used to characterize similar microstructural entities and monitor twin reorientation [26]. To measure magnetic moments of the individual twin variants, neutron scattering is best suited, as the neutrons carry a spin [26] and with spin-polarized neutrons the rotation of magnetic moments can be separated from the crystallographic twin reorientation.

Small-angle neutron scattering has been used to observe the existence of nanosomic magnetic clusters at low temperatures in ferromagnetic shape memory alloys, which, along with the magnetometry data, helps in understanding physical phenomena such as nanoscale magnetic inhomogeneity, spatial distribution of clusters, their mean spacing and diameter, nature of magnetic order in *martensite* matrix and the spatial extent of the intercluster magnetic interactions [134]. The techniques of characterization complement each other, as can be seen from the results of neutron diffraction experiments which confirm the *martensite*-to-*martensite* transformation in Fe–Pd alloys identified using DSC [127]. High-resolution neutron diffraction experiments are usually performed to study changes in crystallographic structure with respect to temperature. An example of this kind of study is found in [135], where over a temperature range from 400 K to 20 K, the lattice parameters for the transformation sequence of *austenite* ($L2_1$)–*pre-martensite* (3O)–*martensite* (7O) were established.

Scanning electron microscope has a depth of field for resolved detail much greater than the spatial resolution in the field of view and, consequently, the flatness of the topological and morphological detail in the optical or transmission electron microscope (TEM) is replaced by an image that is very similar to the play of light and shade over hills and valleys [136]. TEM, on the other hand, extends the resolution available for morphological studies to the order of 0.1 nm or even sub-angstrom. TEM combines real space data at excellent resolution and the information from reciprocal space, i.e., electron diffraction patterns, can be recorded [137]. TEM has been used to investigate the evolution of *martensite* morphology, shown in Figure 18, as the composition of $Ti_{50}Ni_{50-x}Pd_x$ system is tuned to

achieve geometric compatibility at the austenite–martensite interface [55,138]. The perfect one-to-one correspondence between the antiphase boundaries (APBs) and the magnetic domain walls in the parent phase of Ni₂Mn(Al, Ga) has been studied by combining Lorentz TEM [139].

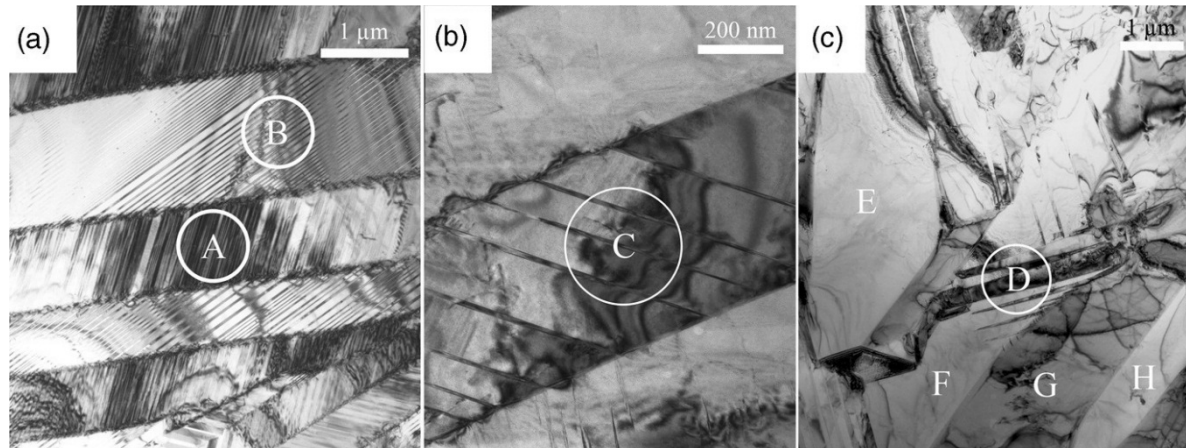


Figure 18. Evolution of microstructure with composition: (a) internally twinned martensite plates in Ti₅₀Ni₂₅Pd₂₅, A, B; (b) plate in Ti₅₀Ni₃₀Pd₂₀ with a smaller twin ratio, C; (c) example of microstructure in Ti₅₀Ni₃₉Pd₁₁ composed of a mosaic of twinless martensite plates (denoted E, F, G, H) and a group of compound twins (D) [138], with copyright permission from © Taylor and Francis.

The use of electron backscattered diffraction (EBSD) to determine the orientation information of the martensitic lamellae is demonstrated in [140,141]. EBSD patterns of bulk Ni₂Mn_{1.44}In_{0.56} are shown in Figure 19a for an incommensurate 6M modulated martensite, and the calculated Kikuchi lines (solid red) can be seen from Figure 19b [142]. The main and satellite reflections are highlighted by the white dashed line.

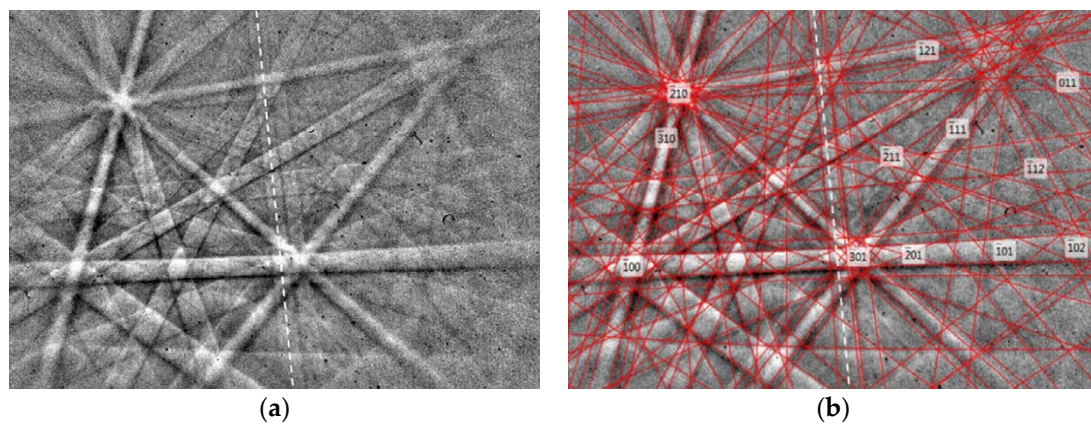


Figure 19. (a) Measured and (b) simulated electron backscattered diffraction (EBSD) Kikuchi patterns. One of the satellite reflections is highlighted with a white dashed line [142], with copyright permission from © Elsevier.

Magnetization measurements are usually carried out by magnetometry on a superconducting quantum interference device (SQUID) magnetometer or a vibrating sample magnetometer (VSM) to establish the temperature dependence of magnetization $M(T)$ in applied magnetic fields. The SQUID magnetometer can detect incredibly small magnetic fields of the order of fields in living organisms [143]. Most of the SQUID magnetometers have a temperature range of $0\text{ K} \leq T \leq 400\text{ K}$, while measurements up to 700 K are also possible. The measurements are done in sequential zero-field-cooled (ZFC),

field-cooled (FC) and field-heated (FH) protocols. During ZFC, the specimen is cooled from higher temperature to lower temperature without the application of the magnetic field. The specimen is then heated to higher temperature in the presence of a magnetic field while recording the magnetization values with increasing temperature. With the magnetic field still present, the specimen is cooled to lower temperature for the FC protocol. The specimen is subsequently heated in the applied magnetic field to a higher temperature for an FH protocol.

An observed hysteresis in the FC and FH curves is indicative of structural transition, while the observed split between the ZFC and FC curves is surmised as the effect of pinning by antiferromagnetic (AF) or non-collinear magnetic structures present in the ferromagnetic (FM) matrix or in the twin boundaries of martensite. The magnetic properties are further characterized by measuring the magnetic field dependence of magnetization $M(H)$ in applied fields up to 50 kOe. Examples of magnetic characterization of $\text{Ni}_{0.50}\text{Mn}_{0.50-x}\text{Sn}_x$ for $x = 0.15$ by SQUID magnetometry are shown in Figure 20a–d [130].

From Figure 20a, it can be seen the sample is ferromagnetic (FM) below $T_C^A = 320$ K down to about 190 K, beyond which the magnetization decreases. Figure 20b shows the splitting between the ZFC and FC, which is wider in the martensitic state because the lattice distortions in the martensitic state greatly influence the pinning of non-collinear magnetic configurations in the ferromagnetic domain. Hysteresis observed near 190 K, as seen in Figure 20c, indicates a first-order structural transition, and $M(H)$ curves in Figure 20d indicate the samples are ferromagnetic below the martensitic temperature.

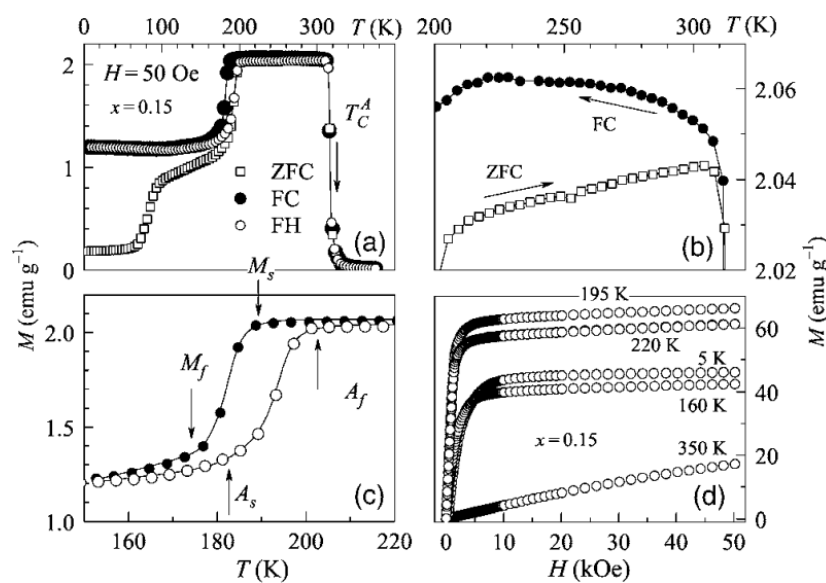


Figure 20. (a–d) Temperature-dependent magnetization ($M(T)$) and magnetic-field-dependent magnetization ($M(H)$) curves of $\text{Ni}_{0.50}\text{Mn}_{0.35}\text{Sn}_{0.15}$ alloy [130], with copyright permission from © IOP Publishing.

4. Microstructural Effects on Properties

In this section, the various microstructural factors which affect all or any of the magnetostructural properties of ferromagnetic Heusler alloys are discussed. It begins with a description of the effect of composition on the properties.

The most important aspect concerning the magnetostructural effects, microstructures, properties and functions of ferromagnetic Heusler alloys is the composition. $\text{Ni}_{54}\text{Mn}_{20}\text{Ga}_{26}$ thin films prepared by magnetron sputtering demonstrated martensitic phase transformation above room temperature [144] because of a greater extent of hybridization between the excess Ni and Ga in the alloy besides film stress. The effect of composition is not restricted to the prototype Ni–Mn–Ga alloys alone. Metamagnetic shape memory alloys are growing to be technologically significant [100,124,145–148], where the stoichiometric

composition is varied by tuning the compositions at will with remarkable magnetocaloric effects. To cap it all is the tuning of the composition to draw a perfect austenite–martensite interface with no stressed transition layer, which yielded the highest saturation magnetization several orders higher than normally observed [54]. The alloy $\text{Ni}_{45}\text{Co}_5\text{Mn}_{40}\text{Sn}_{10}$ resulting from the tuning was later used in direct energy conversion [25].

While the crystal structure has a certain effect on the magnetostructural properties, tuning the composition changes it, affecting the property being studied. The exact martensitic structure that would evolve for a particular composition and its effect on the properties could not be predicted, as there are no rules to predict them. Nevertheless, the structure may evolve as cubic–10M–14M–L1₀, as seen earlier, in accordance with an increasing e/a ratio and temperature [2].

In the case of Ga-doped NiMn alloys, for the structure to be technologically significant, the twinning stress has to be minimum, for which the lattice distortion, c/a , of the martensite has to be minimum. 5M and 7M martensites were suitable for MFIS by virtue of the low twinning stress and high anisotropy in them, while the nonlayered tetragonal $T(L1_0)$ reportedly exhibited high anisotropy and high twinning stress, but not MFIS [149]. However, addition of small amounts of Co and Cu to NiMnGa [150], as shown in Table 1, yielded a non-modulated structure with an MFIS of 12%.

Table 1. Crystal structure and magnetic field-induced strain (MFIS) in magnetic/metamagnetic shape memory (MSM/MMSM) alloys retrieved from literature.

Example Alloys	Process	Crystal Structure	MFIS	Ref.
$\text{Ni}_{49.8}\text{Mn}_{28.5}\text{Ga}_{21.7}$	Bridgman	bct, $I4/mmm$	6%	[6]
$\text{Ni}_{48.8}\text{Mn}_{29.7}\text{Ga}_{21.5}$	Bridgman	7M orthorhombic	9.50%	[5]
Ni_2MnGa	Single crystal	bct	0.20%	[3]
$\text{Ni}_{506}\text{Mn}_{28.3}\text{Ga}_{21.1}$	Arc-melting	7M	500 ppm	[151]
$\text{Ni}_{48.0}\text{Mn}_{30.6}\text{Ga}_{21.5}$	Arc-melting	5M	160 ppm	
$\text{Ni}_{46}\text{Mn}_{24}\text{Ga}_{22}\text{Co}_4\text{Cu}_4$	Induction melting	NM	12%	[150]
$\text{Ni}_{45}\text{Co}_5\text{Mn}_{36.7}\text{In}_{13.3}$	Induction melting	L2 ₁ and 14M	3%	[11]
$\text{Ni}_{43}\text{Co}_7\text{Mn}_{39}\text{Sn}_{11}$	Induction melting	L2 ₁ and 10M/6M	1.00%	[12]
$\text{Ni}_{45.7}\text{Co}_{4.8}\text{Mn}_{35.6}\text{In}_{13.8}$	Bridgman	L2 ₁	3.10%	[152]
$\text{Ni}_{45}\text{Mn}_{36.5}\text{Co}_5\text{In}_{13.5}$	Induction melting	L2 ₁ and 6M	1.20%	[153]
$\text{Ni}_{0.50}\text{Mn}_{0.34}\text{In}_{0.16}$	Arc-melting	10M	0.12%	[123]
$\text{Ni}_{46}\text{Co}_4\text{Mn}_{39}\text{Sn}_{11}$	Arc-melting	L2 ₁	0.01%	[154]
$\text{Ni}_{50}\text{Mn}_{34}\text{In}_{16}$		-	-4.5%	
$\text{Ni}_{44.9}\text{Co}_{5.1}\text{Mn}_{37.5}\text{In}_{12.5}$	Density functional theory	-	-5.1%	[155]
$\text{Ni}_{40.9}\text{Co}_{9.1}\text{Mn}_{37.5}\text{Sn}_{12.5}$	using PBE formulation	-	-2.6%	
$\text{Ni}_{35.2}\text{Co}_{14.8}\text{Mn}_{37.5}\text{Sb}_{12.5}$		-	-2.7%	

Table 2 shows a list of example MC alloys along with the magnetic entropy change ΔS_m values.

Table 2. Crystal structure and ΔS_m values in magnetocaloric (MC) alloys retrieved from literature.

Example Alloys	Process	Crystal Structure	ΔS_m (J/kgK)	Ref.
$\text{Ni}_{45}\text{Mn}_{43}\text{CrSn}_{11}$	Arc-melting, annealed	Cubic and tetragonal	39.7	[24]
$\text{Ni}_{41}\text{Co}_9\text{Mn}_{40}\text{Sn}_{10}$	Arc-melting, annealed	6M	31.9	[146]
$\text{Ni}_{43}\text{Co}_7\text{Mn}_{39}\text{Sn}_{11}$	As-spun annealed	L2 ₁ and L1 ₀	9.5	[99]
		L2 ₁ and L1 ₀	23.9	
$\text{Ni}_{42.6}\text{Mn}_{39.6}\text{Sn}_{9.7}\text{Fe}_{8.1}$	Melt-spun	7M	11.0	[156]
$\text{Ni}_{42}\text{Co}_8\text{Mn}_{39}\text{Sn}_{11}$	Arc-melting, annealed at 1170 K, 14 d	L2 ₁	-	[145]
$\text{Ni}_{49}\text{Mn}_{39}\text{Sn}_{12}$	Melt-spun	L2 ₁	8.2	[94]
$\text{Ni}_{50}\text{Mn}_{34}\text{Co}_2\text{Sn}_{14}$	Arc-melting	L2 ₁	48.8	[157]
$\text{Ni}_{48}\text{Co}_2\text{Mn}_{38}\text{Sn}_{12}$	Melt-spun	Austenite	32	[100]
$\text{Ni}_{0.50}\text{Mn}_{0.34}\text{In}_{0.16}$	Arc-melting	10M	12	[123]
$\text{Ni}_{50}\text{Mn}_{33.66}\text{Cr}_{0.34}\text{In}_{16}$	Arc-melting	Austenite and orthorhombic	17.7	[23]
$\text{Ni}_{49.5}\text{Mn}_{25.4}\text{Ga}_{25.1}$	Single crystal	Austenite	~11	[17]
$\text{Ni}_{2.19}\text{Mn}_{0.81}\text{Ga}$	Arc-melting	Monophase	20	[16]
$\text{Ni}_{54.8}\text{Mn}_{20.3}\text{Ga}_{24.9}$	Arc-melting	Non-modulated	-7.0	[158]
$\text{Ni}_{55}\text{Mn}_{18.9}\text{Ga}_{26.1}$	Arc-melting	7M	-5.2	[158]
$\text{Ni}_{55.3}\text{Mn}_{18.1}\text{Ga}_{26.6}$	Arc-melting	Austenite	-1.3	[158]
$\text{Ni}_{55}\text{Mn}_{20.6}\text{Ga}_{24.4}$	Melt-spun	7M	-9.5	[159]
$\text{Ni}_{55}\text{Mn}_{19.6}\text{Ga}_{25.4}$	Melt-spun	7M	-10.4	[159]

The differences in ΔS_m in off-stoichiometric Ni-Co-Mn-Sn alloys are due changes in composition, as seen from arc-melted $\text{Ni}_{41}\text{Co}_9\text{Mn}_{40}\text{Sn}_{10}$, $\text{Ni}_{43}\text{Co}_7\text{Mn}_{39}\text{Sn}_{11}$ and $\text{Ni}_{50}\text{Mn}_{34}\text{Co}_2\text{Sn}_{14}$ alloys and melt-spun $\text{Ni}_{48}\text{Co}_2\text{Mn}_{38}\text{Sn}_{12}$ alloy. The composition apparently overrides the crystal structure in the determination of the properties. It may be seen that intermartensitic or martensite-to-martensite transformations yield intermediate structures which may undergo irreversible transformation to b.c.t structures capable of deteriorating the MSM effect [127]. On the other hand, steplike thermoelastic martensite transformations are likely to enhance magnetocaloric properties [64]. Intermartensitic and steplike transformations, however, are still not clearly understood [149].

Across the martensitic transformation, a change in the unit cell volume has a profound effect on the magnetostructural properties, particularly magnetocaloric, and also on the martensitic transformation [160–162]. One has to know the orientation relationship between austenite and martensite to better understand the effect of lattice and, consequently, the volume change, as can be seen from Figure 21, where the variations of $\sqrt{2}a_M$, $\sqrt{2}c_M/6$ and b_M (instead of a_M , c_M and b_M) and $V_M/3$ (instead of V_M) are plotted. The lattice can be seen to expand along a_M and c_M axes and shrink along b_M axis. The volume contraction is -1.31% , accounting for a magnetic entropy of 31.9 J/kgK [146]. Similarly, a volume change of 4% accounted for an entropy change of -47.3 J/kgK in Mn-Co-Ge-B alloy [163,164]. This correlation between the unit cell volume change, structural entropy change and magnetic entropy change [163] can be used to predict high-performance magnetocaloric materials from crystallographic data [146].

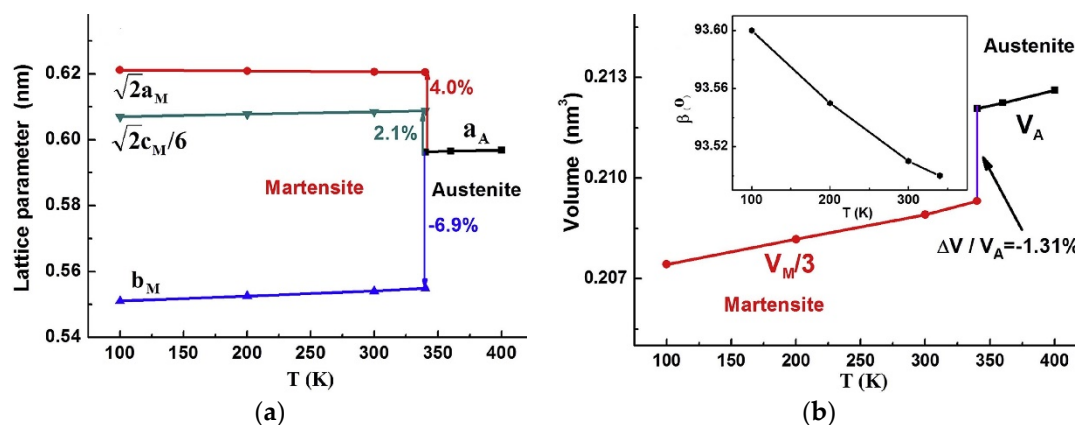


Figure 21. (a) Effect of lattice parameters; (b) unit cell volume change with respect to temperature [146], with copyright permission from © Elsevier BV.

The degree of long-range $L2_1$ atomic order significantly lowers the transformation entropy change through large shifts in the transformation temperatures in relation to the change in magnetization of the austenite phase [165–168]. While $L2_1$ atomic order refers to the fraction of atoms located in the correct sublattice of $L2_1$ structure, studies show it can be varied by thermal treatment. Thermal treatments are better than post-quench, as quenching does not affect the retained degree of $L2_1$ atomic order to be able to have appreciable effect on the martensitic transformation [169]. Post-quench aging (post-quench atomic ordering), as in polycrystalline $\text{Ni}_{45}\text{Mn}_{36.7}\text{In}_{13.3}\text{Co}_5$, has the effect of increasing the difference between the austenite Curie temperature (due to improved ferromagnetic coupling between Mn atoms) and the martensitic transformation temperature, thereby lowering the martensitic entropy change [169].

Microstructural changes through tuning of stoichiometry also have the effect of increasing the transformation temperatures, thus transporting the alloys into the realm of high-temperature shape memory alloys (HTSMAs, with temperatures up to $300 \text{ }^\circ\text{C}$ above the standard SMAs, such as TiNi with operating temperature of $100 \text{ }^\circ\text{C}$). The structure remains cubic $L2_1$ at higher temperatures and transforms to tetragonal upon cooling. Such alloys are useful for applications in automotive and

aerospace engines, limited by issues such as brittleness of the alloys. The formation of a ductile γ phase with [84,170] or without [171] addition of dopants like Co improves the ductility of the alloy, however, it does not contribute to shape memory effect (SME). The loss of SM/MSM is offset by an improvement in the mechanical properties [171]. No SME is observed when the martensite is two-phase, including γ phase. On the contrary, the single-phase martensite with no γ phase in $\text{Ni}_{54}\text{Mn}_{25}\text{Ga}_{21}$ recorded a good SME, whose microstructure shown in Figure 22a consists of coarse (1–5 μm) and fine (0.05–0.1 μm) microtwins, both twinned along [111] directions, which strongly favors thermoelasticity.

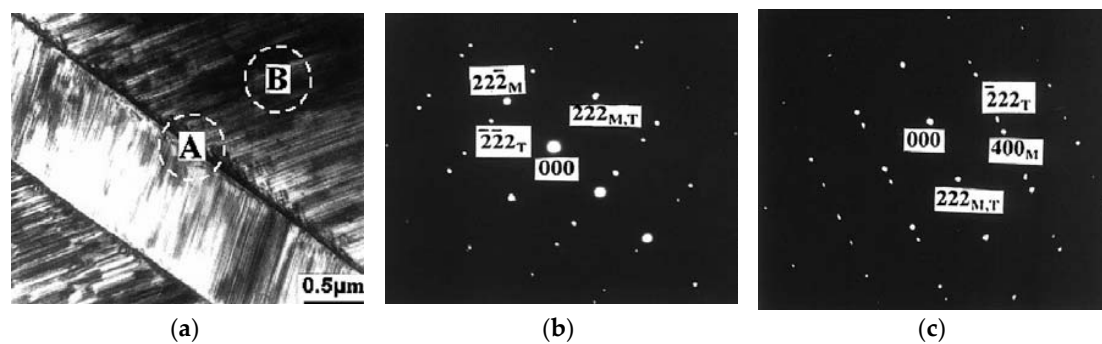


Figure 22. (a) TEM bright-field image of $\text{Ni}_{54}\text{Mn}_{25}\text{Ga}_{21}$ alloy (b); SAED pattern in the $[1\bar{1}0]$ taken from area A in (a); (c) SAED taken from area B in (a) with the incident electron beam tilted to $[0\bar{1}1]$ [171], with copyright permission from © Elsevier.

Where there has been an appreciable shape memory effect (SME) in two-phase martensite with γ phase, it is because the grain size of the γ phase is smaller, with circular morphology brought about by annealing [170] and thermomechanical [172] treatments. The stress–strain behavior in these alloys is characterized by dislocation slip and high strain hardening.

It is important also to note that γ phase is dependent on whether the Co atoms substitute Ni alone or Mn alone or both Ni and Mn. Figure 23a shows the microstructure of $\text{Ni}_{56}\text{Mn}_{17}\text{Co}_8\text{Ga}_{19}$ alloy (Co substituted for Mn) with the highest volume of γ phase amongst the various alloys investigated, wherein the γ phases join together to form slender bars (black arrows), and Figure 23b shows the recovery strain decreasing to almost zero at the highest γ phase content of 43% for various values of prestrain [84]. This was because the γ phase affected reversible martensitic transformation by hampering the martensite reorientation. To retain the MSME at high temperatures even though the temperatures are not as high as conventional SME, the choice of the doping element has to be judicious.

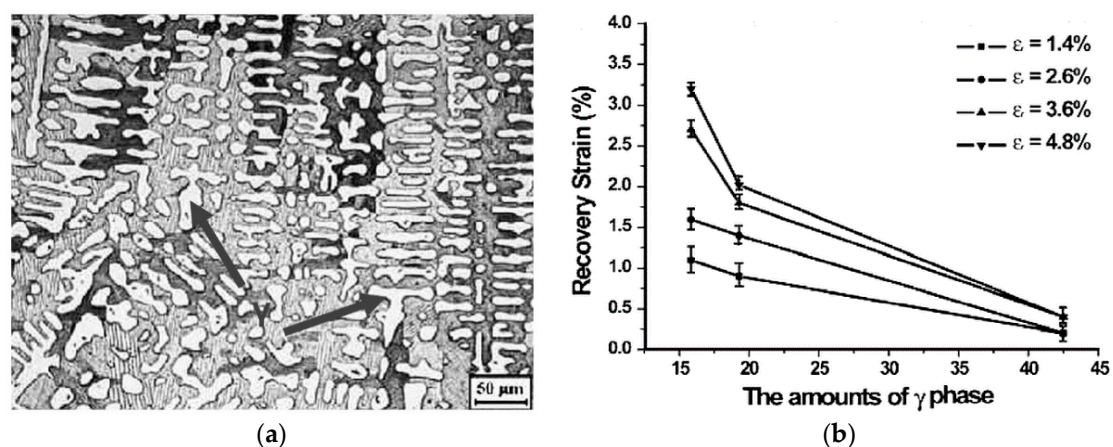


Figure 23. (a) Optical micrograph of $\text{Ni}_{56}\text{Mn}_{17}\text{Co}_8\text{Ga}_{19}$ with highest γ phase content; (b) shape memory effect in relation to the volume content of γ phase [84], with copyright permission from © Elsevier.

While rare earth elements like Gd, Tb or Nd serve the purpose [173] in addition to improving the mechanical properties by way of grain refinement, the most suitable high-temperature magnetic shape memory alloy so far has been reported as the six-element $\text{Ni}_{45}\text{Co}_5\text{Mn}_{21}\text{Fe}_4\text{Ga}_{20}\text{Cu}_5$ alloy [174], in which doping with Co, Cu and Fe instead of Co/Cu or Fe/Co increased the martensitic transformation temperature to 400 K and a Curie temperature to 458 K.

The microstructures of the alloys which wield enormous influence on their magnetostructural properties are greatly dependent on the heat treatment methods adopted. Long-period annealing achieves structural and chemical homogenization [21], after which the magnetostructural behavior is conspicuous. The reasons are understandable because multiphase solidification leads to compositional variations which persist even after short anneals and are capable of annulling the magnetostructural behavior [76]. Annealing of $\text{Ni}_{48}\text{Mn}_{39}\text{In}_{13}$ ribbons caused changes in the atomic ordering and the grain size of the alloy ribbon, due to which the transition temperatures and magnetic entropy change increased considerably [175]. Low-temperature annealing of homogenized samples (1223 K for 4 weeks) of $\text{Ni}_{50}\text{Mn}_{50-x}\text{Sn}_x$ ($x = 10\text{--}25$) alloys at 773 K caused decomposition to compositions near $x = 1$ and $x = 20$. While one composition would likely exhibit transformation above 700 K, the other exhibited none [74,176]. It was confirmed that the L_{21} phase is metastable at 773 K over an intermediate composition range and that transformations below 400 K account for the ferromagnetic shape memory behavior.

The combination of processes and heat treatments also contribute to the microstructure. Heat-treated ribbons exhibited ~ 1.7 times larger GS/t (grain size to thickness ratio) than solutionized bulk sample and were more suited for magnetocaloric applications [96]. Wheel speed and annealing temperature have been reported to be controlling factors for grain size, interatomic distance, smaller thermal hysteresis and degree of atomic ordering in order to achieve remarkable magnetic properties, such as high values of magnetic entropy change (ΔS_M) and refrigeration capacity (RC) [94,177]. There are, however, conflicting claims that in alloys in which L_{21} – B_2 ordering transition is absent, thermal treatments are in vain with regards to the tuning of the magnetostructural properties [178], while high-temperature annealing has been reported to favor the tuning of the degree of atomic order in $\text{Ni}_{49}\text{Mn}_{39}\text{Sn}_{12}$ alloy ribbons with L_{21} – B_2 ordering [94]. This aspect requires further investigation.

In the case of microwires, the inhibiting influence of internal stresses on the magnetostructural characteristics are compensated by annealing them, with and without the glass coating. Internal stresses are induced during solidification and by the difference in the coefficients of thermal expansion of the glass coating and the metallic alloy. Microwires annealed after glass coating removal showed an increased value of saturation magnetization (495 emu/cm^3) [89]. However, their remanence (245 emu/cm^3) and coercivity (248 Oe) are decreased in comparison with the microwire annealed with glass coating first and then after removal. Relaxation of the induced stresses in the microwire improved the atomic ordering, thus reducing the coercivity and remanence. On the other hand, high-temperature annealing of $\text{Ni}_{63}\text{Mn}_{12}\text{Ga}_{25}$ microwire resulted in a partial evaporation of Mn from the outer region of the metallic core [90]. This combined with the glass melting led to the formation of MnO_x at the surface. The middle part consisted of Mn-depleted Ni_3Ga and an L_{21} structure with a composition of $\text{Ni}_{60}\text{Mn}_9\text{Ga}_{31}$. Such a structure resulted in a soft ferromagnetic behavior below 270 K [90].

5. Summary

In this paper, we have reviewed the Ni–Mn-based ferromagnetic Heusler alloys from the perspective of design, synthesis, characterization and structure–property relationships.

- On the basis of design, given that NiMn-based Heusler alloys are multiferroic and multifunctional, adaptation of cofactor conditions from GNLTM will certainly be useful in arriving at highly superior multifunctional compositions which can be readily used in applications. Combinatorial approach combined with GNLTM has the potential to revolutionize materials search by accelerating discovery and optimization of new and known materials.

- Processing methods and techniques have an influence on the MSM/MMSM and MC properties of these materials through benign changes in their microstructures. Every method has its advantages and disadvantages. While liquid processing ensures homogeneity of the alloys, issues such as multiphase solidification and chemical segregation, which tend to cover up the magnetostructural transitions, still persist. Melt-spinning can be useful in terms of homogeneity of grain size and avoidance of annealing but may still require secondary treatment for the realization of desired characteristics. In view of this, exclusion of a particular method, like P/M, may not be justified. The disadvantages of incomplete martensitic transformation, formation of secondary and intermetallic phases, etc., which are characteristic of P/M, can be overcome by appropriate heat treatment or thermomechanical procedures and through exact characterization of the starting powders.
- Various factors, such as composition, crystal structure, atomic ordering, volume of unit cell, grain size, presence or absence of secondary phases and heat treatment methods, which influence the MSM/MMSM and MC effects of these alloys, have been reviewed. The overriding factor is the composition, which influences both martensitic and magnetic transformations, the transformation temperatures, crystal structures, saturation magnetization and consequently the magnetostructural effects.

Funding: This research received no external funding.

Conflicts of Interest: The authors declare no conflict of interest.

References

1. James, R.D.; Zhang, Z. A way to search for multiferroic materials with “unlikely” combinations of physical properties. In *Magnetism and Structure in Functional Materials*; Manosa, L., Planes, A., Saxena, A., Eds.; Springer: New York, NY, USA, 2005.
2. Planes, A.; Mañosa, L.; Acet, M. Magnetocaloric effect and its relation to shape-memory properties in ferromagnetic Heusler alloys. *J. Phys. Condens. Matter* **2009**, *21*, 233201. [[CrossRef](#)] [[PubMed](#)]
3. Ullakko, K.; Huang, J.K.; Kantner, C.; O’Handley, R.C.; Kokorin, V.V. Large magnetic-field-induced strains in Ni₂MnGa single crystals. *Appl. Phys. Lett.* **1996**, *69*, 1966–1968. [[CrossRef](#)]
4. James, R.D.; Tickle, R.; Wuttig, M. Large field-induced strains in ferromagnetic shape memory materials. *Mater. Sci. Eng. A* **1999**, *273*, 320–325. [[CrossRef](#)]
5. Sozinov, A.; Likhachev, A.A.; Lanska, N.; Ullakko, K. Giant magnetic-field-induced strain in NiMnGa seven-layered martensitic phase. *Appl. Phys. Lett.* **2001**, *80*, 1746–1748. [[CrossRef](#)]
6. Murray, S.J.; Marioni, M.; Allen, S.M.; O’Handley, R.C.; Lograsso, T.A. 6% magnetic-field-induced strain by twin-boundary motion in ferromagnetic Ni-Mn-Ga. *Appl. Phys. Lett.* **2000**, *77*, 886–888. [[CrossRef](#)]
7. Murray, S.J. Large field induced strain in single crystalline Ni-Mn-Ga ferromagnetic shape memory alloy. *J. Appl. Phys.* **2000**, *87*, 5774–5776. [[CrossRef](#)]
8. Sozinov, A.; Likhachev, A.A.; Lanska, N.; Ullakko, K.; Lindroos, V.K. *Crystal Structure, Magnetic Anisotropy, and Mechanical Properties of Seven-Layered Martensite in Ni-Mn-Ga*; International Society for Optics and Photonics: San Diego, CA, USA, 2002; pp. 195–205.
9. Sutou, Y.; Imano, Y.; Koeda, N.; Omori, T.; Kainuma, R.; Ishida, K.; Oikawa, K. Magnetic and martensitic transformations of NiMnX (X = In, Sn, Sb) ferromagnetic shape memory alloys. *Appl. Phys. Lett.* **2004**, *85*, 4358–4360. [[CrossRef](#)]
10. Krenke, T.; Duman, E.; Acet, M.; Wassermann, E.F.; Moya, X.; Manosa, L.; Planes, A. Inverse magnetocaloric effect in ferromagnetic Ni-Mn-Sn alloys. *Nat. Mater.* **2005**, *4*, 450–454. [[CrossRef](#)] [[PubMed](#)]
11. Kainuma, R.; Imano, Y.; Ito, W.; Sutou, Y.; Morito, H.; Okamoto, S.; Kitakami, O.; Oikawa, K.; Fujita, A.; Kanomata, T.; et al. Magnetic-field-induced shape recovery by reverse phase transformation. *Nature* **2006**, *439*, 957–960. [[CrossRef](#)] [[PubMed](#)]
12. Kainuma, R.; Imano, Y.; Ito, W.; Morito, H.; Sutou, Y.; Oikawa, K.; Fujita, A.; Ishida, K.; Okamoto, S.; Kitakami, O.; et al. Metamagnetic shape memory effect in a Heusler-type Ni₄₃Co₇Mn₃₉Sn₁₁ polycrystalline alloy. *Appl. Phys. Lett.* **2006**, *88*, 192513. [[CrossRef](#)]

13. Planes, A.; Manosa, L.; Acet, M. Recent Progress and future perspectives in magnetic and metamagnetic shape-memory Heusler alloys. *Mater. Sci. Forum* **2013**, *738–739*, 391–399. [[CrossRef](#)]
14. Pecharsky, V.K.; Gschneidner, K.A., Jr. Giant magnetocaloric effect in $\text{Gd}_5(\text{Si}_2\text{Ge}_2)$. *Phys. Rev. Lett.* **1997**, *78*, 4494. [[CrossRef](#)]
15. Hu, F.-X.; Shen, B.-G.; Sun, J.-R. Magnetic entropy change in $\text{Ni}_{51.5}\text{Mn}_{22.7}\text{Ga}_{25.8}$ alloy. *Appl. Phys. Lett.* **2000**, *76*, 3460–3462. [[CrossRef](#)]
16. Pareti, L.; Solzi, M.; Albertini, F.; Paoluzi, A. Giant entropy change at the co-occurrence of structural and magnetic transitions in the $\text{Ni}_{2.19}\text{Mn}_{0.81}\text{Ga}$ Heusler alloy. *Eur. Phys. J. B* **2003**, *32*, 303–307. [[CrossRef](#)]
17. Marcos, J.; Planes, A.; Manosa, L.; Casanova, F.; Batlle, X.; Labarta, A.; Martinez, B. Magnetic field induced entropy change and magnetoelasticity in Ni-Mn-Ga alloys. *Phys. Rev. B* **2002**, *66*, 224413. [[CrossRef](#)]
18. Marcos, J.; Planes, A.; Manosa, L.; Casanova, F.; Batlle, X.; Labarta, A. Multiscale origin of the magnetocaloric effect in Ni-Mn-Ga shape-memory alloys. *Phys. Rev. B* **2003**, *68*, 094401. [[CrossRef](#)]
19. Roy, S.B. First order magneto-structural phase transition and associated multi-functional properties in magnetic solids. *J. Phys. Condens. Matter* **2013**, *25*, 183201. [[CrossRef](#)] [[PubMed](#)]
20. Franco, V.; Blázquez, J.S.; Ingale, B.; Conde, A. The magnetocaloric effect and magnetic refrigeration near room temperature: Materials and models. *Annu. Rev. Mater. Res.* **2012**, *42*, 305–342. [[CrossRef](#)]
21. Schlagel, D.L.; Yuhasz, W.M.; Dennis, K.W.; McCallum, R.W.; Lograsso, T.A. Temperature dependence of the field-induced phase transformation in $\text{Ni}_{50}\text{Mn}_{37}\text{Sn}_{13}$. *Scr. Mater.* **2008**, *59*, 1083–1086. [[CrossRef](#)]
22. Moya, X.; Manosa, L.; Planes, A.; Krenke, T.; Duman, E.; Wassermann, E.F. Calorimetric study of the inverse magnetocaloric effect in ferromagnetic Ni-Mn-Sn. *J. Magn. Magn. Mater.* **2007**, *316*, e572–e574. [[CrossRef](#)]
23. Sharma, V.K.; Chattopadhyay, M.K.; Roy, S.B. Large magnetocaloric effect in $\text{Ni}_{50}\text{Mn}_{33.66}\text{Cr}_{0.34}\text{In}_{16}$ alloy. *J. Phys. D Appl. Phys.* **2010**, *43*, 22. [[CrossRef](#)]
24. Pandey, S.; Quetz, A.; Aryal, A.; Dubenko, I.; Mazumdar, D.; Stadler, S.; Ali, N. Large Inverse Magnetocaloric Effects and Giant Magnetoresistance in Ni-Mn-Cr-Sn Heusler Alloys. *Magnetochemistry* **2017**, *3*, 3. [[CrossRef](#)]
25. Srivastava, V.; Song, Y.; Bhatti, K.; James, R.D. The direct conversion of heat to electricity using multiferroic alloys. *Adv. Energy Mater.* **2011**, *1*, 97–104. [[CrossRef](#)]
26. Pramanick, A.; Wang, X.-L. Characterization of magnetoelastic coupling in ferromagnetic shape memory alloys using neutron diffraction. *JOM* **2012**, *65*, 54–64. [[CrossRef](#)]
27. Franco, V.; Blázquez, J.S.; Ipus, J.J.; Law, J.Y.; Moreno-Ramírez, L.M.; Conde, A. Magnetocaloric effect: From materials research to refrigeration devices. *Prog. Mater. Sci.* **2018**, *93*, 112–232. [[CrossRef](#)]
28. Khovaylo, V.V.; Rodionova, V.V.; Shevyrtalov, S.N.; Novosad, V. Magnetocaloric effect in “reduced” dimensions: Thin films, ribbons, and microwires of Heusler alloys and related compounds. *Phys. Status Solidi B* **2014**, *251*, 2104–2113. [[CrossRef](#)]
29. Graf, T.; Felser, C. Heusler compounds at a glance. In *Spintronics From Materials to Devices*, 1st ed.; Felser, C., Fecher, G.H., Eds.; Springer: Dordrecht, The Netherlands, 2013; pp. 1–13.
30. Pons, J.; Chernenko, V.A.; Santamarta, R.; Cesari, E. Crystal structure of martensitic phases in Ni-Mn-Ga shape memory alloys. *Acta Mater.* **2000**, *48*, 3027–3038. [[CrossRef](#)]
31. Halder, M.; Mukadam, M.D.; Suresh, K.G.; Yusuf, S.M. Electronic, structural, and magnetic properties of the quaternary Heusler alloy NiCoMnZ ($Z = \text{Al, Ge, and Sn}$). *J. Magn. Magn. Mater.* **2015**, *377*, 220–225. [[CrossRef](#)]
32. Srivastava, V.; Bhatti, K.P. Ferromagnetic shape memory Heusler alloys. In *Ferroids and Multiferroids*; Virk, H.S., Kleeman, W., Eds.; Trans Tech Publications Ltd.: Zurich, Switzerland, 2012; Volume 189, pp. 189–208.
33. Ito, W.; Imano, Y.; Kainuma, R.; Sutou, Y.; Oikawa, K.; Ishida, K. *Martensitic and Magnetic Transformation Behaviors in Heusler-Type NiMnIn and NiCoMnIn Metamagnetic Shape Memory Alloys*; Springer Boston: Norwell, MA, USA, 2007; pp. 759–766.
34. Khovaylo, V.V.; Kanomata, T.; Tanaka, T.; Nakashima, M.; Amako, Y.; Kainuma, R.; Umetsu, R.Y.; Morito, H.; Miki, H. Magnetic properties of $\text{Ni}_{50}\text{Mn}_{34.8}\text{In}_{15.2}$ probed by Mössbauer spectroscopy. *Phys. Rev. B* **2009**, *80*, 144409. [[CrossRef](#)]
35. Righi, L.; Albertini, F.; Fabbri, S.; Paoluzi, A. Crystal structures of modulated martensitic phases of FSM Heusler alloys. In *Advances in Magnetic Shape Memory Materials*; Chernenko, V.A., Ed.; Trans Tech Publications Ltd.: Zurich, Switzerland, 2011; Volume 684, pp. 105–116.

36. Bersuker, I.B. Recent Developments in the Jahn–Teller Effect. In *The Jahn-Teller Effect. Fundamentals and Implications. For Physics and Chemistry*; Köppel, H., Yarkony, D.R., Barentzen, H., Eds.; Springer: New York, NY, USA, 2009; pp. 3–23.
37. Haritha, L.; Gangadhar Reddy, G.; Ramakanth, A.; Ghatak, S.K.; Nolting, W. Interplay of magnetic order and Jahn–Teller distortion in a model with strongly correlated electrons system. *Physica B* **2010**, *405*, 1701–1705. [[CrossRef](#)]
38. Cong, D.Y.; Roth, S.; Schultz, L. Magnetic properties and structural transformations in Ni-Co-Mn-Sn multifunctional alloys. *Acta Mater.* **2012**, *60*, 5335–5351. [[CrossRef](#)]
39. Sharma, V.K.; Chattopadhyay, M.K.; Roy, S.B. Kinetic arrest of the first order austenite to martensite phase transition in Ni₅₀Mn₃₄In₁₆: Dc magnetization studies. *Phys. Rev. B* **2007**, *76*, 140401. [[CrossRef](#)]
40. Zubar, T.I.; Panina, L.V.; Kovaleva, N.N.; Sharko, S.A.; Tishkevich, D.I.; Vinnik, D.A.; Gudkova, S.A.; Trukhanova, E.L.; Trofimov, E.A.; Chizhik, S.A.; et al. Anomalies in growth of electrodeposited Ni–Fe nanogranular films. *Cryst. Eng. Comm.* **2018**, *20*, 2306–2315. [[CrossRef](#)]
41. Zubar, T.I.; Sharko, S.A.; Tishkevich, D.I.; Kovaleva, N.N.; Vinnik, D.A.; Gudkova, S.A.; Trukhanova, E.L.; Trofimov, E.A.; Chizhik, S.A.; Panina, L.V.; et al. Anomalies in Ni-Fe nanogranular films growth. *J. Alloy. Compd.* **2018**, *748*, 970–978. [[CrossRef](#)]
42. Wang, X.; Shang, J.-X.; Wang, F.-H.; Jiang, C.-B.; Xu, H.-B. Origin of unusual properties in the ferromagnetic Heusler alloy Ni–Mn–Sn: A first-principles investigation. *Scr. Mater.* **2014**, *89*, 33–36. [[CrossRef](#)]
43. Pérez-Reche, F.J.; Vives, E.; Mañosa, L.; Planes, A. Athermal Character of Structural Phase Transitions. *Phys. Rev. Lett.* **2001**, *87*, 19. [[CrossRef](#)] [[PubMed](#)]
44. Zheng, H.; Wang, W.; Wu, D.; Xue, S.; Zhai, Q.; Frenzel, J.; Luo, Z. Athermal nature of the martensitic transformation in Heusler alloy Ni-Mn-Sn. *Intermetallics* **2013**, *36*, 90–95. [[CrossRef](#)]
45. Kakeshita, T.; Kuroiwa, K.; Shimizu, K.; Ikeda, T.; Yamagishi, A.; Date, M. A New Model Explainable for Both the Athermal and Isothermal Natures of Martensitic Transformations in Fe-Ni-Mn Alloys. *Mater. Trans. JIM* **1993**, *34*, 423–428. [[CrossRef](#)]
46. Faran, E.; Shilo, D. Twin motion faster than the speed of sound. *Phys. Rev. Lett.* **2010**, *104*, 155501. [[CrossRef](#)] [[PubMed](#)]
47. Kakeshita, T.; Kuroiwa, K.; Shimizu, K.; Ikeda, T.; Yamagishi, A.; Date, M. Effect of Magnetic Fields on Athermal and Isothermal Martensitic Transformations in Fe-Ni-Mn Alloys. *Mater. Trans. JIM* **1993**, *34*, 415–422. [[CrossRef](#)]
48. Lee, Y.-H.; Todai, M.; Okuyama, T.; Fukuda, T.; Kakeshita, T.; Kainuma, R. Isothermal nature of martensitic transformation in an Ni₄₅Co₅Mn_{36.5}In_{13.5} magnetic shape memory alloy. *Scr. Mater.* **2011**, *64*, 927–930. [[CrossRef](#)]
49. Kustov, S.; Golovin, I.; Corró, M.L.; Cesari, E. Isothermal martensitic transformation in metamagnetic shape memory alloys. *J. Appl. Phys.* **2010**, *107*, 053525. [[CrossRef](#)]
50. Chen, F.; Tong, Y.X.; Tian, B.; Zheng, Y.F.; Liu, Y. Time effect of martensitic transformation in Ni₄₃Co₇Mn₄₁Sn₉. *Intermetallics* **2010**, *18*, 188–192. [[CrossRef](#)]
51. Ito, W.; Ito, K.; Umetsu, R.Y.; Kainuma, R.; Koyama, K.; Watanabe, K.; Fujita, A.; Oikawa, K.; Ishida, K.; Kanomata, T. Kinetic arrest of martensitic transformation in the NiCoMnIn metamagnetic shape memory alloy. *Appl. Phys. Lett.* **2008**, *92*, 021908. [[CrossRef](#)]
52. Lakhani, A.; Banerjee, A.; Chaddah, P.; Chen, X.; Ramanujan, R.V. Magnetic glass in shape memory alloy: Ni₄₅Co₅Mn₃₈Sn₁₂. *J. Phys. Condens. Matter* **2012**, *24*, 386004. [[CrossRef](#)] [[PubMed](#)]
53. Song, Y.; Chen, X.; Dabade, V.; Shield, T.W.; James, R.D. Enhanced reversibility and unusual microstructure of a phase-transforming material. *Nature* **2013**, *502*, 85–88. [[CrossRef](#)] [[PubMed](#)]
54. Srivastava, V.; Chen, X.; James, R.D. Hysteresis and unusual magnetic properties in the singular Heusler alloy Ni₄₅Co₅Mn₄₀Sn₁₀. *Appl. Phys. Lett.* **2010**, *97*, 014101. [[CrossRef](#)]
55. Delville, R.; Schryvers, D.; Zhang, Z.; James, R.D. Transmission electron microscopy investigation of microstructures in low-hysteresis alloys with special lattice parameters. *Scr. Mater.* **2009**, *60*, 293–296. [[CrossRef](#)]
56. Lei, C.H.; Li, L.J.; Shu, Y.C.; Li, J.Y. Austenite-martensite interface in shape memory alloys. *Appl. Phys. Lett.* **2010**, *96*, 141910. [[CrossRef](#)]
57. Gebhardt, T.; Music, D.; Takahashi, T.; Schneider, J.M. Combinatorial thin film materials science: From alloy discovery and optimization to alloy design. *Thin Solid Films* **2012**, *520*, 5491–5499. [[CrossRef](#)]

58. Yang, S.; Wang, C.; Liu, X. Phase equilibria and composition dependence of martensitic transformation in Ni-Mn-Ga ternary system. *Intermetallics* **2012**, *25*, 101–108. [[CrossRef](#)]
59. Miyamoto, T.; Nagasako, M.; Kainuma, R. Phase equilibria in the Ni-Mn-In alloy system. *J. Alloy. Compd.* **2013**, *549*, 57–63. [[CrossRef](#)]
60. Porthun, S.; ten Berge, P.; Lodder, J.C. Bitter colloid observations of magnetic structures in perpendicular magnetic recording media. *J. Magn. Magn. Mater.* **1993**, *123*, 199–208. [[CrossRef](#)]
61. Ao, W.Q.; Liu, F.S.; Li, J.Q.; Du, Y.; Liu, F.L. Isothermal section of the Ni-Mn-In ternary system at 773 K. *J. Alloy. Compd.* **2015**, *622*, 149–154. [[CrossRef](#)]
62. Wachtel, E.; Henninger, F.; Predel, B. Constitution and magnetic properties of Ni-Mn-Sn alloys-solid and liquid state. *J. Magn. Magn. Mater.* **1983**, *38*, 305–315. [[CrossRef](#)]
63. Graf, T.; Felser, C.; Parkin, S.S.P. Simple rules for the understanding of Heusler compounds. *Prog. Solid State Chem.* **2011**, *39*, 1–50. [[CrossRef](#)]
64. Chen, F.; Tong, Y.X.; Li, L.; Sánchez Llamazares, J.L.; Sánchez-Valdés, C.F.; Müllner, P. The effect of step-like martensitic transformation on the magnetic entropy change of Ni_{40.6}Co_{8.5}Mn_{40.9}Sn₁₀ unidirectional crystal grown with the Bridgman-Stockbarger technique. *J. Alloy. Compd.* **2017**, *691*, 269–274. [[CrossRef](#)]
65. Laudise, R.A.; Sunder, W.A.; O'Bryan, H.M.; Carlson, D.J.; Witt, A.F. Czochralski growth of single crystals of Ni_{3-x}MnxSn. *J. Cryst. Growth* **1992**, *118*, 277–286. [[CrossRef](#)]
66. Ito, K.; Ito, W.; Umetsu, R.Y.; Nagasako, M.; Kainuma, R.; Fujita, A.; Oikawa, K.; Ishida, K. Martensitic transformation in NiCoMnSn metamagnetic shape memory alloy powders. *Mater. Trans.* **2008**, *49*, 1915–1918. [[CrossRef](#)]
67. Ahamed, R.; Ghomashchi, R.; Xie, Z.; Chen, L.; Munroe, P.; Xu, S. Powder processing and characterisation of a quinary Ni-Mn-Co-Sn-Cu Heusler alloy. *Powder Technol.* **2018**, *324*, 69–75. [[CrossRef](#)]
68. Ito, K.; Ito, W.; Umetsu, R.Y.; Karaman, I.; Ishida, K.; Kainuma, R. Mechanical and shape memory properties of Ni₄₃Co₇Mn₃₉Sn₁₁ alloy compacts fabricated by pressureless sintering. *Scr. Mater.* **2010**, *63*, 1236–1239. [[CrossRef](#)]
69. Ito, K.; Ito, W.; Umetsu, R.Y.; Karaman, I.; Ishida, K.; Kainuma, R. Metamagnetic shape memory effect in Porous Ni₄₃Co₇Mn₃₉Sn₁₁ alloy compacts fabricated by pressureless sintering. *Mater. Trans.* **2011**, *52*, 2270–2273. [[CrossRef](#)]
70. Ito, K.; Ito, W.; Umetsu, R.Y.; Tajima, S.; Kawaura, H.; Kainuma, R.; Ishida, K. Metamagnetic shape memory effect in polycrystalline NiCoMnSn alloy fabricated by spark plasma sintering. *Scr. Mater.* **2009**, *61*, 504–507. [[CrossRef](#)]
71. Monroe, J.A.; Cruz-Perez, J.; Yegin, C.; Karaman, I.; Geltmacher, A.B.; Everett, R.K.; Kainuma, R. Magnetic response of porous NiCoMnSn metamagnetic shape memory alloys fabricated using solid-state replication. *Scr. Mater.* **2012**, *67*, 116–119. [[CrossRef](#)]
72. Anandh Vacuum Induction Melting Unit. Available online: <http://home.iitk.ac.in/~anandh/lab/Induction%20Melting%20Unit2.pdf> (accessed on 20 April 2018).
73. Pérez-Sierra, A.M.; Pons, J.; Santamarta, R.; Vermaut, P.; Ochín, P. Solidification process and effect of thermal treatments on Ni-Co-Mn-Sn metamagnetic shape memory alloys. *Acta Mater.* **2015**, *93*, 164–174. [[CrossRef](#)]
74. Yuhasz, W.M.; Schlagel, D.L.; Xing, Q.; Dennis, K.W.; McCallum, R.W.; Lograsso, T.A. Influence of annealing and phase decomposition on the magnetostructural transitions in Ni₅₀Mn₃₉Sn₁₁. *J. Appl. Phys.* **2009**, *105*, 07A921. [[CrossRef](#)]
75. Murakami, Y.; Watanabe, Y.; Kanaizuka, T.; Kachi, S. Magnetic Properties and Phase Change of Ni_{3-y}Mn_ySn Alloy. *Trans. Jpn Inst. Metals* **1981**, *22*, 551–557. [[CrossRef](#)]
76. Schlagel, D.L.; McCallum, R.W.; Lograsso, T.A. Influence of solidification microstructure on the magnetic properties of Ni-Mn-Sn Heusler alloys. *J. Alloy. Compd.* **2008**, *463*, 38–46. [[CrossRef](#)]
77. Bridgman-Stockbarger Technique. Available online: https://en.wikipedia.org/wiki/Bridgman%E2%80%9393Stockbarger_technique (accessed on 1 May 2018).
78. Huang, L.; Cong, D.Y.; Suo, H.L.; Wang, Y.D. Giant magnetic refrigeration capacity near room temperature in Ni₄₀Co₁₀Mn₄₀Sn₁₀ multifunctional alloy. *Appl. Phys. Lett.* **2014**, *104*, 132407. [[CrossRef](#)]
79. Provenzano, V.; Shapiro, A.J.; Shull, R.D. Reduction of hysteresis losses in the magnetic refrigerant Gd₅Ge₂Si₂ by the addition of iron. *Nature* **2004**, *429*, 853–857. [[CrossRef](#)] [[PubMed](#)]

80. Phan, T.-L.; Zhang, P.; Dan, N.H.; Yen, N.H.; Thanh, P.T.; Thanh, T.D.; Phan, M.H.; Yu, S.C. Coexistence of conventional and inverse magnetocaloric effects and critical behaviors in $\text{Ni}_{50}\text{Mn}_{50-x}\text{Sn}_x$ ($x = 13$ and 14) alloy ribbons. *Appl. Phys. Lett.* **2012**, *101*, 212403. [[CrossRef](#)]
81. Huang, Y.J.; Liu, J.; Hu, Q.D.; Liu, Q.H.; Karaman, I.; Li, J.G. Applications of the directional solidification in magnetic shape memory alloys. In Proceedings of the 4th International Conference on Advances in Solidification Processes, Windsor, UK, 8–11 July 2014.
82. Cong, D.Y.; Wang, Y.D.; Zetterstrom, P.; Peng, R.L.; Delaplane, R.; Zhao, X.; Zuo, L. *Crystal Structures and Textures of Hot Forged $\text{Ni}_{48}\text{Mn}_{30}\text{Ga}_{22}$ Alloy. Investigated by Neutron Diffraction Technique*; Maney Publishing: London, UK, 2005; pp. 1412–1416.
83. Cong, D.Y.; Wang, Y.D.; Lin Peng, R.; Zetterstrom, P.; Zhao, X.; Liaw, P.K.; Zuo, L. Crystal structures and textures in the hot-forged Ni-Mn-Ga shape memory alloys. *Metall. Mater. Trans. A Phys. Met. Mater. Sci.* **2006**, *37*, 1397–1403. [[CrossRef](#)]
84. Ma, Y.; Yang, S.; Liu, Y.; Liu, X. The ductility and shape-memory properties of Ni-Mn-Co-Ga high-temperature shape-memory alloys. *Acta Mater.* **2009**, *57*, 3232–3241. [[CrossRef](#)]
85. Larin, V.S.; Torcunov, A.V.; Zhukov, A.; González, J.; Vazquez, M.; Panina, L. Preparation and properties of glass-coated microwires. *J. Magn. Magn. Mater.* **2002**, *249*, 39–45. [[CrossRef](#)]
86. Rodionova, V.; Ilyn, M.; Granovsky, A.; Perov, N.; Zhukova, V.; Abrosimova, G.; Aronin, A.; Kiselev, A.; Zhukov, A. Internal stress induced texture in Ni-Mn-Ga based glass-covered microwires. *J. Appl. Phys.* **2013**, *114*, 123914. [[CrossRef](#)]
87. Zhukov, A.; Rodionova, V.; Ilyn, M.; Aliev, A.M.; Varga, R.; Michalik, S.; Aronin, A.; Abrosimova, G.; Kiselev, A.; Ipatov, M.; et al. Magnetic properties and magnetocaloric effect in Heusler-type glass-coated NiMnGa microwires. *J. Alloy. Compd.* **2013**, *575*, 73–79. [[CrossRef](#)]
88. Shevyrtalov, S.; Zhukov, A.; Lyatun, I.; Medvedeva, S.; Miki, H.; Zhukova, V.; Rodionova, V. Martensitic transformation behavior of $\text{Ni}_{2.44}\text{Mn}_{0.48}\text{Ga}_{1.08}$ thin glass-coated microwire. *J. Alloy. Compd.* **2018**, *745*, 217–221. [[CrossRef](#)]
89. Shevyrtalov, S.; Zhukov, A.; Zhukova, V.; Rodionova, V. Internal stresses influence on magnetic properties of Ni-Mn-Ga Heusler-type microwires. *Intermetallics* **2018**, *94*, 42–46. [[CrossRef](#)]
90. Shevyrtalov, S.; Zhukov, A.; Medvedeva, S.; Lyatun, I.; Zhukova, V.; Rodionova, V. Radial elemental and phase separation in Ni-Mn-Ga glass-coated microwires. *J. Appl. Phys.* **2018**, *123*, 173903. [[CrossRef](#)]
91. Suryanarayana, C. Rapid Solidification Processing. In *Encyclopedia of Materials: Science and Technology*, 2nd ed.; Veyssi re, P., Buschow, K.H.J., Cahn, R.W., Flemings, M.C., Ilschner, B., Kramer, E.J., Mahajan, S., Eds.; Elsevier: Oxford, UK, 2002; pp. 1–10.
92. Sari, U.; Aksoy,  . Electron microscopy study of 2H and 18R martensites in Cu–11.92 wt % Al–3.78 wt % Ni shape memory alloy. *J. Alloy. Compd.* **2006**, *417*, 138–142. [[CrossRef](#)]
93. Sade, M.; Lovey, F.C. The structure of the modified 2H martensite in Cu-Zn-Al. *Scr. Metall.* **1983**, *17*, 333–338. [[CrossRef](#)]
94. Wang, W.; Li, H.; Ren, J.; Fu, J.; Zhai, Q.; Luo, Z.; Zheng, H. Enhanced magnetocaloric properties in annealed Heusler Ni-Mn-Sn ribbons. *J. Magn. Magn. Mater.* **2015**, *374*, 153–156. [[CrossRef](#)]
95. Caballero-Flores, R.; Gonz lez-Legarreta, L.; Rosa, W.O.; S nchez, T.; Prida, V.M.; Escoda, L.; Su nol, J.J.; Batdalov, A.B.; Aliev, A.M.; Koledov, V.V.; et al. Magnetocaloric effect, magnetostructural and magnetic phase transformations in $\text{Ni}_{50.3}\text{Mn}_{36.5}\text{Sn}_{13.2}$ Heusler alloy ribbons. *J. Alloy. Compd.* **2015**, *629*, 332–342. [[CrossRef](#)]
96. Bruno, N.M.; Yegin, C.; Karaman, I.; Chen, J.-H.; Ross, J.H.; Liu, J.; Li, J. The effect of heat treatments on $\text{Ni}_{43}\text{Mn}_{42}\text{Co}_4\text{Sn}_{11}$ meta-magnetic shape memory alloys for magnetic refrigeration. *Acta Mater.* **2014**, *74*, 66–84. [[CrossRef](#)]
97. Rama Rao, N.V.; Gopalan, R.; Manivel Raja, M.; Arout Chelvane, J.; Majumdar, B.; Chandrasekaran, V. Magneto-structural transformation studies in melt-spun Ni-Mn-Ga ribbons. *Scr. Mater.* **2007**, *56*, 405–408. [[CrossRef](#)]
98. Hernando, B.; Llamazares, J.L.S.; Santos, J.D.; Sanchez, M.L.; Escoda, L.; Sunol, J.J.; Varga, R.; Garcia, C.; Gonzalez, J. Grain oriented NiMnSn and NiMnIn Heusler alloys ribbons produced by melt spinning: Martensitic transformation and magnetic properties. *J. Magn. Magn. Mater.* **2009**, *321*, 763–768. [[CrossRef](#)]

99. Ma, S.C.; Shih, C.W.; Liu, J.; Yuan, J.H.; Lee, S.Y.; Lee, Y.I.; Chang, H.W.; Chang, W.C. Wheel speed-dependent martensitic transformation and magnetocaloric effect in Ni-Co-Mn-Sn ferromagnetic shape memory alloy ribbons. *Acta Mater.* **2015**, *90*, 292–302. [[CrossRef](#)]
100. Chen, X.; Naik, V.B.; Mahendiran, R.; Ramanujan, R.V. Optimization of Ni-Co-Mn-Sn Heusler alloy composition for near room temperature magnetic cooling. *J. Alloy. Compd.* **2014**, *618*, 187–191. [[CrossRef](#)]
101. Chen, F.; Tong, Y.X.; Huang, Y.J.; Tian, B.; Li, L.; Zheng, Y.F. Suppression of gamma phase in Ni₃₈Co₁₂Mn₄₁Sn₉ alloy by melt spinning and its effect on martensitic transformation and magnetic properties. *Intermetallics* **2013**, *36*, 81–85. [[CrossRef](#)]
102. Pandey, S.; Quetz, A.; Ibarra-Gaytan, P.J.; Sanchez-Valdes, C.F.; Aryal, A.; Dubenko, I.; Mazumdar, D.; Sanchez Llamazares, J.L.; Stadler, S.; Ali, N. Effects of annealing on the magnetic properties and magnetocaloric effects of B doped Ni-Mn-In melt-spun ribbons. *J. Alloy. Compd.* **2018**, *731*, 678–684. [[CrossRef](#)]
103. Vajpai, S.K.; Dube, R.K.; Chatterjee, P.; Sangal, S. A novel powder metallurgy processing approach to prepare fine-grained Cu-Al-Ni shape-memory alloy strips from elemental powders. *Metall. Mater. Trans. A Phys. Met. Mater. Sci.* **2012**, *43*, 2484–2499. [[CrossRef](#)]
104. Perez-Saez, R.B.; Recarte, V.; No, M.L.; Ruano, O.A.; San, J.J. Advanced shape memory alloys processed by powder metallurgy. *Adv. Eng. Mater.* **2000**, *2*, 49–53. [[CrossRef](#)]
105. Monastyrsky, G.E.; Odnosum, V.; Van Humbeeck, J.; Kolomytsev, V.I.; Koval, Y.N. Powder metallurgical processing of Ni–Ti–Zr alloys undergoing martensitic transformation: Part I. *Intermetallics* **2002**, *10*, 95–103. [[CrossRef](#)]
106. Monastyrsky, G.E.; Van Humbeeck, J.; Kolomytsev, V.I.; Koval, Y.N. Powder metallurgical processing of Ni–Ti–Zr alloys undergoing martensitic transformation—Part II. *Intermetallics* **2002**, *10*, 613–624. [[CrossRef](#)]
107. Valeanu, M.; Lucaci, M.; Crisan, A.D.; Sofronie, M.; Leonat, L.; Kuncser, V. Martensitic transformation of Ti₅₀Ni₃₀Cu₂₀ alloy prepared by powder metallurgy. *J. Alloy. Compd.* **2011**, *509*, 4495–4498. [[CrossRef](#)]
108. Terayama, A.; Kyogoku, H. Shape memory characteristics of the P/M-processed Ti–Ni–Cu alloys. *Mater. Sci. Eng. A* **2010**, *527*, 5484–5491. [[CrossRef](#)]
109. Ibarra, A.; Rodriguez, P.P.; Recarte, V.; Perez-Landazabal, J.I.; No, M.L.; San Juan, J. Internal friction behaviour during martensitic transformation in shape memory alloys processed by powder metallurgy. *Mater. Sci. Eng. A* **2004**, *370*, 492–496. [[CrossRef](#)]
110. Kim, Y.-W.; Chung, Y.-S.; Choi, E.; Nam, T.-H. *Microstructure and Shape Memory Characteristics of Powder-Metallurgical-Processed Ti-Ni-Cu Alloys*; Springer Boston: Norwell, MA, USA, 2012; pp. 2932–2938.
111. Bertheville, B. Powder metallurgical processing of ternary Ni₅₀Ti_{50-x}Zr_x (x = 5, 10 at %) alloys. *J. Alloy. Compd.* **2005**, *398*, 94–99. [[CrossRef](#)]
112. Zhang, X.; Xiang, Y. Combinatorial approaches for high-throughput characterization of mechanical properties. *J. Mater.* **2017**, *3*, 209–220. [[CrossRef](#)]
113. Zarnetta, R.; Ehmann, M.; Savan, A.; Ludwig, A. Identification of optimized Ti–Ni–Cu shape memory alloy compositions for high-frequency thin film microactuator applications. *Smart Mater. Struct.* **2010**, *19*, 065032. [[CrossRef](#)]
114. Zarnetta, R.; Savan, A.; Thienhaus, S.; Ludwig, A. Combinatorial study of phase transformation characteristics of a Ti–Ni–Pd shape memory thin film composition spread in view of microactuator applications. *Appl. Surf. Sci.* **2007**, *254*, 743–748. [[CrossRef](#)]
115. Cui, J.; Chu, Y.S.; Famodu, O.O.; Furuya, Y.; Hattrick-Simpers, J.; James, R.D.; Ludwig, A.; Thienhaus, S.; Wuttig, M.; Zhang, Z.; et al. Combinatorial search of thermoelastic shape-memory alloys with extremely small hysteresis width. *Nat. Mater.* **2006**, *5*, 286–290. [[CrossRef](#)] [[PubMed](#)]
116. Zarnetta, R.; Takahashi, R.; Young, M.L.; Savan, A.; Furuya, Y.; Thienhaus, S.; Maa, B.; Rahim, M.; Frenzel, J.; Brunken, H.; et al. Identification of quaternary shape memory alloys with near-zero thermal hysteresis and unprecedented functional stability. *Adv. Funct. Mater.* **2010**, *20*, 1917–1923. [[CrossRef](#)]
117. Takeuchi, I.; Famodu, O.O.; Read, J.C.; Aronova, M.A.; Chang, K.S.; Craciunescu, C.; Lofland, S.E.; Wuttig, M.; Wellstood, F.C.; Knauss, L.; et al. Identification of novel compositions of ferromagnetic shape-memory alloys using composition spreads. *Nat. Mater.* **2003**, *2*, 180. [[CrossRef](#)] [[PubMed](#)]

118. Famodu, O.O.; Hatrick-Simpers, J.; Aronova, M.; Chang, K.-S.; Murakami, M.; Wuttig, M.; Okazaki, T.; Furuya, Y.; Knauss, L.A.; Bendersky, L.A.; et al. Combinatorial Investigation of Ferromagnetic Shape-Memory Alloys in the Ni-Mn-Al Ternary System Using a Composition Spread Technique. *Mater. Trans.* **2004**, *45*, 173–177. [[CrossRef](#)]
119. Dwivedi, A.; Wyrobek, T.J.; Warren, O.L.; Hatrick-Simpers, J.; Famodu, O.O.; Takeuchi, I. High-throughput screening of shape memory alloy thin-film spreads using nanoindentation. *J. Appl. Phys.* **2008**, *104*, 073501. [[CrossRef](#)]
120. Liu, Z.; Wu, Z.; Yang, H.; Liu, Y.; Wang, W.; Ma, X.; Wu, G. Martensitic transformation and magnetic properties in ferromagnetic shape memory alloy $\text{Ni}_{43}\text{Mn}_{46}\text{Sn}_{11-x}\text{Six}$. *Intermetallics* **2011**, *19*, 1605–1611. [[CrossRef](#)]
121. Aksoy, S.; Acet, M.; Wassermann, E.F.; Krenke, T.; Moya, X.; Manosa, L.; Planes, A.P.; Deen, P. Structural properties and magnetic interactions in martensitic Ni-Mn-Sb alloys. *Magazin* **2009**, *89*, 2093–2109. [[CrossRef](#)]
122. Dubenko, I.; Quetz, A.; Pandey, S.; Aryal, A.; Eubank, M.; Rodionov, I.; Prudnikov, V.; Granovsky, A.; Lahderanta, E.; Samanta, T.; et al. Multifunctional properties related to magnetostructural transitions in ternary and quaternary Heusler alloys. *J. Magn. Magn. Mater.* **2015**, *383*, 186–189. [[CrossRef](#)]
123. Krenke, T.; Duman, E.; Acet, M.; Wasserman, E.F.; Moya, X.; Manosa, L.; Planes, A.; Suard, E.; Ouladdiaf, B. Magnetic superelasticity and inverse magnetocaloric effect in Ni-Mn-In. *Phys. Rev. B* **2007**, *75*, 104414. [[CrossRef](#)]
124. Krenke, T.; Duman, E.; Acet, M.; Moya, X.; Manosa, L.; Planes, A. Effect of Co and Fe on the inverse magnetocaloric properties of Ni-Mn-Sn. *J. Appl. Phys.* **2007**, *102*, 033903. [[CrossRef](#)]
125. Wu, Z.; Liu, Z.; Yang, H.; Liu, Y.; Wu, G. Effect of Co addition on martensitic phase transformation and magnetic properties of $\text{Mn}_{50}\text{Ni}_{40-x}\text{In}_{10}\text{Cox}$ polycrystalline alloys. *Intermetallics* **2011**, *19*, 1839–1848. [[CrossRef](#)]
126. Wang, Z.L.; Cong, D.Y.; Nie, Z.H.; Gao, J.; Liu, W.; Wang, Y.D. The suppression and recovery of martensitic transformation in a Ni-Co-Mn-In magnetic shape memory alloy. *J. Alloy. Compd.* **2012**, *511*, 41–44. [[CrossRef](#)]
127. Pérez-Landazábal, J.L.; Lambri, O.A.; Bonifacich, F.G.; Sánchez-Alarcos, V.; Recarte, V.; Tarditti, F. Influence of defects on the irreversible phase transition in Fe-Pd ferromagnetic shape memory alloys. *Acta Mater.* **2015**, *86*, 110–117. [[CrossRef](#)]
128. Meng, Q.; Yang, H.; Liu, Y.; Nam, T.-H.; Chen, F. Thermal arrest analysis of thermoelastic martensitic transformations in shape memory alloys. *J. Mater. Res.* **2011**, *26*, 1243–1252. [[CrossRef](#)]
129. Brandon, D.; Kaplan, W.D. Optical Microscopy. In *Microstructural Characterization of Materials*; John Wiley & Sons, Ltd.: Hobo, NJ, USA, 2008; pp. 123–177.
130. Krenke, T.; Acet, M.; Wasserman, E.F.; Moya, X.; Manosa, L.; Planes, A. Martensitic transitions and nature of ferromagnetism in the austenitic and martensitic states of Ni-Mn-Sn alloys. *Phys. Rev. B* **2005**, *72*, 014412. [[CrossRef](#)]
131. Xu, X.; Ito, W.; Katakura, I.; Tokunaga, M.; Kainuma, R. In situ optical microscopic observation of NiCoMnIn metamagnetic shape memory alloy under pulsed high magnetic field. *Scr. Mater.* **2011**, *65*, 946–949. [[CrossRef](#)]
132. Katakura, I.; Tokunaga, M.; Matsuo, A.; Kawaguchi, K.; Kindo, K.; Hitomi, M.; Akahoshi, D.; Kuwahara, H. Development of high-speed polarizing imaging system for operation in high pulsed magnetic field. *Rev. Sci. Instrum.* **2010**, *81*, 043701. [[CrossRef](#)] [[PubMed](#)]
133. Brandon, D.; Kaplan, W.D. Diffraction Analysis of Crystal Structure. In *Microstructural Characterization of Materials*; John Wiley & Sons, Ltd.: Hobo, NJ, USA, 2008; pp. 55–122.
134. Bhatti, K.P.; El-Khatib, S.; Srivastava, V.; James, R.D.; Leighton, C. Small-angle neutron scattering study of magnetic ordering and inhomogeneity across the martensitic phase transformation in $\text{Ni}_{50-x}\text{Co}_x\text{Mn}_{40}\text{Sn}_{10}$ alloys. *Phys. Rev. B* **2012**, *85*, 134450. [[CrossRef](#)]
135. Brown, P.J.; Crangle, J.; Kanomata, T.; Matsumoto, M.; Neumann, K.U.; Ouladdiaf, B.; Ziebeck, K.R.A. The crystal structure and phase transitions of the magnetic shape memory compound Ni_2MnGa . *J. Phys. Condens. Matter* **2002**, *14*, 10159. [[CrossRef](#)]
136. Brandon, D.; Kaplan, W.D. Scanning Electron Microscopy. In *Microstructural Characterization of Materials*; John Wiley & Sons, Ltd.: Hobo, NJ, USA, 2008; pp. 261–331.
137. Brandon, D.; Kaplan, W.D. Transmission Electron Microscopy. In *Microstructural Characterization of Materials*; John Wiley & Sons, Ltd.: Hobo, NJ, USA, 2008; pp. 179–260.

138. Delville, R.; Kasinathan, S.; Zhang, Z.; Humbeeck, J.V.; James, R.D.; Schryvers, D. Transmission electron microscopy study of phase compatibility in low hysteresis shape memory alloys. *Philos. Mag.* **2010**, *90*, 177–195. [[CrossRef](#)]
139. Murakami, Y.; Yano, T.; Shindo, D.; Kainuma, R.; Arima, T. *Transmission Electron Microscopy on Magnetic Phase Transformations in Functional Materials*; Springer Boston: Norwell, MA, USA, 2007; pp. 815–820.
140. Hurrich, C.; Roth, S.; Wendrock, H.; Potschke, M.; Cong, D.Y.; Rellinghaus, B.; Schultz, L. Influence of grain size and training temperature on strain of polycrystalline Ni₅₀Mn₂₉Ga₂₁ samples. In Proceedings of the Joint European Magnetic Symposia, Krakow, Poland, 23–28 August 2010; Institute of Physics Publishing: Krakow, Poland, 2011.
141. Cong, D.Y.; Zhang, Y.D.; Esling, C.; Wang, Y.D.; Zhao, X.; Zuo, L. Crystallographic features during martensitic transformation in Ni-Mn-Ga ferromagnetic shape memory alloys. In Proceedings of the Materials Processing and Texture—15th International Conference on Textures of Materials, Pittsburgh, PA, USA, 1–6 June 2008; American Ceramic Society: Pittsburgh, PA, USA, 2008; pp. 397–403.
142. Yan, H.; Zhang, Y.; Xu, N.; Senyshyn, A.; Brokmeier, H.-G.; Esling, C.; Zhao, X.; Zuo, L. Crystal structure determination of incommensurate modulated martensite in Ni–Mn–In Heusler alloys. *Acta Mater.* **2015**, *88*, 375–388. [[CrossRef](#)]
143. National SQUID Facility IIT Delhi. What Is Superconducting Quantum Interface Device (SQUID)? Available online: http://squid.iitd.ernet.in/Basic_Literature.htm (accessed on 20 April 2018).
144. Shevtyrtalov, S.; Miki, H.; Ohtsuka, M.; Grunin, A.; Lyatun, I.; Mashirov, A.; Seregina, M.; Khovaylo, V.; Rodionova, V. Martensitic transformation in polycrystalline substrate-constrained and freestanding Ni-Mn-Ga films with Ni and Ga excess. *J. Alloy. Compd.* **2018**, *741*, 1098–1104. [[CrossRef](#)]
145. Lázpita, P.; Sasmaz, M.; Cesari, E.; Barandiarán, J.M.; Gutiérrez, J.; Chernenko, V.A. Martensitic transformation and magnetic field induced effects in Ni₄₂Co₈Mn₃₉Sn₁₁ metamagnetic shape memory alloy. *Acta Mater.* **2016**, *109*, 170–176. [[CrossRef](#)]
146. Huang, L.; Cong, D.Y.; Ma, L.; Nie, Z.H.; Wang, M.G.; Wang, Z.L.; Suo, H.L.; Ren, Y.; Wang, Y.D. Large magnetic entropy change and magnetoresistance in a Ni₄₁Co₉Mn₄₀Sn₁₀ magnetic shape memory alloy. *J. Alloy. Compd.* **2015**, *647*, 1081–1085. [[CrossRef](#)]
147. Zhang, X.; Qian, M.; Su, R.; Geng, L. Giant room-temperature inverse and conventional magnetocaloric effects in Ni–Mn–In alloys. *Mater. Lett.* **2016**, *163*, 274–276. [[CrossRef](#)]
148. Zhang, X.; Qian, M.; Miao, S.; Su, R.; Liu, Y.; Geng, L.; Sun, J. Enhanced magnetic entropy change and working temperature interval in Ni–Mn–In–Co alloys. *J. Alloy. Compd.* **2016**, *656*, 154–158. [[CrossRef](#)]
149. Sozinov, A.; Likhachev, A.A.; Lanska, N.; Soderberg, O.; Ullakko, K.; Lindroos, V.K. *Effect of Crystal Structure on Magnetic-Field-Induced Strain in Ni-Mn-Ga*; International Society for Optics and Photonics: San Diego, CA, USA, 2003; pp. 586–594.
150. Sozinov, A.; Lanska, N.; Soroka, A.; Zou, W. 12% magnetic field-induced strain in Ni-Mn-Ga-based non-modulated martensite. *Appl. Phys. Lett.* **2013**, *102*, 021902. [[CrossRef](#)]
151. Khalid, F.A.; Abbas, S.Z. Characterization and properties of ferromagnetic shape memory alloys. *Mater. Charact.* **2011**, *62*, 1134–1140. [[CrossRef](#)]
152. Monroe, J.A.; Karaman, I.; Basaran, B.; Ito, W.; Umetsu, R.Y.; Kainuma, R.; Koyama, K.; Chumlyakov, Y.I. Direct measurement of large reversible magnetic-field-induced strain in Ni-Co-Mn-In metamagnetic shape memory alloys. *Acta Mater.* **2012**, *60*, 6883–6891. [[CrossRef](#)]
153. Karaca, H.E.; Karaman, I.; Basaran, B.; Ren, Y.; Chumlyakov, Y.I.; Maier, H.J. Magnetic field-induced phase transformation in NiMnCoIn magnetic shape-memory alloys—a new actuation mechanism with large work output. *Adv. Funct. Mater.* **2009**, *19*, 983–998. [[CrossRef](#)]
154. Li, Z.; Xu, K.; Zhang, Y.L.; Jing, C. Reproducible magnetostain behavior induced by structure transformation for Ni₄₆Co₄Mn₃₉Sn₁₁ Heusler alloy. *J. Appl. Phys.* **2015**, *117*, 023902. [[CrossRef](#)]
155. He, W.Q.; Huang, H.B.; Liu, Z.H.; Ma, X.Q. First-principles investigation of magnetic properties and metamagnetic transition of NiCoMnZ (Z = In, Sn, Sb) Heusler alloys. *Intermetallics* **2017**, *90*, 140–146. [[CrossRef](#)]
156. Aguilar-Ortiz, C.O.; Soto-Parra, D.; Álvarez-Alonso, P.; Lázpita, P.; Salazar, D.; Castillo-Villa, P.O.; Flores-Zúñiga, H.; Chernenko, V.A. Influence of Fe doping and magnetic field on martensitic transition in Ni–Mn–Sn melt-spun ribbons. *Acta Mater.* **2016**, *107*, 9–16. [[CrossRef](#)]

157. Yang, L.H.; Zhang, H.; Hu, F.X.; Sun, J.R.; Pan, L.Q.; Shen, B.G. Magnetocaloric effect and martensitic transition in $\text{Ni}_{50}\text{Mn}_{36-x}\text{Co}_x\text{Sn}_{14}$. *J. Alloy. Compd.* **2014**, *588*, 46–48. [[CrossRef](#)]
158. Ingale, B.; Gopalan, R.; Raja, M.M.; Chandrasekaran, V.; Ram, S. Magnetostructural transformation, microstructure, and magnetocaloric effect in Ni-Mn-Ga Heusler alloys. *J. Appl. Phys.* **2007**, *102*, 1. [[CrossRef](#)]
159. Rao, N.V.R.; Gopalan, R.; Chandrasekaran, V.; Suresh, K.G. Microstructure, magnetic properties and magnetocaloric effect in melt-spun Ni-Mn-Ga ribbons. *J. Alloy. Compd.* **2009**, *478*, 59–62. [[CrossRef](#)]
160. Rama Rao, N.V.; Gopalan, R.; Chandrasekaran, V.; Suresh, K.G. Phase coexistence, microstructure and magnetism in Ni-Mn-Sb alloys. *J. Phys. D Appl. Phys.* **2009**, *42*, 6. [[CrossRef](#)]
161. Zheng, H.; Wang, W.; Yu, J.; Zhai, Q.; Luo, Z. Martensitic transformation in melt-spun Heusler Ni-Mn-Sn-Co ribbons. *J. Mater. Res.* **2014**, *29*, 880–886. [[CrossRef](#)]
162. Zheng, H.; Wang, W.; Xue, S.; Zhai, Q.; Frenzel, J.; Luo, Z. Composition-dependent crystal structure and martensitic transformation in Heusler Ni-Mn-Sn alloys. *Acta Mater.* **2013**, *61*, 4648–4656. [[CrossRef](#)]
163. Gschneidner Jr, K.A.; Mudryk, Y.; Pecharsky, V.K. On the nature of the magnetocaloric effect of the first-order magnetostructural transition. *Scr. Mater.* **2012**, *67*, 572–577. [[CrossRef](#)]
164. Trung, N.T.; Zhang, L.; Caron, L.; Buschow, K.H.J.; Brück, E. Giant magnetocaloric effects by tailoring the phase transitions. *Appl. Phys. Lett.* **2010**, *96*, 172504. [[CrossRef](#)]
165. Pérez-Sierra, A.M.; Bruno, N.M.; Pons, J.; Cesari, E.; Karaman, I. Atomic order and martensitic transformation entropy change in Ni-Co-Mn-In metamagnetic shape memory alloys. *Scr. Mater.* **2016**, *110*, 61–64. [[CrossRef](#)]
166. Kustov, S.; Corró, M.L.; Pons, J.; Cesari, E. Entropy change and effect of magnetic field on martensitic transformation in a metamagnetic Ni-Co-Mn-In shape memory alloy. *Appl. Phys. Lett.* **2009**, *94*, 191901. [[CrossRef](#)]
167. Recarte, V.; Pérez-Landazábal, J.I.; Sánchez-Alarcos, V.; Rodríguez-Velamazán, J.A. Dependence of the martensitic transformation and magnetic transition on the atomic order in Ni-Mn-In metamagnetic shape memory alloys. *Acta Mater.* **2012**, *60*, 1937–1945. [[CrossRef](#)]
168. Sánchez-Alarcos, V.; Recarte, V.; Pérez-Landazábal, J.I.; Gómez-Polo, C.; Rodríguez-Velamazán, J.A. Role of magnetism on the martensitic transformation in Ni-Mn-based magnetic shape memory alloys. *Acta Mater.* **2012**, *60*, 459–468. [[CrossRef](#)]
169. Sánchez-Alarcos, V.; Recarte, V.; Pérez-Landazábal, J.; Cesari, E.; Rodríguez-Velamazán, J. Long-Range Atomic Order and Entropy Change at the Martensitic Transformation in a Ni-Mn-In-Co Metamagnetic Shape Memory Alloy. *Entropy* **2014**, *16*, 2756. [[CrossRef](#)]
170. Yang, S.; Wang, C.; Shi, Z.; Wang, J.; Zhang, J.; Huang, Y.; Liu, X. Microstructure, martensitic transformation, mechanical and shape memory properties of Ni-Co-Mn-In high-temperature shape memory alloys under different heat treatments. *Mater. Sci. Eng. A* **2016**, *655*, 204–211. [[CrossRef](#)]
171. Ma, Y.; Jiang, C.; Li, Y.; Xu, H.; Wang, C.; Liu, X. Study of $\text{Ni}_{50+x}\text{Mn}_{25}\text{Ga}_{25-x}$ ($x = 2-11$) as high-temperature shape-memory alloys. *Acta Mater.* **2007**, *55*, 1533–1541. [[CrossRef](#)]
172. Yang, S.; Su, Y.; Wang, C.; Zhu, J.; Liu, X. Microstructure, martensitic transformation and shape memory effect of $\text{Ni}_{38}\text{Co}_{12}\text{Mn}_{41}\text{In}_9$ alloy. *Mater. Lett.* **2013**, *108*, 215–218. [[CrossRef](#)]
173. Tan, C.; Zhang, K.; Tian, X.; Cai, W. Effect of Gd addition on microstructure, martensitic transformation and mechanical properties of $\text{Ni}_{50}\text{Mn}_{36}\text{Sn}_{14}$ ferromagnetic shape memory alloy. *J. Alloy. Compd.* **2017**, *692*, 288–293. [[CrossRef](#)]
174. Pérez-Checa, A.; Feuchtwanger, J.; Musiienko, D.; Sozinov, A.; Barandiaran, J.M.; Ullakko, K.; Chernenko, V.A. High temperature $\text{Ni}_{45}\text{Co}_5\text{Mn}_{25-x}\text{Fe}_x\text{Ga}_{20}\text{Cu}_5$ ferromagnetic shape memory alloys. *Scr. Mater.* **2017**, *134*, 119–122. [[CrossRef](#)]
175. Zhao, X.G.; Hsieh, C.C.; Lai, J.H.; Cheng, X.J.; Chang, W.C.; Cui, W.B.; Liu, W.; Zhang, Z.D. Effects of annealing on the magnetic entropy change and exchange bias behavior in melt-spun Ni-Mn-In ribbons. *Scr. Mater.* **2010**, *63*, 250–253. [[CrossRef](#)]
176. Yuhasz, W.M.; Schlagel, D.L.; Xing, Q.; McCallum, R.W.; Lograsso, T.A. Metastability of ferromagnetic Ni-Mn-Sn Heusler alloys. *J. Alloy. Compd.* **2010**, *492*, 681–684. [[CrossRef](#)]

177. Das, R.; Saravanan, P.; Arvindha Babu, D.; Perumal, A.; Srinivasan, A. Influence of solidification rate and heat treatment on magnetic refrigerant properties of melt spun Ni₅₁Mn₃₄In₁₄Si₁ ribbons. *J. Magn. Magn. Mater.* **2013**, *344*, 152–157. [[CrossRef](#)]
178. Sánchez-Alarcos, V.; Pérez-Landazábal, J.I.; Recarte, V.; Lucia, I.; Vélez, J.; Rodríguez-Velamazán, J.A. Effect of high-temperature quenching on the magnetostructural transformations and the long-range atomic order of Ni–Mn–Sn and Ni–Mn–Sb metamagnetic shape memory alloys. *Acta Mater.* **2013**, *61*, 4676–4682. [[CrossRef](#)]



© 2018 by the authors. Licensee MDPI, Basel, Switzerland. This article is an open access article distributed under the terms and conditions of the Creative Commons Attribution (CC BY) license (<http://creativecommons.org/licenses/by/4.0/>).

10 Appendix 2

Techniques to characterize ternary and quaternary magnetic shape memory alloys.

Ahamed Khan, R.A.; Ghomashchi, R.; Xie, Z.; Chen, L

Ferromagnetic shape memory Heusler alloys are traditionally characterized through differential scanning calorimetry (DSC), microscopy, diffractometry, and magnetization measurements using superconducting quantum interference device (SQUID) magnetometer or a vibrating sample magnetometer (VSM). Of all characterization procedures, crystal structure determination and quantification of phases using diffraction techniques such as X-ray diffraction (XRD), neutron diffraction (ND) and selected area electron diffraction (SAED) using transmission electron microscopy (TEM) are very significant even though all of them complement each other very well. Diffraction studies in particular can be rewarding or frustrating depending upon the equipment being used, nature of alloys being synthesized for analysis, available search/match databases, tools for analysis and expertise of the analyst. Frustration arises where exact search/match of peaks in the diffraction patterns to available phases in the databases could not be obtained making the whole process complex and tedious. This is because the databases are still evolving. This calls for a knowledge of space groups to which the resultant structures of martensitic transformation may belong or a look up of possible unit cell structures to proceed with. This work documents from literature, characterization studies of several NiMn-based Heusler alloys using XRD with a view to assist researchers in the characterization of new and significant alloy compositions.

Statement of Authorship

Title of Paper	Techniques to characterize ternary and quaternary ferromagnetic shape memory alloys	
Publication Status	<input type="checkbox"/> Published <input type="checkbox"/> Submitted for Publication	<input type="checkbox"/> Accepted for Publication <input checked="" type="checkbox"/> Unpublished and Unsubmitted work written in manuscript style
Publication Details		

Principal Author

Name of Principal Author (Candidate)	Riaz Ahamed Ahamed Khan	
Contribution to the Paper	I was responsible for the literature review required for the work, and conducting of experiments discussed in the paper. Wrote the first draft of the manuscript and incorporated and addressed all comments/suggestions by other authors in subsequent revisions. Interpretation of results was primarily my responsibility.	
Overall percentage (%)	90%	
Certification:	This paper reports on original research I conducted during the period of my Higher Degree by Research candidature and is not subject to any obligations or contractual agreements with a third party that would constrain its inclusion in this thesis. I am the primary author of this paper.	
Signature		Date 21/6/19

Co-Author Contributions

By signing the Statement of Authorship, each author certifies that:

- i. the candidate's stated contribution to the publication is accurate (as detailed above);
- ii. permission is granted for the candidate to include the publication in the thesis; and
- iii. the sum of all co-author contributions is equal to 100% less the candidate's stated contribution.

Name of Co-Author	Lei Chen	
Contribution to the Paper	Supervising development of work, evaluating methods and theories, helping with experimental setup and evaluating manuscript.	
Signature		Date 21/06/19

Name of Co-Author	Reza Ghomashchi	
Contribution to the Paper	Supervising development of work, evaluating methods and theories, helping with experimental setup and evaluating and editing the manuscript.	
Signature		Date 25/6/2019

Name of Co-Author	Zonghan Xie		
Contribution to the Paper	Supervising development of work, evaluating methods and theories, helping with experimental setup and evaluating manuscript.		
Signature		Date	25/06/19

TECHNIQUES TO CHARACTERIZE TERNARY AND QUATERNARY FERROMAGNETIC SHAPE MEMORY ALLOYS

Riaz Ahamed^{1,*}, Reza Ghomashchi¹, Zonghan Xie¹ and Lei Chen¹

¹ School of Mechanical Engineering, University of Adelaide, Adelaide, SA 5005, Australia.

* Corresponding author: riazahamed.ahamedkhan@adelaide.edu.au

Abstract

Ni-Mn-X (X = group IIIA-VA elements) Heusler alloys have been seen to exhibit multiferroic effects such as magnetic/metamagnetic shape memory (MSM/MMSM), magnetocaloric (MC), direct energy conversion etc. and have a large potential for diverse applications in actuation, magnetic refrigeration and conversion of low grade waste heat into electricity. Beneath the multifunctional potential of these alloys is a magnetostructural coupling encompassing structural and magnetic transformations, which in turn depends on alloy compositions. As compositions are varied different crystal structures are evolved and it becomes essential that the structures are accurately characterized for their microstructures. This paper provides a short review of characterization techniques such as X-ray diffraction (XRD), transmission electron microscopy (TEM) and differential scanning calorimetry (DSC) with examples from our work as well as literature. Emphasis is laid on XRD, TEM and DSC, which are very important for microstructural characterization.

Introduction

Ni-Mn-X (X = group IIIA-VA elements) Heusler alloys can be considered multiferroic by phase transformation involving sensitivity of electromagnetic properties to crystal lattice changes. An example is seen in Ni₂MnGa, which transforms martensitically with a 25% increase in saturation magnetization accompanied by a dramatic change in magnetic anisotropy [1]. The Mn atoms are shown placed far apart in an expanded lattice after martensitic transformation to explain the dependence of electromagnetic properties to structural changes [1]. Multiferroic effects such as magnetic/metamagnetic shape memory (MSM/MMSM) [2-4], magnetocaloric (MC) [5] and direct energy conversion [6] seen in such alloys are outcomes of a magnetostructural coupling brought about by a combined first-order structural martensitic transformation and second-order magnetic transition. The former transforms high-temperature austenite phase to low-temperature martensite phase and the latter brings about a change in electromagnetic ordering in the phases in a biased field .

Martensitic transformation which holds the key to the emergence of magnetostructural coupling depends on alloy composition usually represented as the valence electron concentration (e/a). The composition dependence of martensitic transformation is explained as formation of martensite in response to a free energy build-up in the alloy when a change in e/a ratio destabilizes the parent $L2_1$ -structured austenite. Even a unit-cell contraction of the parent austenite changes the relative positions between the Fermi surface and Brillouin zone and causes martensitic transformation [7]. The electrons above the Fermi surface move to the corner states of the (1 1 0) Brillouin zone distorting the lattice structure to minimize the free energy. This distortion of the lattice above the Fermi surface is termed as a nesting phenomenon considered responsible for various modulations of the martensite structure. During martensitic transformation the original $L2_1$ structure transforms to body-centered-tetragonal (bct), orthorhombic or monoclinic symmetry depending on the composition. The nesting phenomenon expands the bct (or other) unit cell along certain crystal axes to give modulated structures such as $5M$, $7M$ etc. with numbers 5, 7 defining the times the unit cell expanded. The atomic positions overlap after every 5th or 7th layer along the given axis. Where the modulation wave vector is absent, the structure is termed as non-modulated (NM). Other representations include $4O$ for the four layered orthorhombic or notations such as $5R$, $7R$ for

five-layered or seven layered structures. A superspace (3+1)-dimensional approach [8] is being adopted as a powerful mathematical tool for the determination of the structural, compositional and physical modulations and commensuratness or incommensuratness associated with them [9].

What has been seen is that the material composition is a very significant factor for the occurrence of magnetostructural coupling and evolution of crystal structure of austenite and martensite phases. However the exact martensitic structure that would evolve for a particular composition and its effect on the magnetostructural characteristics could not be predicted [10] even though a transition from cubic $\rightarrow 10M(5M) \rightarrow 14M(7M) \rightarrow L1_0$ in accordance with an increasing e/a ratio and temperature has been the norm [11]. Some martensitic structures such as tetragonal five-layered ($5M$) and orthorhombic seven-layered ($7M$) martensitic phase in NiMnGa alloys are seen to favour magnetic field induced strain (MFIS) while a non-modulated tetragonal $L1_0$ does not favour (MFIS), when exposed to a magnetic field [12].

For higher order multicomponent Heusler alloys, the martensitic structure is also composition dependent as for instance in a giant magnetocaloric material with composition $Ni_{40}Co_{10}Mn_{40}Sn_{10}$ [13], the structure is not known while in another large magnetocaloric/magneto-resistance material with composition $Ni_{41}Co_9Mn_{40}Sn_{10}$ [14] the structure is monoclinic $6M$. The monoclinic $6M$ structure is representative of Ni-Co-Mn-In alloys with martensitic transformation near room temperature and incommensurate from the superspace standpoint [15]. In the singular $Ni_{45}Co_5Mn_{40}Sn_{10}$ [6] alloy capable of energy conversion at very low temperature difference, the martensitic structure is monoclinic $5M$. Hence it is the composition, which yields the resultant structure and it is necessary that the structures are accurately determined.

Ferromagnetic shape memory Heusler alloys are traditionally characterized through differential scanning calorimetry (DSC), microscopy, diffractometry, and magnetization measurements using superconducting quantum interference device (SQUID) magnetometer or a vibrating sample magnetometer (VSM). DSC allows us to know details about the temperatures at which the first-order phase and second-order magnetic transformations happen, the Curie temperatures, effects of compositions on these temperatures and phases in

the alloys above and below the transformation temperatures. Microscopy, optical (OM) and scanning electron microscopes (SEM), identifies the phases, morphologies and their compositions. Magnetometry reveals the magnetic behaviour of the alloys and the levels of magnetization attained in the alloys during transformation. In situ procedures involving all of these characterization techniques provide an insight into the magnetostructural transformations in real-time. For instance, in situ optical microscopy throws light on the phenomenon called kinetic arrest (KA) which is freezing of austenite upon removal of the magnetic field applied during a magnetic field induced transformation (MFIT) in Ni-Co-Mn-In alloys [16]. Of all characterization procedures, crystal structure determination and quantification of phases using diffraction techniques such as X-ray diffraction (XRD), neutron diffraction (ND) and selected area electron diffraction (SAED) using transmission electron microscopy (TEM) are very significant even though all of them complement each other very well. Diffraction studies in particular can be rewarding or frustrating depending upon the equipment being used, nature of alloys being synthesized for analysis, available search/match databases, tools for analysis and expertise of the analyst. Frustration arises where exact search/match of peaks in the diffraction patterns to available phases in the databases could not be obtained making the whole process complex and tedious. This is because the databases are still evolving. This calls for a knowledge of space groups to which the resultant structures of martensitic transformation may belong or a look up of possible unit cell structures to proceed with. This work documents from literature, characterization studies of several NiMn-based Heusler alloys using XRD with a view to assist researchers in the characterization of new and significant alloy compositions. Additionally methods and examples of transmission electron microscopy (TEM) procedures used to supplement XRD are also dealt with. DSC has been explained briefly to emphasize its significance in ferromagnetic Heusler alloys characterization. As a short review, it is not very exhaustive, but still can be very useful.

Diffraction

X-ray and neutron diffraction

When a collimated beam of X-rays is directed at a material sample, a constructive interference of the spectrum of elastic scattering of these X-rays at Bragg positions defined by the Bragg equation ($n\lambda = 2d\sin\theta$) show unique diffraction patterns characteristic of the crystal structures

of the material sample. Ideally, a plot between the intensity of the diffracted beam and the scattering angle (twice the Bragg diffraction angle) provides microstructural information such as the Bravais point lattice, unit cell dimensions and atomic numbers of constituent atoms (chemical species). The intensities of the diffracted spectra depend on the atomic numbers and the diffraction angle depends on Bravais point lattice and unit cell dimensions. High-energy X-ray diffractometers and synchrotron X-ray diffractometers have in-situ capabilities wherein the material properties such as phase composition, crystal structure, epitaxy, texture, orientation, crystallite size and macro/microstrain are evaluated as functions of time, temperature and gas environment [17].

The diffraction spectrum is a 'fingerprint' of the crystal structure and is usually compared with a diffraction standard such as the Powder Diffraction File (PDF) from the International Centre for Diffraction Data (ICDD). An ensemble of d-spacings ('d's) and intensities ('I's) are compared with the d-I files in the PDF to determine phases. The spectrum can also be compared with other calculated spectra and based on the degree of fit the phases are ascertained. Powder diffraction is often used in microstructure characterization of NiMn-based ferromagnetic Heusler alloys as it is easier and more convenient than single crystal diffraction which requires individual crystals to be made. The process is well suited for determination of phases and their crystal structures including superlattices of modulated structures besides being rapid with ease of data interpretation. However samples need be ground to fine powders less than $\sim 10 \mu\text{m}$ (or 200-mesh) in size [18].

Neutron diffraction is different from X-ray diffraction in that scattering depends on the nature of the scattering nuclides (atoms of a specific isotope) and consequently atoms of similar atomic number have different scattering lengths which is very hard to distinguish in X-ray diffraction [19]. Furthermore magnetic scattering by neutrons resulting from an interaction of neutrons with both spin and orbital magnetic moments in a magnetic material makes it useful to study magnetism on an atomic scale. Neutron diffraction is used to exactly monitor twin reorientation in ferromagnetic shape memory alloys while polarized neutron diffraction helps in separating the rotation of magnetic moments from the twin reorientation. A brief description of how these studies are carried out is available in [20]. Through a combination of small-angle neutron scattering (SANS) and in-situ magnetometry, Leighton et al. provide a clear

understanding of the superparamagnetic freezing of nanoscopic spin clusters of unknown origin and the nature of the ground-state magnetic ordering in the martensitic phase of $\text{Ni}_{50-x}\text{Co}_x\text{Mn}_{40}\text{Sn}_{10}$ ($x = 6$ and 8) alloys [21].

High-resolution synchrotron X-ray diffraction is necessitated by the limitations of laboratory-based diffraction techniques in terms of resolution of the d-space range, signal-to-noise ratio and shape and width of observed reflections. The high-resolution diffractometry possible using synchrotron diffraction makes it suitable for precise in situ examination of chemical processes, structure/property studies, phase identification and quantification and examination of stress and strain. Small lattice distortions such as seen in the adaptive phases of ferromagnetic Heusler materials, Jahn-Teller distortions etc. appear as subtle peak splitting or weak superlattice reflections in diffraction data. Synchrotron diffraction is best suited to resolve these issues. Rietveld refinement (adopting a least squares approach to refine a theoretical line profile) in (3+1)-dimensional space for precise structural refinement and ab initio methodologies for atomic occupancies provide a complete crystal structure information. The structural refinement by itself is not straight forward as numerous interdependent structural parameters such as lattice parameters, modulation wave vector function and its coefficients, atomic displacements and atom occupancies are to be refined to arrive at a calculated diffraction pattern. An identical calculated pattern with an unknown sample pattern is then used to obtain crystal structure information. No standards are needed to achieve accurate results to within $\pm 1\%$ and this makes Rietveld refinement an exceptionally valuable method for structural analysis for all classes of crystalline materials not available as single crystals. Rietveld refinement and ab initio techniques are now software driven. Commercial packages such as FullProf, Jana2006 for Rietveld and Vienna ab initio simulation package are available for analysis, however requires an extensive knowledge of crystallography and powder diffraction for a credible structural analysis. We present here examples of XRD characterization of ferromagnetic Heusler alloys.

At around the stoichiometric compositions, martensitic transformation in Ni_2MnSn alloys may yield $L2_1$ or DO_3 structures with the binaries Ni-Mn and Ni-Sn yielding tetragonal or hexagonal phases [22]. Krenke et al. [22] performed a series of room temperature XRD studies using Cu-K α radiation on $\text{Ni}_{50}\text{Mn}_{50-x}\text{Sn}_x$ ($x = 5, 10, 13, 15, 18, 20$ and 25 ; composition rewritten) alloys to determine the crystal structure variation from $L2_1$ to modulated $10M$, $14M$ and $L1_0$

structures as the Sn concentration decreased. The samples were prepared by arc-melting and annealed at 1273 K for 2 h and then ice water quenched. The XRD patterns of $\text{Ni}_{50}\text{Mn}_{50-x}\text{Sn}_x$ ($x = 25, 13, 10$ and 5) and the corresponding optical micrographs

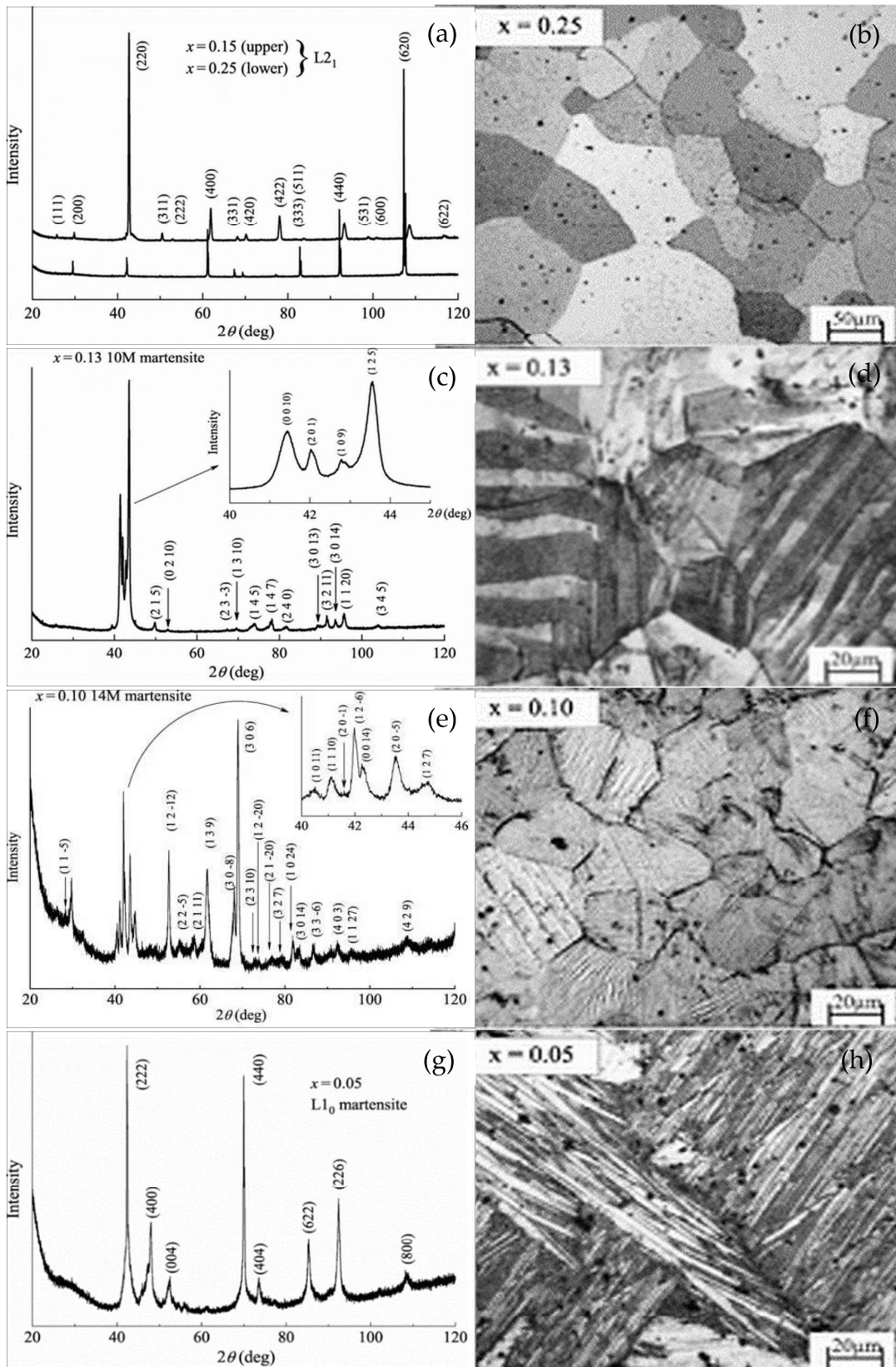


Figure 1. Room temperature XRD patterns and corresponding optical micrographs of $\text{Ni}_{50}\text{Mn}_{50-x}\text{Sn}_x$ alloy compositions: (a) & (b) $x = 25$; (c) & (d) $x = 13$; (e) & (f) $x = 10$ and (g) & (h) $x = 5$ [21].

depicting the microstructures are shown in Figure 1. The unit cells were orthorhombic for 10M, monoclinic for 14M and tetragonal for $L1_0$. The grain sizes of all structures are within 50 – 300 μm and the morphology of the martensites is platelike even though they are broad for 10M, finer for 14M and intermediate for $L1_0$.

From among the alloys discussed above $\text{Ni}_{50}\text{Mn}_{37}\text{Sn}_{13}$ is significant because it exhibits martensitic transformation at room temperature as well as a large inverse magnetocaloric effect (MCE) of 20 J/kg/K comparable with giant MCE materials such as $\text{Gd}_5(\text{Si}_x\text{Ge}_{1-x})_4$ [5]. Inverse MCE refers to a positive value of magnetic entropy change and is potentially useful for room-temperature refrigeration. A few more XRD patterns of this alloy prepared using identical or different processing conditions are shown in Figure 2. In the upper panel of Figure 2 (a), at room temperature a 10M modulated orthorhombic structure is seen for this composition prepared by arc-melting and annealed at 1000 °C (1273 K) for 24 h followed by slow cooling [23]. The XRD patterns of this alloy structure including the lattice parameters are in full agreement with the 10M structure seen in [22]. However, the same arc-melted alloy exhibited both $L2_1$ austenitic and orthorhombic 4O martensitic structures, middle pattern in Figure 2 (c), which after annealing at 1273 K for 4 h and water quench exhibited only 4O structure, middle pattern in Figure 2 (d). The $L2_1$ structure is seen suppressed [7]. This work [7] also reveals a martensitic structural evolution sequence of 4O – 10M – 14M – $L1_0$ in bulk Ni-Mn-Sn alloys [7]. A melt-spun $\text{Ni}_{50}\text{Mn}_{37}\text{Sn}_{13}$ alloy on the other hand exhibited a $L2_1$ austenite structure at room temperature, in Figure 2 (b), and an orthorhombic 7M martensite at 150 K which is lower than its martensitic transformation temperature [24]. The unit cell is orthorhombic in all these. It turns out that the basic unit cell is orthorhombic for the composition $\text{Ni}_{50}\text{Mn}_{37}\text{Sn}_{13}$ even though the final modulated structure depended on the processing condition.

Pons et al. [25] studied the crystal structures of martensitic phases in Ni-Mn-Ga alloys from the perspective of two approaches varying used to describe the structures. The first approach considered long period stacking of {110} closed packed planes of austenite or {111} planes of the face-centered tetragonal $L1_0$ unit cell. The second approach considered harmonic modulation due to a periodic shuffling of the basal planes. The crystallographic axes along which the unit cells are aligned are the same in both approaches, given by $[\bar{1}10]$ (a -axis), [001]

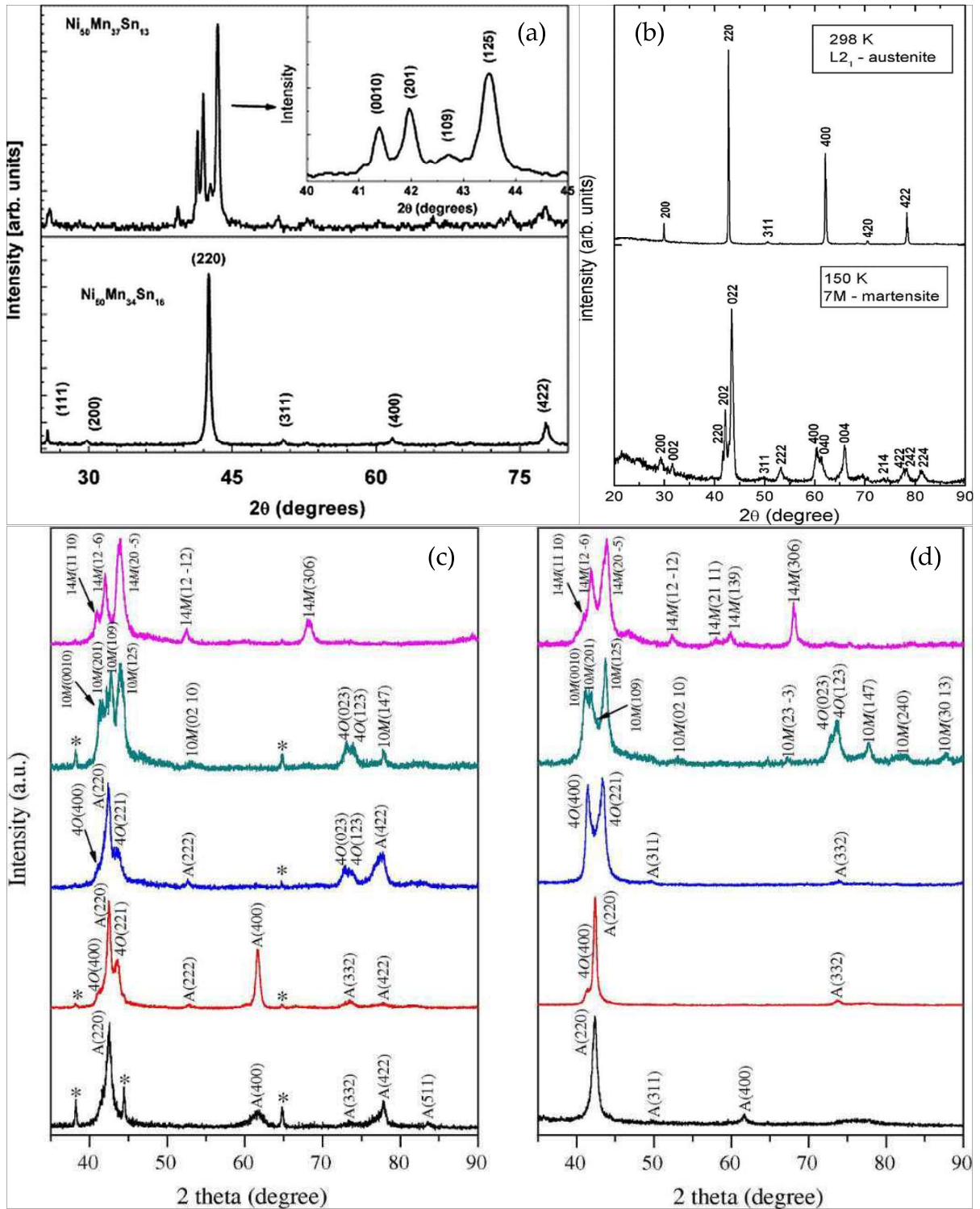


Figure 2 XRD patterns of: (a) $\text{Ni}_{50}\text{Mn}_{37}\text{Sn}_{13}$ (up) and $\text{Ni}_{50}\text{Mn}_{34}\text{Sn}_{16}$ (down) [22]; (b) as-quenched $\text{Ni}_{50}\text{Mn}_{37}\text{Sn}_{13}$ ribbons at 298 K (up) and 150 K (down) [23]; (c) as-cast and (d) annealed patterns of $\text{Ni}_{50}\text{Mn}_{41}\text{Sn}_9$, $\text{Ni}_{50}\text{Mn}_{39}\text{Sn}_{11}$, $\text{Ni}_{50}\text{Mn}_{37}\text{Sn}_{13}$, $\text{Ni}_{48}\text{Mn}_{39}\text{Sn}_{13}$ and $\text{Ni}_{46}\text{Mn}_{41}\text{Sn}_{13}$, top-down respectively [7].

(b -axis) and $[110]$ (c -axis) of the cubic austenite. The unit cell is monoclinic and the crystallographic axes are termed 'monoclinic' in the former. In the latter these axes are termed

‘cubic’ because of the correspondence between the basic body-centered martensite structures and the cubic austenite. While the approaches are different the structures are nearly similar. Taking into account the superspace formulation, this study found five-layered martensite as a shuffling modulated structure and the seven-layered martensite as a long period stacking of basal planes with $(5\bar{2})_2$ Zhdanov sequence. The kind of structuring seen in the $7M$ structure qualifies it to be treated as an adaptive phase of microtwinned $L1_0$ structure as seen in $14M$ which also has a $(5\bar{2})_2$ stacking sequence. Five- and seven-layered ($5M$ and $7M$) martensites are also referred to as $10M$ and $14M$ respectively with respect to a new notation for martensites. Shown in Figure 3 (a) below is the XRD pattern of the melt-spun ribbon of $\text{Ni}_{53.1}\text{Mn}_{26.6}\text{Ga}_{20.3}$ indexed according to a $14M$ structure while the bulk alloy of same composition exhibited a $L1_0$ (non-modulated tetragonal) structure, similar to that shown for $\text{Ni}_{45.7}\text{Mn}_{37.2}\text{Ga}_{17.1}$ in Figure 3 (b), attributed to the grain size reduction and introduction of internal stresses in melt-spun ribbons.

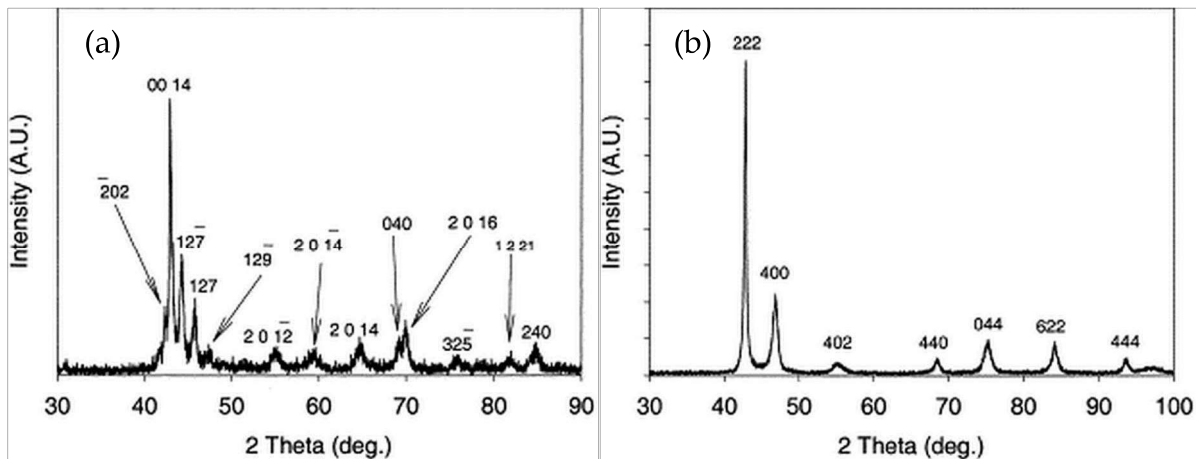


Figure 3. (a) XRD pattern of the melt-spun ribbon of $\text{Ni}_{53.1}\text{Mn}_{26.6}\text{Ga}_{20.3}$ at room temperature indexed according to $14M$ structure; (b) XRD pattern of $\text{Ni}_{45.7}\text{Mn}_{37.2}\text{Ga}_{17.1}$ indexed according to a $L2_1$ order which is a ‘double’ $L1_0$ unit cell although second neighbour ordering is not seen [24].

The modulated lattice approach following a harmonic shuffling of $(100)_{bct}$ unit cell along $[010]_{bct}$ yielded a $5R$ ($5M$) structure for the low temperature martensite in single crystal $\text{Ni}_{49}\text{Mn}_{29.5}\text{Ga}_{21.5}$ alloy (composition rewritten), homogenized at 1273 K for 72 h and annealed at 1070 K for 48 h. This is shown in Figure 4 (a) [26]. The XRD patterns of $\text{Ni}_{55}\text{Mn}_{20.6}\text{Ga}_{24.4}$ and $\text{Ni}_{55}\text{Mn}_{19.6}\text{Ga}_{25.4}$ alloy ribbons melt-spun at a wheel speed of 17 m/s in Figure 4 (b) are indexed to show an orthorhombic structure of $7M$ modulation. Here the structures are analysed splitting the $\{202\}$ peaks into (220) , (202) and (022) peaks [27]. A maximum value of $\Delta S_M \approx 10.4$

J/kgK at room temperature for a field change of 2 T and net refrigeration capacity of 45.5 J/kg was observed in the $\text{Ni}_{55}\text{Mn}_{19.6}\text{Ga}_{25.4}$ alloy with a low average hysteresis loss of ≈ 1.5 J/kg at the merged structural and magnetic transition temperatures.

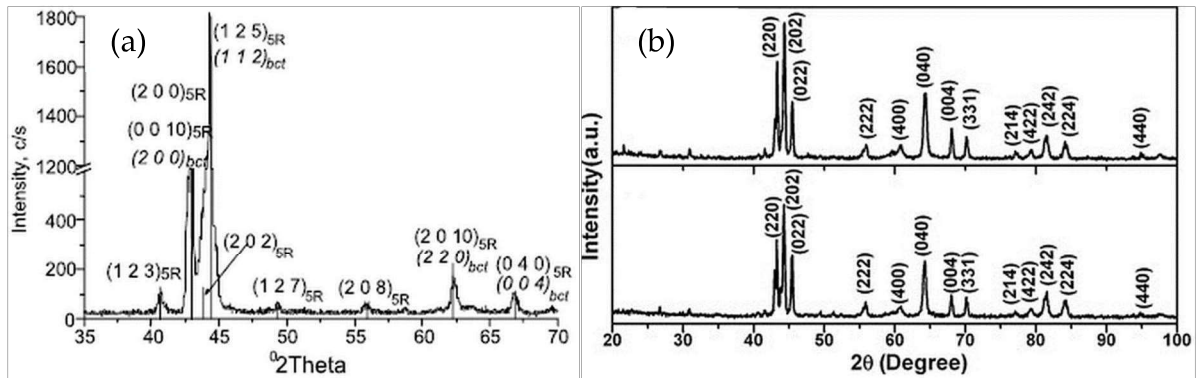


Figure 4. (a) Experimental (line) and simulated (bar) θ - 2θ diffraction patterns of 5R martensite in $\text{Ni}_{1.96}\text{Mn}_{1.18}\text{Ga}_{0.86}$ alloy at room temperature [25]; (b) XRD patterns of melt spun $\text{Ni}_{55}\text{Mn}_{20.6}\text{Ga}_{24.4}$ (upper panel) and $\text{Ni}_{55}\text{Mn}_{19.6}\text{Ga}_{25.4}$ (lower panel) ribbons [26].

Diffraction in reciprocal space is sometimes necessitated for the exact identification of crystal structures between peaks and can be carried out by conducting ω - 2θ scans conforming to Ewald's sphere in reciprocal space, Figure 5 (a). A Q-type scan between (400) and (620) is seen to show six approximately equally spaced additional peaks corresponding to a seven-layered (7M) orthorhombic martensite in $\text{Ni}_{48.8}\text{Mn}_{29.7}\text{Ga}_{21.5}$ alloy in Figure 5 (b), which interestingly exhibited intermartensitic transformation with the low temperature structure being tetragonal. The single crystal of the alloy was prepared by Bridgman procedure at the

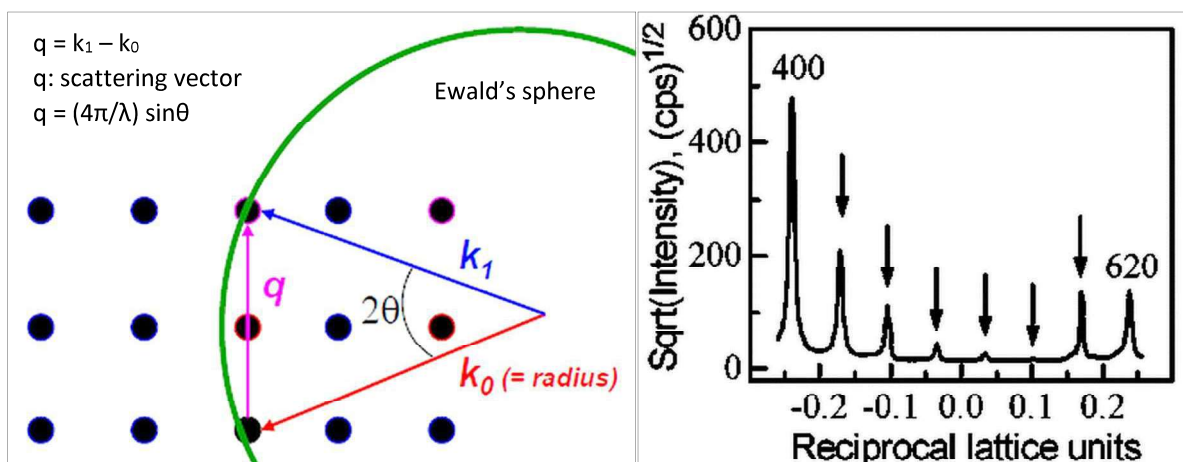


Figure 5. (a) High resolution diffraction in reciprocal space; (b) Scattered intensity distribution in reciprocal space between (400) and (620) nodes in the orthorhombic phase of $\text{Ni}_{48.8}\text{Mn}_{29.7}\text{Ga}_{21.5}$ alloy with arrows marking additional peaks connected with seven layered modulation of the lattice [27].

rate of 0.5 mm/min, homogenized at 1253 K for 20 h, aged at 1073 K for 30 h and cooled in air to room temperature. This alloy is significant for the fact that a giant magnetic field-induced strain of about 9.5% was observed in it at ambient temperature in a magnetic field of less than 1 T [28]. Two Ga-free $\text{Ni}_{50}\text{Mn}_{36.5}\text{Sn}_{13.5}$ and $\text{Ni}_{50}\text{Mn}_{38}\text{In}_{12}$ alloy ribbons exhibited $L2_1$ austenite and modulated orthorhombic martensite structures respectively as shown in Figure 6. The crystallographic direction in the martensite is (112) [29].

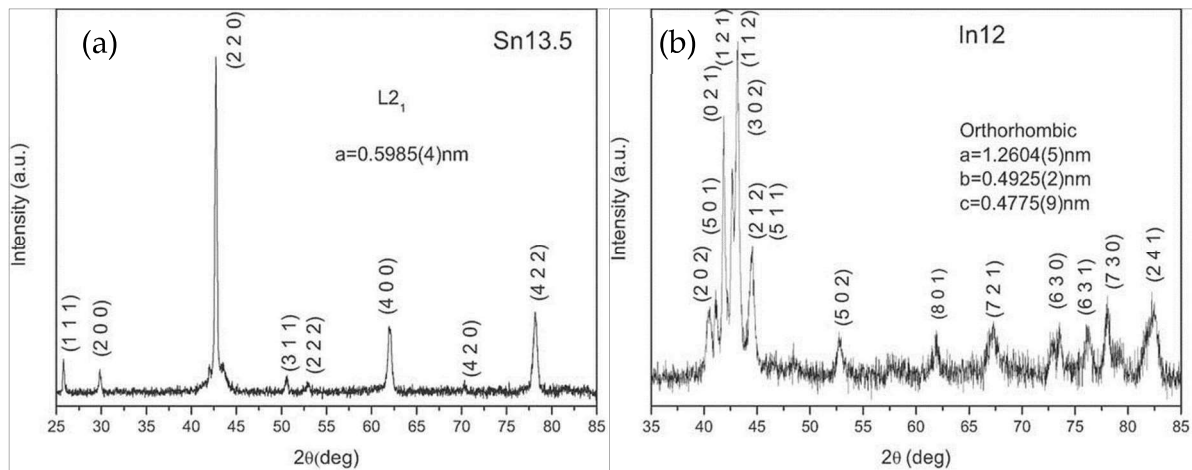


Figure 6. Room temperature XRD patterns of melt spun: (a) $\text{Ni}_{50}\text{Mn}_{36.5}\text{Sn}_{13.5}$ and (b) $\text{Ni}_{50}\text{Mn}_{38}\text{In}_{12}$ alloys [28].

The superspace (3+1) scheme of crystal structure determination requires elaboration in light of the fact that the supercell scheme previously used to describe modulations is inadequate. The supercell contained a number of basic unit cells in three-dimensional space. By counting the number of satellite spots between two main reflections the number of unit cells were determined. A sinusoidal function or a simple uniform shear is applied to the atoms of the supercell to achieve structural modulation [15]. This approach, although described the atomic arrangements obtained through high-resolution transmission electron microscopy (HRTEM) or diffraction analysis, isn't rigorous enough to accurately represent the structural modulation features such as the translational symmetry of the crystal lattice in three-dimensional space. The superspace (3+1) scheme seeks to redress this and other anomalies such as evolution of different modulated structures in some alloys with the same composition under similar processing environments. The superspace model carries an additional supplementary vector (modulation vector) is used to describe the periodicity of structural modulation. The generic diffraction vector H becomes $H = ha^* + kb^* + lc^* + mq$ where $q = \alpha a^* + \beta b^* + \gamma c^*$. Each Bragg reflection has four indices $hklm$ corresponding to a^* , b^* , c^*

(conventional lattice) and q , which is the modulation vector. When coefficients α , β and γ of the modulation wave vector correspond to a rational number, the modulation is commensurate and when they correspond to an irrational number, the modulation is incommensurate [8]. Thus both commensurate and incommensurate structures could be effectively characterized [15].

Yan et al. provide a very detailed account of the determination of incommensurate modulated martensitic structures in Ni-Mn-In alloys using synchrotron X-ray diffraction, ND, Rietveld refinement and ab initio structure solution [15]. This study is a very elaborate structural analysis of ferromagnetic Ni-Mn-based Heusler materials which can be used for the understanding of the mechanisms of magnetostructural behaviour and hence property optimization of these alloys. In order to successfully perform structural refinement, spurious diffraction data arising from factors such as retained austenite in transformed structures are addressed through a crystallographic inheritance of martensitic transformation represented by peak splitting. The exact crystal structure determination of martensite involved three steps: depiction of the unit cell of the average martensite structure (neglecting modulation) in three-dimensional space based on neutron diffraction data, derivation of modulation wave vector from the peak positions of satellite reflections from neutron diffraction data and finally structural refinement of the modulated martensite from synchrotron X-ray diffraction data using Rietveld and ab initio methods [15].

Figure 7 (a) shows the powder neutron diffraction spectrum of $\text{Ni}_{50}\text{Mn}_{35}\text{In}_{15}$ (composition rewritten), austenitic at room temperature and confirmed by DSC measurements. Crystal structure analysis through Rietveld technique showed the austenite to possess a $L2_1$ cubic structure with space group $Fm\bar{3}m$ and lattice parameter 6.0062 Å. Vertical arrows pointing to very small peaks resulted from 'surface martensite'. With DSC measurements confirming a martensite structure at room temperature for $\text{Ni}_{50}\text{Mn}_{36}\text{In}_{14}$ (composition rewritten) alloy, the powder diffraction pattern shown in Figure 7 (b) is of martensite. The figure carries the diffraction pattern of $\text{Ni}_{50}\text{Mn}_{35}\text{In}_{15}$ alloy as a reference. As both compositions are nearly equal, the austenite structures are approximated one with the other. The martensite has been generated through a distortion of the austenite lattice during transformation resulting in the symmetry breaking of austenite. This could be seen as splitting in the diffraction patterns.

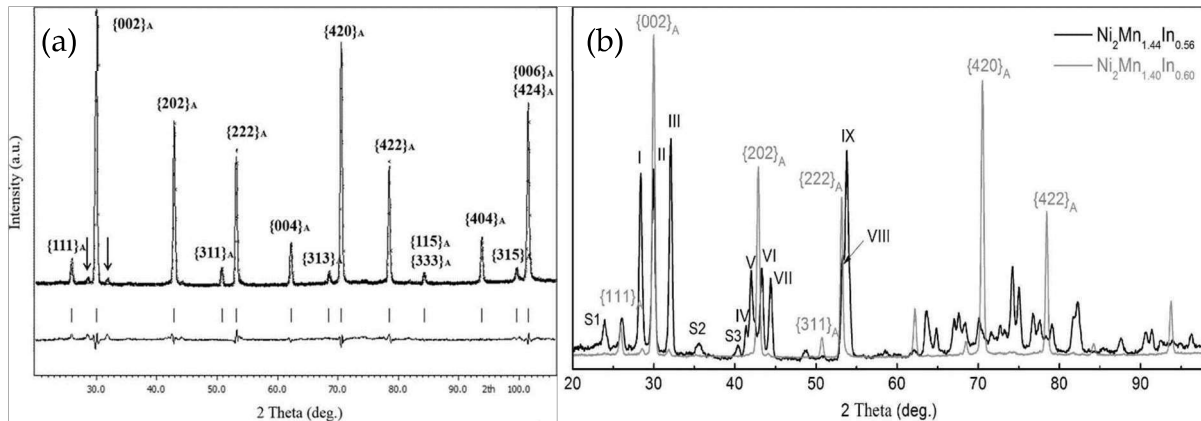


Figure 7. Powder neutron diffraction pattern of: (a) $\text{Ni}_{50}\text{Mn}_{35}\text{In}_{15}$ alloy at room temperature showing measured and Rietveld fitted spectra and their difference; (b) $\text{Ni}_{50}\text{Mn}_{36}\text{In}_{14}$ alloy at room temperature with $\text{Ni}_{50}\text{Mn}_{35}\text{In}_{15}$ shown as reference. (Compositions of both alloys are rewritten) [15].

Peaks are numbered I, II and III around $\{002\}_A$ reflection, IV, V, VI and VII around $\{202\}_A$ and VIII and IX around $\{222\}_A$. From the nature of splitting the average martensitic structure is deduced as monoclinic with space group $I2/m$. Using Bain correspondence between cubic austenite and monoclinic martensite, as many martensitic reflections seen from the splittings are unambiguously identified. Additional S_1 , S_2 , S_3 peaks in Figure 7 (b) which could not be indexed with the average structure model is analysed using the (3+1)-dimensional superspace approach. Through application of crystallographic principles, structural refinement and ab initio calculations the space group of the modulated structure is specified as $I2/m(\alpha 0\gamma)00$ and the incommensurateness of the modulation is established. The incommensurate structure has further been confirmed through EBSD analysis (not discussed here) and belonged to the $P2/m$ space group. Figure 8 shows the high-energy synchrotron XRD patterns of $\text{Ni}_{50}\text{Mn}_{36}\text{In}_{14}$ alloy which was used for the final resolution of the crystal structures with the satellite peaks of martensite and a single reflection from the retained austenite clearly shown.

Rietveld refinement can be applied using free software such as FullProf, to diffraction analysis on a laboratory scale where access to sophisticated synchrotron and neutron diffraction equipment is unlikely. The austenite and martensite unit cells can still be indexed however, precise description of the modulation of martensite including commensurate/incommensurate nature may not be possible. Additional SAED patterns from

TEM are to be obtained to complete the characterization. We present additional examples of cases where structural refinement is performed as well as those corroborated by SAED data.

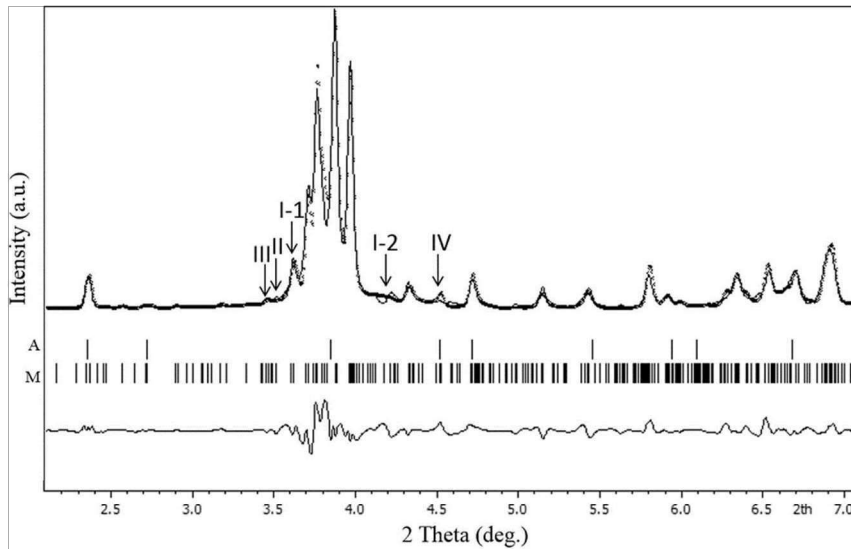


Figure 8. High-energy synchrotron XRD patterns of $\text{Ni}_{50}\text{Mn}_{36}\text{In}_{14}$ alloy at room temperature. The vertical arrow at reflection IV is resolved for retained austenite and all other arrows indicate satellite peaks of martensite [15].

Figure 9 (a) shows the refined crystal structures of both austenite (upper panel) and martensite (lower panel) of $\text{Ni}_{44}\text{Co}_6\text{Mn}_{40}\text{Sn}_{10}$ alloy obtained through wide-angle X-ray diffraction (WAXRD), in situ, on a temperature-dependent Bruker Advance D8 diffractometer [21]. The austenite at 410 K, above the martensitic transformation temperature of 390 K, is indexed to a $L2_1$ structure with space group $Fm\bar{3}m$ and lattice parameter 5.987 Å. The martensite at 300 K, below the martensitic transformation, is indexed to a monoclinic $5M$ modulated structure with space group $P2_1$ and having $a = 4.407$ Å, $b = 5.643$ Å, $c = 21.69$ Å and $\beta = 87.05^\circ$ ($\alpha = \gamma = 90^\circ$). Incidentally this alloy belonged to the category of low thermal hysteresis alloys derived using cofactor conditions for enhanced reversibility of martensitic transformation [30].

Figure 9 (b) shows the refined room temperature structure of $\text{Ni}_{44}\text{Cu}_6\text{Mn}_{39}\text{Sn}_{11}$ alloy in the upper panel and that of $\text{Ni}_{43}\text{Cu}_7\text{Mn}_{39}\text{Sn}_{11}$ alloy in the lower panel [31]. Note that in these alloys Cu instead of Co substitutes Ni and a small difference in composition gives two different structures at room temperature, namely orthorhombic $4O$ martensite in $\text{Ni}_{44}\text{Cu}_6\text{Mn}_{39}\text{Sn}_{11}$ and $L2_1$ cubic austenite in $\text{Ni}_{43}\text{Cu}_7\text{Mn}_{39}\text{Sn}_{11}$. The orthorhombic structure belonged to the space group $Pmma$ with lattice parameters $a = 8.54$ Å, $b = 5.72$ Å and $c = 4.31$ Å. The austenite is of

$Fm\bar{3}m$ space group with lattice parameter 6.00 Å. The compositional difference also has the effect of lowering the transformation temperature from 305 K to 279 K. The alloys are arc-melted and further annealed at 1173 K for one week before quenching in ice water. Figure 9 (c) shows the refined structures of another Cu-doped alloy, Cu substituting Mn and influencing the magnetocaloric properties of the alloys. In the upper panel of Figure 9 (c) is shown the XRD pattern of $Ni_{50}Mn_{32.7}Cu_{1.3}In_{16}$ alloy and in the bottom panel of Figure 9 (c) is shown that of $Ni_{50}Mn_{32.4}Cu_{1.6}In_{16}$ alloy [32]. Both structures are austenitic with fundamental lattice reflections of (220), (400) and (422). Superstructure reflections at (111), (311) and (331) indicate an ordered Heusler structure. The lattice parameters are given as 5.987 Å and 5.975 Å respectively. The compositional difference however increases the martensitic

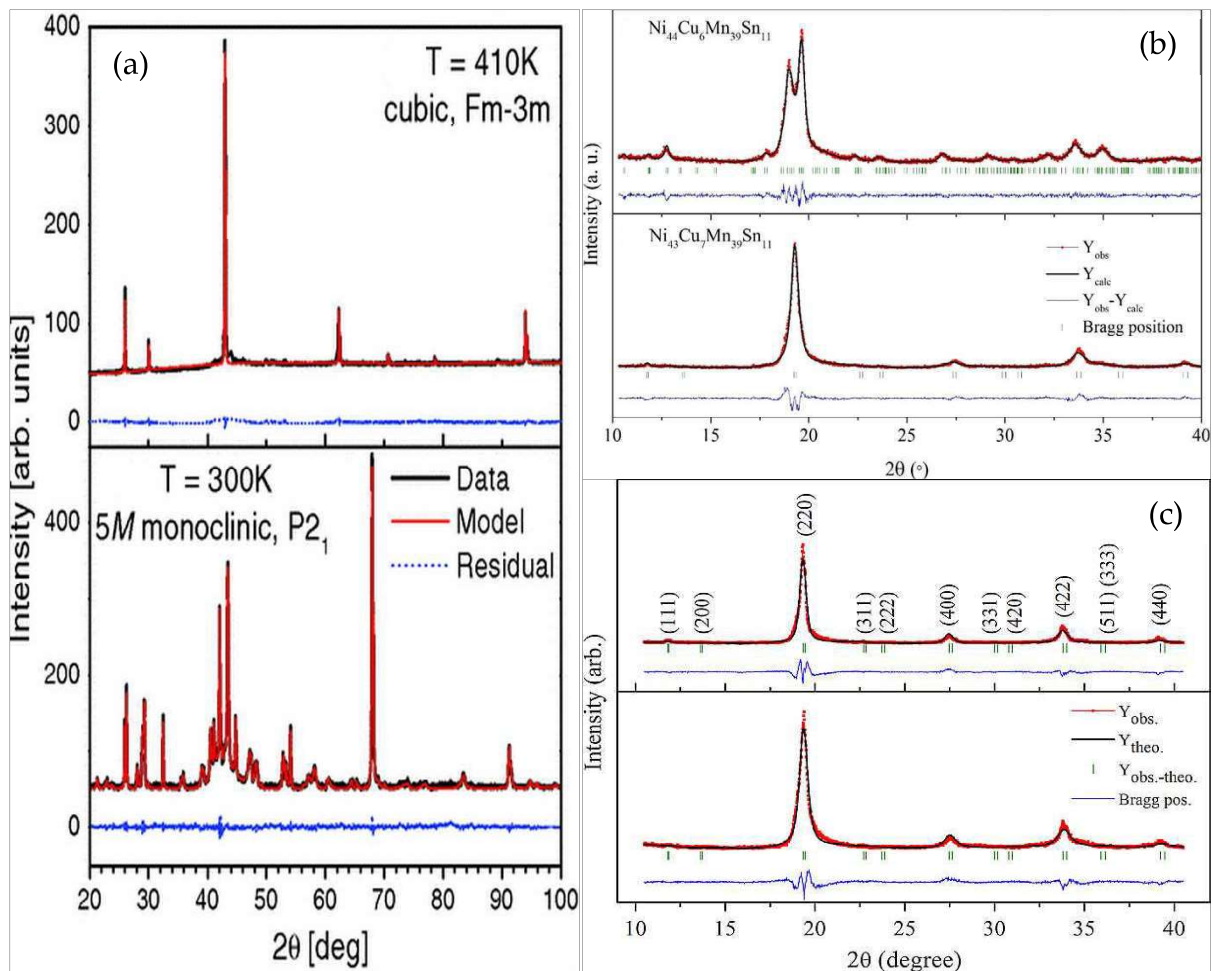


Figure 9. (a) WAXRD patterns from $Ni_{44}Co_6Mn_{40}Sn_{10}$ at $T = 410$ K (up) and $T = 300$ K (down) above and below the martensitic transformation. Heavy and light solid lines represent experimental data and the structural refinement, respectively. The dotted line shows the residual between the experiment and model [20]; (b) XRD patterns of $Ni_{44}Cu_6Mn_{39}Sn_{11}$ (up) and $Ni_{43}Cu_7Mn_{39}Sn_{11}$ (down) alloys at room temperature [30]; (c) XRD patterns of $Ni_{50}Mn_{32.7}Cu_{1.3}In_{16}$ (up) and $Ni_{50}Mn_{32.4}Cu_{1.6}In_{16}$ (down) alloys at room temperature [31].

transformation temperature from 267.5 K to 276.5 K. The alloys measured large positive values of magnetic entropy changes at 25.2 J/kg/K and 5.7 J/kg/K respectively by Maxwell relation. It is to be seen that when Cu substitutes Ni the transformation temperature decreases and when it substitutes Mn the temperature increases. Furthermore, substituting In instead of Sn favours a large magnetic entropy change making it suitable for magnetic refrigeration.

In yet another example of in situ X-ray diffraction carried out on a Bruker D8 Advance diffractometer in the temperature range of 227 K to 465 K we present the case of polycrystalline $\text{Ni}_{50-x}\text{Fe}_x\text{Mn}_{40}\text{Sn}_{10}$ ($x = 0, 2, 4, 6, 8$) alloy ribbons [33]. Structure refined XRD patterns of $\text{Ni}_{48.5}\text{Fe}_{2.2}\text{Mn}_{39.5}\text{Sn}_{9.8}$ alloy are presented in Figure 10. The crystal structures above and below the austenite finish temperature of 386 K and the austenite start temperature of 377 K are indexed to a cubic $P222$, Figure 10 (a) and an orthorhombic $6M$ modulated martensite, Figure 10 (b), respectively. Note that the austenite in this case is not of $L2_1$ formulation.

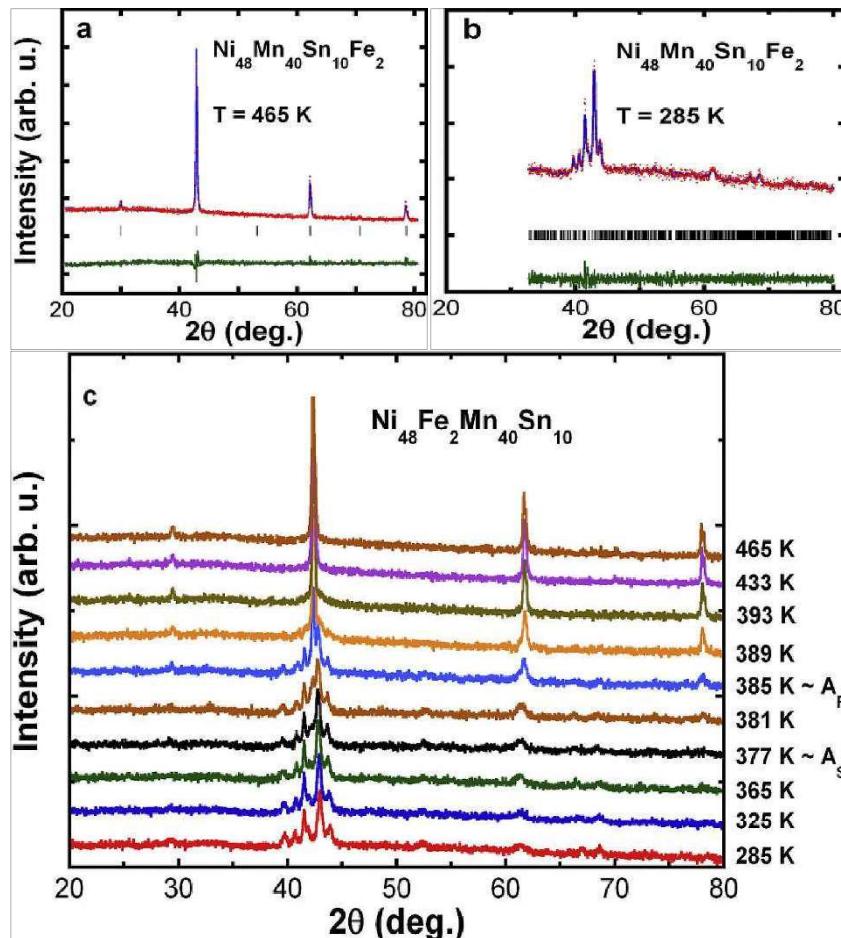


Figure 10. XRD patterns of $\text{Ni}_{48.5}\text{Fe}_{2.2}\text{Mn}_{39.5}\text{Sn}_{9.8}$ ribbons: (a) cubic; (b) orthorhombic and (c) temperature evolution of XRD patterns across martensitic transformation [32].

Between the two temperatures both austenite and martensite coexist. Additional (200) reflections near 30° correspond to a $B2$ structure. The temperature evolution of the XRD patterns across martensitic transformation is shown in Figure 10 (c).

Perez-Sierra et al. [34] observed multiphase solidification in quaternary $\text{Ni}_{45}\text{Co}_5\text{Mn}_{40}\text{Sn}_{10}$, $\text{Ni}_{44.5}\text{Co}_{5.5}\text{Mn}_{39.5}\text{Sn}_{10.5}$ and $\text{Ni}_{43}\text{Co}_7\text{Mn}_{39}\text{Sn}_{11}$ alloys. The phases are $L2_1$ /6-layered martensite, $\text{D}0_3$ phase and γ -phase. While $\text{D}0_3$ dissolved during subsequent annealing, the γ -phase has been reported to dissolve in low Co content (6.4 and 7.2 at%) alloys and stabilized in high Co content (9 at%) alloys. The XRD patterns for the alloy phases are shown in Figure 11, with the top and middle spectra obtained from $\text{Ni}_{44.5}\text{Co}_{5.5}\text{Mn}_{39.5}\text{Sn}_{10.5}$ and the bottom spectrum obtained from $\text{Ni}_{43}\text{Co}_7\text{Mn}_{39}\text{Sn}_{11}$ alloys, even though all alloys exhibited three phases. The pure martensite has been indexed to a monoclinic unit cell with lattice parameters $a = 4.42 \text{ \AA}$, $b = 5.54 \text{ \AA}$, $c = 12.90 \text{ \AA}$ and $\beta = 92.5^\circ$ consistent with a six-layered modulation. The $\text{D}0_3$ unit cell has a lattice parameter of 6.01 \AA while the $L2_1$ and γ -phase unit cells corresponded to 5.96 \AA and 3.71 \AA respectively. To obtain the top spectrum, $\text{Ni}_{44.5}\text{Co}_{5.5}\text{Mn}_{39.5}\text{Sn}_{10.5}$ was homogenized for 14 days at 900°C and for the middle spectrum it was melted and resolidified.

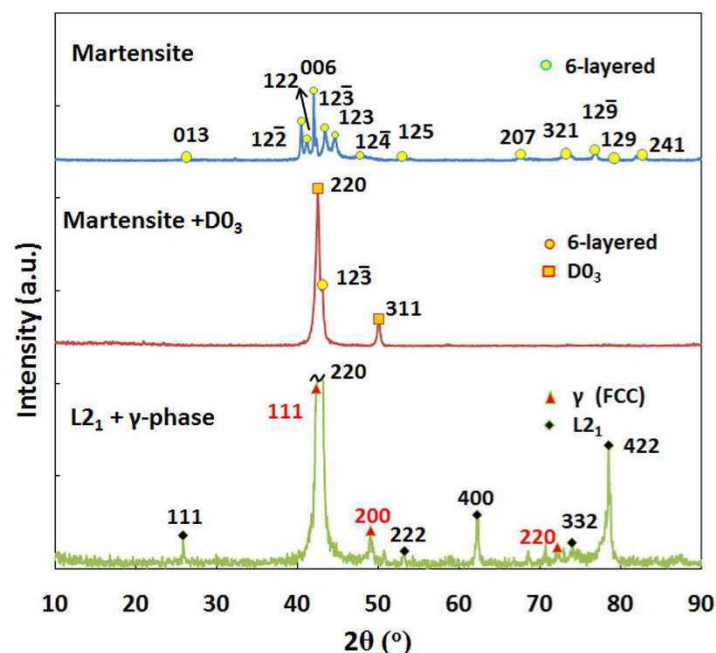


Figure 11. XRD spectra of: (up) $\text{Ni}_{44.5}\text{Co}_{5.5}\text{Mn}_{39.5}\text{Sn}_{10.5}$ alloy showing a pure 6-layered martensite state; (middle) $\text{Ni}_{44.5}\text{Co}_{5.5}\text{Mn}_{39.5}\text{Sn}_{10.5}$ alloy showing a large proportion of $\text{D}0_3$ phase and (bottom) $\text{Ni}_{43}\text{Co}_7\text{Mn}_{39}\text{Sn}_{11}$ alloy containing a mixture of $L2_1$ austenite and γ -phase [33].

The lower spectrum was obtained after annealing the sample for 7 days at 950 °C. The XRD data is corroborated by the SAED data obtained using TEM [34].

Transmission electron microscopy extends the resolution available for morphological studies to the order of 0.1 nm or even sub-angstrom [35]. It combines real space data at excellent resolution and the information from reciprocal space, i.e. electron diffraction patterns can be recorded [35]. SAED is a crystallographic experimental technique to identify crystal structure as well as phases' orientation relationships in a crystalline material. Interested readers may refer [36] for a better understanding of TEM procedures. Preparing a good specimen to be examined using TEM is of paramount importance for the success of TEM analysis. Good samples need to be uniformly thinned to less than 100 nm, while those for lattice imaging in high resolution TEM should be less than 20 nm thick. Samples are thinned by mechanical thinning, electrochemical thinning and ion milling [35]. Ion milling is performed on specialized equipment such as a focused ion beam machining system. An account of TEM sample preparation using a dual beam FIB equipment can be read from [37].

The SAED patterns of the different structures indexed in Figure 11 of [34] are shown in Figure 12. Figure 12 (a) shows patterns corresponding to a disordered face-centred cubic structure of the γ -phase. In Figure 12 (b) can be seen patterns corresponding to different ordered structures of DO_3 and $L2_1$, phases. DO_3 and $L2_1$ are both derived from the *bcc* lattice and incorporate next-nearest-neighbours ordering within one sublattice of the basic unit cell. The sublattice alternates atoms from different elements introducing a face-centred symmetry in the unit cell. In Figure 12 (c) can be seen a single variant of the six-layered martensite, seen in all three alloys in [34].

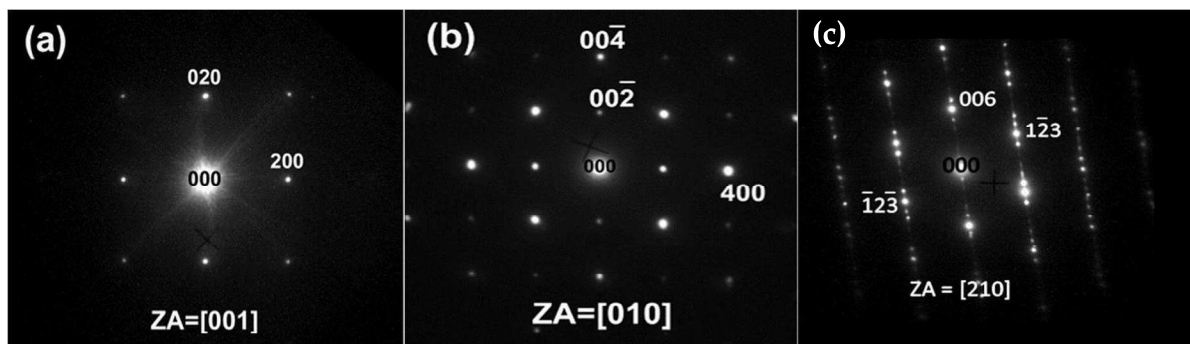


Figure 12. SAED patterns corresponding to: (a) γ -phase along [001] zone axes; (b) DO_3 and $L2_1$ structures along [010] zone axes and (c) 6-layered martensite for a single variant [33].

Similarly the SAED patterns corresponding to the indexed $4O$, $10M$ and $14M$ respectively, of alloys $\text{Ni}_{50}\text{Mn}_{37}\text{Sn}_{13}$, $\text{Ni}_{50}\text{Mn}_{39}\text{Sn}_{11}$ and $\text{Ni}_{50}\text{Mn}_{41}\text{Sn}_9$ [7], are shown in Figure 13 (a) to (c). The XRD data of these alloys is seen in Figure 2 (c) and (d). Interestingly alloy $\text{Ni}_{50}\text{Mn}_{39}\text{Sn}_{11}$ also had coexistent $4O$ and $L1_0$ martensites (not shown). Three satellite spots between the fundamental maxima in the SAED patterns of the $4O$ modulated structure of $\text{Ni}_{50}\text{Mn}_{37}\text{Sn}_{13}$, four satellite spots in the $10M$ structure of $\text{Ni}_{50}\text{Mn}_{39}\text{Sn}_{11}$ and six satellite spots in the $14M$ structure of $\text{Ni}_{50}\text{Mn}_{41}\text{Sn}_9$ can be seen from the Figures.

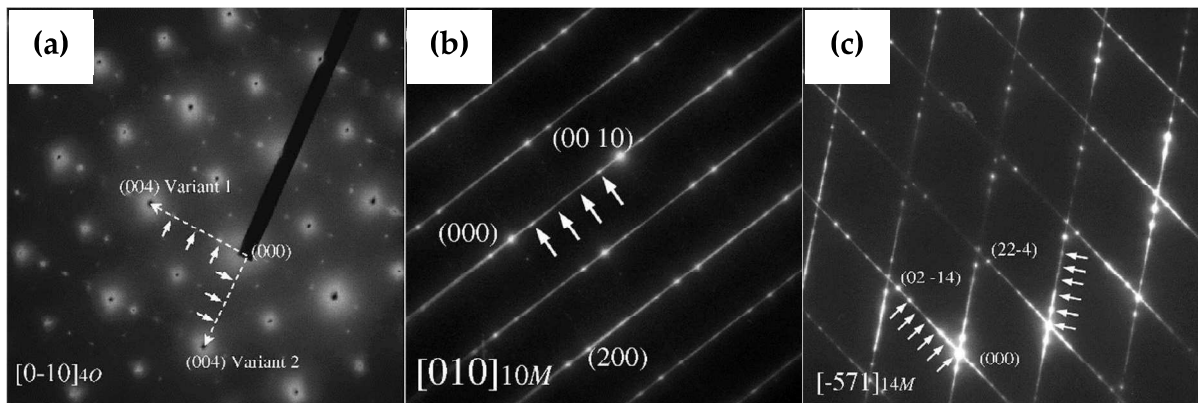


Figure 13. SAED patterns of: (a) $4O$ martensite in $\text{Ni}_{50}\text{Mn}_{37}\text{Sn}_{13}$ (b) $10M$ martensite in $\text{Ni}_{50}\text{Mn}_{39}\text{Sn}_{11}$ and (c) $14M$ martensite in $\text{Ni}_{50}\text{Mn}_{41}\text{Sn}_9$ alloys [7].

Through in situ high-energy XRD procedures, Huang et al. obtained a cubic structure at 400 K and a monoclinic six-layered martensite at 100 K. This is shown in Figure 14 (a) and (b). The SAED diffraction pattern in Figure 14 (c) is seen to have five extra satellite spots between main reflections which are characteristic of the indexed martensite [14]. Even in an uncommon case of a powder processed quinary Ni-Co-Mn-(Sn, Cu) alloy prepared by conventional press and sinter technique using elemental powders, a $6M$ monoclinic structure was indexed as seen from the XRD pattern which is also corroborated by SAED pattern along $[\overline{210}]$ zone axis [38]. This is shown in Figure 15. Room temperature diffraction patterns of $\text{Ni}_{50}\text{Mn}_{37.5}\text{Sn}_{12.5-x}\text{In}_x$ ($x = 0, 2, 4, 6$ at%) synthesized by vacuum hot pressing show a coexistent $L2_1$ and $4O$ martensite for $x = 0$ and $x = 2$ which however changes to a single phase at higher concentrations [39]. It is $4O$ at $x = 4$ and $10M$ at $x = 6$. Based on the X-ray diffraction patterns in Figure 16 and with the help of scanning transmission electron microscope and high angle angular dark field (STEM-HAADF) imaging mode, Figure 17 (a), with atomic number contrast, the microstructure of $\text{Ni}_{50}\text{Mn}_{37.5}\text{Sn}_{12.5}\text{In}_0$ consisted of equiaxed grains of austenite and martensite of size $\sim 2 \mu\text{m}$. This

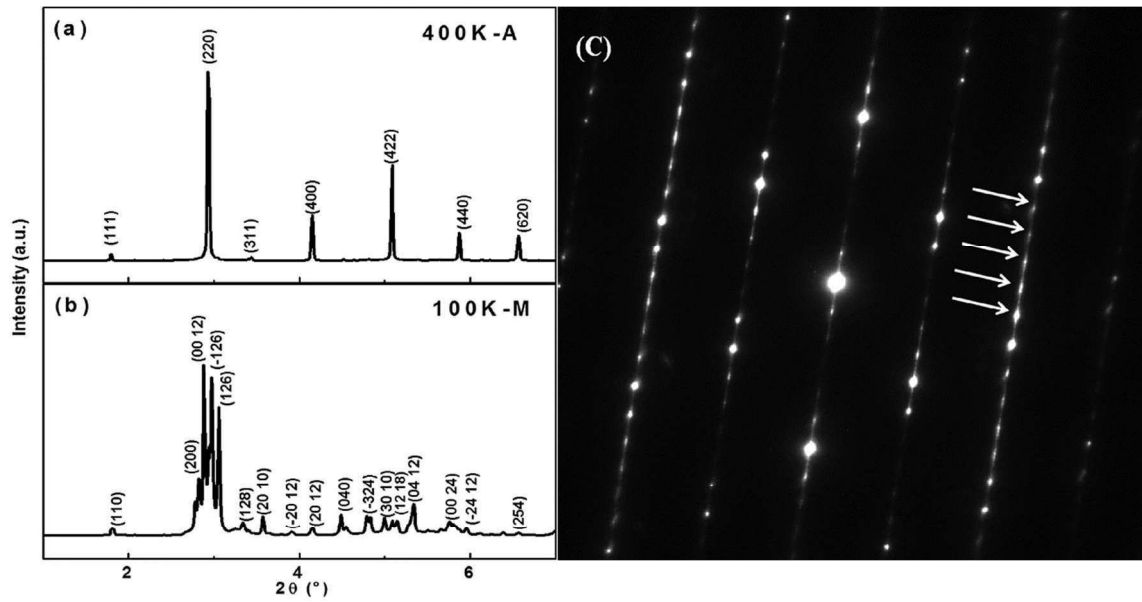


Figure 14. High energy X-ray diffraction patterns at 400 K (a) and 100 K (b) corresponding to austenite (A) and martensite (M) phase respectively; (c) Selected area diffraction pattern (SAEDP) for martensite at room temperature [14].

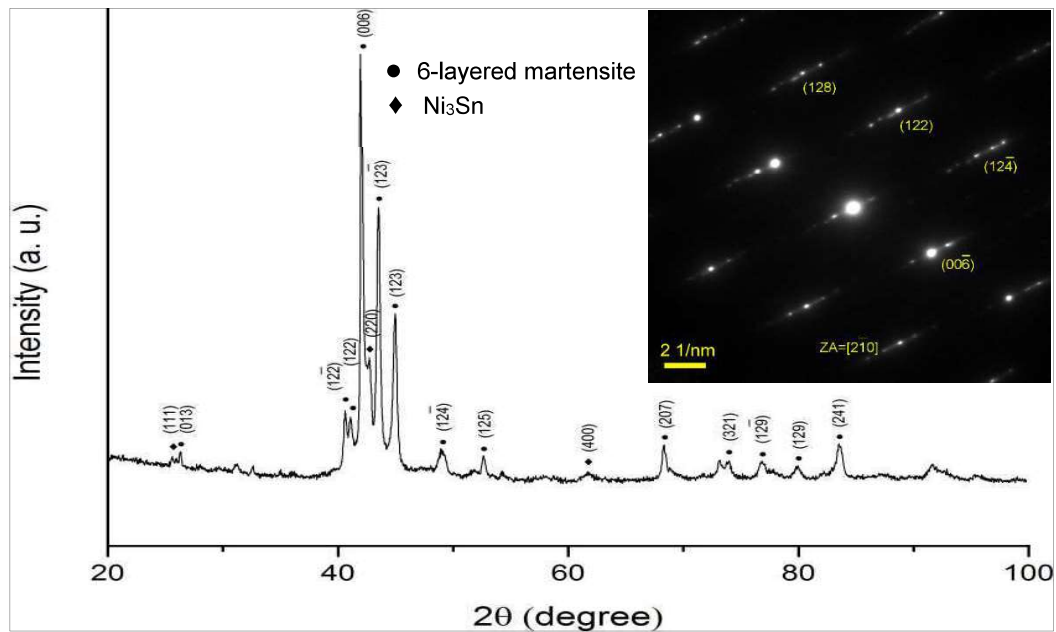


Figure 15. XRD spectrum of the alloy showing a 6M structure and Ni_3Sn phase (Inset) SAED pattern of the 6M martensite along $[2\bar{1}0]$ zone axis [37].

grain size refinement was the reason for the 5% plasticity and 2000 MPa strength observed in this alloy. Dislocations within the austenite grain, whose existence is related to factors such as order of $L2_1$ phase, location at antiphase boundaries, stress induced dislocations during sintering or incompatibility between austenite and martensite crystal structures are shown in Figure 17 (b). The structure of 4O modulated martensite is shown in Figure 17 (c).

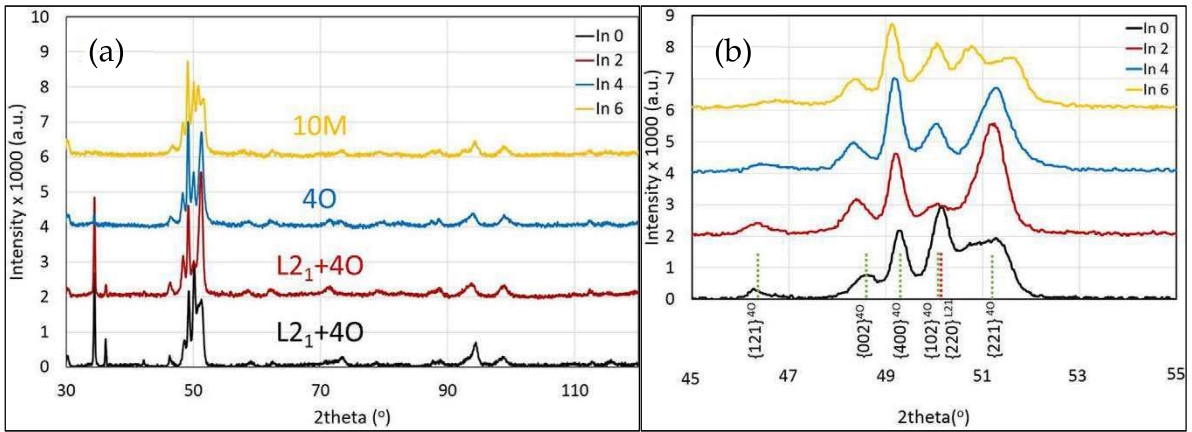


Figure 1716. X-Ray diffraction patterns of sintered alloys in 2theta range a) 30 – 115°; (b) 45 – 55° [38].

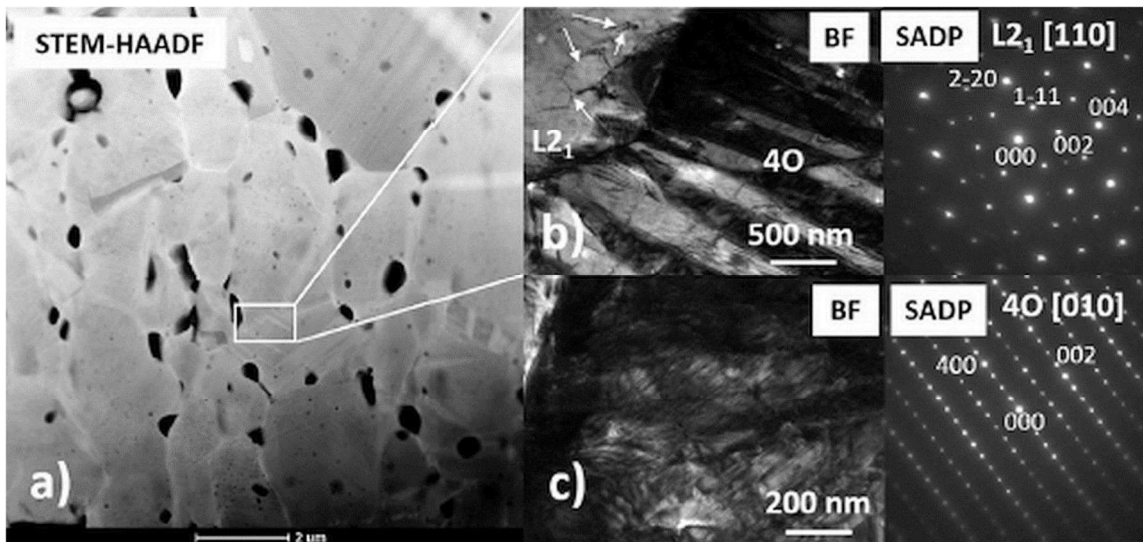


Figure 1617. Set of TEM microstructures consist of (a) STEM-HAADF image; (b) and (c) bright field images and corresponding selected area diffraction patterns of In0 sintered sample [38].

Secondary phases such as γ -phase are seen when the Co content is higher (≥ 8 at %) [40]. This is shown in Figure 18 (a), where traces of fcc- γ structures are detected in $\text{Ni}_{42}\text{Co}_8\text{Mn}_{39}\text{Sn}_{11}$ alloys at 8 at % of Co [41]. In Figure 18 (b) the γ -phase seen in the as-cast structure is absent in the melt-spun alloy of $\text{Ni}_{38}\text{Co}_{12}\text{Mn}_{41}\text{Sn}_9$ composition with 12 at % Co [42]. The melt-spinning process aids in suppressing secondary phases. This aspect has also been confirmed in [43]. Annealing also suppresses spurious phases such as shown by asterisks at 38.2° corresponding to MnSn_2 and at 44.5° and 64.8° corresponding to MnNi in the as-cast structures of [7] in Figure 2 (c), absent in the annealed structures in Figure 2 (d).

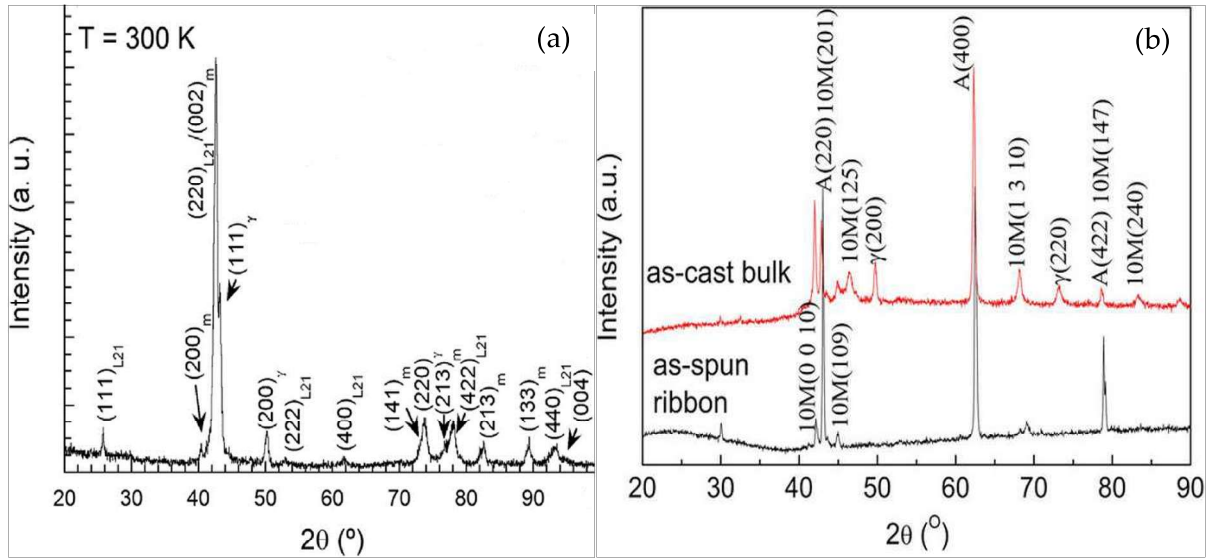


Figure 18. Room temperature XRD patterns of: (a) $\text{Ni}_{42}\text{Co}_8\text{Mn}_{39}\text{Sn}_{11}$ alloy [40]; (b) $\text{Ni}_{38}\text{Co}_{12}\text{Mn}_{41}\text{Sn}_9$ bulk and as-spun alloys [41].

In the case of $\text{Ni}_{51}\text{Mn}_{34}\text{In}_{14}\text{Si}_1$ alloys higher wheel speeds and hence higher solidification rates resulted in partially ordered $B2$ structure instead of the ordered L_{21} austenite [44]. The authors use X-ray diffraction analysis to describe the transition from L_{21} to $B2$ structure. L_{21} structure is identified by reflections from (111) and (311) planes. The presence of (200) reflection and no L_{21} reflections in Figure 19 point to a $B2$ structure. Bragg reflections with non-zero structure factors result from the cubic L_{21} structure when the Miller indices are all even or odd. From the Figure 19 for the first three reflections, the structure factors are $F(111) = 4(f_y - f_z)$, $F(200) = 4[2f_x - (f_y + f_z)]$, and $F(220) = 4[2f_x + f_y + f_z]$, where f_x , f_y and f_z are the average scattering amplitudes for respective sublattices X, Y and Z. In the $B2$ structure the atoms from Y and Z sub-lattices are intermixed and hence the structure factor $F(111)$ is zero (no peaks with all odd indices) indicating a transition from L_{21} to $B2$. Additionally an estimation of the degree of L_{21} order from the patterns using the relation $(I_{111}/I_{220})_{exp}/(I_{111}/I_{220})_{th}$, where I_{hkl} represent the intensity of reflection from the plane with Miller indices (hkl) and the suffices 'exp' and 'th' correspond to experimental and theoretical data, is necessary. A decrease in the degree of order with increasing solidification rate will show that disordered $B2$ structures will form as a result of this.

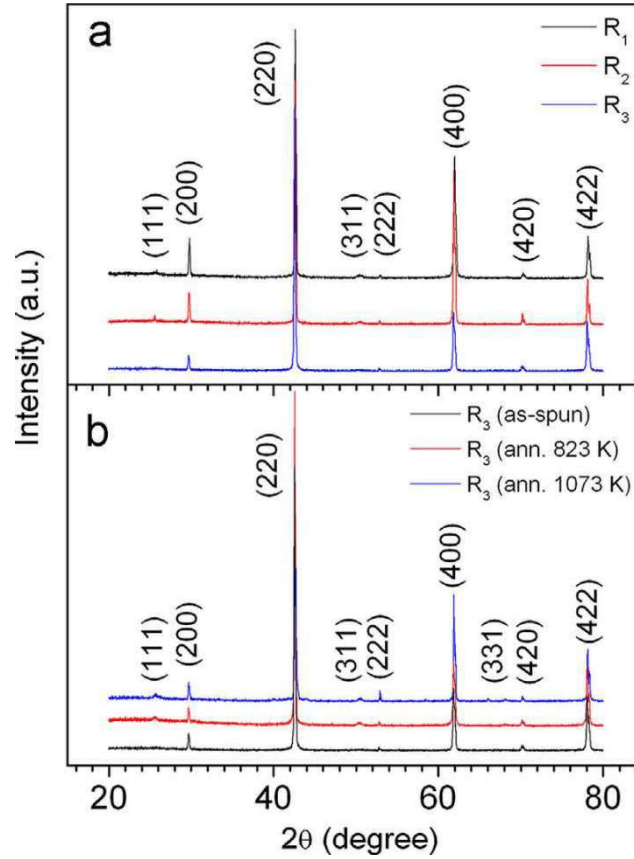


Figure 19. Room temperature XRD patterns of (a) as-spun ribbons and (b) R_3 ribbons annealed at different temperatures [43].

Çakır et al. studied magneto-structural phase transitions and the stability of the different crystallographic structures of $Ni_{50}Mn_{50-x}Sn_x$ alloys under varying temperatures for a broad range of composition $5.1 \leq x \leq 20.3$ ($7.91 \leq e/a \leq 8.34$) [45]. Figure 20 (a) to (k) show the temperature dependent diffraction patterns of the alloys. Using superspace approach [8], the different modulated phases of martensites are indexed as $5M$ (IC), $7M$ (IC) in addition to austenite, $5M$ and $L1_0$ structures for various cooling and warming sequences. IC refers to an incommensurate structure. Added to the austenite-to-martensite transformation, intermartensitic transformation¹ are observed at lower temperatures in Figure 20 (e), (f) and (i). In Figure 20 (e) an intermartensitic transition changes the $5M$ (IC) martensite to $5M$ (IC) + $L1_0$ mixed martensite on cooling. In Figure 20 (f) similar transformation yielded $5M$ (IC) + $7M$ (IC) mixed martensite on cooling and at further lower temperature intermartensitic

¹ Intermartensitic transformations happen when the martensitic phase transforms to other modulated phases at lower temperatures. These are important because reversal back to the original martensitic phase may be difficult and may lead to loss of magnetic shape memory effect.

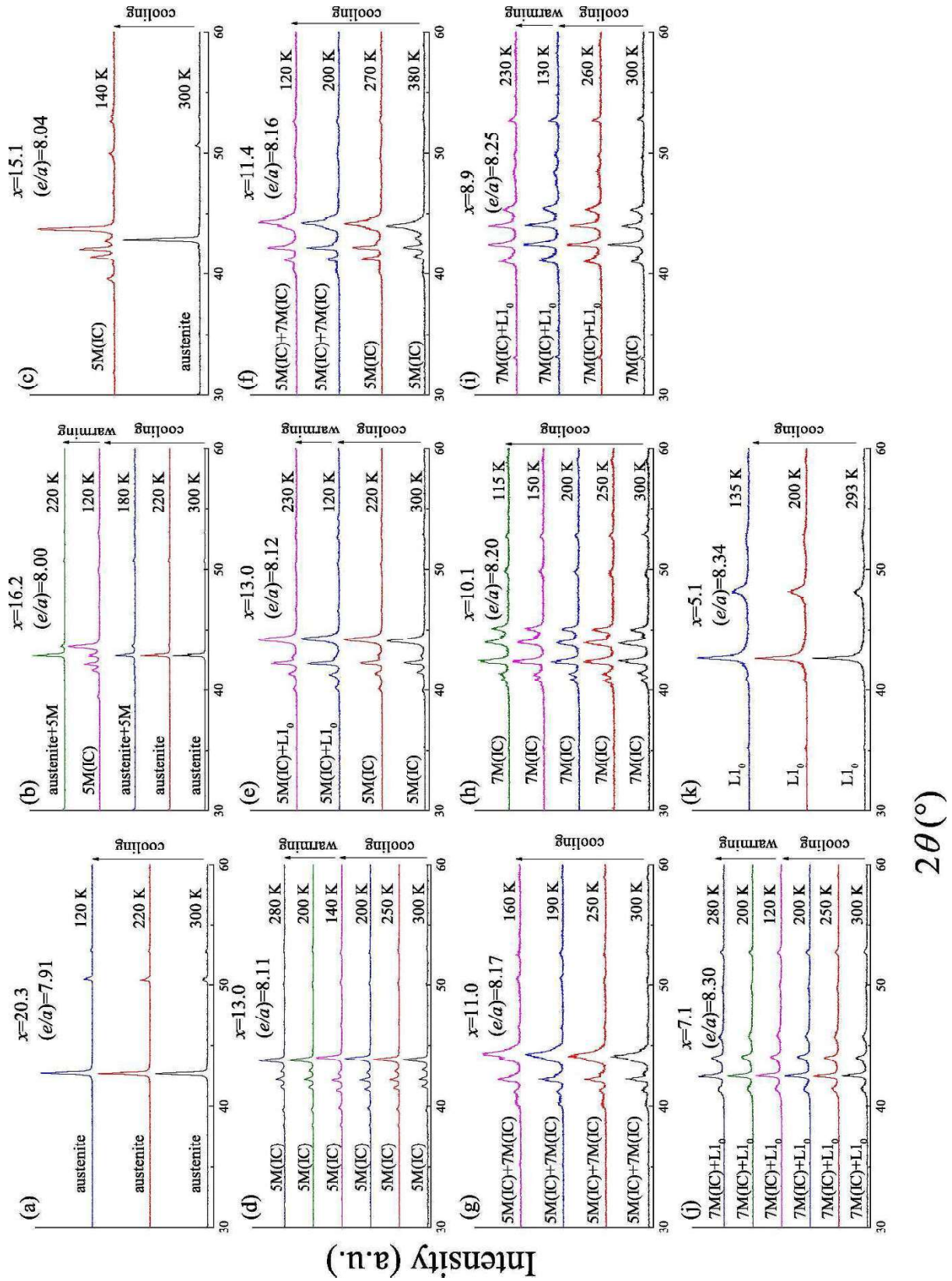


Figure 20. X-ray diffraction patterns shown in the range $30^\circ \leq 2\theta \leq 60^\circ$. (a)-(k) show patterns with varying temperature for $x = 20.3, 16.2, 15.1, 13.0, 11.4, 11.0, 10.1, 8.8, 7.1$ and 5.1 respectively [44].

transformation resulted in a mixed $7M$ (IC) + $L1_0$ from $7M$ (IC). It has been found that intermartensitic transitions lead to stabilization of the $L1_0$ structure and involve broad hysteresis of up to 100 K. This meant that functional properties of the Heusler alloys will be affected if the temperature of the working material is lowered below the intermartensitic start temperature.

Differential scanning calorimetry

Differential scanning calorimetry is a technique of thermal analysis which measures, depending on whether heat is absorbed (endothermic) or liberated (exothermic), the enthalpy of phase transformation in a structurally transforming material as a function of time or temperature. Other physical processes involving change in heat capacity such as glass transition are characterized using DSC. It essentially measures the energy needed to maintain a zero/near-zero difference in temperature between the sample and a reference in controlled heating or cooling regimes. The sample pan with the sample and an empty reference pan are placed on small platforms inside a chamber with thermocouples arranged below [46], as shown in Figure 21 .

The energy is measured in two modes – power compensation and heat-flux modes. The former measures the electrical energy provided to heaters below the pans necessary to

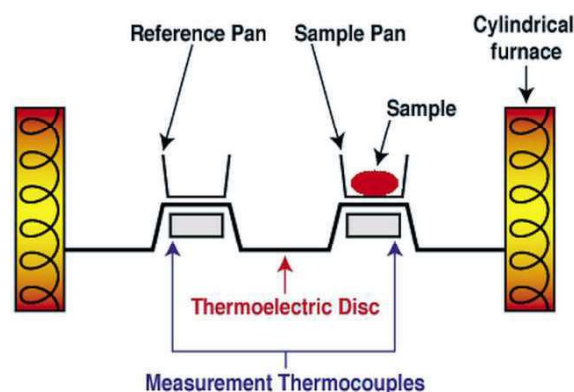


Figure 21. Schematic of a DSC equipment [45].

maintain the two pans at the same temperature, while the latter measures the heat flow (differential temperature) as a function of sample temperature. The output is the differential heat flow (heat/time), q , between the sample and the reference. The heat capacity is

determined from $C_p = \frac{q}{\Delta T}$ where C_p is the heat capacity of the sample and ΔT is the change in temperature over that same time [46]. Heat changes within a transforming sample provide the energy difference required to maintain them at near identical temperatures. A small temperature that may develop between the two is proportional to the heat flow through the platforms on which the pans are placed. This small temperature difference is important to ensure that both pans are within the same temperature regime. An important advantage of DSC is that only a small quantity of material is needed for analysis in order that a uniform temperature distribution and high resolution is ensured as well as the low operational heating and cooling rates, which lead to higher accuracies. First-order transformations obey the classical Clausius-Clapeyron law and are identified by the evolution of latent heat whereas second-order transitions do not evolve latent heat, however are identified by abrupt variations in compressibility, heat capacity, thermal expansion coefficients, etc. [47]. When studying solid-state transformations greater care is needed because the enthalpy changes are smaller or even infinitesimal. Also stored energy in the form of elastic strains and defects reduce the enthalpy change [47].

DSC is used for the determination of martensitic and magnetic transition temperatures, heat flow curves, thermal hysteresis and enthalpy/entropy changes in ferromagnetic Heusler alloys [48-51]. Compositional dependence of martensitic transformation [52], progressive evolution of the martensitic transformation in response to increasing Co content in $Mn_{50}Ni_{40-x}In_{10}Co_x$ alloys [53] and the mechanism of suppression and recovery of martensitic transformation in Ni-Co-Mn-In alloys fabricated under non-equilibrium conditions [54] have been established using DSC. The structural transformation temperatures of interest are the martensitic start (M_s) and finish (M_f) temperatures, exothermic peak of martensitic transformation (M_p), austenitic start (A_s) and finish (A_f) temperatures and the endothermic peak of austenitic transformation (A_p) [40]. Other notations such as T_{AS} , T_{AF} , T_{MS} and T_{MF} respectively for austenitic and martensitic start and finish temperatures are also used [41]. The martensitic transformation temperature T_M is then calculated from $(M_s + M_f + A_s + A_f)/4$. It is also computed as $(M_s + A_f)/2$ [6, 51]. Thermal hysteresis given by $A_s - M_f$ is desired to be minimum (less than 10 °C) for improved reversibility of phase transformation [6].

Figure 22 (a) shows the DSC curves of $\text{Ni}_{42}\text{Co}_8\text{Mn}_{39}\text{Sn}_{11}$ alloy with martensitic and magnetic transformations clearly seen [41]. The austenitic and martensitic start and finish temperatures are clearly marked on the plot and are determined by drawing tangents to the base and largest slope of the peaks. The Curie temperature T_C is identified as the minimum point in both exothermic and endothermic peaks in the cooling and heating curves. DSC scans for $\text{Ni}_{50}\text{Mn}_{37}\text{Sn}_{13}$ are shown in Figure 22 (b) corresponding to the as-cast and heat-treated samples at various durations of heat-treatment [55]. These curves demonstrate that longer durations of heat treatment lower the compositional variations, which tend to mask the intrinsic martensitic transformation and magnetostructural behaviour. This can be seen from either the absence of or broad variations representing martensitic transformation in DSC curves of as-cast and 2h annealed samples and also from the increasing sharpness and intensity of the DSC peaks with increasing duration of annealing in Figure 22 (b).

Magnetization measurements are measured using standard protocols such as field cooled (FC) and field heated (FH) either with or without the application of a magnetic field. The measurement procedures can be read from a review paper on magnetocaloric effect in ferromagnetic Heusler alloys [11]. Maziarz et al. present in Figure 23 (a) and (b), the thermomagnetization curves measured in FC and FH protocols superimposed with DSC curves

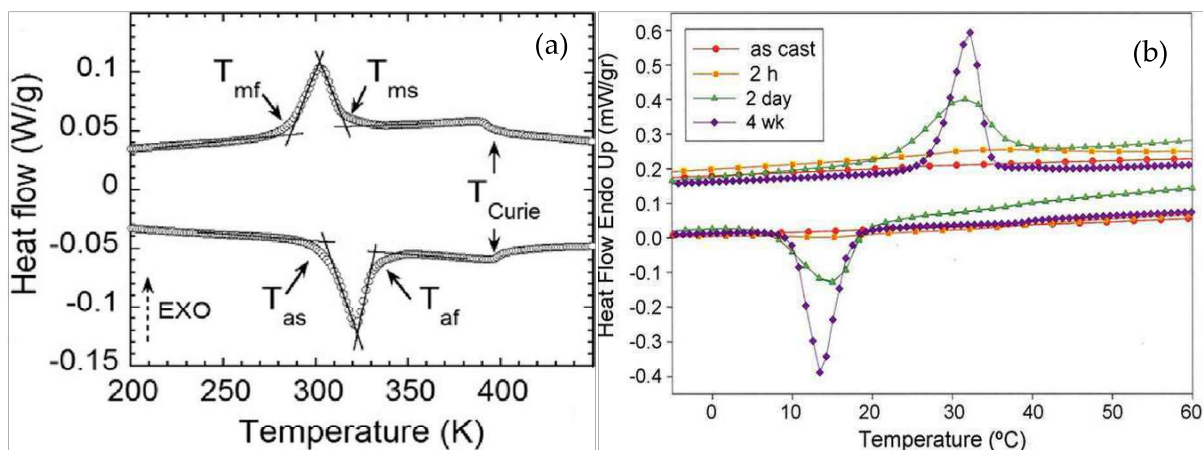


Figure 22. (a) DSC curves showing forward and reverse martensitic transformation and Curie temperature of $\text{Ni}_{42}\text{Co}_8\text{Mn}_{39}\text{Sn}_{11}$ alloy [39]; (b) DSC data $\text{Ni}_{50}\text{Mn}_{37}\text{Sn}_{13}$ showing the effect of heat treatment duration at 950°C on the occurrence, temperature, and sharpness of the martensitic shape memory transformation [54].

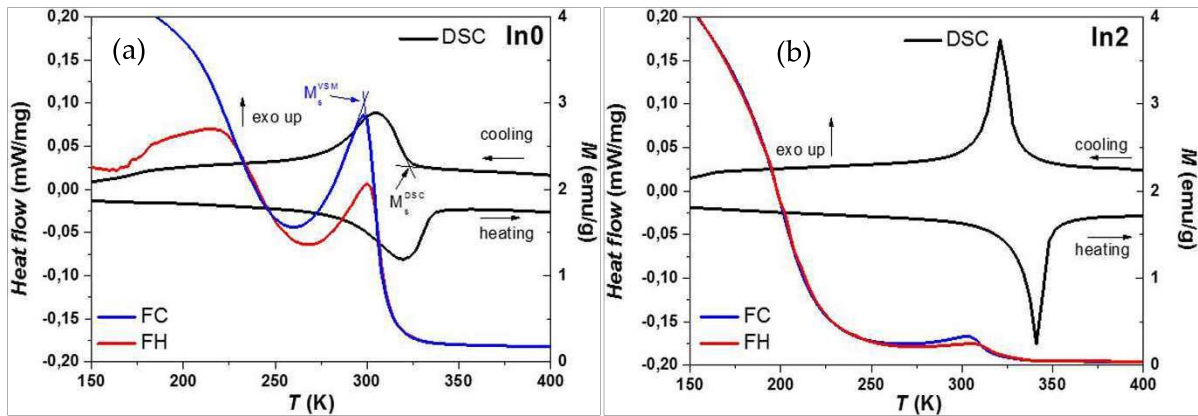


Figure 23. Thermomagnetization curves at low magnetic field (100 Oe) during FC and FH sequences with superimposed DSC curves in the same temperature range for $\text{Ni}_{50}\text{Mn}_{37.5}\text{Sn}_{12.5-x}\text{In}_x$ with: (a) $x = 0$ (In0) and (b) $x = 2$ (In2) alloys [38].

in the same temperature range in order to explain the difference in magnetization between different compositions in $\text{Ni}_{50}\text{Mn}_{37.5}\text{Sn}_{12.5-x}\text{In}_x$ ($x = 0, 2, 4, 6$) alloy system as the relative proximity and essential overlap between the martensitic transformation temperature and the T_C^A [39].

Conclusions

In this paper we have reviewed the microstructural characterization techniques of ferromagnetic Heusler alloys such as XRD, TEM and DSC which are necessary for the comprehension of their structure-property relationship. The results presented in this report are very useful for researchers in this field as sometimes the interpretation of results become very cumbersome due to complexity the spectra (XRD, DSC) or even electron diffraction patterns. To have the information provided here will be quite useful, as a basis of comparison, to analyse the experimental results.

- Martensitic transformation in ferromagnetic Heusler alloys yields a product martensite phase from the parent austenite phase. The crystal structure of austenite is of $L2_1$ Heusler formulation although a cubic $P222$ structure has been reported.
- The unit cell of martensite is either body-centred tetragonal, orthorhombic or monoclinic with modulation leading to the martensitic structure being defined as $5M$, $7M$, $4O$, $5R$, $7R$, depending upon the number of times the unit cell is repeated along certain crystallographic axes. When modulation is absent, the structure is described as non-modulated (NM).

- A superspace (3+1) approach is needed to exactly describe the modulations.
- Sophisticated diffraction procedures using synchrotron and neutron diffraction with in-situ capabilities help in accurately defining the crystal structures.
- On a laboratory scale, simple X-ray diffraction is to be augmented by selected area diffraction patterns from transmission electron microscopy to determine the modulated structures.
- DSC helps in identifying the phases before and after the transformation. However, a combination of DSC and magnetization representation is more definitive than just DSC or magnetization graph.

References

[1] R. Tickle, R.D. James, Magnetic and magnetomechanical properties of Ni₂MnGa, *Journal of Magnetism and Magnetic Materials*, 195 (1999) 627-638.

[2] K. Ullakko, J.K. Huang, C. Kantner, R.C. O'Handley, V.V. Kokorin, Large magnetic-field-induced strains in Ni₂MnGa single crystals, *Applied Physics Letters*, 69 (1996) 1965-1968.

[3] R. Kainuma, Y. Imano, W. Ito, Y. Sutou, H. Morito, S. Okamoto, O. Kitakami, K. Oikawa, A. Fujita, T. Kanomata, K. Ishida, Magnetic-field-induced shape recovery by reverse phase transformation, *Nature*, 439 (2006) 957-960.

[4] R. Kainuma, Y. Imano, W. Ito, H. Morito, Y. Sutou, K. Oikawa, A. Fujita, K. Ishida, S. Okamoto, O. Kitakami, T. Kanomata, Metamagnetic shape memory effect in a Heusler-type Ni₄₃Co₇Mn₃₉Sn₁₁ polycrystalline alloy, *Applied Physics Letters*, 88 (2006).

[5] T. Krenke, E. Duman, M. Acet, E.F. Wassermann, X. Moya, L. Manosa, A. Planes, Inverse magnetocaloric effect in ferromagnetic Ni-Mn-Sn alloys, *Nature Materials*, 4 (2005) 450-454.

[6] V. Srivastava, Y. Song, K. Bhatti, R.D. James, The direct conversion of heat to electricity using multiferroic alloys, *Advanced Energy Materials*, 1 (2011) 97-104.

[7] H. Zheng, W. Wang, S. Xue, Q. Zhai, J. Frenzel, Z. Luo, Composition-dependent crystal structure and martensitic transformation in Heusler Ni-Mn-Sn alloys, *Acta Materialia*, 61 (2013) 4648-4656.

[8] L. Righi, F. Albertini, S. Fabbrici, A. Paoluzi, Crystal structures of modulated martensitic phases of FSM Heusler alloys, in: V.A. Chernenko (Ed.) *Advances in Magnetic Shape Memory Materials*, Trans Tech Publications Ltd, Switzerland, 2011, pp. 105-116.

- [9] A. Pramanick, X.P. Wang, K. An, A.D. Stoica, J. Yi, Z. Gai, C. Hoffmann, X.L. Wang, Structural modulations and magnetic properties of off-stoichiometric Ni-Mn-Ga magnetic shape memory alloys, *Physical Review B*, 85 (2012) 144412.
- [10] R. Ahamed Khan, R. Ghomashchi, Z. Xie, L. Chen, Ferromagnetic Shape Memory Heusler Materials: Synthesis, Microstructure Characterization and Magnetostructural Properties, *Materials*, 11 (2018) 988.
- [11] A. Planes, L.I. Mañosa, M. Acet, Magnetocaloric effect and its relation to shape-memory properties in ferromagnetic Heusler alloys, *Journal of Physics: Condensed Matter*, 21 (2009).
- [12] A. Sozinov, A.A. Likhachev, N. Lanska, O. Soderberg, K. Ullakko, V.K. Lindroos, Effect of crystal structure on magnetic-field-induced strain in Ni-Mn-Ga, in: D.C. Lagoudas (Ed.) *Smart Structures and Materials 2003: Active Materials: Behavior and Mechanics*, Proceedings of SPIE, 2003, pp. 586-594.
- [13] L. Huang, D.Y. Cong, H.L. Suo, Y.D. Wang, Giant magnetic refrigeration capacity near room temperature in Ni₄₀Co₁₀Mn₄₀Sn₁₀ multifunctional alloy, *Applied Physics Letters*, 104 (2014).
- [14] L. Huang, D.Y. Cong, L. Ma, Z.H. Nie, M.G. Wang, Z.L. Wang, H.L. Suo, Y. Ren, Y.D. Wang, Large magnetic entropy change and magnetoresistance in a Ni₄₁Co₉Mn₄₀Sn₁₀ magnetic shape memory alloy, *Journal of Alloys and Compounds*, 647 (2015) 1081-1085.
- [15] H. Yan, Y. Zhang, N. Xu, A. Senyshyn, H.-G. Brokmeier, C. Esling, X. Zhao, L. Zuo, Crystal structure determination of incommensurate modulated martensite in Ni-Mn-In Heusler alloys, *Acta Materialia*, 88 (2015) 375-388.
- [16] X. Xu, W. Ito, I. Katakura, M. Tokunaga, R. Kainuma, In situ optical microscopic observation of NiCoMnIn metamagnetic shape memory alloy under pulsed high magnetic field, *Scripta Materialia*, 65 (2011) 946-949.
- [17] S.A. Speakman, *Basics of X-ray Powder Diffraction*, Massachusetts Institute of Technology.
- [18] B.L. Dutrow, C.M. Clark, *X-ray Powder Diffraction (XRD)*.
- [19] G.J. Long, 2.6 - Neutron Diffraction, in: J.A. McCleverty, T.J. Meyer (Eds.) *Comprehensive Coordination Chemistry II*, Pergamon, Oxford, 2003, pp. 83-90.
- [20] A. Pramanick, X.-L. Wang, Characterization of Magnetoelastic Coupling in Ferromagnetic Shape Memory Alloys Using Neutron Diffraction, *JOM*, 65 (2013) 54-64.
- [21] K.P. Bhatti, S. El-Khatib, V. Srivastava, R.D. James, C. Leighton, Small-angle neutron scattering study of magnetic ordering and inhomogeneity across the martensitic phase transformation in Ni_{50-x}Co_xMn₄₀Sn₁₀ alloys, *Physical Review B*, 85 (2012) 134450.
- [22] T. Krenke, M. Acet, E.F. Wasserman, X. Moya, L. Manosa, A. Planes, Martensitic transitions and nature of ferromagnetism in the austenitic and martensitic states of Ni-Mn-Sn alloys, *Physical Review B*, 72 (2005).

- [23] M. Khan, A.K. Pathak, M.R. Paudel, I. Dubenko, S. Stadler, N. Ali, Magnetoresistance and field-induced structural transitions in $\text{Ni}_{50}\text{Mn}_{50-x}\text{Sn}_x$ Heusler alloys, *Journal of Magnetism and Magnetic Materials*, 320 (2008) L21-L25.
- [24] J.D. Santos, T. Sanchez, P. Alvarez, M.L. Sanchez, J.L.S. Llamazares, B. Hernando, L. Escoda, J.J. Sunol, R. Varga, Microstructure and magnetic properties of $\text{Ni}_{50}\text{Mn}_{37}\text{Sn}_{13}$ Heusler alloy ribbons, *Journal of Applied Physics*, 103 (2008).
- [25] J. Pons, V.A. Chernenko, R. Santamarta, E. Cesari, Crystal structure of martensitic phases in Ni-Mn-Ga shape memory alloys, *Acta Materialia*, 48 (2000) 3027-3038.
- [26] G. Mogylnyy, I. Glavatskyy, N. Glavatska, O. Söderberg, Y. Ge, V.K. Lindroos, Crystal structure and twinning in martensite of $\text{Ni}_{1.96}\text{Mn}_{1.18}\text{Ga}_{0.86}$ magnetic shape memory alloy, *Scripta Materialia*, 48 (2003) 1427-1432.
- [27] N.V.R. Rao, R. Gopalan, V. Chandrasekaran, K.G. Suresh, Microstructure, magnetic properties and magnetocaloric effect in melt-spun Ni-Mn-Ga ribbons, *Journal of Alloys and Compounds*, 478 (2009) 59-62.
- [28] A. Sozinov, A.A. Likhachev, N. Lanska, K. Ullakko, Giant magnetic-field-induced strain in NiMnGa seven-layered martensitic phase, *Appl. Phys. Lett.*, 80 (2002) 1746-1746.
- [29] J.J. Sunol, L. Escoda, B. Hernando, W.O. Rosa, T. Sanchez, J.D. Santos, V.M. Prida, V.G. Shavrov, Structure of rapidly quenched Ga-free Heusler alloys, *Physica Status Solidi (A) Applications and Materials Science*, 208 (2011) 2281-2283.
- [30] Y. Song, X. Chen, V. Dabade, T.W. Shield, R.D. James, Enhanced reversibility and unusual microstructure of a phase-transforming material, *Nature*, 502 (2013) 85-88.
- [31] M. Kaya, I. Dincer, Magnetic and magnetocaloric properties of $\text{Ni}_{50-x}\text{Cu}_x\text{Mn}_{39}\text{Sn}_{11}$ alloys, *Solid State Communications*, 267 (2017) 10-13.
- [32] M. Kaya, S. Yildirim, E. Yüzüak, I. Dincer, R. Ellialtioglu, Y. Elerman, The effect of the substitution of Cu for Mn on magnetic and magnetocaloric properties of $\text{Ni}_{50}\text{Mn}_{34}\text{In}_{16}$, *Journal of Magnetism and Magnetic Materials*, 368 (2014) 191-197.
- [33] C.O. Aguilar-Ortiz, D. Soto-Parra, P. Álvarez-Alonso, P. Lázpita, D. Salazar, P.O. Castillo-Villa, H. Flores-Zúñiga, V.A. Chernenko, Influence of Fe doping and magnetic field on martensitic transition in Ni-Mn-Sn melt-spun ribbons, *Acta Materialia*, 107 (2016) 9-16.
- [34] A.M. Pérez-Sierra, J. Pons, R. Santamarta, P. Vermaut, P. Ochín, Solidification process and effect of thermal treatments on Ni-Co-Mn-Sn metamagnetic shape memory alloys, *Acta Materialia*, 93 (2015) 164-174.
- [35] D. Brandon, W.D. Kaplan, *Transmission Electron Microscopy, Microstructural Characterization of Materials*, John Wiley & Sons, Ltd, 2008, pp. 179-260.
- [36] D.B. Williams, C.B. Carter, *The Instrument, Transmission Electron Microscopy: A Textbook for Materials Science*, Springer US, Boston, MA, 2009, pp. 141-171.

- [37] P.R. Munroe, The application of focused ion beam microscopy in the material sciences, *Materials Characterization*, 60 (2009) 2-13.
- [38] R. Ahamed, R. Ghomashchi, Z. Xie, L. Chen, P. Munroe, S. Xu, Powder processing and characterisation of a quinary Ni-Mn-Co-Sn-Cu Heusler alloy, *Powder Technology*, 324 (2018) 69-75.
- [39] W. Maziarz, A. Wójcik, J. Grzegorek, A. Żywczak, P. Czaja, M.J. Szczerba, J. Dutkiewicz, E. Cesari, Microstructure, magneto-structural transformations and mechanical properties of $\text{Ni}_{50}\text{Mn}_{37.5}\text{Sn}_{12.5-x}\text{In}_x$ ($x=0, 2, 4, 6$ % at.) metamagnetic shape memory alloys sintered by vacuum hot pressing, *Journal of Alloys and Compounds*, 715 (2017) 445-453.
- [40] D.Y. Cong, S. Roth, L. Schultz, Magnetic properties and structural transformations in Ni-Co-Mn-Sn multifunctional alloys, *Acta Materialia*, 60 (2012) 5335-5351.
- [41] P. Lázpita, M. Sasmaz, E. Cesari, J.M. Barandiarán, J. Gutiérrez, V.A. Chernenko, Martensitic transformation and magnetic field induced effects in $\text{Ni}_{42}\text{Co}_8\text{Mn}_{39}\text{Sn}_{11}$ metamagnetic shape memory alloy, *Acta Materialia*, 109 (2016) 170-176.
- [42] F. Chen, Y.X. Tong, Y.J. Huang, B. Tian, L. Li, Y.F. Zheng, Suppression of gamma phase in $\text{Ni}_{38}\text{Co}_{12}\text{Mn}_{41}\text{Sn}_9$ alloy by melt spinning and its effect on martensitic transformation and magnetic properties, *Intermetallics*, 36 (2013) 81-85.
- [43] J.-K. Yu, H.-W. Li, Q.-J. Zhai, J.-X. Fu, Z.-P. Luo, H.-X. Zheng, Crystal structure and formation mechanism of the secondary phase in Heusler Ni-Mn-Sn-Co materials, *Advances in Manufacturing*, 2 (2014) 353-357.
- [44] R. Das, P. Saravanan, D. Arvindha Babu, A. Perumal, A. Srinivasan, Influence of solidification rate and heat treatment on magnetic refrigerant properties of melt spun $\text{Ni}_{51}\text{Mn}_{34}\text{In}_{14}\text{Si}_1$ ribbons, *Journal of Magnetism and Magnetic Materials*, 344 (2013) 152-157.
- [45] A. Çakır, L. Righi, F. Albertini, M. Acet, M. Farle, Intermartensitic transitions and phase stability in $\text{Ni}_{50}\text{Mn}_{50-x}\text{Sn}_x$ Heusler alloys, *Acta Materialia*, 99 (2015) 140-149.
- [46] T. Instruments, TA Instruments Differential Scanning Calorimeter.
- [47] H.K.D.H. Bhadeshia, *Differential Scanning Calorimetry*, 2002.
- [48] S. Aksoy, M. Acet, E.F. Wassermann, T. Krenke, X. Moya, L. Manosa, A. Planes, P. P. Deen, Structural properties and magnetic interactions in martensitic Ni-Mn-Sb alloys, *Philosophical Magazine*, 89 (2009) 2093-2109.
- [49] I. Dubenko, A. Quetz, S. Pandey, A. Aryal, M. Eubank, I. Rodionov, V. Prudnikov, A. Granovsky, E. Lahderanta, T. Samanta, A. Saleheen, S. Stadler, N. Ali, Multifunctional properties related to magnetostructural transitions in ternary and quaternary Heusler alloys, *Journal of Magnetism and Magnetic Materials*, 383 (2015) 186-189.

- [50] T. Krenke, E. Duman, M. Acet, E.F. Wasserman, X. Moya, L. Manosa, A. Planes, E. Suard, B. Ouladdiaf, Magnetic superelasticity and inverse magnetocaloric effect in Ni-Mn-In Physical Review B, 75 (2007).
- [51] Z. Liu, Z. Wu, H. Yang, Y. Liu, W. Wang, X. Ma, G. Wu, Martensitic transformation and magnetic properties in ferromagnetic shape memory alloy $\text{Ni}_{43}\text{Mn}_{46}\text{Sn}_{11-x}\text{Si}_x$, Intermetallics, 19 (2011) 1605-1611.
- [52] T. Krenke, E. Duman, M. Acet, X. Moya, L. Manosa, A. Planes, Effect of Co and Fe on the inverse magnetocaloric properties of Ni-Mn-Sn, Journal of Applied Physics, 102 (2007).
- [53] Z. Wu, Z. Liu, H. Yang, Y. Liu, G. Wu, Effect of Co addition on martensitic phase transformation and magnetic properties of $\text{Mn}_{50}\text{Ni}_{40-x}\text{In}_{10}\text{Co}_x$ polycrystalline alloys, Intermetallics, 19 (2011) 1839-1848.
- [54] Z.L. Wang, D.Y. Cong, Z.H. Nie, J. Gao, W. Liu, Y.D. Wang, The suppression and recovery of martensitic transformation in a Ni-Co-Mn-In magnetic shape memory alloy, Journal of Alloys and Compounds, 511 (2012) 41-44.
- [55] D.L. Schlagel, R.W. McCallum, T.A. Lograsso, Influence of solidification microstructure on the magnetic properties of Ni-Mn-Sn Heusler alloys, Journal of Alloys and Compounds, 463 (2008) 38-46.